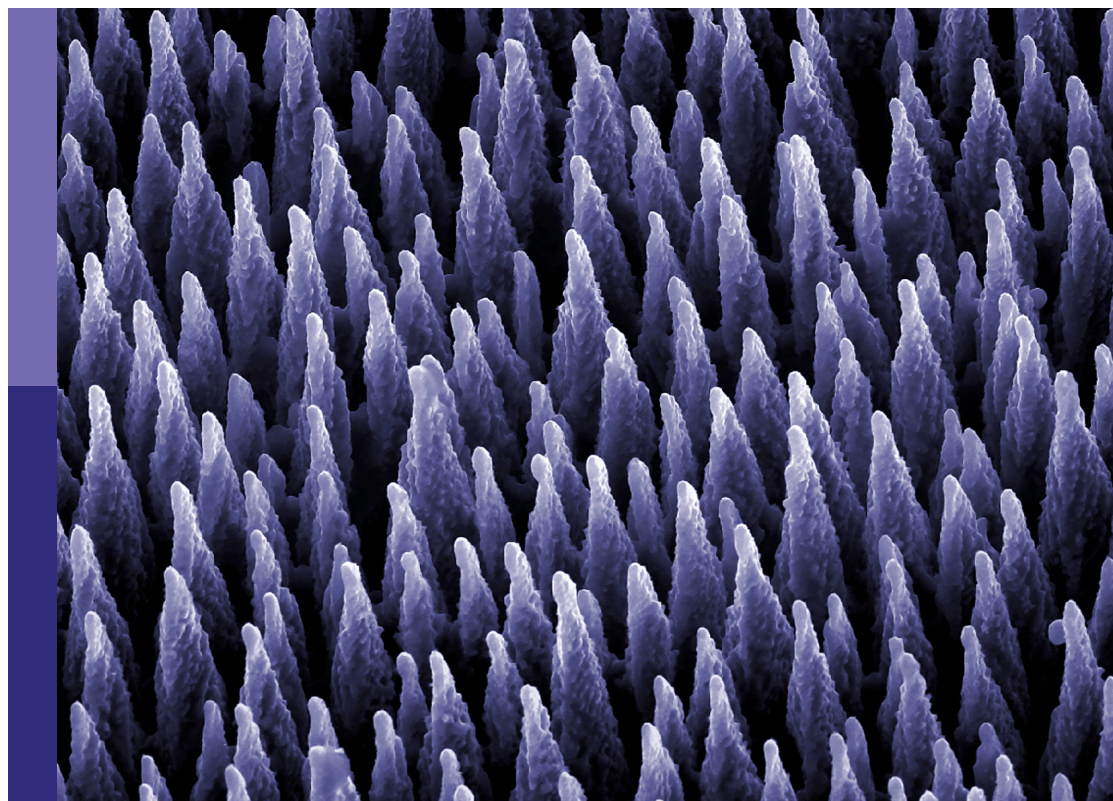# Static and dynamic performance analysis of structures and materials under complex loads and environmental excitation

Edited by
Ping Xiang, Abdelmoumen Anis Bousahla, Huaping Wang and Adesola Ademiloye

About Frontiers

Frontiers is more than just an open access publisher of scholarly articles: it is a pioneering approach to the world of academia, radically improving the way scholarly research is managed. The grand vision of Frontiers is a world where all people have an equal opportunity to seek, share and generate knowledge. Frontiers provides immediate and permanent online open access to all its publications, but this alone is not enough to realize our grand goals.

Frontiers journal series

The Frontiers journal series is a multi-tier and interdisciplinary set of open-access, online journals, promising a paradigm shift from the current review, selection and dissemination processes in academic publishing. All Frontiers journals are driven by researchers for researchers; therefore, they constitute a service to the scholarly community. At the same time, the *Frontiers journal series* operates on a revolutionary invention, the tiered publishing system, initially addressing specific communities of scholars, and gradually climbing up to broader public understanding, thus serving the interests of the lay society, too.

Dedication to quality

Each Frontiers article is a landmark of the highest quality, thanks to genuinely collaborative interactions between authors and review editors, who include some of the world's best academicians. Research must be certified by peers before entering a stream of knowledge that may eventually reach the public – and shape society; therefore, Frontiers only applies the most rigorous and unbiased reviews. Frontiers revolutionizes research publishing by freely delivering the most outstanding research, evaluated with no bias from both the academic and social point of view. By applying the most advanced information technologies, Frontiers is catapulting scholarly publishing into a new generation.

What are Frontiers Research Topics?

Frontiers Research Topics are very popular trademarks of the *Frontiers journals series*: they are collections of at least ten articles, all centered on a particular subject. With their unique mix of varied contributions from Original Research to Review Articles, Frontiers Research Topics unify the most influential researchers, the latest key findings and historical advances in a hot research area.

Find out more on how to host your own Frontiers Research Topic or contribute to one as an author by contacting the Frontiers editorial office: frontiersin.org/about/contact

Static and dynamic performance analysis of structures and materials under complex loads and environmental excitation

Topic editors

Ping Xiang — Central South University, China
Abdelmoumen Anis Bousahla — University of Sidi-Bel-Abbès, Algeria
Huaping Wang — Lanzhou University, China
Adesola Ademiloye — Swansea University, United Kingdom

Table of contents

Editorial: Static and dynamic performance analysis of structures and materials under complex loads and environmental excitation

Ping Xiang[1]*, Adesola S. Ademiloye[2], Huaping Wang[3] and Abdelmoumen Anis Bousahla[4]

[1]School of Civil Engineering, Central South University, Changsha, China, [2]Faculty of Science and Engineering, Swansea University, Swansea, United Kingdom, [3]School of Civil Engineering and Mechanics, Lanzhou University, Lanzhou, China, [4]Multiscale Modeling and Simulation Laboratory, Department of Physics, Faculty of Exact Sciences, University of Sidi Bel Abbés, Sidi Bel Abbés, Algeria

Editorial on the Research Topic
Static and dynamic performance analysis of structures and materials under complex loads and environmental excitation

The rapid evolution of structural materials and construction methodologies has ushered in a transformative era for civil engineering, driven by the urgent need to achieve carbon neutrality and enhance infrastructure resilience. As societies demand safer, more durable, and environmentally adaptive structures, the imperative to understand the static and dynamic behaviors of materials and systems under complex loads has never been more critical. This Research Topic seeks to address these challenges by consolidating cutting-edge research on the interplay between innovative materials, advanced analytical techniques, and real-world engineering applications. The contributions within this Research Topic reflect a multidisciplinary effort to bridge theoretical insights with practical solutions, offering novel perspectives on structural integrity, damage mitigation, and performance optimization across diverse engineering domains.

The global push toward sustainable infrastructure has catalyzed the adoption of novel materials such as fiber-reinforced composites, high-performance concrete, and smart sensing technologies. However, their integration into large-scale projects necessitates rigorous evaluation under realistic conditions, such as seismic events, typhoon-level wind loads and prolonged environmental degradation. This research emphasizes the dual focus on macro-scale structural resilience and micro-scale material behavior, recognizing that the durability of infrastructures hinges on both the robustness of their components and the adaptability of their design. By exploring interactions between dynamic loads, environmental factors, and material properties, the featured studies collectively advance our capacity to predict, monitor, and enhance structural performance in increasingly volatile climates.

The ten articles published in this Research Topic exemplify the diversity and depth of contemporary research in this field. Ji et al. investigate the cyclic performance of steel-tube-enabled precast column connections, offering a paradigm shift in emulative design for seismic-resistant structures. Their experimental findings underscore the potential of modular construction to balance prefabrication efficiency with seismic durability. Complementing this, Qin et al. delve into fatigue damage mechanisms in plain and steel fiber-reinforced concrete, proposing a microplane model that correlates stiffness degradation with cyclic loading patterns. This work not only refines predictive tools for material fatigue but also provides actionable insights for designing longer-lasting pavements and bridge decks subjected to repetitive vehicular stresses.

Environmental exposure remains a persistent threat to material longevity, particularly in coastal and industrial settings. Li et al. examine the dynamic mechanics of reef limestone concrete during dry-wet carbonation cycles, revealing how microcrack propagation under fluctuating humidity accelerates energy dissipation. Their findings highlight the vulnerability of marine structures to climate-induced degradation, urging the adoption of corrosion-resistant additives in coastal infrastructure. Similarly, Guo et al. explore the flexural behavior of high-performance concrete (HPC) under prolonged alkaline immersion, linking mesoscale fracture mechanisms to the efficacy of alkali-silica reaction (ASR) inhibition measures. These studies collectively advocate for material innovations that harmonize strength with environmental adaptability. The intersection of traditional materials and modern reinforcement techniques is exemplified by Li et al., who demonstrate how carbon fiber-reinforced polymer (CFRP) strengthening can revitalize aging wooden arch bridges. Through experimental and numerical validation, their work provides a blueprint for retrofitting heritage structures without compromising historical aesthetics. Meanwhile, Zhang et al. address a ubiquitous yet understudied issue: the compression behavior of steel angles with bolt-hole defects. By quantifying the load-bearing penalties imposed by localized imperfections, their research informs safer fabrication standards for steel frameworks in high-rise buildings and transmission towers.

Dynamic load modeling and computational mechanics form another pillar of this Research Topic. Jianqiu et al. present a theoretical framework for predicting soil column deformation under impact loads, integrating the Duncan-Chang constitutive model with real-world validation. This approach enhances the accuracy of geotechnical simulations for scenarios such as pile driving or landslide impacts. On the structural health monitoring front, Ying et al. investigate the coupled static-dynamic response of thermally damaged mortar, offering a methodology to assess fire-affected buildings' residual capacity.

The Research Topic also ventures into granular material science, with He et al. establishing empirical relationships between micro-texture, Vickers hardness, and the polished stone value (PSV) of high-friction aggregates. Their models enable pavement engineers to select skid-resistant materials proactively, reducing accident risks on highways. Lastly, Huang et al. analyze the lateral impact resistance of notched steel tubes, revealing how localized flaws alter energy absorption mechanisms.

Collectively, these studies highlight pivotal advancements in understanding how materials and structures respond to complex challenges, emphasizing the critical need for multiscale analysis that connects atomic-level behavior to large-scale structural performance, the transformative potential of smart technologies like fiber-optic sensing and advanced computational modeling in enabling real-time infrastructure monitoring, and the urgent requirement to align innovation with sustainability goals to ensure new materials and methods support global decarbonization efforts. As climate change accelerates the occurrence and intensity of extreme events, the knowledge generated through this Research Topic equips engineers to develop infrastructure that is not only more robust and intelligent but also inherently adaptable to the unpredictable demands of the 21st century. Looking ahead, challenges persist in standardizing performance metrics for emerging materials, scaling laboratory findings to field applications, and optimizing life-cycle costs for sustainable systems. Future research must prioritize cross-disciplinary collaboration, leveraging advances in artificial intelligence, nanotechnology, and renewable materials to address these gaps. We extend our gratitude to all authors, reviewers, and editors who contributed to this Research Topic, fostering a dialogue that will shape the next-generation of civil engineering solutions.

Author contributions

Funding

Conflict of interest

The authors declare that the research was conducted in the absence of any commercial or financial relationships that could be construed as a potential conflict of interest.

The author(s) declared that they were an editorial board member of Frontiers, at the time of submission. This had no impact on the peer review process and the final decision.

Generative AI statement

The authors declare that no Generative AI was used in the creation of this manuscript.

Publisher's note

Lateral impact response of circular hollow steel tubes with mid-span localized penetrating notches

Xiaoli Huang[1] and Yulin Wang[2]*

[1]Urban and Rural Architectural School, Minxi Vocational and Technical College, Longyan, China, [2]College of Civil Engineering, Huaqiao University, Xiamen, China

In this study, 32 numerical models of CHST columns were established in the ABAQUS program to evaluate the effect of mid-span local defects on the impact resistance of circular hollow steel tube (CHST) columns. The simulation studies were conducted from three aspects: notch length, notch angle, and impact energy. The results showed that under a lateral impact load, the mid-span of the CHST column presented global bending failure patterns accompanied by local indentation deformation in the impact region and local buckling deformation at the bottom of the fixed end. Compared with the mid-span indentation displacement of the non-notch model, when the impact velocities were 30 km/h and 60 km/h, the horizontal notch model surpassed the maximum by 29.3% and 36.3%, the oblique notch model surpassed the maximum by 47.8% and 115.6%, and the vertical notch model only increased by 9.7% and 1.1%. The local damage area and impact force time-history curves of the vertical notch model agreed well with those of the non-notch model. Among the three notch angles, the impact plateau values of the vertical notch model and the global bending displacement in the mid-span were least affected by the notch length, notch location, and impact energy. The energy absorption of the CHST column was mainly due to indentation deformation in the mid-span, and the global bending deformation was auxiliary. Compared with the energy absorption ratio (EAR) of the non-notch model, with increased impact energy, the EAR of the vertical notch model increased by 20.2%, 13.5%, and 17.3% on average. The horizontal and oblique notch models decreased by 28.2%, 61.0%, 42.4%, and 29.1%, 62.7%, and 49.3%, respectively. The R_d of all notch models showed an overall upward trend as the impact energy increased, and the R_d of the horizontal notch model increased the most. According to the parametric analysis results, the dynamic flexural capacity prediction formula of the CHST columns section was obtained, considering the influence of notch length, notch angle, and impact energy within the parameter range of this study.

1 Introduction

Circular steel tubes are widely used in marine, industrial, and large spatial structures such as stadiums, airports, bridges, offshore oil platforms, power towers, communication towers, and billboards. The performance of these structures in corrosive environments is critical to ensure their overall safety and extend their service life. Although anti-corrosion coatings are widely used in existing steel structures, steel components are unavoidably corroded in complex and changeable environments. Depending on the environment in which the

structure is located, uniform and localized corrosion of structural members may occur, with uniform corrosion being easier to control. In addition to using anti-corrosion coatings in practical designs, thin-walled steel members can resist corrosion by adding additional thickness; however, localized corrosion is more unpredictable and difficult to perceive (Hu et al., 2014).

Several researchers have conducted a series of studies on the mechanical properties of thin-walled structures in fully corrosive environments. Under the combined action of long-term loading and chloride corrosion, the bearing capacity, stiffness, and ductility of concrete-filled steel tubes (CFST) are reduced to varying degrees (Hou et al., 2013; Han et al., 2014; Li et al., 2015; Hou et al., 2016). The bearing capacity and energy dissipation capacity of CFST are reduced under the corrosive effect of an acid rain environment (Chen et al., 2018; Yuan et al., 2018). In addition, numerous researchers have conducted comprehensive analyses of the mechanical properties of steel members under local corrosion conditions. Localized galvanic coupling corrosion significantly reduces the ultimate strength of steel tubes and changes their buckling direction. Both circumferential and longitudinal corrosion lead to deviations in the centroid of the section, and the influence of circumferential corrosion on the bearing capacity of a steel tube is greater than that of longitudinal corrosion (Wang H. et al., 2020a). To simulate local corrosion, many scholars have used artificial notches in steel members to simulate local region weakening and have proposed corresponding prediction models to calculate the residual strength of members (Jiang and Soares, 2012; Saad-Eldeen et al., 2013; Ahn et al., 2016; Liang et al., 2020). Both local hole-type and crack-type corrosion reduced the load-deformation capacity and ultimate strength of the members, and the mechanical properties of the hole-notch members were superior to those of the crack-notch members. Local buckling after the yield of the notch region primarily caused the failure of the member, and the closure phenomenon occurred in both types of corrosion notches. The double-peak phenomenon of horizontal notch members after the notch is closed is more conducive to the post-buckling behavior of steel tubes (Wang et al., 2020b; Shan et al., 2022).

However, during the normal service period of steel members, it is impossible to avoid low-frequency, frequent, and extremely harmful impact hazards, such as impact loads caused by automobiles, temporary construction facilities, mountain floods, rockfalls, explosions, earthquakes, or coastal steel members hit by ships. Although the duration of the impact load is short, its instantaneous energy is huge, which poses serious safety risks to steel members. Thus far, several scholars have studied and analyzed the impact resistance of hollow steel members. Hou (Hou, 2012) studied the mechanical properties of circular hollow steel tubes and concrete-filled steel tubes under low-velocity lateral impact and concluded that, compared with concrete-filled steel tube members, the plastic deformation area of hollow steel tube members was concentrated in the drop hammer impact area, the mid-span deflection was larger, and the local deformation was more serious. Numerous experimental studies and finite element simulation analyses were conducted under the influence of different parameters, such as impact position, repeated impact, axial preloading, impact velocity, and different section types, and the corresponding impact energy absorption relationship and empirical formulas were proposed in ref. (Zeinoddini et al., 2002; Bambach et al., 2008; Al- et al., 2011; Shan et al., 2023).

The above studies have not considered the impact of the corrosion environment on the impact performance of steel members, and it is unavoidable for steel members to encounter impact-corrosion conditions in practical engineering applications. Literature (Yulin et al., 2022) investigated the transverse impact response of concrete-filled steel tubular columns with localized corrosion and obtained the corresponding bearing capacity formulas by considering the influence of the impact surface, the length and angle of the cracks, etc., but did not consider the influence of steel fracture. However, the local defect region of the steel member is prone to fracture failure under impact loading, which is unfavorable for the impact resistance of the member. Recently, some interesting methods, such as the element-free kp-Ritz method and the numerical Galerkin method, have been developed and used to analyze the progressive damage and fracture failure of structural materials (Yin et al., 2023a; Yin et al., 2023b). Therefore, this study aims to introduce the fracture parameters of steel in a finite element analysis (FEA) based on previous studies and further explore the effects of corrosion orientation, corrosion length, and impact energy on the impact resistance of circular steel tube columns with localized corrosion.

In this study, numerical models of the lateral impact of circular hollow steel tube (CHST) columns are established using the ABAQUS program. A local notch was used to simulate the localized corrosion of the CHST columns. The impact velocity, notch angle, and notch length effects on the impact resistance and dynamic flexural bearing capacity coefficients of CHST columns were investigated. Based on the simulation results, the CHST mid-span stress development process and its overall energy dissipation mechanism were analyzed. The development trend of the mid-span damage paths of various notch models was described. Subsequently, a prediction method was proposed to consider these parameters for the cross-sectional bearing capacity of a locally notched CHST under lateral impact.

2 Overview of numerical simulation

2.1 Model design

The initial CHST model was established using the ABAQUS software. The initial model had a section diameter $D = 500$ mm, wall thickness $t = 16$ mm for the steel tube, and length $L = 4,000$ mm. The ends of the steel tube were equipped with end plates of diameter 600 mm and thickness 25 mm. One end of the tube was provided with a fixed constraint, and the other with a simple support constraint. The drop hammer mass used in the model was 1,500 kg. The impact position was at the mid-span. The designed impact velocities (V) were 30 km/h, 45 km/h, 60 km/h, 75 km/h, and 90 km/h, and the corresponding impact energies (E_i) were 52.1 kJ, 117.2 kJ, 208.3 kJ, 325.5 kJ, and 468.8 kJ, respectively. Based on this initial model, local corrosion was simulated by setting a local penetrating notch at the mid-span of the steel tube. The width of the local notch is 16 mm. The notch model adopted semi-arc transitions at the notch ends. Simultaneously, different notch lengths (500, 375, and 250 mm) and notch angles (0°, 45°, and 90°) are designed to explore the influence of the above parameters on the dynamic response of the circular hollow steel tube under lateral impact. The specific local corrosion parameters and model numbers

TABLE 1 Parameters of the CHST model.

Model number	Notch length l_c/mm	Notch angle θ/ (°)	Impact velocity V/ km/h	Impact mass m/t	Impact energy E_i/kJ
K-V30/45/60/75/90	--	--	30/45/60/75/90	1.5	52.1/117.2/208.3/325.5/ 468.8
K-1DH/1DO/1DV-V30/V60/V90	1D	H/O/V	30/60/90		52.1/208.3/468.8
K-75DH/75DO/75DV-V30/ V60/V90	0.75D				
K-05DH/05DO/05DV-V30/ V60/V90	0.5D				

Note: Notch length: 1D = 500 mm, 0.75D = 375 mm, 0.5D = 250 mm; Notch angle: H is 0°, O is 45°, V is 90°.

TABLE 2 Material properties of C350 (Al- et al., 2011).

Fracture strain	Maximum stress triaxiality	Maximum strain rate (s⁻¹)	Evolutionary displacement (mm)	True yield stress/MPa	True ultimate stress/MPa	True failure strain
0.115	0.7	14.2	0.291	456	584.64	0.145

are listed in Table 1, and the local corrosion locations and overall model are shown in Supplementary Figure S1A,B.

2.2 Constitutive model of steel

Steel structures or members are subjected to high strain rates under dynamic conditions, such as high-velocity impacts and explosions. To consider the strain rate effect on steel, scholars at home and abroad have proposed strain rate effect models that can be used to predict the dynamic mechanical properties of metallic materials. The commonly used models are the Cowper-Symonds (C-S) and Johnson-Cook (J-C). The steel used in this model was the C350 steel test data provided in (Al- et al., 2011). According to the test results in (Jones, 1997), the Cowper-Symonds model (Eq. 1) with $D = 40.4 \text{ s}^{-1}$ and $p = 5$ was adopted to consider the strain-rate effect of the material. The material performance and failure parameters are listed in Table 2. In the ABAQUS material setup, an ideal elastic-plastic model based on the Von Mises yield criterion was adopted for steel. The density, yield strength, ultimate strength, elastic modulus, and Poisson's ratio of the steel were 7,850 kg/m³, 455 MPa, 504 MPa, 200 GPa, and 0.3, respectively (Al- et al., 2011).

$$C-S \text{ model:} \quad \frac{\sigma_d}{\sigma_s} = 1 + \left(\frac{\dot{\varepsilon}}{D}\right)^{\frac{1}{p}} \quad (1)$$

Where σ_d is the dynamic stress; σ_s is the static stress; $\dot{\varepsilon}$ is the strain rate; D and p are material constants, which can be obtained by fitting the material property test at all levels of strain rate.

2.3 Boundary conditions and loading methods

The ABAQUS finite element analysis (FEA) model is mainly composed of a circular hollow steel tube, a circular end plate, and a simplified drop hammer (impactor), as shown in Supplementary Figure S1C. The impact position was directly above the mid-span of the circular hollow steel tube. Reference points were set for the drop hammer and circular end plates to facilitate the application of the boundary conditions and impact effects. In this case, fixed and simply supported constraints were set as the reference points of the two endplates. The simply supported constraints allow the axial translation ($U_x = U_y = 0$) and rotational freedom corresponding to the impact direction ($UR_y = UR_z = 0$) of the circular hollow steel tube, whereas for the drop hammer, the translational degrees of freedom in two directions ($U_x = U_z = 0$) and the rotational degrees of freedom in three directions ($UR_x = UR_y = UR_z = 0$) are constrained, except for the translation in the impact direction (vertically downward).

In the finite element (FE) model setting, hard contact was used for the normal direction of the contact surface; that is, the pressure was completely transferred when the two contact surfaces were in contact, and the force was not transferred when the two contact surfaces were separated. Solid unit C3D8R was used to simulate the circular hollow steel tube and end plate. The drop hammer ignored the deformation during impact, and the discrete rigid body unit R3D4 was used for the simulation. The mesh size of the model was 40 mm, and it was locally encrypted within 500 mm of the impact position of the drop hammer to improve the model calculation accuracy. From Supplementary Figure S1D,E, it can be seen that the impact force-time history curves of the model with mesh size 40/ 10 mm (10 mm is the mesh size of the locally encrypted region) have good stability and accuracy through a series of mesh sensitivity checks for the model (K-V60). As can be seen from the comparison Supplementary Figure S1D,E, the model with a 40/10 mm mesh size achieves the best balance between calculation accuracy and efficiency.

2.4 Model verification

To verify the validity and reliability of the numerical simulation method adopted in this study, the drop hammer tests in (Bambach et al., 2008; Zeinoddini et al., 2002) were simulated and analyzed,

TABLE 3 Parameters of testing specimens (Bambach et al., 2008).

Specimen number	$b \times d \times t$ (mm)	L (mm)	v_o (m/s)	m (kg)	Yield stress (MPa)	Ultimate stress (MPa)	Failure strain
50SHS	$50 \times 50 \times 1.6$	700	6.2	600	455	504	0.16

Note: b, d, t and L are the section length, section width, wall thickness and effective length of the steel tube, while v_o and m are the falling velocity and mass of drop hammer, respectively.

TABLE 4 Material failure parameters (Al- et al., 2011).

Fracture strain	Maximum stress triaxiality	Maximum strain rate (s^{-1})	u_f(m)	ε_f
0.115	0.7	14.2	0.000291	0.1455

Note: ε_f is the equivalent plastic strain of the steel at complete fracture and u_f is the total plastic displacement of the steel at the failure site.

TABLE 5 Basic information of the specimens (Zeinoddini et al., 2002).

Specimen number	N_o(kN)	$D \times t$ (mm)	L (mm)	H(m)	m (kg)	V_o(m/s)
Pd1	0	100×2	1,000	2.5	25.45	7
Pd2	88	100×2	1,000	2.5	25.45	7

Note: N_o indicates the axial pre-loading value of the steel tube, D, t and L indicate the diameter, wall thickness and effective length of the steel tube, respectively. H, m and v_o are the falling height, mass and falling velocity of drop hammer, respectively.

and the numerical simulation results were compared with the experimental results.

Bambach et al. (2008) tested a square hollow steel tube specimen (No. 50SHS) with an effective length of 700 mm. The mid-span of the specimen was impacted using a drop hammer with a mass of 600 kg at a falling velocity of 6.2 m/s. The density, elastic modulus, engineering yield stress, and Poisson's ratio of the steel were 7,850 kg/m³, 200,000 N/mm², 455N/mm², and 0.3, respectively (Bambach et al., 2008). Table 3 lists the section sizes and material properties of the specimens. Supplementary Figure S2A shows a detailed diagram of the test device and the FE model. This model validation used the progressive damage and failure models available in ABAQUS/Explicit to detect and track the initiation and evolution of damage until the material unit failed completely. The model considers the equivalent plastic strain at damage initiation as the failure initiation criterion. The failure parameters, such as the strain, triaxial stress, and strain rate values used in the FE model at damage initiation, are listed in Table 4 (Al- et al., 2011).

Zeinoddini et al. (2002) conducted an experimental study on the lateral impact responses of axially pre-loaded circular steel tubes. Basic information on the specimens is presented in Table 5. In these tests, the steel tubes were pre-loaded to different axial compression levels and then impacted at mid-span with a drop hammer weighing 25.45 kg at a fall velocity of approximately 7 m/s. The test device and finite element validation model are shown in Supplementary Figure S2B. The steel tube is simulated using a 3D shell element, and the endplate and stiffening rib are simulated using a 3D solid element. Because the drop hammer hardly deforms during impact, it is simulated using a rigid shell element. The classical metal plasticity model in ABAQUS/Explicit was adopted for the steel. The density, elastic modulus, yield stress, and Poisson's ratio of the steel tube were 7,850 kg/m³, 200,000 N/mm², 516 N/mm², and 0.3 respectively (Hou, 2012). The contact algorithm between the drop hammer and the steel tube is surface-to-surface contact, and the effective contact surface with

high stiffness is defined as the main surface. The normal 'hard' contact method and tangential frictionless method are used to define the interaction between the two contact surfaces. The motion contact strengthening method was used in the model, and the contact between the two bodies was detected according to the finite sliding formula. A compressive load was applied in the axial direction of the model using a linear spring. The linear spring in the steel tube model was set according to the steps of the axial force-impact coupling model in (Hou, 2012).

The simulation results were compared with the test results. Supplementary Figure S2C–E shows the results of comparing the impact force time-history curve and impact force-displacement curve with overall good agreement. Supplementary Figure S2F accurately simulates the complete tensile tear failure of the specimen at the support. A comparison of the experimental and simulation results shows that the damage initiation and failure criteria of the proposed model are correct when simulating the tensile failure of materials. This indicates that the material constitutive and FE models adopted in this study are reasonable and effective.

3 Impact resistance of local notch CHST columns

3.1 Failure pattern

3.1.1 Comprehensive analysis of non-notch model

All the CHST columns were constrained with fixed simple supports in the finite element simulation. Therefore, under the lateral impact load, the failure of the entire CHST column mainly presented localized indentation and buckling failure, as shown in Supplementary Figure S3A. The plastic hinge area was concentrated in the mid-span drop hammer impact and fixed-end areas, as shown in Supplementary Figure S3B. The upper mid-span

surface of the non-notched CHST column exhibited localized indentation at the contact position with the drop hammer.

With an increase in the impact energy, the localized indentation amplitude of the member increased correspondingly, as shown in Supplementary Figure S3C. When the impact velocity was 45 km/h, the mesh on the surface of the CHST model in the impact contact area was deleted, indicating that under the impact velocity, excessive local stress in the indentation area led to element failure, and the surface element lost the ability to sustain the stress. Because of the excessive local deformation of the steel tube at both ends of the impact contact area, the stress was gradually transferred from the outer surface of the steel tube to the interior until the steel in this area completely failed along the thickness direction, resulting in local cracking at an impact velocity of 60 km/h. Additionally, the bottom area of the steel tube near the fixed end began to buckle. When impact velocity of the drop hammer reached 90 km/h, the steel tube in the mid-span contact area with the impact was completely broken, and the bottom of the steel tube near the fixed end exhibited excessive compressive stress and buckling, eventually leading to compressive fracture failure. Generally, with a gradual increase in impact velocity, the local indentation level of the impact area of the impactor and the buckling amplitude of the fixed-end area increased gradually.

CHST columns with a drop hammer impact velocity of 60 km/h were selected for a comprehensive analysis to understand the stress of the CHST column under lateral impact in detail. Supplementary Figure S3D shows the time-history curves of F/F_m, v/v_m, v_s/v_{sm}, and u/u_m of the K-V60 model, where F、v、v_s, and u are the impact force, hammer velocity, mid-span velocity, and mid-span deflection of the model respectively, and the symbols with subscript "m" represent the corresponding maximum values.

Three phases are involved in these time-history curves: 1) the ascending phase (from point O to point A): the contact between the drop hammer and the CHST causes the velocity of the CHST to increase rapidly, and when the peak velocity is reached, the velocities of both decrease almost simultaneously. As shown in Supplementary Figure S3F–H, at point A, the contact area between the CHST and drop hammer had a certain extent of indentation, but the global lateral deformation was small. Local damage occurred on the inner and outer surfaces of the steel tube in the impact area, and the middle stress in the direction of the wall thickness of the steel tube in the depression area increased gradually. The impact direction stress generated by the CHST column under the impact of the drop hammer was transferred from the middle of the section to both ends, while a large axial stress also appeared at both ends and the bottom area of the steel tube. 2) Plateau phase (from point A to point B): The drop hammer and CHST column velocities oscillate at small amplitudes and decrease significantly. At point B, the velocities of the model and drop hammer were reduced to zero, the deflection of the CHST column reached its maximum, and the impact force began to decrease. When point B was reached, the internal stress in the impact area of the steel tube spread to the edge of the end, the accumulation of local plastic deformation was too large, and ductile fracture occurred. The impact-direction stress of the section decreased significantly, whereas the axial stress increased, as shown in Supplementary Figure S3F–H. 3) Decline phase (from point B to point C): The deformation of the model begins to recover elasticity. At point C, the impact force decreased to zero, and the

model began the free vibration of the rebound process at this phase, with the drop hammer moving away from the model at the final rebound velocity. When point C is reached, local complete fracture occurs at both ends of the section, the stress on both sides of the impact direction increases again with the rebound of the model, and the stress value at both ends of the top of the cross-section of the steel tube in the drop hammer contact area exceeds points A and B. The axial stress in this section was reduced. With increased rebound amplitude, the axial stress in the local fracture area changed from compressive to tensile stress.

As shown in Supplementary Figure S3E, the global energy dissipated by the CHST model ($E_{p,\ CHST}$) no longer increases after point B. Combined with Supplementary Figure S3D and the time-history curve of CHST kinetic energy ($E_{k,\ CHST}$), it can be seen that the impact force of the CHST column is close to the peak point at point A when the impact contact area has a local indentation, the CHST kinetic energy reaches the maximum. Subsequently, the kinetic energies of the drop hammer and CHST column decreased to zero simultaneously, and the bottom steel tube near the fixed end of the CHST column exhibited local indentation in the process of curve decline. The kinetic energy of the CHST column rebound in the BC section was much smaller than that in the OA section, indicating that the kinetic energy of the drop hammer ($E_{k,\ drop\ hammer}$) was mainly dissipated by the global and local deformations of the steel tube during the entire impact process. In addition, the ALLAE/ALLIE ratio was stable within 5%, indicating that the hourglass technology of the FE calculation results could be controlled, ensuring the reliability of the numerical simulation results.

Supplementary Figure S3I–J shows the time-history curves of the impact force and hourglass ratio for each non-notched model. An increase in the impact energy can increase the peak point of the impact force and the impact duration of the CHST column. However, the impact plateau value did not improve significantly, and the plateau value was basically stable at approximately 1200 kN. Compared with K-V30, the peak impact points of K-V45–K-V90 increased by 23.5%, 29.9%, 29.3%, and 42.5%, respectively, and the impact duration was extended by 6.18%, 28.1%, 47.5%, and 113.1%, respectively, whereas the impact plateau value increased by approximately 18%. In addition, the ALLAE/ALLIE ratio of each CHST column was stable at approximately 5%, which ensured reasonable validity of the material constitutive model and the established FE model. Notably, when the impact energy was large, i.e., K-V90, the proportion of hourglass energy increased, indicating variability in the impact energy on the hourglass energy. This phenomenon has also been pointed out in (Fu et al., 2021); however, the hourglass energy is within 10%, indicating that the calculation process and results are hourglass-controllable and the calculation results are reliable.

The indentation deformation of the model under the impact load reflects its deformation resistance. The residual indentation displacement after the impact rebound was compared to observe the indentation degree of each horizontal notch model. The local notch increased the global deformation, local indentation, and buckling amplitude of the model. With changes in the angle and impact energy, the CHST columns exhibited different failure patterns. Supplementary Figure S3K shows the local residual indentation deformation of the model in the mid-span impact

area, where the indentation displacement is the measured value of the indentation in the mid-span section when the CHST model impact force drops to zero. For the non-notch model, with a step-by-step increase in the impact velocity, the mid-span indentation displacement of the model at all levels increased by 52.9%, 33.3%, 31.9%, and 17.3%, respectively, compared to that of the model at lower levels, as shown in Supplementary Figure S3M. In addition, when the impact velocity reached 45 km/h, the growth range of the indentation displacement gradually decreased as the impact velocity increased. This is because when the impact velocity gradually increased to 60 km/h, the steel tube at the bottom area of the fixed end of the model began to buckle outwards, and the buckling amplitude became increasingly evident with a gradual increase in the impact velocity. This indicates that when the impact potential energy in the model was low, the energy was mainly consumed by the deformation of the mid-span indentation. With an increase in the impact potential energy, the local buckling deformation at the bottom of the fixed end began absorbing a part of the impact potential energy. Consequently, the amplitude growth of the mid-span indentations slowed.

3.1.2 Horizontal notch model

Supplementary Figure S4A shows the final failure patterns of the model with a horizontal notch at mid-span. When the impact velocity was 30 km/h, the model with the smallest notch length exhibited local damage on the surface area at both ends of the notch, and the stress distribution in the middle of the notch was small. This indicated that the local deformation at both ends of the notch was large, resulting in excessive stress. However, with an increase in the notch length, the local deformation ability increased, and the local stress at both ends of the notch decreased. With an increase in the impact velocity, a fracture occurred in the impact area of the drop hammer, and the damaged surface started from both ends of the notch and extended to both sides. Through an analysis of the influence of the impact velocity, the horizontal notch model showed local buckling at the bottom of the fixed end only when the impact velocity reached 90 km/h, as shown in Supplementary Figure S4B.

The mid-span indentation displacement of the model with impact velocities of 30 km/h and 60 km/h were compared. Supplementary Figure S4C shows that the notch length had little effect on the degree of indentation; however, increasing the impact velocity increased the mid-span indentation displacement of the model significantly. The global increase range is about 109.8%–117.8%. The global indentation displacements of the three notch models with different lengths were similar because the horizontal notch direction was consistent with the cross-sectional direction of the model. This was beneficial for the elastic recovery of the model after impact within the elastic range. The model with an impact velocity of 30 km/h exhibited no cracking in the notch area during the impact process, whereas the model with an impact velocity of 60 km/h exhibited cracking damage at both ends of the notch during the impact process, and the damage path extended to both sides. Therefore, the indentation degree of each notch length model was essentially the same after the rebound. Compared with the non-notch model, when the impact

velocity was increased to 60 km/h, the displacement of the horizontal notch model increased by approximately 4%–16%. Supplementary Figure S4D shows that with an increase in impact velocity, the indentation displacement of the non-notch model increased by 103.8% and 57.7%. However, the mid-span indentation displacements of the notched model with velocities of 30 and 60 km/h were approximately 29.3% and 36.3% higher than those of the non-notched model, respectively.

3.1.3 Oblique notch model

Supplementary Figure S5A shows the damage pattern of the oblique notch model in the local notch area. When the impact energy is low, slight damage or cracking occurs at both ends of the notch. As the notch length increases, the range of local buckling in the impact region increases. The damage depth in the span is proportional to the increase in the impact velocity, and increasing the notch length expands the damage area of the impact area.

The increase in the impact velocity had an obvious influence on the oblique notch model. CHST models with an oblique notch length of 375 mm were used for the analysis. From the perspective of the entire impact process, when the impact velocity was 60 km/h, the impact failure of the oblique notch model exhibited two successive failure paths. Point 1 at the end of the notch appeared to fracture first, and point 2 began to fracture when the crack developed downward to point A. When the impact velocity was 90 km/h, three failure paths successively appeared in the impact damage of the notch model. The fracture began at point 3, and as it descended to point B, point 4 fractured. Until the fracture path developed to point C, the fracture failure also occurred at point 5, as shown in Supplementary Figure S5B. The global failure patterns of a typical model are presented in Supplementary Figure S5C. Similar to the horizontal notch model, local buckling occurred at the bottom of the fixed end of the model when the impact velocity reached 90 km/h; however, the buckling amplitude was smaller than that of the horizontal notch model. This may be because the oblique notch model has multiple failure paths in the mid-span notch region, in which more energy is dissipated and the buckling deformation of the end is reduced. Generally, tensile fractures (points 1 and 3), compressive fractures (points 2, 4, and 5), and local buckling were observed in the oblique notch model.

Supplementary Figure S5D compares the mid-span indentation displacements of the oblique notch model with impact velocities of 30 km/h and 60 km/h. As the notch length and impact velocity increased, the corresponding notch models improved by 183.8%, 172.9%, and 197.3%, respectively. Supplementary Figure S5E compares the indentation displacements between the oblique notch and non-notch models. Compared with the non-notch model, the maximum increases in indentation displacement were 47.8% and 115.6%, respectively. For the oblique notch model with impact velocities of 30 km/h and 60 km/h, with an increase in the notch length, the mid-span indentation displacement of the model increased by approximately 7.6% and 10.2%, respectively, on average. Compared to the horizontal notch model, the oblique notch had a greater influence on the indentation displacement in the model, and the indentation displacement of the model was proportional to the increase in notch length.

3.1.4 Vertical notch model

Supplementary Figure S6A shows the damage patterns in the mid-span impact region of the vertical notch model. The local deformation degree of the model increased gradually with the impact velocity, and a local closure phenomenon appeared in the middle of the notch. In addition, the local deformation of the model is less affected by the notch length. Compared with the horizontal and oblique notch models, the impact damage range and degree of the vertical notch model in local indentation and local buckling deformation were the smallest, and the vertical notch model showed better impact resistance.

In the vertical notch model, when the impact velocity reaches 60 km/h, significant damage begins to appear in the impact area. The CHST models with a vertical notch length of 375 mm (0.75D) were used for the analysis. Considering the entire impact process, when the impact velocity increased to 90 km/h, significant damage occurred in the impact area of the model. The damage patterns and paths are shown in Supplementary Figure S6B. Damage and failure began at point 1 and spread to the surroundings and both sides of the steel tube. Local buckling and fracture failure also occurred at the bottom of the fixed end. The global damage patterns of the model are shown in Supplementary Figure S6C. When the impact velocity was 60 km/h, slight buckling occurred at the end of the model. When the impact velocity reached 90 km/h, obvious local buckling and fracture failure occurred at the bottom of the fixed end, which was much greater than the damage degree of the horizontal and oblique notch models. Compared with the horizontal and oblique notch models, when the impact velocity was small, the global damage degree of the vertical notch model was lighter, showing a relatively better impact resistance performance. With increased impact velocity, the vertical notch model had the smallest mid-span indentation depth, but the most evident buckling damage occurred in the fixed-end area.

Supplementary Figure S6D shows that the notch length has little influence on the mid-span indentation displacement of the overall model. With an increase in the notch length and impact velocity, the corresponding mid-span notch model increased by 96.0%, 88.6%, and 86.1%, respectively. Supplementary Figure S6E shows that for the oblique notch model with impact velocities of 30 km/h and 60 km/h, respectively, the model's mid-span indentation displacement increased by 3.6% and 1.9% on average with increased notch length, and the maximum increase in the indentation displacement were 9.7% and 1.1% compared with the non-notch model. In general, among the three notch models, the vertical notch model was the least affected by notch length and impact velocity, and the indentation displacement had the smallest variation range. Therefore, the vertical notch model exhibited the best impact resistance performance.

At a given impact velocity (60 km/h), the deformation and damage in the localized region of the mid-span of the model were observed. In Supplementary Figure S6F, the damage areas of the horizontal and oblique notch models rapidly expand with cracking of the notch ends, while the vertical notch model only shows relatively stable localized damage on both sides of the notch. A simplified diagram of the damaged area in the mid-span region of the model for different notch angles and notch lengths is shown in Supplementary Figure S6G. It can be seen that with the increase of the notch length, the damaged regions of the horizontal notch and vertical notch models were essentially unaffected, while the damaged region of the oblique notch model was more affected, and its damaged region along the longitudinal and transverse directions would gradually be closer to the notch location.

3.2 Impact force time-history curve

The CHST column impact process can be divided into four stages: contact, common movement, peak displacement, rebound, and separation. The drop hammer was placed 5 mm away from the impact area of the CHST column because the drop hammer freefall process was not considered in the FE model. Therefore, the four stages of the entire impact process correspond to the time-history curve of the impact force and mid-span displacement in Supplementary Figure S7A. The stages are divided into an ascending phase corresponding to the common movement stage, a plateau phase corresponding to the peak displacement stage, and a descending phase corresponding to the rebound and separation stages.

In the plateau phase of the impact time-history curve, because the CHST column entered the plastic-hinge energy-dissipation stage, the model's acceleration was relatively small and stable. The impact force at this stage reflects the dynamic restoring force level of the component and, to a certain extent, the plastic energy dissipation capacity of the model. Therefore, the calculation method for the average impact force after the peak value proposed by Wang (Wang et al., 2014) provides a reasonable estimation of the impact platform value F_p of the CHST column under lateral impact, as shown in Eq. 2.

$$F_p = \frac{\int_{u_o}^{u_m} F dw}{u_m - u_o} \qquad (2)$$

Where w_o is the global mid-span displacement when the impact force reaches the maximum F_m, u_m is the global maximum mid-span displacement, and F is the impact force.

Because the impact velocity was relatively small, the impact resistance of the model was less significantly affected by various factors. Therefore, the model with an impact velocity of 60 km/h was selected for comparative analysis. Supplementary Figure S7B shows that the initial damage points of both the horizontal and oblique notch models were located at the notch end, whereas those of the vertical notch models were more similar to those of the non-notch models. Compared with the initial damage time point of the non-notch model, the damage times of the horizontal and oblique notch models were approximately 6.7% and 26.7% earlier, respectively, whereas that of the vertical notch models was approximately 16.7% later. Based on the impact force value corresponding to the initial damage point of the non-notch model, the impact force values corresponding to the initial damage points of the horizontal, oblique, and vertical notch models decreased, and the reduction amplitudes were 16.9%, 28.5%, and 1%, respectively. Compared to the non-notch model, the horizontal and oblique notches increased the shock amplitude of the platform section of the impact force time-history curve, and the presence of the notch slightly prolonged the impact duration.

When the drop hammer acted directly on the notch position, the degree of damage was significantly greater than that in the non-notch model, and the impact duration was slightly longer. Supplementary Figure S7C–E compares the descending section of the impact force time-history curve of the non-notch and mid-span notch models. A notch length of 250 mm (0.5D) was used for analysis. The damaged area of the mid-span horizontal notch model expanded when the curve entered the descending phase, the impact plateau phase decreased significantly, and the oscillation was evident. The end of the plateau phase of the impact force time-history curve of the oblique notch model was recovered; however, the damage area was larger, and the degree of damage was more serious. The damage area of the vertical notch model was close to that of the non-notch model, and the performance of the impact force time-history curve at each stage was stable. Among the three notch angles, the vertical notch model exhibited the highest impact resistance.

Supplementary Figure S7F compares the impact time-history curves of the notch model under different impact velocities. With an increase in impact velocity, the impact plateau of each model increased slightly, but the plateau segment duration and the overall impact duration were significantly extended. Compared to the non-notch model with an impact velocity of 30 km/h, the overall impact duration of the non-notch model increased by 28.1% and 113.1%, and that of the horizontal notch model increased by 2.7%, 37.0%, and 56.6%, respectively. The K-05DH-V90 model exhibited a sharp increase in the impact time-history curve during the impact process. This is because the stress of the steel tube at both ends of the notch in the horizontal notch model increased sharply when in contact with the drop hammer in the face of a high impact velocity, resulting in fracture cracks in the notch area that developed along both sides (i.e., point A). The mid-span deflection of the model was almost constant. The steel tube in the area of the curved contact surface of the drop hammer was then thrust off, and the drop hammer contacted the steel tube only on two sides (i.e., point B). At this point, the mid-span deflection of the model gradually increased. The steel tube in the contact area between the two sides was damaged and destroyed, and the drop hammer continued to fall (point C). Mid-span deflection increased significantly during this time. Until the steel tube in the two-sided contact area was no longer damaged or destroyed, the kinetic energy of the drop hammer decreased (i.e., point D), and the impact force gradually decreased to zero. Similar phenomena also appeared in the impact force time-history curves of models K-75/1DH-V90 and K-05/75/1DO-V90. The fundamental reason is that the steel tube in the drop hammer contact area was damaged prematurely, resulting in the drop hammer being directly in contact with the side steel tube under a large kinetic energy. Then, the impact force time-history curve showed a sharp rise. The K-05DH-V90 model was compared with K-90, as shown in Supplementary Figure S7F. The impact plateau segment of the impact force time-history curve of the model with this phenomenon obviously increased; however, the overall impact duration was shortened to a certain extent, and the corresponding improvement and shortening ranges were approximately 77.3% and 26.5%, respectively.

A comparison of the impact plateau values of each model is shown in Supplementary Figure S3G–I. In general, the notch length did not influence the impact plateau value. When the impact velocity was 30 km/h, the impact plateau value of the model was lower than that of the non-notch model, and the impact plateau values of the oblique and horizontal notch models decreased significantly. With the increase in the impact velocity, the impact plateau value of the model gradually increased with the change in the notch angle (i.e., vertical, oblique, and horizontal). In general, the impact plateau value of the vertical notch model was the least affected by the notch length, notch location, and impact velocity, showing good impact resistance stability, whereas the increase in impact velocity effectively increased the impact plateau value of the horizontal gap model, which corresponds to the sharp rise of the impact force time-history curve in Supplementary Figure S7F.

3.3 Mid-span displacement time-history curve

The mid-span displacement time-history curve of the non-notch model is shown in Supplementary Figure S8A. When the impact velocities were 30 km/h and 45 km/h, the rebound amplitude of the mid-span displacement of the model was not obvious after reaching the peak, showing a wavy curve. As the impact velocity continued to increase, the mid-span displacement time-history curves of the model exhibited an obvious rebound. Overall, with a step-by-step increase in the impact velocity, the increase in the mid-span peak displacement of each stage was 203.0%, 118.1%, 105.6%, and 108.2, respectively. Supplementary Figure S8B shows that the ratios of the local indentation degree to the peak displacement under different impact velocities were 9.3%, 18.5%, 30.2%, 47.1%, and 83.6%. It was again shown that the CHST columns were dominated by global bending and local indentation deformation under lateral impact.

The influence of the notch angle and length on the model mid-span displacement is also different. The effects of changes in the notch angle and length on the mid-span displacement of the model were also different. As shown in Supplementary Figure S8C–E, compared with the non-notch models, when the impact velocity is 30 km/h, the variation ranges of peak displacement in the horizontal, oblique, and vertical notch models are 4.9%, −6.3%, and 12.5%, respectively. When the impact velocity increased to 60 km/h, the horizontal, oblique, and vertical notch models changed by −47.2%, −45.5% and 7.2%, respectively. When the velocity continued to increase to 90 km/h, the changes of peak displacement in the horizontal and oblique notch models were −50.2% and −50.5%, respectively, while that in the mid-span vertical notch model was increased by 32.4%. Therefore, the horizontal and oblique notches reduced the mid-span displacement of the model. Supplementary Figure S8F compares the mid-span displacement time-history curves of the horizontal notch model and the non-notch model when the impact velocity is 60 km/h. Based on the displacement time history curve of the K-05DH-V60 model, with the change in notch length, the change in the amplitude of the peak displacement in the span of the notch model was 15.5%, whereas that of the peak displacement in the non-notch model was 90.3%.

Overall, the global displacement of the vertical notch model with impact velocity of 30 km/h and 60 km/h was close to that of the non-notch model, and the curve trend was consistent with that of the non-notch model. With an increase in the impact velocity, the global

displacement of the horizontal and oblique notch models decreased. This may be because the horizontal and oblique notch models exhibited relatively large local deformations or damage in the impact region of the drop hammer, and more impact energy was dissipated during the process of local deformation and damage; therefore, the global displacement of the model was relatively small. However, the degree of local deformation and damage in the impact area of the vertical notch model was smaller than that of the horizontal and oblique notch models, and the impact energy needed to be dissipated by the global bending deformation; therefore, the global displacement of the vertical notch model was increased. Notably, when the impact velocity was 90 km/h, the mid-span displacement curve of the vertical notch model was inconsistent with that of the horizontal and oblique notch models. This is because there was no obvious impact damage in the impact area of the drop hammer. However, the larger impact energy caused the two sides of the mid-span section and the end area to exhibit buckling and fracture, and the global bending range of the model was larger.

3.4 Energy absorption ratio

In this study, the rebound of the drop hammer and other energy losses were ignored, and the energy (E_g) absorbed by the global bending deformation of the CHST column was defined as the area surrounded by the impact force-displacement curve obtained by the drop hammer impact. The instantaneous kinetic energy before the impact of the drop hammer was adopted as the impact energy of the whole system, that is $E_i = 0.5mv^2$. A typical impact force-global bending displacement curve for the CHST column is shown in Supplementary Figure S8G. Thus, the energy absorption ratio (EAR) of the global deformation of the model can be obtained as EAR = E_g/E_i. The impact resistance of the CHST column under a lateral impact load was evaluated based on the variation in the EAR of each model. Supplementary Figure S8H shows the displacement nephogram of the impact direction of the drop hammer and the global bending displacement picking position at the mid-span for the K-V30 and K-05DH-V90 models. The model EAR calculated from the top and bottom points of the mid-span section corresponding to the impact force-global bending displacement curve were compared. In Supplementary Figure S8I, the EAR calculated using the impact force-global bending displacement curve corresponding to the peak points on the top and bottom surfaces are significantly different. With an increase in the impact energy, the pick points of the top and bottom surfaces increased by 3.0%, 2.5%, 1.9%, and 1.7%, and 164.9%, 59.1%, 39.6%, and 35.1%, respectively, compared with those of the upper model. Overall, with an increase in the impact energy, the increasing trend was approximately linear, but the rate of increase gradually decreased. The EAR calculated at the top picking point was in the range of 88.5%–96.7%, while the EAR calculated at the bottom picking point was in the range of 5.5%–43.3%. The reason for the obvious difference in the EAR between the two is that when the model impact energy was low, its global bending displacement was much smaller than that of the local indentation displacement at the mid-span. In this case, the impact energy was mainly absorbed by the mid-span local deformation, whereas the energy absorbed by the global deformation of the model was very

small. With an increase in impact energy, the growth rate of the global bending displacement of the model was greater than that of the local deformation; therefore, the corresponding growth rate of the bottom points was larger.

Notably, the linear rise of the impact force at the beginning of the impact in Supplementary Figure S8G occurs because the impact force increases too rapidly at the same time, while the displacement increment at the bottom is too small; therefore, a linear rise occurs at the beginning of the impact force-global bending displacement curve. In addition, a negative increase in displacement occurs after the straight upward section because the peak point is at the bottom. At the moment of the impact of the drop hammer, there was no support inside the steel tube. Under inertia, the bottom steel tube moved in the direction opposite to the impact of the drop hammer; however, the movement duration was very short.

The bottom point of the FE model is the energy absorbed by the global deformation of the model, whereas the top point contains the local and global deformations in the span. Therefore, the impact force-global bending displacement curve corresponding to the top surface point better reflects the absorption of the impact energy of the entire model. Supplementary Figure S8J shows the proportion of energy absorbed by the global and local indentation deformations in each non-notched model. With an increase in impact energy, the energy absorbed by the local indentation (top surface point) gradually decreased, whereas the energy absorbed by the global deformation (bottom surface point) gradually increased. However, the distribution of the two ratios indicated that the global impact energy of the CHST column was mainly absorbed by the local indentation deformation in the mid-span under the action of lateral impact. It is worth noting that Supplementary Figure S8H shows that the mid-span horizontal notch model is prone to local failure when the impact energy is large, resulting in the inability to obtain the top point of the mid-span cross-section to observe its energy absorption. Therefore, the impact force-global bending displacement curve corresponding to the bottom point of the notch model was used to analyze the influence of different notch lengths and notch angles on the global EAR of the model.

Supplementary Figure S8K shows that the EAR of the mid-span notch model is proportional to the improvement in impact energy, whereas the notch length has little effect on the EAR of the FE model. The vertical notch increased the EAR of the model, whereas the horizontal and oblique notches significantly decreased it. Compared with the EAR of the non-notch model, the EAR of the vertical notch model at the three impact velocities (30 km/h, 60 km/h, 90 km/h) increased by 20.2%, 13.5%, and 17.3%, respectively, whereas the EAR of the horizontal notch and oblique notch models decreased by 28.2%, 61.0%, 42.4%, and 29.1%, 62.7%, and 49.3%, respectively. Among the three notch angles, the vertical notch was beneficial for EAR improvement, whereas the oblique notch was the most unfavorable.

In general, the EAR was proportional to the increase in impact energy, and the impact energy of the model was absorbed by the local indentation deformation and global bending deformation in the span. With an increase in the impact energy, the energy absorbed by the mid-span local indentation deformation decreased gradually, and the energy absorbed by the global

bending deformation increased gradually. However, most of the impact energy was absorbed mainly by the mid-span local indentation deformation.

3.5 Comparison of dynamic flexural capacity of section

To analyze the influence of various parameters on the dynamic flexural capacity of CHST columns, the simplified formula of the dynamic flexural capacity (M_{cr}) of the notch model under the action of mid-span lateral impact is defined as follows:

$$M_{cr} = R_d \cdot M_u \qquad (3)$$

where M_{cr} is the bending moment corresponding to the maximum value of the global mid-span bending displacement of the notched model, and M_u is the bending moment corresponding to the maximum value of the mid-span global bending displacement of the non-notched model. The specific data of both are obtained from the FEA results.

R_d is the influence coefficient of the dynamic bending capacity of the model, which can also be regarded as the ratio of the maximum mid-span global bending displacement corresponding to the bending moment value (M_{cr}) of the notch model to the maximum mid-span global bending displacement corresponding to the bending moment (M_u) of the non-notch model, which is related to the notch length, notch angle, and impact velocity.

Supplementary Figure S9A–C shows the ratio of the dynamic bending capacity between each notch model and the non-notch model. It can be observed from the figure that when the impact velocity is low, the R_d variation trend of the notch model is inversely proportional to the increase in the notch length. With the change of notch angle (H, O, V), when the impact velocity is 30 km/h, the maximum change amplitude of model R_d is −36.5%, −11.5%, and −19.2%, respectively. With increased impact velocity, the R_d of each notch model improved overall. Because R_d is an artificially defined practical calculation factor, its local variation trend may not be monotonous. As shown in Supplementary Figure S9C, an increase in the impact velocity brings greater impact energy to the model, which causes more local damage to the impact region. When the strain rate of the material increased after the impact, the dynamic flexural capacity of the model increased without damage. However, owing to the damage to the material and the existence of a local notch, the local mesh of the model has a certain variability under a large impact energy, which leads to large fluctuations and a certain discreteness of the data. In general, with an increase in the impact velocity, the R_d of the horizontal notch model increased significantly, whereas the R_d of the oblique and vertical notch models increased slightly.

4 Dynamic flexural capacity of section

CHST columns are mainly characterized by local indentation and global bending deformation under lateral impact loads, and the appearance of local notches affects the failure pattern and

TABLE 6 Application range of practical formula of R_d.

Notch length l_c/mm	Notch angle θ/(°)	Impact energy E_i/kJ
250–500	0° ~ 90°	52.1–468.8

failure degree of the model. An important index for measuring the impact resistance of CHST columns is the influence coefficient R_d of the dynamic bending capacity of CHST columns under an impact load. The dynamic bending strength of the model section can then be calculated. Based on a large number of FE results, this study selected the key factors affecting R_d in the FEA results, including the notch length (l_c), notch angle (θ), and impact energy (E_i). Through regression analysis, a practical calculation formula for the influence coefficient R_d of the dynamic flexural bearing capacity of the CHST column section was obtained, as shown in Eq. 4.

$$R_d = 0.856 \cdot f(l_c) \cdot f(\theta) \cdot f(E_i) \qquad (4)$$

where, $f(l_c) = 1.281 - 1.41 \times 10^{-3} l_c + 1.47 \times 10^{-6} l_c^2$

$$f(\theta) = 0.3128 - 1.105 \times 10^{-3} \theta + 1.01 \times 10^{-5} \theta^2$$

$$f(E_i) = 3.439 - 3.35 \times 10^{-4} E_i + 1.74 \times 10^{-5} E_i^2$$

The units and range of application of parameters of the practical calculation formula are shown in Table 6.

Supplementary Figure S9D–E compare the FEA values of R_d and M_{cr} for each notch model with the values predicted by the simplified formula. The relative error between the two results is less than 10%, which indicates that the fitting formula is in good agreement with the influence coefficient of the FE dynamic bending capacity, and the fitting accuracy is high.

5 Conclusion

In this study, the localized corrosion of a CHST was simulated by a localized penetrating notch through a series of numerical simulations. The lateral impact responses of the CHST columns were simulated using different impact energies, notch lengths, and notch angles. The following conclusions were drawn.

(1) The CHST column exhibited global bending failure under a mid-span lateral impact load, accompanied by local indentation deformation in the impact area and local buckling deformation at the bottom of the fixed end. The global and local deformation amplitudes of the model were proportional to the increase in the impact energy. Compared with the non-notch model, the horizontal notch model had a relatively stable increase in mid-span indentation displacement at impact velocities of 30 km/h and 60 km/h, with average increases of 29.3% and 36.3%, respectively. For the oblique and vertical notch models, the displacement of the mid-span indentation increased slightly with increased notch length at impact velocities of 30 km/h and 60 km/h. In this case, the maximum increase of the oblique notch model was approximately 47.8% and 115.6%, and the vertical notch

model was approximately 9.7% and 1.1%, respectively. The mid-span indentation displacements of the horizontal and vertical notch models were less.

(2) The impact force time-history curve of the entire process of the CHST column can be divided into three phases: the ascending, plateau, and decline phases; the end of the plateau phase of the curve corresponds to the peak point of the mid-span displacement curve. Compared to the non-notch model, the horizontal and oblique notches increased the amplitude of oscillations in the plateau section of the impact force time-history curve, and the existence of a notch slightly prolonged the impact duration. The local damage area and impact time history curves of the vertical notch model were more consistent with those of the non-notched model, and increasing the impact energy and decreasing the notch angle increased the impact plateau value of the model gradually. Among the three notch angles, the impact plateau value of the vertical notch model and the global bending displacement in the mid-span were the least affected by the notch length and impact energy.

(3) The EAR of the model was proportional to the increase in impact energy, and the energy absorbed by the local indentation in the mid-span was significantly greater than the energy absorbed by global bending. Compared to the non-notch model EAR, at 30 km/h, 60 km/h and 90 km/h, the vertical notch model EAR increased by 20.2%, 13.5%, and 17.3% on average, whereas the horizontal notch model EAR decreased by 28.2%, 61.0%, and 42.4%, and the oblique notch model EAR decreased by 29.1%, 62.7%, and 49.3%, respectively.

(4) When the impact energy was low, the variation trend of the notch model R_d was inversely proportional to the increase in notch length. When the impact velocity is 30 km/h, the R_d of each notch model changes with the notch angles (H, O, and V), and the maximum variation range of R_d is −36.5%, −11.5%, and −19.2%, respectively; however, with the increase of impact velocity, the R_d of each notch model showed an overall upward trend, and the R_d of horizontal notch model increased the most.

(5) Based on the results of the parametric analysis, a prediction formula for the dynamic bending capacity of the CHST column section considering the influences of the notch length, notch angle, and impact energy was proposed by regression analysis, which is in good agreement with the numerical results.

Data availability statement

The original contributions presented in the study are included in the article/Supplementary Material, further inquiries can be directed to the corresponding author.

Author contributions

Funding

Conflict of interest

The authors declare that the research was conducted in the absence of any commercial or financial relationships that could be construed as a potential conflict of interest.

Publisher's note

All claims expressed in this article are solely those of the authors and do not necessarily represent those of their affiliated organizations, or those of the publisher, the editors and the reviewers. Any product that may be evaluated in this article, or claim that may be made by its manufacturer, is not guaranteed or endorsed by the publisher.

Supplementary material

The Supplementary Material for this article can be found online at: https://www.frontiersin.org/articles/10.3389/fmats.2023.1321892/full#supplementary-material

References

Ahn, J., Choi, R. W., Jeon, H. S., Kim, S. H., and Kim, I. T. (2016). Residual compressive strength of inclined steel tubular members with local corrosion. *Appl. Ocean Res.* 59, 498–509. doi:10.1016/j.apor.2016.07.002

Al-Thairy, H., and Wang, Y. (2011). A numerical study of the behaviour and failure modes of axially compressed steel columns subjected to transverse impact. *Int. J. Impact Eng.* 38 (8), 732–744. doi:10.1016/j.ijimpeng.2011.03.005

Bambach, M., Jama, H., Zhao, X., and Grzebieta, R. (2008). Hollow and concrete filled steel hollow sections under transverse impact loads. *Eng. Struct.* 30 (10), 2859–2870. doi:10.1016/j.engstruct.2008.04.003

Chen, M. C., Zhang, F. M., Huang, H., Wang, C., et al. (2018). Study on seismic performance of concrete filled square steel tubes subjected to simulated acid rain attack. *J. China Railw. Soc.* 40 (06), 106–114.

Fu, C. J., Wang, Z. H., and Wang, K. (2021). Study on the residual bearing capacity and damage of concrete-filled steel tube (CFST) column subjected to transverse impact. *Build. Sci.* 37 (05), 11–20+27. doi:10.13614/j.cnki.11-1962/tu.2021.05.002

Han, L., Hou, C., and Wang, Q. (2014). Behavior of circular CFST stub columns under sustained load and chloride corrosion. *J. Constr. Steel Res.* 103, 23–36. doi:10.1016/j.jcsr.2014.07.021

Hou, C. C. (2012). *Study on performance of circular concrete-filled steel tubular (CFST) members under low velocity transverse impact.* China National Knowledge Infrastructure.

Hou, C., Han, L., Wang, Q., Hou, C., et al. (2016). Flexural behavior of circular concrete filled steel tubes (CFST) under sustained load and chloride corrosion. *Thin-Walled Struct.* 107, 182–196. doi:10.1016/j.tws.2016.02.020

Hou, C., Han, L., and Zhao, X. (2013). Full-range analysis on square CFST stub columns and beams under loading and chloride corrosion. *Thin-Walled Struct.* 68, 50–64. doi:10.1016/j.tws.2013.03.003

Hu, J., Tian, Y., Teng, H., Yu, L., and Zheng, M. (2014). The probabilistic life time prediction model of oil pipeline due to local corrosion crack. *Theor. Appl. Fract. Mech.*, 70. doi:10.1016/j.tafmec.2014.04.002

Jiang, X., and Soares, G. C. (2012). Ultimate capacity of rectangular plates with partial depth pits under uniaxial loads. *Mar. Struct.* 26 (1), 27–41. doi:10.1016/j.marstruc.2011.12.005

Jones, N. (1997). *Structural impact*. 2nd ed. UK: Cambridge University Press.

Li, W., Han, L., and Zhao, X. (2015). Behavior of CFDST stub columns under preload, sustained load and chloride corrosion. *J. Constr. Steel Res.* 107, 12–23. doi:10.1016/j.jcsr.2014.12.023

Liang, F., Jingke, H., Luocun, H., Shi, H., Yu, C., Wang, S., et al. (2020). A parametric study on effects of pitting corrosion on steel plate's ultimate strength. *Appl. Ocean Res.* 95 (C), 102026. doi:10.1016/j.apor.2019.102026

Saad-Eldeen, S., Garbatov, Y., and Soares, G. C. (2013). Ultimate strength assessment of corroded box girders. *Ocean. Eng.* 58, 35–47. doi:10.1016/j.oceaneng.2012.09.019

Shan, G., Youchun, X., Sumei, Z., and Anna, D. (2023). Performance of square concrete-filled steel tubular columns under repeated lateral impact. *Eng. Struct.*, 280. doi:10.1016/j.engstruct.2023.115719

Shan, G., Yulin, W., Lanhui, G., Xu, Y., and Iyama, J. (2022). Axial behavior of circular steel tube with localized penetrating corrosion simulated by artificial notch. *Thin-Walled Struct.*, 172. doi:10.1016/J.TWS.2022.108944

Wang, H., Zhang, Z., Qian, H., Liu, Y., Hu, N., and Fan, F. (2020a). Galvanic corrosion induced localized defects and resulting strength reduction of circular steel tubes under axial compression: an experimental study. *Thin-Walled Struct.*, 154. doi:10.1016/j.tws.2020.106881

Wang, R., Guo, H., and Shenoi, A. R. (2020b). Experimental and numerical study of localized pitting effect on compressive behavior of tubular members. *Mar. Struct.* 72 (C), 102784. doi:10.1016/j.marstruc.2020.102784

Wang, Y., Qian, X., Liew, R. J., and Zhang, M.-H. (2014). Experimental behavior of cement filled pipe-in-pipe composite structures under transverse impact. *Int. J. Impact Eng.*, 72. doi:10.1016/j.ijimpeng.2014.05.004

Yin, B. B., Akbar, A., Yang, Z., and Liew, K. M. (2023b). Modeling progressive failure and crack evolution in a randomly distributed fiber system via a coupled phase-field cohesive model. *Compos. Struct.*, 313. doi:10.1016/j.compstruct.2023.116959

Yin, B. B., Sun, W. K., Yang, Z., and Liew, K. M. (2023a). Modeling via peridynamics for large deformation and progressive fracture of hyperelastic materials. *Comput. Methods Appl. Mech. Eng.*, 403. doi:10.1016/j.cma.2022.115739

Yuan, F., Chen, M., Huang, H., Xie, L., and Wang, C. (2018). Circular concrete filled steel tubular (CFST) columns under cyclic load and acid rain attack: test simulation. *Thin-Walled Struct.* 122, 90–101. doi:10.1016/j.tws.2017.10.005

Yulin, W., Shan, G., Youchun, X., and Li, F. (2022). Lateral impact response of concrete-filled square steel tubes with local defects. *Build.* 12 (7), 996. doi:10.3390/buildings12070996

Zeinoddini, M., Parke, G., and Harding, J. (2002). Axially pre-loaded steel tubes subjected to lateral impacts: an experimental study. *Int. J. Impact Eng.* 27 (6), 669–690. doi:10.1016/s0734-743x(01)00157-9

Experimental analysis and modeling of micro-texture and vickers hardness impact on polished stone value in high-friction aggregates

Zhenqing He[1], Jun Li[1]*, Juanni Nian[2]* and Bowen Guan[1]

[1]School of Materials Science and Engineering, Chang'an University, Xi'an, China, [2]Shaanxi Key Laboratory of Environmental Monitoring and Forewarning of Trace Pollutants, Xi'an, China

This article intends to study the influence of micro-texture and Vickers hardness on the Polished Stone Value (PSV) of four types of high friction aggregates (90# Bauxite, 75# Bauxite, Basalt, and Granite) during the long-term polishing process. For this purpose, profile roughness, Vickers hardness, and PSV were tested. The relationship between profile roughness, Vickers hardness, and PSV was analyzed with gray correlation analysis and mathematical fitting. The results show that arithmetic mean roughness (R_a) and maximum height (R_z) influenced PSV significantly while root mean square height (R_q), skewness (R_{sk}), kurtosis (R_{ku}), and load length ratio (R_{mr} (c)) had a relatively weak effect. Because of the high correlation with PSV, R_a and R_z were chosen as indicators, and the relationship between variables (R_a, R_z) and PSV was established. There is a good linear relationship between the attenuation rate of R_a and R_z per polishing cycle (K_1 and K_2) and Vickers hardness. Finally, a model of estimation of the polished stone value of high friction aggregate based on micro-texture and Vickers hardness during the long-term polishing process is developed. Measuring the profile roughness and Vickers hardness to obtain R_a, R_z, and H correlation values and substituting them into the modeling equations in this paper can be used for optimal selection and life estimation of high friction aggregates, which belong to the raw materials, and the optimal selection of high friction aggregates will be helpful for the design of wear-resistant coatings, especially for high friction surface treatments.

KEYWORDS

wearing course, aggregates, micro-texture, vickers hardness, polished stone

1 Introduction

Wearing course is the top layer of pavement. The surface texture of the wearing course is the key factor affecting the skid resistance of the pavement which is essential to traffic safety (Pranjić et al., 2020; Zhu et al., 2022). Therefore, optimization of surface texture characteristics which have a significant influence on pavement friction is an effective method to increase traffic safety and reduce crashes (Leng et al., 2023). Pavement texture is typically broken up into categories of micro-texture, macro-texture, and mega-texture which are based on wavelength and vertical amplitude characteristics (ISO, 2019). The definitions of the texture categories have been proposed

TABLE 1 Chemical composition of aggregates (%).

Type	SiO_2	TiO_2	Al_2O_3	Fe_2O_3	MgO	CaO	Na_2O	K_2O	P_2O_5	MnO
90#Bauxite	3.32	4.47	90.29	1.55	0.15	0.17	<0.01	0.17	0.24	0.01
75#Bauxite	19.19	3.29	75.51	1.12	0.16	0.3	<0.01	0.18	0.17	<0.01
Basalt	49.51	3.61	14	12.62	0.16	4.97	8.67	1.92	1.4	0.05
Granite	66.64	0.38	15.94	2.7	0.05	3.71	4.41	1.86	0.11	0.16

TABLE 2 Physical properties of aggregates.

| Type	Apparent density (g/cm^3)	Surface-dry density (g/cm^3)	Bulk density (g/cm^3)	Water absorption (%)
90#Bauxite	3.128	3.035	2.991	0.0146
75#Bauxite	3.080	2.790	2.640	0.054
Basalt	2.826	2.782	2.743	0.211
Granite	3.035	3.012	3.001	0.372

FIGURE 1
Four types of PSV specimens.

by the Committee on Surface Characteristics of the World Road Association as follows (Henry, 2000). Macro-texture is texture in a pavement with a wavelength ranging from 0.5 to 50 mm. Micro-texture is texture in a pavement with a wavelength ranging from 1 µm to 1 mm. As many previous researches reported, the micro-texture of pavement surface is more important and plays a decisive role in the long-term performance of skid resistance (Gardziejczyk and Wasilewska, 2016; Chen et al., 2020; Jiang et al., 2020; Guo et al., 2021).

Aggregate is the main component of asphalt concrete and an important part of pavement. The micro-texture of aggregate surface has attracted much attention and lots of research has been done. Ge et al. found a certain regularity between aggregate surface texture and wear attenuation (Ge et al., 2018). Ergin et al. analyzed the relationship between aggregate micro-texture and pavement skid resistance (Ergin et al., 2020). Kane reported that there is a close relationship between the mineral composition of aggregates and their anti-slip properties when used in pavements (Kane and Edmondson, 2020). According to previous research results, there is a significant correlation between micro-texture and surface friction (Chen et al., 2022). However, few studies reported the relationship between micro-texture change and surface friction during the long-term polishing process. Hardness is the relative resistance of an aggregate to deformation, and it may have a relationship with surface texture characteristics change during the polishing process (Zong et al., 2021). In summary, up to now the existence of the relationship between aggregate surface texture and skid resistance is more qualitative and lacks quantitative studies as well as accurate model derivation. Secondly, many studies only focus on the parameters related to surface texture, without considering the effect of hardness, so if the PSV of high friction
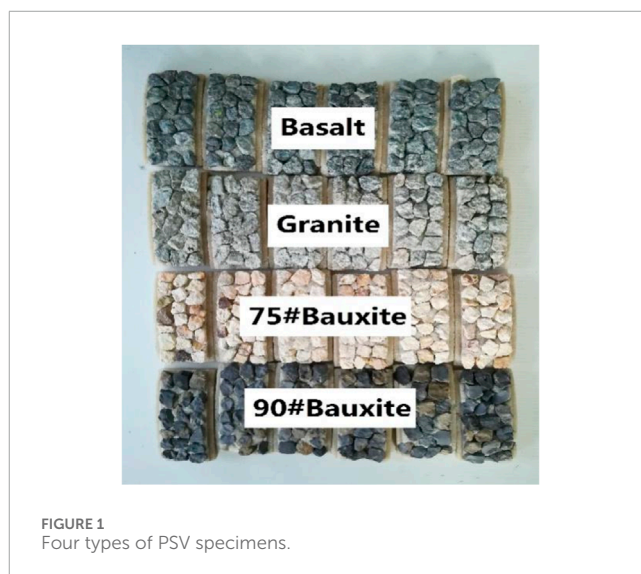
aggregates in the case of long-term polishing is combined with surface friction and Vickers hardness, it will be conducive to the theoretical development of the relevant direction of high friction aggregates.

Polished Stone Value (PSV) is used to evaluate the skid resistance of aggregate. The higher the PSV, the better the skid resistance of aggregate (Descantes and Hamard, 2015). With the passage of time, the surface texture of the aggregate in the wear-resistant layer of the pavement is susceptible to abrasion by round-trip traffic, resulting in a gradual reduction of the skid resistance to an equilibrium value. In addition to the polished stone value (PSV), a number of methods have been used to determine the polishing properties of aggregates, such as the petrography counting approach, mechanical polishing test methods, and image analysis techniques. However, PSV is more widely used, and the polishing resistance of coarse aggregates used for pavements is usually quantified by the Polished Stone Value (PSV) uniform test method in Europe (Slimane et al., 2008; Huang, 2010; Descantes and Hamard, 2015). Profile roughness is often used to describe surface texture (Praticò and Astolfi, 2017). The Vickers test is a suitable method that could quantify the hardness of aggregates and is more convenient to use than other hardness tests (Liu et al., 2020). Therefore, this article explores the influence of profile roughness and Vickers hardness on the Polished Stone Value (PSV) of four high-friction aggregates (90# Bauxite,
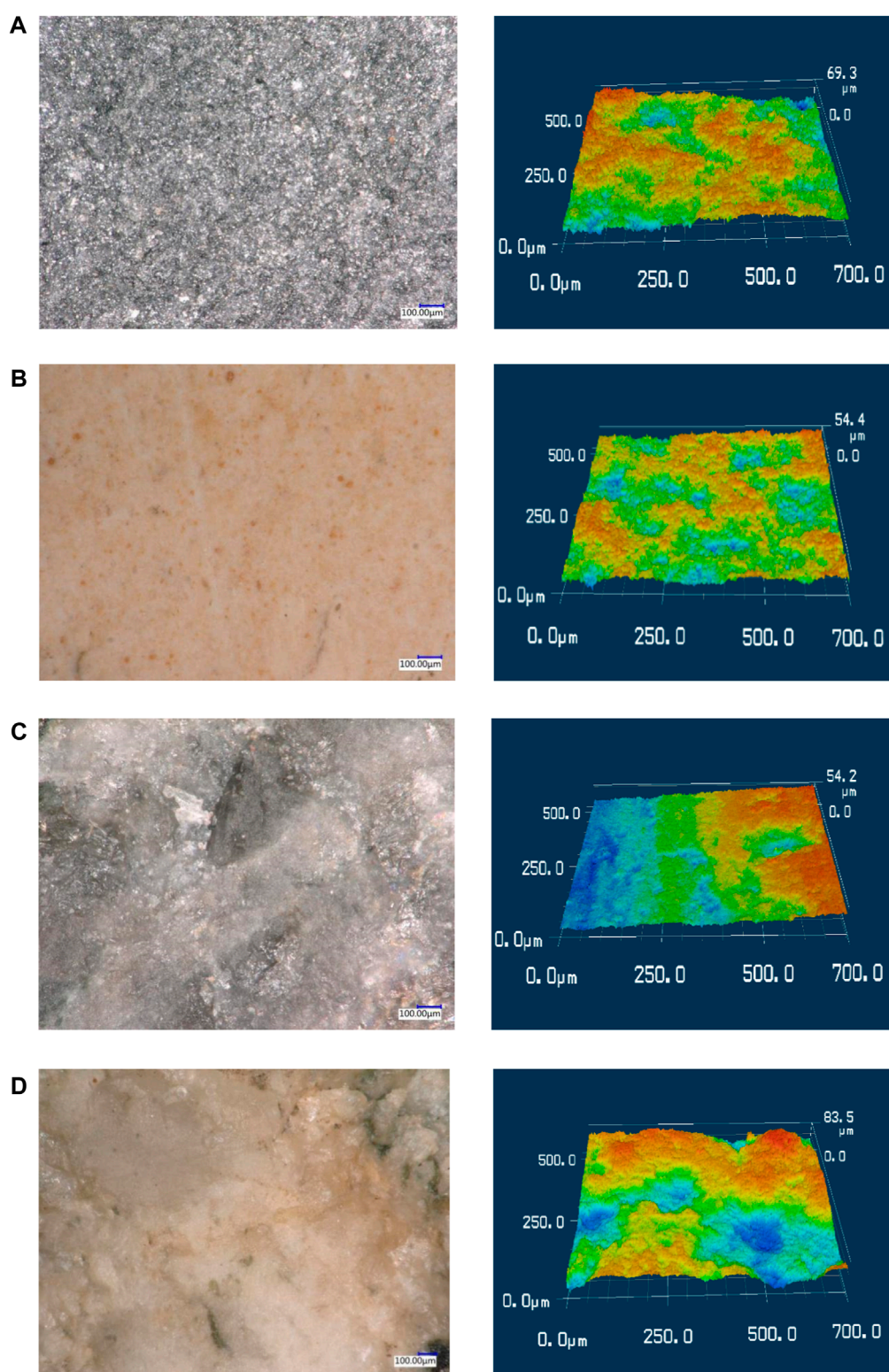
FIGURE 2
Four aggregates under laser microscopy and its 3D profile **(A)** 90#Bauxite **(B)** 75#Bauxite **(C)** Basalt **(D)** Granite.

75# Bauxite, Basalt, and Granite) during different polishing cycles. It investigates the relationship between profile roughness, Vickers hardness, and PSV, using gray correlation analysis and mathematical fitting methods to understand their impact patterns. Ultimately, it establishes a model to estimate the Polished Stone Value of high-friction aggregates.
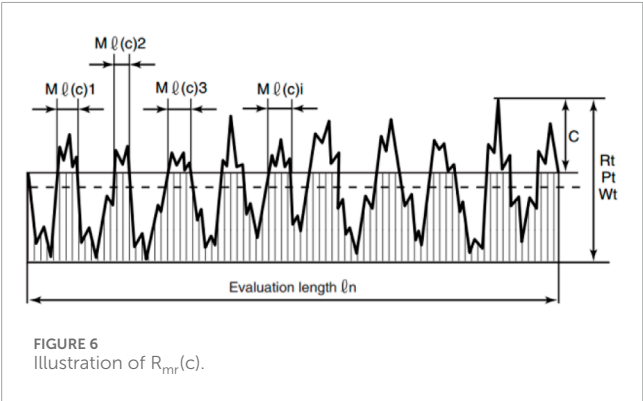
FIGURE 3
Illustration of R_a.

FIGURE 4
Illustration of R_z.

FIGURE 5
Illustration of R_q.

FIGURE 6
Illustration of $R_{mr}(c)$.
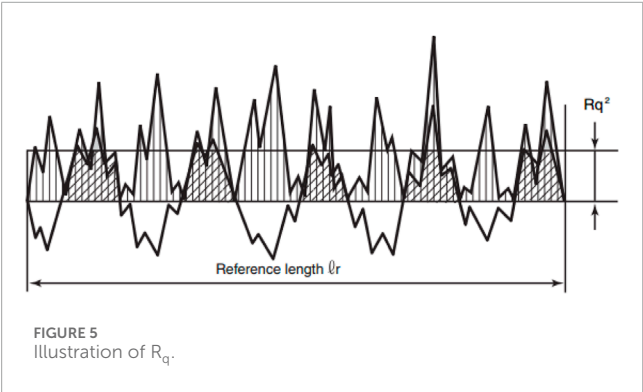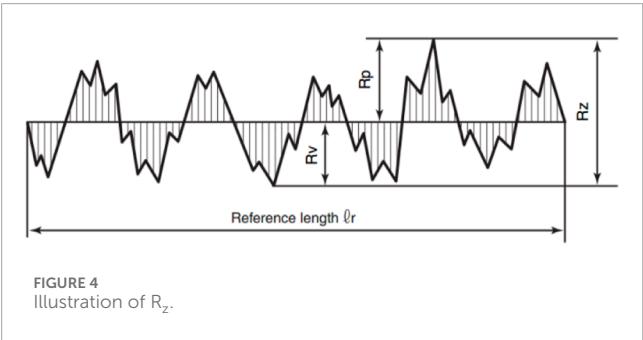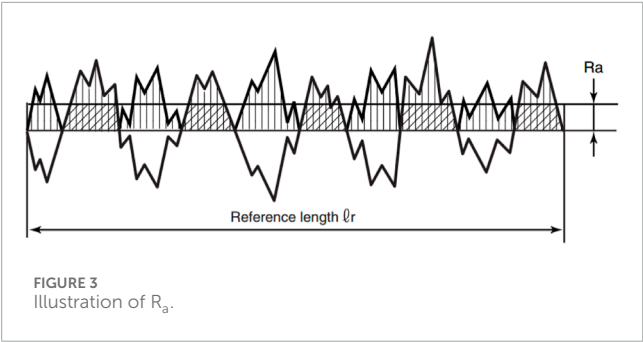
TABLE 3 Roughness parameters.

Symbol	Parameters	Definition
R_a	Arithmetic mean roughness	the average of the absolute height value along the reference length
R_z	Maximum height	the absolute vertical distance between the highest peak and the deepest valley along the reference length
R_q	Root mean square height	the root mean square along the reference length
R_{sk}	Skewness	the degree of symmetry of the surface heights about the mean plane
R_{ku}	Kurtosis	the kurtosis and steepness of texture, it indicates the nature of the height distribution
$R_{mr}(c)$	Load length ratio	the ratio of the load length $M_r(c)$ of profile curve elements to the evaluation length at cut level c

2 Materials and methods

2.1 Raw materials

Bauxite, granite, and basalt with the size of 9.5/13.2 mm were used to study the surface morphology, hardness, and anti-polishing in this study. Bauxite is was provided by Yangquan Co., Ltd. According to the dosage of Al_2O_3, there are two kinds of bauxite which are 90# and 75#, respectively. Chemical compositions of four kinds of aggregates are shown in Table 1 and their physical properties are shown in Table 2.

2.2 Experimental method

2.2.1 PSV test

The PSV test was carried out with an Accelerated Polishing Machine according to the literature (Guan et al., 2018). Four types of PSV specimens are shown in Figure 1. The polishing velocity was 320 ± 5 r/min and the load was 725 ± 10N. Then 40000, 80000, 120000,160000, and 200000 cycles of polishing with emery flour were followed. The specimen polish degree was measured by a British Pendulum device. Each test group was repeated six times to acquire the reliable value of PSV.

2.2.2 Profile roughness measurement

In this experiment, the micro-texture profile was observed by a 3D color laser microscope which was produced by Keyence Inc. The scanning range was 500 × 700µm, scanning resolution was 0.01 µm. Five stone surfaces of each specimen were obtained to reduce acquisition error. Besides, each stone has been tested three times in an attempt to improve the accuracy of the data and avoid excessive discretization results. Figure 2 illustrates microscopy and its 3D profile of four aggregates. The 3D surface topography images illustrate that 90# bauxite and granite have excellent

TABLE 4 Original data of each factor.

Type	Cycles (×10⁴)	PSV	R_a (μm)	R_q (μm)	R_z (μm)	R_{sk}	R_{ku}	R_{mr}(c) (%)
		X_0	X_1	X_2	X_3	X_4	X_5	X_6
90# Bauxite	0	74.100	11.292	18.738	97.469	0.621	2.772	35.660
	4	70.600	9.824	12.240	94.447	−0.356	2.895	49.440
	8	66.800	8.533	11.055	81.309	0.337	2.546	27.280
	12	59.300	7.865	8.551	69.293	−0.336	3.178	71.980
	14	53.200	7.283	7.673	65.240	0.006	2.454	56.810
	20	50.500	6.343	6.895	57.252	−0.024	2.519	80.760
75# Bauxite	0	63.700	10.763	16.764	92.799	−0.267	2.123	62.390
	4	61.200	9.022	12.678	82.340	−0.462	2.303	68.960
	8	59.100	7.652	10.074	64.922	0.273	2.587	33.020
	12	55.500	7.556	9.343	58.071	−0.414	2.150	67.450
	14	49.300	5.988	6.178	54.370	−0.208	2.705	67.610
	20	46.800	4.965	4.802	44.680	−0.113	2.653	57.190
Basalt	0	60.800	9.578	12.183	93.630	−0.346	2.255	47.210
	4	56.700	7.719	9.604	80.456	−0.351	1.909	69.410
	8	44.500	5.487	7.115	65.309	0.005	2.435	67.150
	12	39.200	3.679	4.124	53.965	−0.725	2.150	91.580
	14	34.800	3.101	3.718	43.968	−0.060	3.541	76.920
	20	30.200	2.881	3.483	42.527	−0.019	2.324	64.560
Granite	0	63.400	10.340	15.256	86.080	−0.389	1.953	41.590
	4	60.600	9.191	13.413	80.463	−0.255	2.378	65.490
	8	58.500	8.350	11.803	69.182	0.067	2.627	48.520
	12	50.300	6.031	8.342	55.222	0.173	2.053	81.150
	14	40.600	5.262	5.322	49.725	−0.379	2.150	80.430
	20	36.100	4.687	4.542	38.045	−0.276	2.481	62.360

surface microstructure; the micro-roughness of basalt shows poorly. Although the 75# bauxite looks more flat under the microscope, it still has a lot of small and dense micro-texture.

In order to measure the degree of change in the microscopic texture of aggregate, there are a total of six typical roughness parameters being chosen as indicators. The profile roughness parameters are obtained by VK-Analyzer software of a 3D color laser microscope. The six profile roughness parameters include arithmetic mean roughness (R_a), maximum height (R_z), root mean square height (R_q), skewness (R_{sk}), kurtosis (R_{ku}), and load length ratio (R_{mr} (c)), as shown in Table 3.

1) Arithmetic mean roughness (R_a) indicates the average of the absolute height value along the reference length. R_a calculation determines the absolute value of the height difference between the reference surface and the measured surface, and then calculates the average of the distance between each dot on the roughness curve surface and the reference surface, which is illustrated in Figure 3.

$$R_a = \frac{1}{l_r} \int_0^{l_r} |Z(x)| dx \qquad (1)$$

TABLE 5 Data Initialization for each factor.

Type	X_0	X_1	X_2	X_3	X_4	X_5	X_6
90# Bauxite	2.053	2.409	4.125	2.562	−2.248	1.117	0.572
	1.956	2.096	2.695	2.483	1.291	1.167	0.793
	1.850	1.821	2.434	2.137	−1.221	1.026	0.437
	1.643	1.678	1.883	1.821	1.217	1.281	1.154
	1.474	1.554	1.689	1.715	−0.023	0.989	0.911
	1.399	1.353	1.518	1.505	0.086	1.015	1.295
75# Bauxite	1.765	2.296	3.691	2.439	0.967	0.856	1.000
	1.695	1.925	2.791	2.164	1.674	0.928	1.106
	1.637	1.633	2.218	1.706	−0.989	1.043	0.530
	1.537	1.612	2.057	1.526	1.499	0.867	1.082
	1.366	1.278	1.360	1.429	0.754	1.090	1.084
	1.296	1.059	1.057	1.174	0.410	1.069	0.917
Basalt	1.684	2.044	2.682	2.461	1.252	0.909	0.757
	1.571	1.647	2.114	2.115	1.271	0.769	1.113
	1.233	1.171	1.566	1.717	−0.017	0.981	1.077
	1.086	0.785	0.908	1.418	2.626	0.867	1.469
	0.964	0.662	0.819	1.156	0.217	1.427	1.233
	0.837	0.615	0.767	1.118	0.068	0.937	1.035
Granite	1.756	2.206	3.359	2.263	1.409	0.787	0.667
	1.679	1.961	2.953	2.115	0.924	0.959	1.050
	1.620	1.782	2.599	1.818	−0.241	1.059	0.778
	1.393	1.287	1.837	1.451	−0.625	0.828	1.301
	1.125	1.123	1.172	1.307	1.372	0.867	1.290
	1	1	1	1	1	1	1

2) Maximum height (R_z) indicates the absolute vertical distance between the highest peak and the deepest valley along the reference length, which is illustrated in Figure 4.

$$R_z = \max(Z_n) + |\min(Z_n)| \qquad (2)$$

3) Root mean square height (R_q) indicates the root mean square along the reference length, which is illustrated in Figure 5.

$$R_q = \sqrt{\frac{1}{N} \sum_{n=1}^{N} Z_n{}^2} \qquad (3)$$

4) Skewness (R_{sk}) uses the cube of the root mean square height to display the dimensionless cube of the reference length $Z(x)$, which represents the degree of symmetry of the surface heights about the mean plane.

$$R_{sk} = \frac{1}{R_q{}^3}\left[\frac{1}{N} \sum_{n=1}^{N} Z_n{}^3\right] \qquad (4)$$

5) Kurtosis (R_{ku}) uses the fourth power of the root mean square height to display the dimensionless fourth power of the reference length $Z(x)$, which describes the kurtosis and steepness of texture, it indicates the nature of the height distribution.

$$R_{ku} = \frac{1}{R_q{}^4}\left[\frac{1}{N} \sum_{n=1}^{N} Z_n{}^4\right] \qquad (5)$$

6) Load length ratio (R_{mr} (c)) shows the ratio of the load length M_r (c) of profile curve elements to the evaluation length at cut level c (height in % or μm), which is illustrated in Figure 6.

$$R_{mr}(c) = \frac{100}{l_n} \sum_{n=1}^{m} Ml(c)i(\%) \qquad (6)$$

2.2.3 Vickers hardness test

The Vickers hardness test was carried out according to ASTM E92-2016 (ASTM E92-2016, 2023). Tests with Vickers hardness testers manufactured by Mega (Suzhou) Co., Ltd. The Vickers hardness is obtained by Eq. 7.

$$H = \frac{2F \sin\frac{136°}{2}}{d^2} = 1.854\frac{F}{d^2} \qquad (7)$$

Where H is Vickers hardness (H_v), F is the force applied to the diamond (kgf), d is the average length of the diagonal left by the indenter (mm).

2.3 Methodology of gray correlation analysis

Gray correlation analysis is one of the most widely used models of Grey system theory (Dews and Bishop, 2007). Gray correlation analysis has been used in many fields such as engineering, financial, physical, etc (Deng, 1989; Zhu et al., 2021; Cao et al., 2022; Gosavi and Jaybhaye, 2023). Grey correlation analysis is a suitable mathematical method for researching the correlation with each factor (Li et al., 2023). The polishing process of aggregate is complex, and profile roughness parameters are multiple and interdependent (Wang et al., 2017). The Gray correlation coefficient was adopted to describe the correlation degree between the profile roughness parameters and PSV. A higher gray correlation coefficient shows good corresponding to a correlation degree. The calculation of the Gray correlation coefficient is generally divided into the following four steps:

(1) With the intention of evaluating the significance of each factor, PSV was extracted to determine the reference sequence, $X_0(k)$.

TABLE 6 The absolute differential value of X_0 with X_i.

Type	Δ1	Δ2	Δ3	Δ4	Δ5	Δ6
	$\Delta 1 = X_0(k)-X_1(k)$	$\Delta 1 = X_0(k)-X_2(k)$	$\Delta 1 = X_0(k)-X_3(k)$	$\Delta 1 = X_0(k)-X_4(k)$	$\Delta 1 = X_0(k)-X_5(k)$	$\Delta 1 = X_0(k)-X_6(k)$
90# Bauxite	0.357	2.073	0.509	4.301	0.935	1.481
	0.140	0.739	0.527	0.665	0.789	1.163
	0.030	0.584	0.287	3.072	0.824	1.413
	0.035	0.240	0.179	0.425	0.362	0.488
	0.080	0.216	0.241	1.497	0.484	0.563
	0.046	0.119	0.106	1.313	0.384	0.104
75# Bauxite	0.532	1.926	0.675	0.798	0.909	0.764
	0.230	1.096	0.469	0.022	0.767	0.589
	0.005	0.581	0.069	2.626	0.594	1.108
	0.075	0.520	0.011	0.038	0.671	0.456
	0.088	0.005	0.063	0.612	0.275	0.281
	0.237	0.239	0.122	0.887	0.227	0.379
Basalt	0.359	0.998	0.777	0.432	0.775	0.927
	0.076	0.544	0.544	0.300	0.801	0.458
	0.062	0.334	0.484	1.249	0.251	0.156
	0.301	0.178	0.333	1.541	0.219	0.383
	0.302	0.145	0.192	0.747	0.463	0.269
	0.222	0.070	0.281	0.769	0.100	0.199
Granite	0.450	1.603	0.506	0.348	0.969	1.089
	0.282	1.274	0.436	0.755	0.720	0.628
	0.161	0.978	0.198	1.862	0.562	0.842
	0.107	0.443	0.058	2.018	0.566	0.092
	0.002	0.047	0.182	0.247	0.258	0.165
	0	0	0	0	0	0

TABLE 7 The minimum and the maximum differential value of X_0 with X_i.

min $X_0(k)-X_i(k)$	Max $X_0(k)-X_i(k)$
0	4.3

In addition, the other parameters (R_a, R_q, R_z, R_{sk}, R_{ku}, $R_{mr}(c)$) which were selected on the basis of original data, were specified as comparison sequence, $X_i(k)$; where k = 1,2,3 … … , m.

(2) To eliminate the effect of differences in data between the reference sequence and comparison sequences,

the dimensionless treatment of initial values was normalized by Eq. 8.

$$X_i' = \frac{X_i}{X_i(\text{n})}, i = 0, 1, 2, 3, 4....n \qquad (8)$$

(3) In order to obtain the maximum absolute difference and the minimum absolute difference, Eqs 9, 10 could be used to calculate for each sequence. Afterwards, the gray correlation coefficient ξ was calculated by Eq. 11.

$$\max_i \max_k \Delta_i(k) = \max_i \max_k |x_0(k) - x_i(k)| \qquad (9)$$

TABLE 8 The correlation coefficient $\xi_i(k)$ of each factor.

Type	$\xi_1(k)$	$\xi_2(k)$	$\xi_3(k)$	$\xi_4(k)$	$\xi_5(k)$	$\xi_6(k)$
	0.858	0.509	0.808	0.333	0.697	0.592
	0.939	0.744	0.803	0.764	0.732	0.649
90# Bauxite	0.986	0.787	0.882	0.412	0.723	0.603
	0.984	0.900	0.923	0.835	0.856	0.815
	0.964	0.909	0.899	0.590	0.816	0.793
	0.979	0.947	0.953	0.621	0.849	0.954
	0.802	0.527	0.761	0.729	0.703	0.738
	0.904	0.662	0.821	0.990	0.737	0.785
75# Bauxite	0.998	0.787	0.969	0.450	0.783	0.660
	0.966	0.805	0.995	0.983	0.762	0.825
	0.961	0.997	0.971	0.779	0.886	0.884
	0.901	0.900	0.946	0.708	0.904	0.850
	0.857	0.683	0.735	0.833	0.735	0.699
	0.966	0.798	0.798	0.878	0.729	0.825
Basalt	0.972	0.866	0.816	0.632	0.895	0.932
	0.877	0.924	0.866	0.583	0.907	0.849
	0.877	0.937	0.918	0.742	0.823	0.889
	0.906	0.969	0.884	0.737	0.956	0.915
	0.827	0.573	0.809	0.861	0.689	0.664
	0.884	0.628	0.831	0.740	0.749	0.774
Granite	0.930	0.687	0.916	0.536	0.793	0.718
	0.953	0.829	0.974	0.516	0.792	0.959
	0.999	0.979	0.922	0.897	0.893	0.929
	1	1	1	1	1	1

TABLE 9 The grey correlation degree between roughness parameters and PSV.

R_1	R_2	R_3	R_4	R_5	R_6
0.9287	0.8061	0.8834	0.7144	0.8087	0.8042

$$\min_i \min_k \Delta_i(k) = \min_i \min_k |x_0(k) - x_i(k)| \qquad (10)$$

$$\xi(x_0(k), x_i(k)) = \frac{\min_i \min_k |x_0(k) - x_i(k)| + \rho \max_i \max_k |x_0(k) - x_i(k)|}{|x_0(k) - x_i(k)| + \rho \max_i \max_k |x_0(k) - x_i(k)|} \qquad (11)$$

Where, ρ is the distinguishing coefficient ($0 < \rho < 1$); $\rho = 0.5$.

(4) In accordance with the results above, the average value of the correlation coefficient R_i could be calculated by Eq. 12:

$$R_i = \frac{1}{n} \sum_{k=1}^{n} \lambda_k \xi(x_0(k), x_i(k)) \qquad (12)$$

3 Results and discussions

3.1 The correlation degree between the profile roughness parameters and PSV

Profile roughness parameters and PSV of four types of aggregates during different polishing cycles are illustrated in Table 3. The gray correlation coefficient is calculated in four steps. At first, the original data of each factor including R_a, R_q, R_z, R_{sk}, R_{ku}, and PSV was summarized in Table 4. Then, the initial value is normalized after dimensionless processing, and the results are shown in Table 5. The absolute difference between X_0 and X_i was obtained and shown in Table 6. Thirdly, the minimum differential and maximum differential are also calculated and shown in Table 7. After these steps, the correlation coefficient $\xi_i(k)$ of each factor are obtained and shown in Table 8. Finally, the grey correlation degree (R_i) is shown in Table 9, and the correlation degree between PSV and profile roughness parameters is evaluated.

Table 4 shows that the change rule of four kinds of aggregates is basically the same. As the polishing time increases, the values of PSV, R_a, and R_z decrease, which proves that the changes of these two parameters (R_a, R_z) have a certain correlation with PSV.

According to the results of gray correlation analysis in Table 9, the sequence of six factors is $R_a > R_z > R_{ku} > R_{mr}(c) > R_q > R_s$. R_a has the maximum correlation degree with PSV ($R_1 = 0.929$). The correlation degree of R_z is the second largest indicator. The decreasing tendency of the values R_a and R_z could well represent the decay trend of PSV. The value of PSV increased with the increase of R_a and R_z. It indicates that high arithmetic mean roughness and maximum height of the surface is beneficial to the PSV of aggregates. Polishing cycles have a great effect on the PSV of aggregates. With the increase in polishing cycles, the value of R_a, R_z, and R_q decreased. The micro-texture of the surface is destroyed and friction decreases significantly.

The link between roughness parameters and PSV is multiple and difficult to characterize due to such numerous profile roughness parameters. Therefore, fewer parameters need to be selected depending on the correlation degrees between profile roughness parameters and PSV. Moreover, the result of gray correlation entropy indicates that it is difficult to describe the relationship between micro-texture and the polishing resistance of aggregates using only a single parameter. It requires several parameters together to characterize the micro-texture of the surface for describing the relationship between micro-texture and the polishing resistance of aggregates. Because of the high correlation with PSV, R_a, and R_z are chosen as the main indicators.

TABLE 10 Model F-test results.

	DF	Sum of squares	Mean square	F value	Prob > F
Regression	2	71717.23057	35858.61529	3017.83122	0
Residual	22	261.40943	11.88225		
Uncorrected Total	24	71978.64			
Corrected Total	23	3091.905			

TABLE 11 t-Test Results.

Variable		t Statistic	DF	Prob>|t|
R_a	Equal Variance Assumed	−19.17721	46	1.41497E-23
	Equal Variance Assumed	−19.17721	24.97034	1.86785E-16
R_z	Equal Variance Assumed	3.16478	46	0.00275
	Equal Variance Assumed	3.16478	38.99075	0.00301

3.2 Deriving the link between profile roughness parameters and PSV

The relationship between these variables (R_a and R_z) and PSV were analyzed with mathematical fitting by origin 8.0, and the independent variables of the multivariate regression model were established in three variables called R_a and R_z, which is presented as Eq. 13. The correlation coefficient of determination $R^2 = 0.912$. The results of the F-Test are shown in Table 10. Based on the analysis the following model was obtained (F theoretical << F observed) relating PSV with R_a and R_z. Results of the t-Test are summarized in Table 11. All p-values are less than 0.01. F-tests and t-tests are conventional methods of accuracy testing, and their results point to a high degree of accuracy of the model. Therefore, it can be concluded that the relationship between PSV and independent variables is linear for all models.
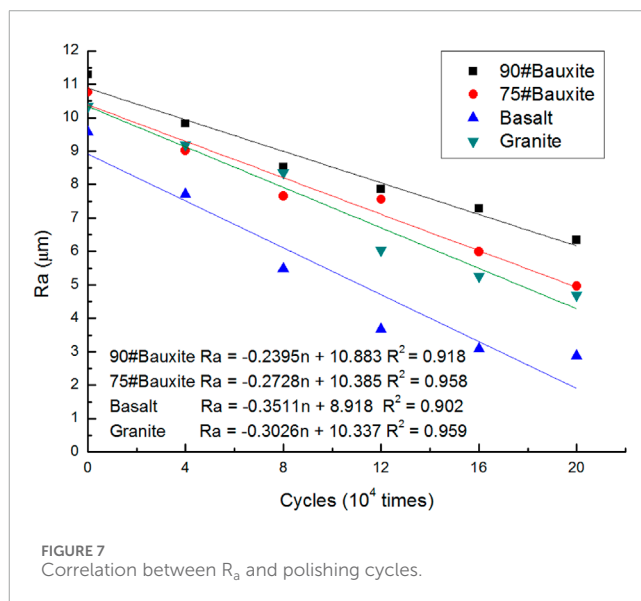
$$PSV = 3.912R_a + 0.034R_z + 19.661 \qquad (13)$$

FIGURE 7
Correlation between R_a and polishing cycles.

3.3 Deriving the link between profile roughness parameters and vickers hardness

3.3.1 Correlation analysis between Ra and vickers hardness

Figure 7 shows the good linear relationship between R_a and polishing cycles. The relationship between R_a and polishing cycles can be described by Eq. 14.

$$R_a = K_1 n + R_{ai} \qquad (14)$$

Where R_a is arithmetic mean roughness (μm), n is polishing cycles (times), R_{ai} is the initial value of R_a (μm), and K_1 is the attenuation rate of R_a per polishing cycle (um/times).
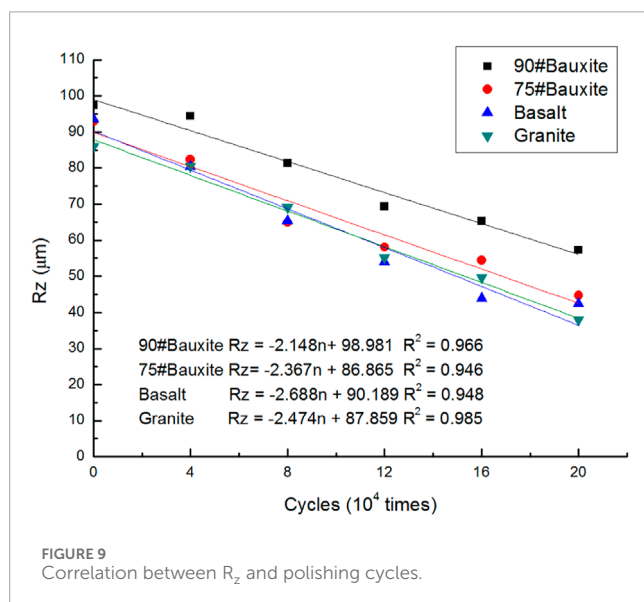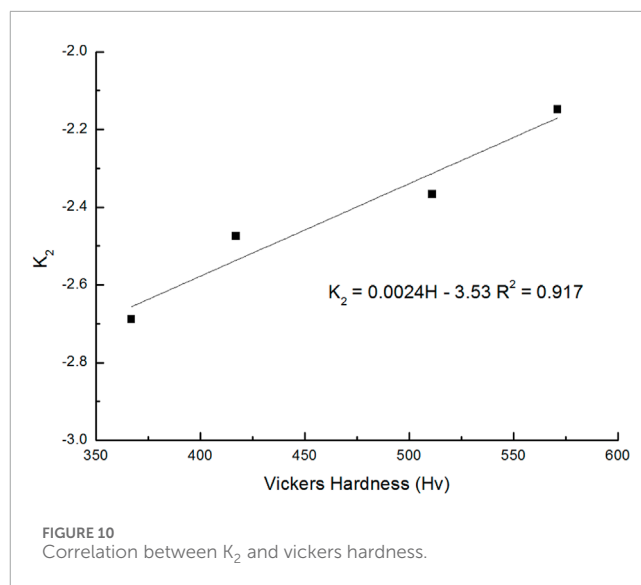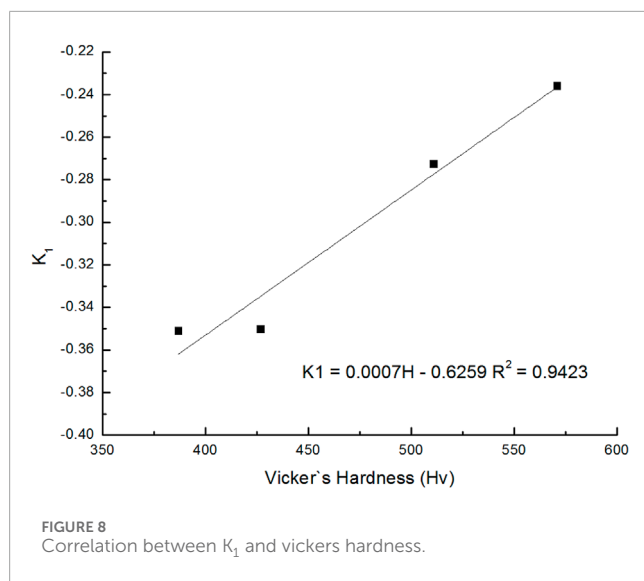
There is a certain relationship between K_1 and Vickers Hardness. The correlations between K_1 and Vickers hardness are shown in Figure 8. From Figure 8, it can be seen that the correlation coefficient of the linear fitted equation is 0.9423, which shows the good correlation between K_1 and Vickers hardness. Thus, K_1 can be obtained by Eq. 15.

$$K_1 = 0.0007H − 0.6259 \qquad (15)$$

Where H is Vickers hardness of aggregate (H_v).
With Eqs 14, 15, R_a can be determined through Eq. 16

$$R_a = (0.0007H − 0.6259)n + R_{ai} \qquad (16)$$

FIGURE 8
Correlation between K_1 and vickers hardness.

FIGURE 10
Correlation between K_2 and vickers hardness.

FIGURE 9
Correlation between R_z and polishing cycles.

TABLE 12 Basic parameters in calculation model.

Type	R_{ai} (μm)	R_{zi} (μm)	H (H_v)
90# Bauxite	10.883	98.981	571
75# Bauxite	10.385	86.865	511
Basalt	8.918	90.189	387
Granite	10.337	87.859	427

obtained by Eq. 18.

$$K_2 = 0.0024H - 3.53 \tag{18}$$

Where H is Vickers hardness of aggregate (H_v).

With Eq. 17 and Eq. 18 R_z can be determined through Eq. 19:

$$R_z = (0.0024H - 3.53)n + R_{zi} \tag{19}$$

In the above mathematical derivation procedure from Eq. 14–19, it is easy to find that the absolute value of K_1 and K_2 decreased with the increase of Vickers Hardness. It indicates that the high Vickers hardness of aggregates can stabilize the micro-texture of aggregates and retard the frictional attenuation during the long-term polishing process.

3.3.2 Correlation analysis between Rz and vickers hardness

Figure 9 shows the good linear relationship between R_z and polishing cycles. The relationship between R_z and polishing cycles can be described by Eq. 17.

$$R_z = K_2 n + R_{zi} \tag{17}$$

Where R_z is maximum height (μm), n is polishing cycles (times), R_{ai} is the initial value of R_z (μm), and K_2 is the attenuation rate of R_z per polishing cycle (μm/times).

There is a certain relationship between K_2 and Vickers Hardness. The correlations between K_2 and Vickers Hardness are shown in Figure 10. From Figure 10, it can be seen that the correlation coefficient of the linear fitted equation is 0.917, which shows the good correlation between K_2 and Vickers hardness. Thus, K_2 can be

3.4 Deriving the link between roughness parameters, vickers hardness, and PSV

From Eqs 13–19, the link between surface profile roughness, hardness, and PSV can be obtained as follows:

$$PSV = 0.0032Hn - 2.859n + 4.376R_{ai} + 0.034R_{zi} + 19.661 \tag{20}$$

Where R_{ai}, R_{zi}, and H are the basic parameters, which can be obtained by profile roughness measurement and Vickers hardness

test. According to these test results, the basic parameters of Bauxite, Basalt, and Granite are shown in Table 12.

The proposal indicators in the regression could well instruct the selection of high friction aggregates so that a practical method that could improve the ability of pavement skid resistance is obviously reported in the further study. Aggregate friction life also can be predicted by this regression, which may contribute to the service life estimation and condition prediction of the wearing course, especially high friction surface treatment.

4 Conclusion

(1) The influence of profile roughness parameters of four types of aggregates was calculated by gray correlation analysis. According to the analysis results, R_a and R_z influenced PSV significantly while R_q, R_{sk}, R_{ku}, and R_{mr} (c) had a relatively weak effect.

(2) The relationship between the variables (R_a, R_z) and PSV was established. The higher the values of Ra and Rz, the more favorable the PSV of the aggregate; there is a good linear relationship between Ra and Rz attenuation rates (K_1 and K_2) and Vickers hardness. The higher the Vickers hardness, the more stable the microtexture of the aggregate and the less frictional attenuation during polishing.

(3) Based on microtexture and Vickers hardness, a multiple regression model was developed for estimating the PSV of high-friction aggregates during long-term polishing.

Data availability statement

The raw data supporting the conclusion of this article will be made available by the authors, without undue reservation.

References

ASTM E92-2016 (2023). *Standard test methods forVickers hardness and KnoopHardness of metallic materials.*

Cao, W., Xuan, X. D., Wu, We.D., Chen, L. H., and Zhang, Q. Y. (2022). A new method for determining the optimal adaptive thermal comfort model with grey relational analysis. *Build. Environ.* 221, 109277. doi:10.1016/j.buildenv.2022.109277

Chen, D., Han, S., Ye, A. J., Ren, X. C., Wang, W., and Wang, T. T. (2020). Prediction of tire-pavement friction based on asphalt mixture surface texture level and its distributions. *Road. Mater. Pavement Des.* 21 (6), 1545–1564. doi:10.1080/14680629.2018.1560354

Chen, S. Y., Liu, X. Y., Luo, H. Y., Yu, J. M., Chen, F. D., Zhang, Y., et al. (2022). A state-of-the-art review of asphalt pavement surface texture and its measurement techniques. *J. Road. Eng.* 2 (2), 156–180. doi:10.1016/j.jreng.2022.05.003

Deng, J. L. (1989). Introduction to grey system theory. *J. Grey. Syst.* 1 (1), 1–24. doi:10.1007/978-3-642-16158-2_1

Descantes, Y., and Hamard, E. (2015). Parameters influencing the polished stone value (PSV) of road surface aggregates. *Constr. Build. Mater.* 100, 246–254. doi:10.1016/j.conbuildmat.2015.10.002

Author contributions

Funding

Acknowledgments

Conflict of interest

The authors declare that the research was conducted in the absence of any commercial or financial relationships that could be construed as a potential conflict of interest.

Publisher's note

All claims expressed in this article are solely those of the authors and do not necessarily represent those of their affiliated organizations, or those of the publisher, the editors and the reviewers. Any product that may be evaluated in this article, or claim that may be made by its manufacturer, is not guaranteed or endorsed by the publisher.

Dews, S. J., and Bishop, R. J. (2007). Factors affecting the skid-resistance of calcined bauxite. *Chem. Technol. Biotechnol. Biotechnol.* 22 (10), 1117–1124. doi:10.1002/jctb.5020221009

Ergin, B., Gökalp, İ., and Uz, V. E. (2020). Effect of aggregate microtexture losses on skid resistance: laboratory-based assessment on chip seals. *Mater. Civ. Eng.* 32 (4), 04020040. doi:10.1061/(asce)mt.1943-5533.0003096

Gardziejczyk, W., and Wasilewska, M. (2016). Evaluation of microtexture changes of coarse aggregate during simulated polishing. *Arch. Civ. Eng.* 62 (2), 19–34. doi:10.1515/ace-2015-0062

Ge, H. T., Sha, A. M., Han, Z. Q., and Xiong, X. W. (2018). Three-dimensional characterization of morphology and abrasion decay laws for coarse aggregates. *Constr. Build. Mater.* 188, 58–67. doi:10.1016/j.conbuildmat.2018.08.110

Gosavi, S. V., and Jaybhaye, M. D. (2023). Friction stir welding process optimization of Al 7075/SiC composites using grey relational analysis. *Mater. Today Proc.* 72 (3), 719–723. doi:10.1016/j.matpr.2022.08.493

Guan, B. W., Wu, J. Y., Xie, C., Fang, J. H., Zheng, H. L., and Chen, H. (2018). Influence of macrotexture and microtexture on the skid resistance of aggregates. *Adv. Mater. Sci. Eng.* 2018 (5), 1–9. doi:10.1155/2018/1437069

Guo, F. C., Pei, J. Z., Zhang, J. P., Li, R., Zhou, B. C., and Chen, Z. X. (2021). Study on the skid resistance of asphalt pavement: a state-of-the-art review and future prospective. *Constr. Build. Mater.* 303, 124411. doi:10.1016/j.conbuildmat.2021. 124411

Henry, J. J. (2000). *National cooperative highway research program*. Washington, D.C. Transportation Research Board. Evaluation of Pavement Friction Characteristics. Synthesis of Highway Practice No.291.

Huang, C. Y. (2010). Texture characteristics of unpolished and polished aggregate surfaces. *Tribol. Int.* 43 (1-2), 188–196. doi:10.1016/j.triboint.2009.05.024

ISO, Characterization of pavement texture by use of surface profiles, part 1: determination of mean profile depth. 2019, 43.

Jiang, W., Yuan, D. D., Shan, J. H., Ye, W. L., Lu, H. H., and Sha, A. M. (2020). Experimental study of the performance of porous ultra-thin asphalt overlay. *Int. J. Pavement Eng.* 6, 2049–2061. doi:10.1080/10298436.2020.1837826

Kane, M., and Edmondson, V. (2020). Long-term skid resistance of asphalt surfacings and aggregates' mineralogical composition: generalisation to pavements made of different aggregate types. *Wear* 454-455, 203339. doi:10.1016/j.wear.2020. 203339

Leng, Z., Fan, Z. P., Liu, P. F., Kollmann, J., Oeser, M., Wang, D. W., et al. (2023). Texturing and evaluation of concrete pavement surface: a state-of-the-art review. *J. Road. Eng.* 3 (3), 252–265. doi:10.1016/j.jreng.2023.08.001

Li, B., Liu, P. Y., Zhao, Y., Li, X. M., and Cao, G. (2023). Effect of graphene oxide in different phases on the high temperature rheological properties of asphalt based on grey relational and principal component analysis. *Constr. Build. Mater.* 362, 129714. doi:10.1016/j.conbuildmat.2022.129714

Liu, J. Y., Guan, B. W., Chen, H. X., Liu, K. P., Xiong, R., and Xie, C. (2020). Dynamic model of polished stone value attenuation in coarse aggregate. *Materials* 13 (8), 1875. doi:10.3390/ma13081875

Pranjić, I., Deluka-Tibljaš, A., Cuculić, M., and Šurdonja, S. (2020). Influence of pavement surface macrotexture on pavement skid resistance. *Transp. Res. Procedia.* 45, 747–754. doi:10.1016/j.trpro.2020.02.102

Pratico, F. G., and Astolfi, A. (2017). A new and simplified approach to assess the pavement surface macrotexture. *Constr. Build. Mater.* 148, 476–483. doi:10.1016/j.conbuildmat.2017.05.050

Slimane, A. B., Khoudeir, M., Brochard, J., and Do, M. T. (2008). Characterization of road microtexture by means of image analysis. *Wear* 264 (5-6), 464–468. doi:10.1016/j.wear.2006.08.045

Wang, Y. R., Gao, Y. M., Sun, L., Li, Y. F., Zheng, B. C., and Zhai, W. Y. (2017). Effect of physical properties of Cu-Ni-graphite composites on tribological characteristics by grey correlation analysis. *Results Phys.* 7, 263–271. doi:10.1016/j.rinp.2016.12.041

Zhu, L. H., Zhao, C., and Dai, J. (2021). Prediction of compressive strength of recycled aggregate concrete based on gray correlation analysis. *Constr. Build. Mater.* 273, 121750. doi:10.1016/j.conbuildmat.2020.121750

Zhu, S. Y., Ji, X. P., Zhang, Z. M., Shao, D. Y., Li, H. L., and Yun, C. (2022). Evolution characteristics of the surface texture of the wearing course on asphalt pavement based on accelerated pavement polishing. *Constr. Build. Mater.* 333, 127266. doi:10.1016/j.conbuildmat.2022.127266

Zong, Y. J., Li, S., Zhang, J. B., Zhai, J. H., Li, C., Ji, K., et al. (2021). Effect of aggregate type and polishing level on the long-term skid resistance of thin friction course. *Constr. Build. Mater.* 282, 122730. doi:10.1016/j.conbuildmat.2021.122730

Mechanical properties of thermally damaged mortar under coupled static-dynamic loading

Chengjuan Ying[1], Haiming Chen[2]*, Jie Chen[2], Liangxiao Xiong[3] and Duoxi Yao[1]

[1]School of Earth and Environment, Anhui University of Science and Technology, Huainan, China, [2]Engineering Research Center of Underground Mine Construction, Ministry of Education, Anhui University of Science and Technology, Huainan, China, [3]School of Civil Engineering and Architecture, East China Jiaotong University, Nanchang, China

In buildings that experience fires, cement mortar is subjected to high-temperature environments and not only the weight of the structure above but also blast loads, leading to structural damage and loss of load-bearing capacity. To investigate the static and dynamic mechanical properties of thermally damaged mortar, a series of tests utilizing modified split Hopkinson pressure bar were conducted. These tests included quasi-static, conventional dynamic and coupled static-dynamic loading tests on mortar specimens that were subjected to seven temperature levels: 20°C, 100°C, 200°C, 300°C, 400°C, 500°C, and 600°C. The test results revealed that both the thermal damage and loading method had an impact on the mechanical properties and damage characteristics of the mortar specimens. The compressive strength, elastic modulus and absorbed energy ratio of mortar decreased as temperature increased. Notably, the quasi-static strength loss rate was 60% when the temperature reached 600°C. Under coupled static-dynamic loading, the specimens exhibited higher strength, elastic modulus, reflected energy ratio, and transmitted energy ratio. Conversely, they had lower average strain rates and absorbed energy ratios. Intriguingly, the dynamic growth factor had a relative increase of 0.7−2.0 compared with other loading methods. Furthermore, the higher temperature, the higher fragmentation of the specimens in the fragmentation pattern. Conventional dynamic loading resulted in the greatest degree of fragmentation. The findings provide a scientific basis for the design and evaluation of concrete shockproof and explosion-resistant structures.

KEYWORDS

mechanical properties, thermal damage, mortar, coupled static-dynamic loading, energy dissipation

1 Introduction

Cement mortar was widely utilized in various architectural structures, including buildings, bridges, and tunnels. In modern times, the complex layout of building pipelines and dense urban landscapes had increased the likelihood and severity of fire, resulting in substantial economic losses (Aitcin, 2003; Hertz, 2005; Liu et al., 2020). Fire posed significant threats to individuals' safety and property, with fire losses in China steadily rising. Fires caused severe damage to the building materials, resulting in a decrease in the structure's load-bearing capacity (Schrefler et al., 2002; Patrick and Pietro, 2014). During a fire incident, the upper building structure experienced high-temperature failure,

while the lower structure was impacted by falling debris, accompanied by the explosive effects of explosive materials. Cementitious materials were subjected to a combination of high temperature and various types of loading failure, ultimately leading to building collapse, posing a significant threat to the safety of individuals and property (Khoury, 2000; Annerel and Taerwe, 2009; Du et al., 2018). Therefore, to further understand the mechanical properties of cement mortar in abnormal environments, it was essential to evaluate the residual properties after thermal damage (Lu et al., 2013; Mukesh and Shashank, 2019; Zhao et al., 2019).

During fire, the simultaneous occurrence of thermal damage and various forms of loading on cement mortar often led to the destruction of the concrete structures (Biolzi, Cattaneo, and Rosati, 2008). Recent studies primarily focused on investigating the static mechanical properties of thermally damaged cement-based materials. Cree, Green, and Noumowé (2013) carried out quasi-static strength tests on thermally damaged cement mortar and concrete, and established typical strength loss model. Bamonte, Gambarova, and Sciarretta (2021) investigated the mechanical properties of mortars after heating to 200, 400 and 600°C and 900°C to evaluate the thermal diffusion coefficient. Jeyaprabha, Elangovan, and Prakash (2016) placed mortar mixtures at temperatures of 200°C, 500°C, 700°C, and 900°C, followed by cooling with water, and measured their compressive strength. Yazıcı, Sezer, and Şengül (2012) investigated the effect of subjecting mortars to temperature ranging from 20°C to 750°C in a ceramic furnace for 1 h on their compressive strength. Zhang et al. (2000) investigated the effects of high temperature duration and curing age on the energy parameters, strength parameters, stiffness parameters, and brittleness parameters of ordinary and high-strength thermally damaged concrete. It was found that these properties generally decreased linearly with increasing temperature. Deng et al. (2020) studied the mechanical properties of recycled aggregate concrete after thermal temperature to provide scientific guidance for the design of recycled concrete fire protection. In addition, some scholars had studied the static-dynamic behaviors of concrete. Chen et al. (2019); Luo et al. (2020) studied the static-dynamic mechanical properties of concrete columns in order to provide reference for earthquake resistance and disaster reduction.

Concrete was susceptible to high temperatures and blast or impact loads. Therefore, the effect of thermal damage on the dynamic mechanical properties of concrete was crucial. However, there was little research on the behavior of cement mortar under the combination of high temperature and impact loads. Bi et al. (2020) found water cooling produced more irregular fragments and smaller fragments than air cooling at the same temperature and strain rate during the dynamic test of concrete. Yao et al. (2017) studied the mortar's dynamic compressive strength treated temperatures ranging from 150°C to 850°C, quantified thermal damage based on microcracks and chemical changes, and developed a dynamic uniaxial loading model with temperature and strain rate effects using damage variables. This model predicted the strength of mortar after high temperatures.

However, there is a lack of research on mechanical properties of thermally damaged cement mortar under different loading forms, especially under coupled static-dynamic loading. In this study,

mortar was first heated to temperatures of 100°C, 200°C, 300°C, 400°C, 500°C, and 600°C, and then naturally cooled. Subsequently, quasi-static, dynamic and coupled static-dynamic loading tests were conducted using a modified SHPB device. The effects of different loading modes on the mechanical properties, damage morphology, and energy dissipation characteristics of the thermally damaged cement mortar were discussed. It was found that when the temperature reached 600°C, the quasi-static strength loss rate was about 60%, and the strength increased under static-dynamic loading. The results of this study will help further understand the effects of different loading methods on dynamic strength and deformation characteristics of thermally damaged mortar, reveal the damage law and dynamic damage mechanism of mortar after high-temperature damage. The research results will provide scientific basis for improving the fire safety performance of buildings and evaluating fire accidents.

2 Materials and methods

2.1 Materials

P·O 42.5 cement was produced from Huainan Conch Cement Co., Ltd. in Huainan city in this study. The natural river sand was collected from the Huaihe River region of China, and had a fine grain modulus of 2.36 and an apparent density of 2,550 kg/m^3. The water was taken from the laboratory tap. The chemical compositions of cement are presented in Table 1.

2.2 Sample preparation

The water-binder ratio of the mortar used in this study was 0.38, and the ratio of binder to sand was 1:1.2 (Xiong and Chen, 2020). Different loading tests were conducted on specimens with a diameter of 50 mm and height of 50 mm, following the method described in the reference by Zhou et al. (2012). The specimens were cured for 28 days after casting. The test program is presented in Table 2.

2.3 Methods

2.3.1 Thermal treatments
To prevent the rapid evaporation of water in the Muffle furnace from damaging the furnace wall, the specimens were dried in a 105°C oven for 1 day. They were heated to temperatures of 100°C, 200°C, 300°C, 400°C, 500°C and 600°C at a rate of 6°C/min after completely cooled. Each temperature was maintained for 120 min to ensure uniform temperature distribution within the specimens then cooled in the furnace before further testing (Gao et al., 2023). A group of nine specimens were used at each temperature. The SX2-8-10A resistance furnace manufactured by the Shangyu Daoxu Scientific Instrument Co., Ltd. in Shaoxing city was utilized in the study. The thermal cycle temperature curve of high-temperature treatment is shown in Figure 1.

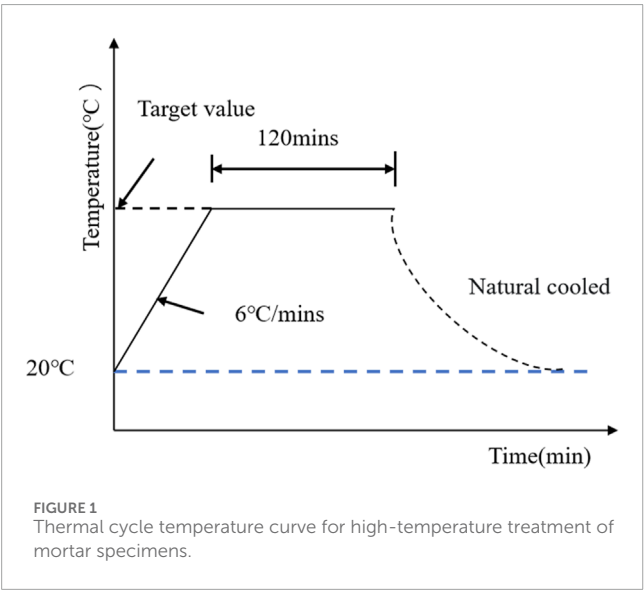### 2.3.2 Quasi-static loading test
The quasi-static compressive strength of the mortar was determined using a DYE-300 universal testing machine. The loading

TABLE 1 Chemical compositions of cement (wt%).

Material	CaO	SiO$_2$	Fe$_2$O$_3$	Al$_2$O$_3$	MgO	SO$_3$	LOI
Cement	49.7	30.6	3.4	7.8	3.7	3.7	1.1

TABLE 2 Test program.

Group (S)	Thermal temperature	Loading condition	Group	Thermal temperature	Loading condition	Group	Thermal temperature	Loading condition
T20	20		T20D	20		T20SD	20	
T100	100		T100D	100		T100SD	100	
T200	200		T200D	200		T200SD	200	
T300	300	Quasi-static	T300D	300	Dynamic	T300SD	300	Static-dynamic
T400	400		T400D	400		T400SD	400	
T500	500		T500D	500		T500SD	500	
T600	600		T600D	600		T600SD	600	

FIGURE 1
Thermal cycle temperature curve for high-temperature treatment of mortar specimens.

rate during the tests was controlled to be approximately 1 kN/s. Three specimens were tested at each thermal treatment temperature.

2.3.3 Dynamic loading test

The dynamic loading tests were conducted using a SHPB device with 50 mm diameter to apply an impact air pressure of 0.3 MPa. The SHPB device, as shown in Figure 2, can also be used for coupled static-dynamic loading tests. The launcher consists of a launch cavity and a spindle-shaped bullet, while the incident and transmitted rods possess an elastic modulus of 210 GPa and a wave propagation velocity of 5,200 m/s. To reduce the radial inertia between the specimens and the rods during dynamic loading,

petroleum jelly was uniformly coated on the cross sections of the incident and transmitted rods. The loading applied on the specimens were determined according to the one-dimensional stress wave propagation theory. It was assumed that stress in SHPB was in state of equilibrium. The stress, strain rate, and strain were calculated by Eqs (1)–(3) (Jiang et al., 2023):

$$\sigma = \frac{A_0 E_0}{A_s} \varepsilon_T \tag{1}$$

$$\dot{\varepsilon} = -\frac{2C_0}{l_s} \varepsilon_R \tag{2}$$

$$\varepsilon = -\frac{2C_0}{l_s} \int_0^t \varepsilon_R dt \tag{3}$$

where E_0, A_0 and C_0 are the elastic modulus, cross-sectional area and longitudinal wave velocity of the bar, respectively; A_s and l_s are the cross-sectional area and length of cement mortar specimens, respectively; ε_T and ε_R are the transmitted and reflected strain on the rod, respectively.

2.3.4 Coupled static-dynamic loading test

The test was conducted using the device in Figure 2. Mortar was performed static-dynamic loading tests with an impact air pressure of 0.3 MPa. In this case, an axial load was applied prior to the impact (Dai et al., 2010), with the magnitude of the axial load being 10% of the quasi-static compressive strength after thermal treatment. The impact dynamic loads were applied by opening the valve and releasing the bullet after a stabilization period of 5s for the axial load indication.

2.3.5 Scanning electron microscope (SEM) test

SEM tests were conducted to investigate the microstructure and morphology of thermally damaged cement mortar's hydration

FIGURE 2
Improved SHPB for dynamic and static-dynamic loading tests.
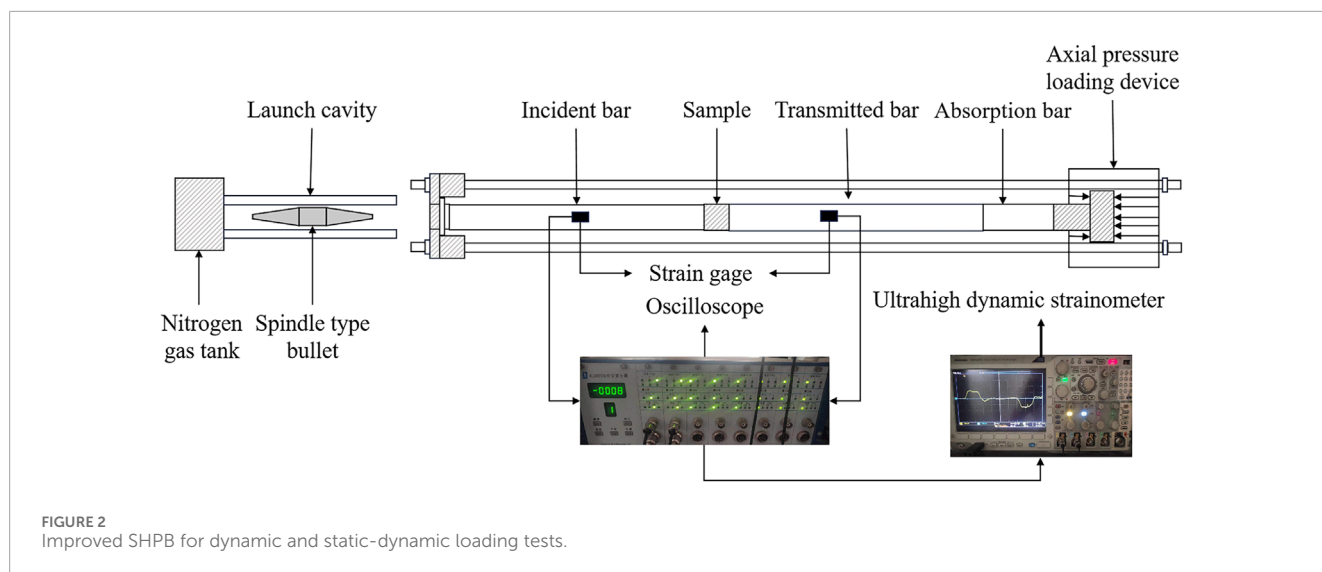
products. This test utilized a Flex1000 electron microscope scanner. The loaded specimens were crushed and sampled, followed by continuous pumping for 24 h in a vacuum pump. Subsequently, they were sprayed with gold, and the SEM images were recorded.

3 Results and discussion

3.1 Mechanical properties of thermally damaged mortar under different loading conditions

Based on the assumption of one-dimensional stress wave theory, the dynamic stress in incident rod is equal to the dynamic stress in the transmitted rod. The results of stress balance tests conducted on specimens are presented in Figure 3, which reveals that the sum of the incident and reflected dynamic stresses was equal to the transmitted dynamic stress. This confirms that the dynamic stresses on both sides of specimens were balanced, thereby ensuring the reliability of the data.

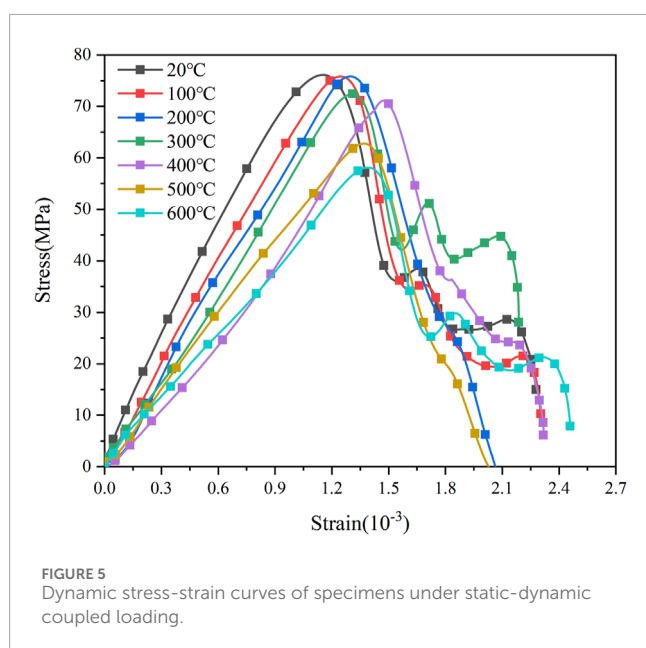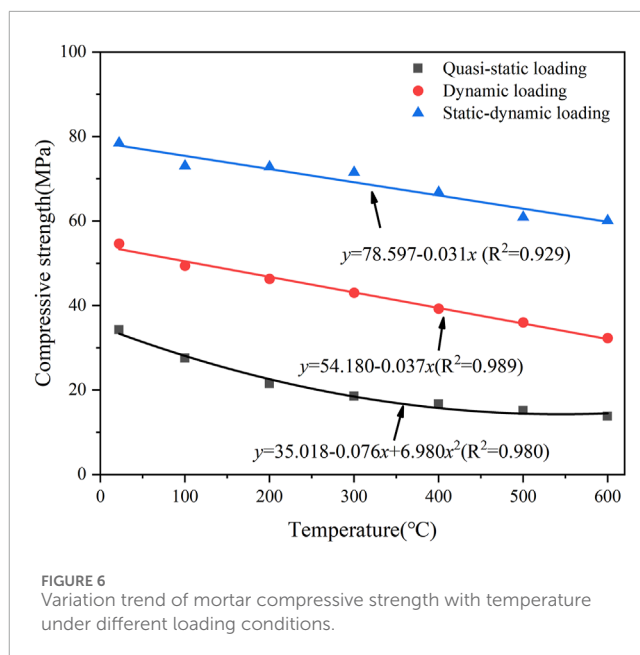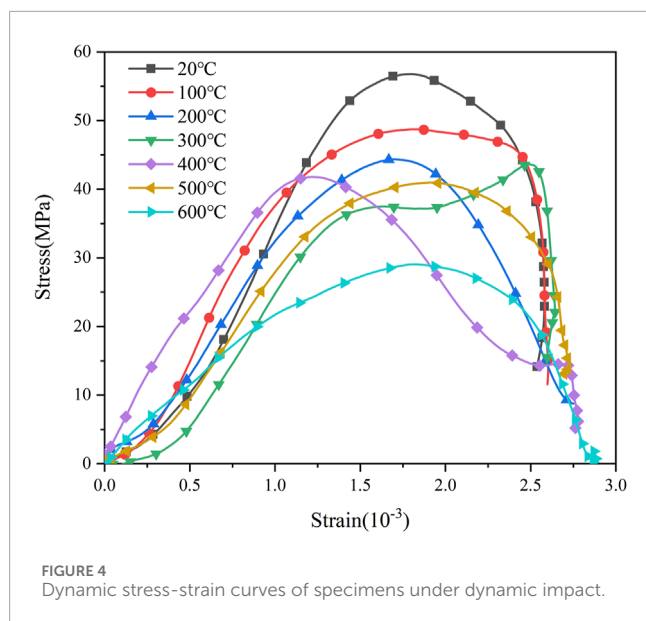### 3.1.1 Dynamic stress-strain curve characteristics

To investigate the effect of thermal damage and different loadings on stress-strain curve characteristics of mortar specimens, typical mortar specimens with compressive strength closest to the average value were selected for further analysis. Figures 4, 5 illustrate the stress-strain curves of thermally damaged specimens under dynamic loading and coupled static-dynamic loading, respectively, which can be divided into three stages.

Stage 1: The elastic deformation stage was characterized by approximately linear growth of mortar stress with strain, a stable dynamic elastic modulus (E_c). The E_c was found to be dependent on the high temperature, with the control group exhibiting the highest value of E_c. However, when the temperature reached 600°C, the E_c was the smallest. At this stage, micro-pores were present within the mortar specimens, and micro-cracks formed between sand particles and cementitious material. These cracks experienced

FIGURE 3
Dynamic stress equilibrium curves of mortar specimens during the dynamic loading tests.
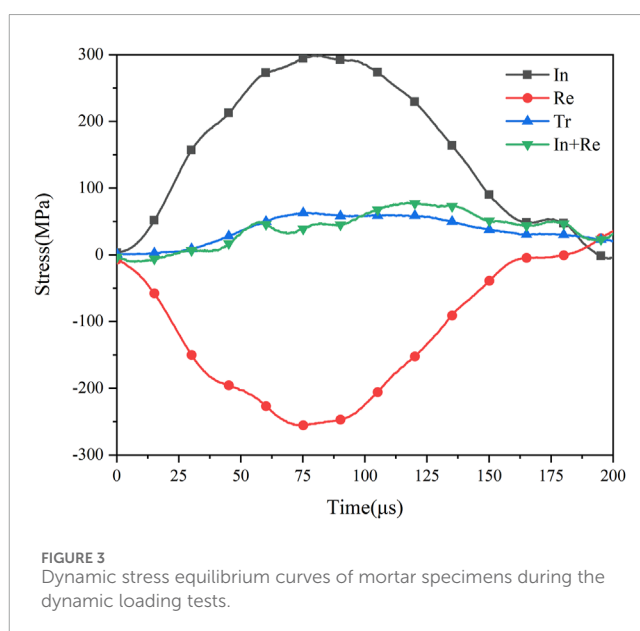
extrusion and shrinkage. Nevertheless, due to the pre-applied axial load during static-dynamic loading tests, this stage was shorter in duration, resulting in higher compactness and a relatively smaller peak strain.

Stage 2: The plastic deformation stage was characterized by a change in the dynamical mechanical properties after the elastic limit stress was reached. As deformation increased, the plastic deformation stage under dynamic loading became more pronounced, while that under coupled static-dynamic loading was shorter. Upon reaching the yield stress, the strain of the specimens increased to a certain extent, but the stress decreased sharply. This phenomenon can be attributed to the axial loading compacting the internal structure of the mortar, thereby exacerbating the damage caused by thermal damage to the specimens.

FIGURE 4
Dynamic stress-strain curves of specimens under dynamic impact.

FIGURE 6
Variation trend of mortar compressive strength with temperature under different loading conditions.

FIGURE 5
Dynamic stress-strain curves of specimens under static-dynamic coupled loading.

Stage 3: The unloading stage was characterized by the rapid decrease in the stress of the specimens under dynamic loading when their internal damage has accumulated to the limit of fracture. Inversely, mortar subjected to static-dynamic loading exhibited one or more secondary stress peaks, indicating that they still possessed a certain load-bearing capacity after damage and had not completely broken down.

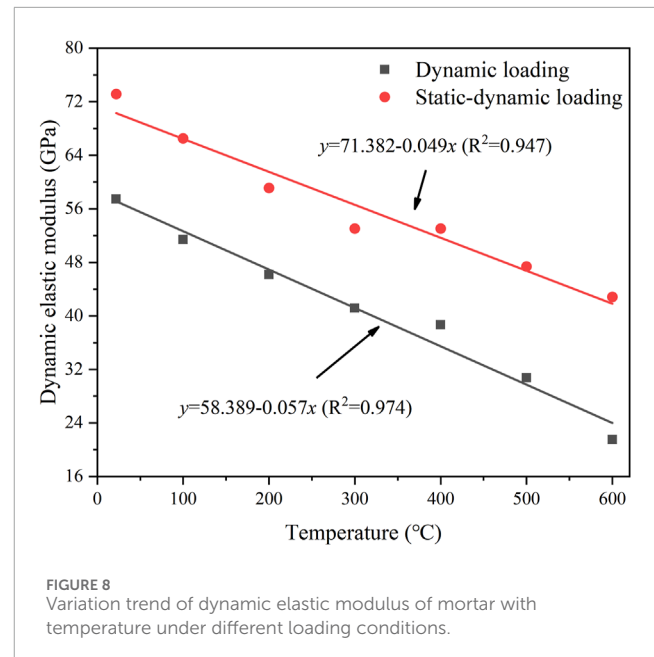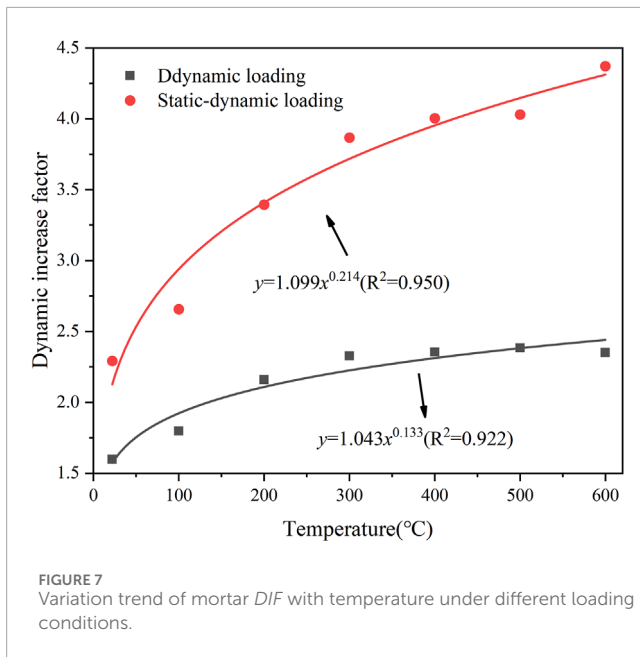### 3.1.2 Compressive strength characteristics

The impact of high-temperature on compressive strength of thermally damaged mortar was a crucial factor that must be considered. As illustrated in Figure 6, it can be observed that the compressive strength of thermally damaged mortar decreased

with temperature under the same loading conditions. The quasi-static compressive strength (σ_s) exhibited a quadratic function trend with temperature, resulting in a correlation coefficient R^2 of 0.980. In contrast, the dynamic compressive strength (σ_d) of mortar under dynamic and static-dynamic loading displayed a linear downward trend, with correlation coefficients R^2 of 0.989 and 0.929, respectively. The results clearly indicated that the compressive strength of mortar was the highest under static-dynamic loading, followed by that under dynamic loading, and lowest under quasi-static loading.

The dynamic increase factor (*DIF*) is defined as the ratio of the average σ_d to the average σ_s for thermally damaged specimens. It is commonly used to assess and compare the influence of impact loads on material strength (Xu and Li, 2011; Yao et al., 2016; Yin et al., 2018; Shu et al., 2022). Variation trend of mortar *DIF* with temperature under different loading conditions is illustrated in Figure 7. Under the same loading conditions, *DIF* increased approximately exponentially with temperature, with correlation coefficients R^2 reaching 0.922 and 0.950, respectively. When axial static pressure and dynamic loading were combined, static pressure caused compaction of the pores, leading to a significant increase in *DIF* (from 0.7 to 2.0). In summary, *DIF* is sensitive to variations in high temperature and pre-applied axial pressure.

3.1.3 Deformation characteristics

Dynamic elastic modulus E_c is a measure of the deformation ability of a specimen under elastic deformation. The corresponding strain is the peak strain when the specimen reaches its peak stress (Chen et al., 2022; Li et al., 2023; Michał et al., 2023; Zhang et al., 2023). The elastic modulus of mortar was determined by selecting the slopes of the tangents at two points on the stress-strain curve, namely, when the stress reached 0.3 times and 0.6 times the peak

FIGURE 7
Variation trend of mortar *DIF* with temperature under different loading conditions.

FIGURE 8
Variation trend of dynamic elastic modulus of mortar with temperature under different loading conditions.

stress σ_{max}. The calculation formula is Eq. (4):

$$E_c = \frac{\sigma_1 - \sigma_2}{\varepsilon_1 - \varepsilon_2} \tag{4}$$

where σ_1 and σ_2 are the stresses at the two points corresponding to 0.6 times σ_{max} and 0.3 times σ_{max} on the stress-strain curve, respectively; ε_1 and ε_2 are the strains at the two points, respectively.

The relationship between E_c of mortar and temperature is shown in Figure 8. E_c decreased linearly with increasing of temperature, with correlation coefficients R^2 of 0.974 and 0.947, respectively. E_c of mortar under dynamic loading and static-dynamic loading at 600°C decreased by 62.58% and 41.44%, respectively, compared to that at 20°C. This reduction was due to the same reason as the decrease in dynamic compressive strength.

3.1.4 Strain rate characteristic

The relationship between the average strain rate and temperature is illustrated in Figure 9. The strain rate of mortar under dynamic loading and static-dynamic loading increased linearly with increasing temperature, with correlation coefficients R^2 of 0.913 and 0.927, respectively. The strain rate of mortar under static-dynamic loading was lower than that under dynamic loading. The strain rate of mortar under dynamic loading ranged from 143.96 to 151.57 s^{-1}, while that under static-dynamic loading ranged from 112.44 to 126.19 s^{-1}. Due to the pre-applied axial load, the structure of mortar became denser, σ_d increased, the peak strain decreased.

3.2 Failure pattern of thermally damaged mortar under different loading conditions

3.2.1 Fracture morphology and failure mode

The mortar failure pattern is closely related to the fragments of the specimens after loading (Shuai et al., 2020; Padmanabha et al.,

FIGURE 9
Variation trend of average strain rate of mortar with temperature under different loading conditions.
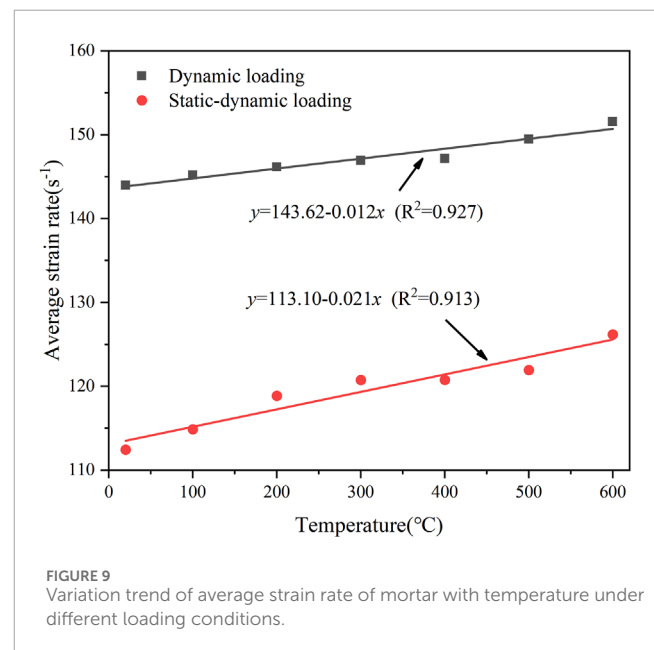
2022; Zheng et al., 2023). As observed from Table 3, as the temperature increased from 20°C to 600°C, the mortar color changed from the usual gray to off-gray and then to pale yellow. As the temperature increased, the thermally damaged mortar became powderier and the degree of fragmentation also increased. Under different loading conditions, the mortar specimens subjected to SHPB impact broke into blocky pieces. Compared with specimens under static-dynamic loading, those under dynamic loading exhibited more irregular and smaller fragmentation. This was because the axial pressure made the pores of mortar denser and the coupled effect of static-dynamic loading enhanced its compressive strength. Despite varying thermal damage

TABLE 3 Typical fracture morphology of mortar.

Loading condition	Thermal temperature (°C)			
	20	200	400	600
Quasi-static				
Dynamic				
Static-dynamic				

temperatures and different forms of loading conditions, the failure mode of the mortar remained consistent - splitting and tensile failure.

3.2.2 Facture surface

The SEM tests were conducted on the thermally damaged mortar specimens (Figure 10). The compressive strength loss of thermally damaged mortar was closely related to the mass loss (Figure 11). With the increased temperature, the number of cracks and pores on the fracture surface gradually increased. The mass loss rate and quasi-static compressive strength loss rate increased exponentially with temperature, with correlation coefficients of 0.952 and 0.926, respectively. In Figure 10A, the gel structure in the mortar was intact at 20°C, and the dense calcium hydroxide was very neat and complete. At temperatures between 100 and 110°C, free water escaped from the cement mortar, and the hydrated calcium silicate gel began to dehydrate. The hydrated calcium aluminate began to dehydrate around 200°C (Li et al., 2012; Chen et al., 2023). At temperature of 300°C, the mass loss rate was about 5%, while the strength loss rate was about 40%. At this stage, the primary cause of damage to the mortar was the micropores and microcracks shown in Figure 10B (Chen et al., 2023; Yu et al., 2023). As the temperature surpassed 300°C, the number of microcracks and pores in Figure 10C increased. Upon reaching a temperature of 600°C, numerous microcracks and pores became evident at the interface, as depicted in Figure 10D (Min-Ho and Sang-Jin, 2006;

Faisal et al., 2018). The maximum strength loss rate of mortar reached 60%, while the mass loss rate increased to approximately 8%. The decomposition temperature range for calcium carbonate in the cement paste was 850°C–900°C (Son and William, 2014; Stoyanov et al., 2023).

3.2.3 Energy dissipation of thermally damaged mortar under dynamic and coupled static-dynamic loading

Equations (5)–(8) for calculating energy dissipation are as follows:

$$E_I = E_0 C_0 A_0 \int_0^t \varepsilon_T^2 \, dt \tag{5}$$

$$E_R = E_0 C_0 A_0 \int_0^t \varepsilon_T^2 \, dt \tag{6}$$

$$E_T = E_0 C_0 A_0 \int_0^t \varepsilon_T^2 \, dt \tag{7}$$

$$E_A = E_I - E_R - E_T \tag{8}$$

where, $E_I(t)$, $E_R(t)$, $E_T(t)$, and $E_A(t)$ are the incident energy, reflected energy, transmitted energy, and absorbed energy, respectively.

Under different loading conditions, the energy dissipation law of mortar specimens was investigated by using energy ratio
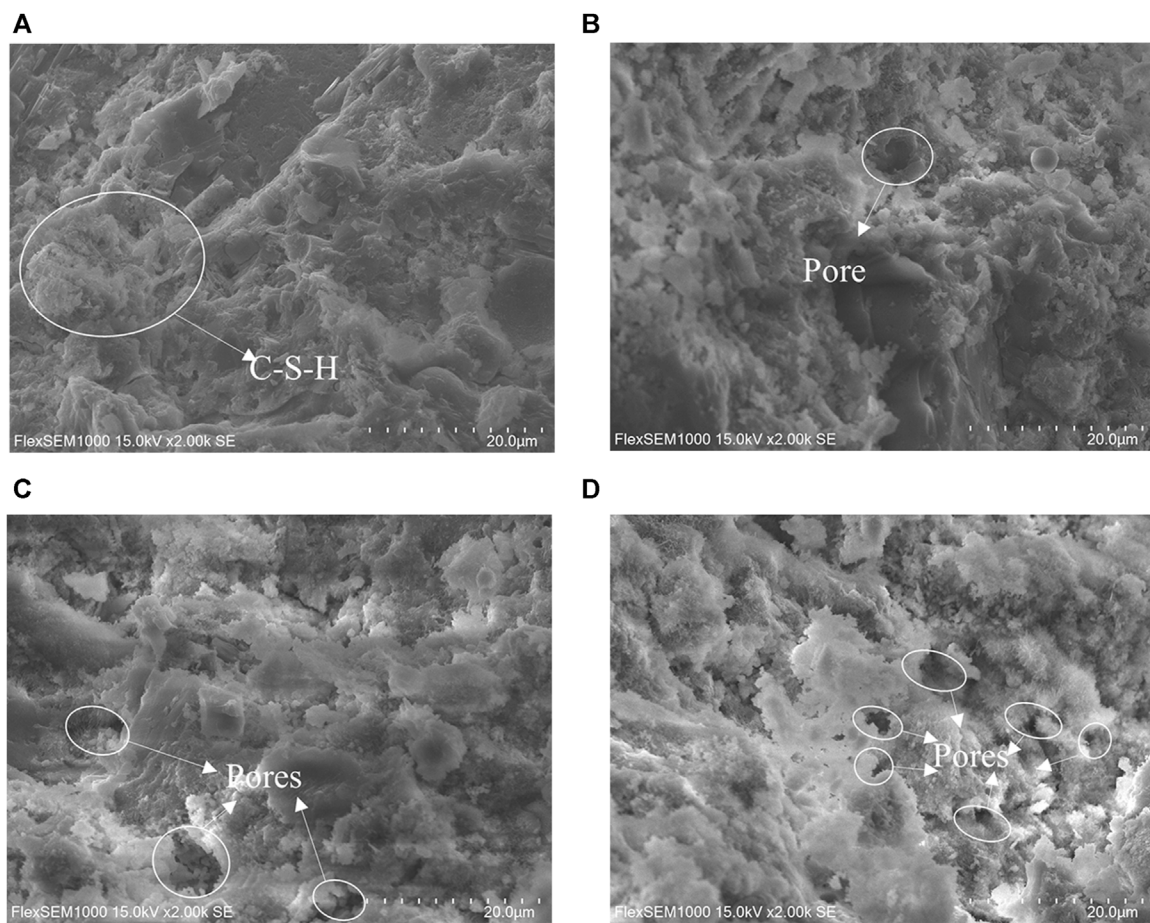
FIGURE 10
SEM images of thermally damaged mortar specimens. **(A)** 20°C, **(B)** 200°C, **(C)** 400°C, **(D)** 600°C.
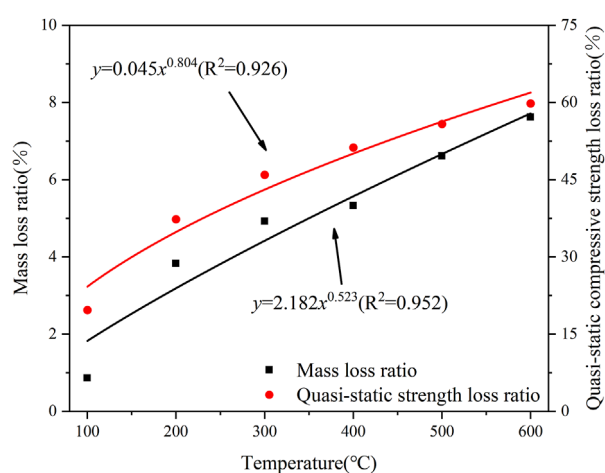
FIGURE 11
Mass and quasi-static compressive strength loss ratio variation of thermally damaged mortar with temperature.

due to the difference of the incident energy (Liu et al., 2020; Yan et al., 2023).

Under different loading conditions, the reflected energy ratio (E_R/E_I) of mortar increased an increase in temperature, as shown in Figure 12A. This was because as thermal treatment temperature increased, the strength of the mortar decreased, resulting in a greater difference in wave impedance between mortar and rod, leading to a worsening energy transfer effect and a larger reflected energy ratio. In terms of numerical value, the reflected energy ratio under static-dynamic loading was larger than that under dynamic loading. This was due to the mortar strength under static-dynamic loading was greater than dynamic loading at same thermal treatment temperature.

Figures 12B, C showed the variation of E_T/E_I and E_A/E_I of mortar with temperature, respectively. From the trend of change, it can be seen that E_T/E_I and E_A/E_I of the mortar under different loading conditions both exhibited a downward trend with increasing temperature. In terms of magnitude, the transmitted energy ratios of the mortar under static-dynamic loading were generally greater than those under dynamic loading, while the absorbed energy ratios

FIGURE 12
Energy proportion variation of thermal mortar with temperature. **(A)** E_R/E_I, **(B)** E_T/E_I, **(C)** E_A/E_I.
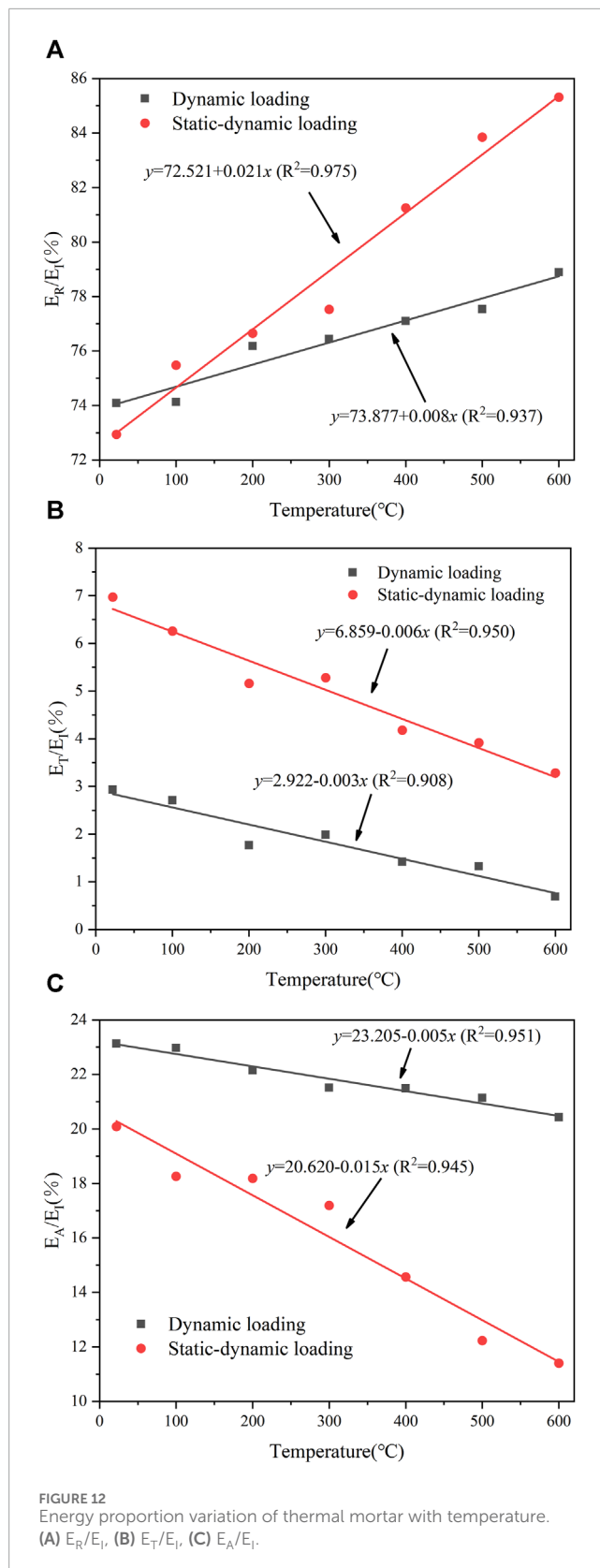
were smaller than those under dynamic loading. This was due to the weakening of mortar strength as the temperature increased, while the pre-applied axial compressive stress helped to enhance its strength.

4 Conclusion

The mechanical properties of thermally damaged mortar specimens under different loading conditions were studied. The findings of this research were intended to offer valuable data for the safety assessment of cement-based structures following a fire event, particularly when subjected to complex loading scenarios. Based on the results, the following conclusions can be drawn:

(1) Under the same loading conditions, compressive strength of thermally damaged mortar decreased as temperature increased. At 600°C, the quasi-static strength loss rate was approximately 60%. *DIF* of the mortar was temperature-sensitive. E_c decreased linearly, while strain rate increased linearly with increasing temperature. It was attributed to the presence of more pores and defects within the mortar's interior following thermal damage, which in return facilitated deformation with increasing temperature.

(2) Under the same thermal treatment temperature, the order of mortar strength under different loading was: static-dynamic loading, dynamic loading and quasi-static loading. In comparison to dynamic loading, mortar subjected to coupled static-dynamic loading exhibited a larger *DIF* and E_c. *DIF* was found to be sensitive to pre-applied axial compressive stress. Additionally, strain rate of mortar under coupled static-dynamic loading was relatively low, ranging from 25 to 30 s^{-1}. It was due to the pre-applied axial pressure before dynamic loading, which helped to compress the pores within the mortar and thus enhance its strength.

(3) Under the same loading condition, increasing temperature resulted in more fragmentation in thermally damage mortar. The increase in pores and microcracks in the mortar was primarily caused by the gradual evaporation of free and bound water, followed by the decomposition of chemical components. Under different loading conditions, the failure mode of thermally damaged mortar was characterized by splitting and tensile failure. Notably, quasi-static loading resulted in the largest broken fragments of mortar, while dynamic loading led to smaller fragments compared to static-dynamic loading. This difference was due to the pre-applied stress, which caused the pore structure to become more compact and thus reduced the degree of mortar crushing.

(4) With increasing temperature, E_R/E_I of mortar increased significantly, while E_T/E_I and E_A/E_I energy ratio decreased. Furthermore, the pre-applied stress had a positive effect on the E_R/E_I and E_T/E_I, while it decreased E_A/E_I. The law governing

the dissipation of energy in mortar was found to be consistent with the strength damage law.

The limitation of this study was that no mortar samples were studied above 600°C. Due to the limitation of instruments and equipment, the maximum thermal temperature of mortar samples only reached 600°C. Subsequently, the dynamical mechanical properties of the cement mortar can be investigated after experiencing higher temperatures.

Data availability statement

The original contributions presented in the study are included in the article/Supplementary Material, further inquiries can be directed to the corresponding author.

Author contributions

CY: Investigation, Methodology, Supervision, Writing–review and editing, Validation. HC: Investigation, Methodology, Supervision, Writing–review and editing, Funding acquisition, Resources. JC: Data curation, Visualization, Writing–original draft. LX: Project administration, Resources, Writing–review and editing, Conceptualization. DY: Supervision, Writing–review and editing.

Funding

Conflict of interest

The authors declare that the research was conducted in the absence of any commercial or financial relationships that could be construed as a potential conflict of interest.

Publisher's note

All claims expressed in this article are solely those of the authors and do not necessarily represent those of their affiliated organizations, or those of the publisher, the editors and the reviewers. Any product that may be evaluated in this article, or claim that may be made by its manufacturer, is not guaranteed or endorsed by the publisher.

References

Aitcin, P. C. (2003). The durability characteristics of high performance concrete: a review. *Cem. Concr. Compos.* 25 (4), 409–420. doi:10.1016/S0958-9465(02)00081-1

Annerel, E., and Taerwe, L. (2009). Revealing the temperature history in concrete after fire exposure by microscopic analysis. *Cem. Concr. Res.* 39 (12), 1239–1249. doi:10.1016/j.cemconres.2009.08.017

Bamonte, P., Gambarova, P. G., and Sciarretta, F. (2021). Thermo-mechanical properties and stress-strain curves of ordinary cementitious mortars at elevated temperatures. *Constr. Build. Mater.* 267, 121027. doi:10.1016/j.conbuildmat.2020.121027

Bi, J., Liu, P. F., and Gan, F. (2020). Effects of the cooling treatment on the dynamic behavior of ordinary concrete exposed to high temperatures. *Constr. Build. Mater.* 248, 118688. doi:10.1016/j.conbuildmat.2020.118688

Biolzi, L., Cattaneo, S., and Rosati, G. (2008). Evaluating residual properties of thermally damaged concrete. *Cem. Concr. Compos.* 30 (10), 907–916. doi:10.1016/j.cemconcomp.2008.09.005

Chen, J., Zhao, C., Ding, F., and Xiang, P. (2019). Experimental study on the seismic behavior of precast concrete column with grouted corrugated sleeves and debonded longitudinal reinforcements. *Adv. Struct. Eng.* 22 (15), 3277–3289. doi:10.1177/1369433219858451

Chen, M., Wang, Y., Zhang, T., and Zhang, M. (2023). Microstructural evolution and dynamic compressive properties of engineered cementitious composites at elevated temperatures. *J. Build. Eng.* 71, 106519. doi:10.1016/j.jobe.2023.106519

Chen, S. G., Zhang, H. M., Wang, L., Yuan, C., Meng, X. Z., Yang, G. S., et al. (2022). Experimental study on the impact disturbance damage of weakly cemented rock based on fractal characteristics and energy dissipation regulation. *Theor. Appl. Fract. Mech.* 122, 103665. doi:10.1016/J.TAFMEC.2022.103665

Chen, Y., Li, X., and Du, H. (2023). A review of high temperature properties of cement based composites: effects of nano materials. *Mater. Today Commun.* 35, 105954. doi:10.1016/j.mtcomm.2023.105954

Cree, D., Green, M., and Noumowé, A. (2013). Residual strength of concrete containing recycled materials after exposure to fire: a review. *Constr. Build. Mater.* 45, 208–223. doi:10.1016/j.conbuildmat.2013.04.005

Dai, F., Huang, S., Xia, K., and Tan, Z. (2010). Some fundamental issues in dynamic compression and tension tests of rocks using split hopkinson pressure bar. *Rock Mech. Rock Eng.* 43 (6), 657–666. doi:10.1007/s00603-010-0091-8

Deng, Z., Huang, H., Ye, B., Xiang, P., and Li, C. (2020). Mechanical performance of RAC under true-triaxial compression after high temperatures. *J. Mater. Civ. Eng.* 32 (8). 04020194. doi:10.1061/(ASCE)MT.1943-5533.0003231

Deng, Z. H., Huang, H. Q., Ye, B. L., Wang, H. P., and Xiang, P. (2020). Investigation on recycled aggregate concretes exposed to high temperature by biaxial compressive tests. *Constr. Build. Mater.* 244, 118048. doi:10.1016/j.conbuildmat.2020.118048

Du, S., Zhang, Y. C., Sun, Q., Gong, W. Y., Geng, J. S., and Zhang, K. J. (2018). Experimental study on color change and compression strength of concrete tunnel lining in a fire. *Tunn. Undergr. Space Technol. incorporating Trenchless Technol. Res.* 71, 106–114. doi:10.1016/j.tust.2017.08.025

Faisal, A., Waleed, A., and Qais, F. (2018). Effect of high temperature and type of cooling on some mechanical properties of cement mortar. *MATEC Web Conf.* 162, 02010. doi:10.1051/matecconf/201816202010

Gao, S., Li, W., Yuan, K., and Rong, C. (2023). Properties and application of thixotropic cement paste backfill with molybdenum tailings. *J. Clean. Prod.* 391, 136169. doi:10.1016/j.jclepro.2023.136169

Hertz, K. D. (2005). Concrete strength for fire safety design. *Mag. Concr. Res.* 57 (8), 445–453. doi:10.1680/macr.2005.57.8.445

Jeyaprabha, B., Elangovan, G., and Prakash, P. (2016). Effects of elevated temperature and water quenching on strength and microstructure of mortars with river sand substitutes. *Constr. Build. Mater.* 114, 688–698. doi:10.1016/j.conbuildmat.2016.03.189

Jiang, Y., Zhang, S., Xue, G., and Wang, W. (2023). Compressive behavior of rubberized concrete under high strain rates. *Structures* 56, 104983. doi:10.1016/j.istruc.2023.104983

Khoury, G. A. (2000). Effect of fire on concrete and concrete structures. *Prog. Struct. Eng. Mater.* 2 (4), 429–447. doi:10.1002/pse.51

Li, Q., Qing, T. D., Huang, C., Yu, B. B., Gao, Z. H., and Wang, K. (2023). Dynamic and damage characteristics of mortar composite under impact load. *KSCE J. Civ. Eng.* 27 (3), 1383–1395. doi:10.1007/S12205-023-1709-1

Li, Z. W., Xua, J. Y., and Baia, E. (2012). Static and dynamic mechanical properties of concrete after high temperature exposure. *Mater. Sci. Eng. A* 544, 27–32. doi:10.1016/j.msea.2012.02.058

Liu, P. F., Zhou, X. P., Qian, Q. H., Berto, F., and Zhou, L. S. (2020). Dynamic splitting tensile properties of concrete and cement mortar. *Fatigue & Fract. Eng. Mater. Struct.* 43 (4), 757–770. doi:10.1111/ffe.13162

Lu, X., Lu, X. Z., Guan, H., and Ye, L. P. (2013). Collapse simulation of reinforced concrete high-rise building induced by extreme earthquakes. *Earthq. Eng. Struct. Dyn.* 42 (5), 705–723. doi:10.1002/eqe.2240

Luo, X., Cheng, J., Xiang, P., and Long, H. (2020). Seismic behavior of corroded reinforced concrete column joints under low-cyclic repeated loading. *Archives Civ. Mech. Eng.* 20 (2), 40–20. doi:10.1007/s43452-020-00043-z

Michał, K., Paweł, B., Łukasz, M., and Jerzy, M. (2023). Comparison of selected blasting constitutive models for reproducing the dynamic fragmentation of rock. *Int. J. Impact Eng.* 173, 104484. doi:10.1016/J.IJIMPENG.2022.104484

Min-Ho, G., and Jung, S.-J. (2006). An experimental study on the characteristics of compressive strength in cement mortar under high temperature conditions in an early age. *J. Archit. Inst. Korea Struct. Constr.* 22 (3), 103–110. www.dbpia.co.kr.

Mukesh, S. T., and Shashank, K. (2019). Impact of passive fire protection on heat release rates in road tunnel fire: a review. *Tunn. Undergr. Space Technol. incorporating Trenchless Technol. Res.* 85, 149–159. doi:10.1016/j.tust.2018.12.018

Padmanabha, V., Schäfer, F., Rae, A. S. P., and Kenkmann, T. (2022). Dynamic split tensile strength of basalt, granite, marble and sandstone: strain rate dependency and fragmentation. *Rock Mech. Rock Eng.* 56 (1), 109–128. doi:10.1007/S00603-022-03075-4

Patrick, B., and Pietro, G. G. (2014). Properties of concrete subjected to extreme thermal conditions. *J. Struct. Fire Eng.* 5 (1), 47–62. doi:10.1260/2040-2317.5.1.47

Schrefler, B. A., Brunello, P., Gawin, D., Majorana, C. E., and Pesavento, F. (2002). Concrete at high temperature with application to tunnel fire. *Comput. Mech.* 29 (1), 43–51. doi:10.1007/s00466-002-0318-y

Shu, R., Huang, L., Zhi, X., Han, Z., Lai, Y., Li, H., et al. (2022). Damage characteristic of thermal shock on the physical and dynamic compressive properties of granite. *Geofluids* 2022, 1–12. doi:10.1155/2022/1623883

Shuai, W., Xu, Y., Xia, K., and Tong, T. (2020). Dynamic fragmentation of microwave irradiated rock. *J. Rock Mech. Geotechnical Eng.* 13 (2), 300–310. doi:10.1016/j.jrmge.2020.09.003

Son, T. P., and William, P. (2014). Effects of high temperature on the microstructure of cement mortar. *Appl. Mech. Mater.* 3207 (556-562), 969–972. doi:10.4028/www.scientific.net/AMM.556-562.969

Stoyanov, V., Petkova, V., Kostova, B., and Kaljuvee, T. (2023). Thermal investigation on high temperature treatment of cement mortars with high content of marble powder. *IOP Conf. Ser. Mater. Sci. Eng.* 1276 (1), 012005. doi:10.1088/1757-899X/1276/1/012005

Xiong, L. X., and Chen, C. (2020). Tests on the mechanical properties of corroded cement mortar after high temperature. *Civ. Eng. J.* 6 (3), 459–469. doi:10.28991/cej-2020-03091483

Xu, Z., Hao, H., and Li, H. N. (2011). Experimental study of dynamic compressive properties of fibre reinforced concrete material with different fibres. *Mater. Des.* 33, 42–55. doi:10.1016/j.matdes.2011.07.004

Yan, Z., Dai, F., Wang, L., Jin, J., and Wang, J. (2023). Dynamic mode II fracture mechanism of rocks using a novel double-edge notched flattened Brazilian disc specimen in the split Hopkinson pressure bar tests. *Eng. Fract. Mech.* 290, 109530. doi:10.1016/J.ENGFRACMECH.2023.109530

Yao, W., Liu, H.-W., Xu, Y., Xia, K., and Zhu, J. (2017). Thermal degradation of dynamic compressive strength for two mortars. *Constr. Build. Mater.* 136, 139–152. doi:10.1016/j.conbuildmat.2017.01.048

Yao, W., Xu, Y., Wang, W., and Kanopolous, P. (2016). Dependence of dynamic tensile strength of longyou sandstone on heat-treatment temperature and loading rate. *Rock Mech. Rock Eng.* 49 (10), 3899–3915. doi:10.1007/s00603-015-0895-7

Yazıcı, Ş., Gözde İnan Sezer, and Şengül, H. (2012). The effect of high temperature on the compressive strength of mortars. *Constr. Build. Mater.* 35, 97–100. doi:10.1016/j.conbuildmat.2012.02.082

Yin, T., Bai, L., Li, X., Li, X., and Zhang, S. (2018). Effect of thermal treatment on the mode I fracture toughness of granite under dynamic and static coupling load. *Eng. Fract. Mech.* 199, 143–158. doi:10.1016/j.engfracmech.2018.05.035

Yu, Z., Meng, Y., Mo, K. H., Liu, H., and Ling, T. C. (2023). Influences of w/c and CO2 curing duration on the high temperature properties of cement pastes. *J. Build. Eng.* 69, 106293. doi:10.1016/j.jobe.2023.106293

Zhang, B., Bicanic, N., Pearce, C. J., and Balabanic, G. (2000). Residual fracture properties of normal- and high-strength concrete subject to elevated temperatures. *Mag. Concr. Res.* 52 (2), 123–136. doi:10.1680/macr.2000.52.2.123

Zhang, X. F., Huang, B. F., and Ma, X. F. (2023). Dynamic compressive impact tests of building sandstone with a large split hopkinson pressure bar. *J. Build. Eng.* 67, 106023. doi:10.1016/J.JOBE.2023.106023

Zhao, Y., Bi, J., Zhou, X. P., and Huang, Y. S. (2019). Effect of high temperature and high pressure of water on micro-characteristic and splitting tensile strength of gritstone. *Front. Earth Sci.* 7. doi:10.3389/feart.2019.00301

Zheng, T., Zhang, Q., Yuan, L., Liu, Z., Niu, L., and Wang, X. (2023). Shape characteristics and crushed law of deep sandstone impact crushed blocks based on digital reconstruction. *Int. J. Impact Eng.* 174, 104525. doi:10.1016/J.IJIMPENG.2023.104525

Zhou, Y. X., Xia, K., Li, X. B., Li, H. B., Ma, G. W., Zhao, J., et al. (2012). Suggested methods for determining the dynamic strength parameters and mode-I fracture toughness of rock materials. *Int. J. Rock Mech. Min. Sci.* 49, 105–112. doi:10.1016/j.ijrmms.2011.10.004

frontiers | Frontiers in Materials

A theoretical model and verification of soil column deformation under impact load based on the Duncan-Chang model

Huang Jianqiu[1], Jin Zhuo[2,3]*, Wang Haiping[1], Ling Tao[1], Peng Xuejun[1], Tang Yu[1], Liu Qin[1] and Li Xi[2,3]*

[1]China Railway Wuju Group the First Engineering Co., Ltd., Changsha, China, [2]National Engineering Research Center of Highway Maintenance Technology, Changsha University of Science and Technology, Changsha, China, [3]School of Traffic and Transportation Engineering, Changsha University of Science and Technology, Changsha, China

The dynamic compaction method has been widely adopted in foundation treatment to densify the soil fillers. However, for the complexity of the impact behavior and soil mechanical properties, the theoretical research of dynamic compaction lags behind its practice for complex soil properties and stress paths. This paper presents a theoretical model applied to describe soil column plastic deformation under impact load. The relationship among stress increment, strain increment, and plastic wave velocity was derived from the aspect of propagation characteristics of stress waves in soil first. Combined with the Duncan-Chang Model, a one-dimensional theoretical model was established then. A numerical model was developed further to check the performance of the model. It showed that the deformation at the end of the soil column was mushroom-shaped. Both the axial and lateral deformation increased with the impact velocity. While some particles located at the side of the soil column end may splash under repeated impact. The theoretical deformations of the soil column were consistent with the experimental results both in the direction of axial and lateral.

KEYWORDS

Duncan-Chang model, earth filling engineering, deformation of soil, dynamic compaction (DC), foundation treatment

1 Introduction

During the construction of airports, roads, earth-rock dams, and similar projects, there is often a significant need for earth-rock filling engineering. To ensure the long-term safety and serviceability of geotechnical structures, it is essential to methodically place and compact earth or stone fillers layer by layer. A prominent technique utilized in this context is dynamic compaction, which employs heavy tampers weighing between 8 and 40 tons, dropped from heights of 10–20 m. This method delivers a powerful instantaneous impact load, rapidly densifying the fillers. Its widespread adoption is attributed to its high compaction efficiency, effective results, and low construction costs (Ye et al., 2020; Xu et al., 2022; Yao et al., 2022).

Significant investigations have been made, which mainly focus on the issue of the reinforcement mechanism of dynamic compaction (Zhang et al., 2017; Zhang et al., 2019;

Wu et al., 2020), the depth of improvement (Dou et al., 2019; Li et al., 2020; Zhou et al., 2020), and factors affecting reinforcement efficiency (Li et al., 2018; Zhang et al., 2018; Jia et al., 2021; Zhou et al., 2022; Li et al., 2023). However, a notable gap exists between current dynamic compaction theory and practical engineering application, leading to a certain level of improvisation in the design and execution of dynamic compaction. This gap hinders the accurate determination of reinforcement effectiveness and assurance of compaction quality in filling projects. Some researchers have tried to explore the time-domain characteristics of the dynamic compaction process. Li et al. (Li et al., 2021; Li et al., 2024) focused on the tamper as their subject, simplifying the dynamic compaction process to an elastic-damping collision, establishing a time-domain model for the process, and introducing a novel method to determine the optimal number of tamping impacts, offering significant engineering value. S. Valliappa et al. (Valliappan et al., 1995) took the dynamic compaction process as a foundation subjected to harmonic loading, using Fourier transform methods to analyze the frequency domain characteristics of dynamic compaction vibrations in two dimensions. Kong and Yuan (Kong and Yuan, 1999) considered the soil as an elastic half-space and established the rigid body motion equations for the tamper.

Notably, the impact of dynamic compaction on the surface layer of soil generates stress waves that propagate to deeper layers, causing densification as the waves transmit. The impact energy gradually transforms into plastic deformation of the soil. Thus, the essence of soil reinforcement through dynamic compaction lies in the transformation of the kinetic energy carried by the tamper into plastic deformation of the soil via stress waves. Conducting theoretical research on dynamic compaction from the perspective of stress wave propagation and dissipation aligns more closely with the objective realities of soil reinforcement. Current research in dynamic compaction theory scarcely addresses this aspect.

This paper focuses on a simplified case of a one-dimensional soil column under impact load. A theoretical model is established to describe the deformation of the soil quantitatively under impact load. Combined with a numerical model, the paper validates the theoretical model's applicability in describing both the axial plastic deformation and lateral deformation at the ends of the soil column. This provides a valuable reference for further establishing three-dimensional deformation models of soil under dynamic compaction and the mechanism of soil densification due to impact.

2 Soil column deformation model under Impact load

Compared to the soil column, the impact tamper typically is made of steel, can be assumed to have virtually infinite stiffness. Based on Newton's Third Law and the principle of relative motion, when the impact tamper strikes the soil column at speed v_0, it can be considered that the soil column impacts a stationary surface with infinite stiffness at initial speed v_0 (as shown in Figure 1). During the impact, both elastic and plastic compressive waves are generated within the soil column. The propagation speed of the elastic wave is faster than that of the plastic wave. Thus, post-impact, the elastic wavefront is labeled B, and the plastic wavefront is labeled P, with wave velocity c_p directed downwards. When the elastic wave reaches

the end of the soil column, it dissipates due to the column's limited tensile strength, causing the top layer of the soil to dislodge. The energy carried by the plastic compression wave gradually transforms into the soil's plastic deformation. As the speed of the tamper decreases from v_0 to zero, the soil column undergoes a complete impact process.

The initial cross-sectional area of the soil column is denoted as A_0, with a unit length of 1. At any given moment after the impact, the front of the plastic wave is represented as B. v_0 indicates the initial impact velocity of the soil column, while σ_1 and ε_1 respectively represents the maximum impact stress experienced by the soil column during the impact process and the maximum axial plastic strain of the soil column.

2.1 Axial plastic strain of the soil column

Considering that the stress on the contact surface between the soil column and a rigid plane is σ, the stress increment $d\sigma$ propagates along the soil column as a plastic wave at velocity $d\sigma$. For a micro-segment of length dx, within dt time, we have:

$$c_p = \frac{dx}{dt} \tag{1}$$

According to the law of conservation of momentum:

$$dFdt = mdv \tag{2}$$

where $F = A\sigma$ and $m = \rho Adx$ substituted into Eq. 2, yield:

$$d(A\sigma)dt = \rho Adxdv \tag{3}$$

Subsequently, substituting Eq. 1 into Eq. 3 and simplifying, we obtain:

$$dv = \frac{1}{\rho}\frac{d\sigma}{c_p} \tag{4}$$

The velocity of the plastic wave is:

$$c_p = \sqrt{\frac{d\sigma}{\rho d\varepsilon}} \tag{5}$$

By substituting Eq. 5 into Eq. 4 and simplifying, the relationship between $d\sigma$、$d\varepsilon$、dv can be derived as:

$$d\varepsilon = \frac{\rho}{d\sigma}(dv)^2 \tag{6}$$

Integrating with the Duncan-Chang model, an explicit formula for the stress-strain relationship curve during the soil compression process is directly provided, as follows:

$$\sigma_1 - \sigma_3 = \frac{\varepsilon_1}{a + b\varepsilon_1} \tag{7}$$

where a、b represents an experimental constant, σ_1 is the major principal stress, and σ_3 is the confining pressure. In the context of this study, the confining pressure is denoted as $\sigma_3 = 0$, which, when substituted into Eq. 7, and upon differentiation of both sides, yields the relationship between $d\sigma_1$ and ε_1:

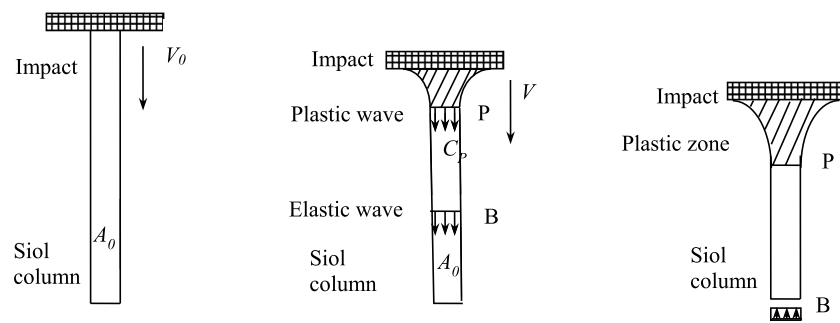$$d\sigma_1 = \frac{a}{(a + b\varepsilon_1)^2}d\varepsilon_1 \tag{8}$$

FIGURE 1
Schematic diagram of tamper impact on soil column.

By substituting Eq. 8 into Eq. 6, the relationship between the maximum strain of the soil column and the impact velocity can be obtained:

$$\frac{1}{a + b\varepsilon_1} d\varepsilon_1 = \sqrt{\frac{\rho}{a}} dv \tag{9}$$

To determine the axial plastic strain produced in the soil column due to the impact from a rigid object, Eq. 9 is therefore integrated as Eq. 10:

$$\int_0^{\varepsilon_1} \frac{1}{a + b\varepsilon_1} d\varepsilon_1 = \int_{v_1}^0 \sqrt{\frac{\rho}{a}} dv \tag{10}$$

This yields:

$$\ln(a + b\varepsilon_1) + b\sqrt{\frac{\rho}{a}} v_1 = \ln(a) \tag{11}$$

From Eq. 11, the theoretical expression for the axial plastic strain of the soil column under the effect of initial impact velocity can be derived as follows:

$$\varepsilon_1 = \frac{e^{\ln(a) - b\sqrt{\frac{\rho}{a}} v_1} - a}{b} \tag{12}$$

2.2 Deformation at the ends of the soil column

As shown in Figure 1, the ends of the soil column undergo lateral deformation when impacted by a rigid planar tamper. At the boundary between elastic and plastic deformation, the soil column changes from the initial cross-sectional area A_0 to A. From the condition of continuity, we have:

$$A_0(c_p + v) = Ac_p \tag{13}$$

Thereby there is:

$$\frac{d_0}{d} = \sqrt{\frac{A_0}{A}} = \sqrt{\frac{c_p}{c_p + v}} \tag{14}$$

In Eq. 14, d_0 and d respectively represent the initial diameter and the deformed diameter of the soil column's cross-section. Utilizing the

relationship between the velocity of material points and the level of stress, we have:

$$\sigma_1 = \rho c_p v \tag{15}$$

By substituting Eq. 15 into Eq. 14, we can obtain:

$$\frac{d_0}{d} = \sqrt{\frac{A_0}{A}} = \sqrt{\frac{c_p}{c_p + v}} = \sqrt{\frac{\sigma_1}{\sigma_1 + \rho v^2}} \tag{16}$$

By substituting Eq. 7 into Eq. 16, we can obtain:

$$\left| \frac{d_0}{d} \right| = \left| \sqrt{\frac{\sigma_1}{\sigma_1 + \rho v^2}} \right| = \sqrt{\frac{|\varepsilon_1|}{|\varepsilon_1| + \rho v^2(a + b|\varepsilon_1|)}} \tag{17}$$

From Eq. 17, the relative magnitude of the lateral deformation at the ends of the soil column, denoted as $\frac{d_0}{d}$, can be deduced using the soil column's maximum axial plastic strain value ε_1, the soil column's mass density ρ, and the soil column's initial velocity v.

2.3 Theoretical prediction of the soil column

Considering that the typical parameter values selected for soil columns should be compatible with the actual situation, let's take $a = 0.11$、 $b = 0.17$, with the soil column's mass density as $\rho = 1.8 g/mm^3$, and the tamper's initial velocities as $v_0 = 1m/s$、 $v_0 = 2m/s$、 $v_0 = 3m/s$、 $v_0 = 4m/s$、 $v_0 = 5m/s$. Substituting these selected parameters into the derived Eqs 12, 17, the values of ε_1 and $\frac{d_0}{d}$ for the soil column under the impact of the tamper at different initial velocities v_0 can be calculated. The theoretical values and their trends are shown in Table 1 and Figure 2.

3 Model verification

Further impact tests on soil columns were conducted to verify the applicability of the established theoretical model. Considering the limitations of indoor tests, particularly the frictional impact between the soil column and rigid impactors, the article adopts numerical methods for the model's applicability verification. Currently, numerical methods commonly include

TABLE 1 Deformation of the soil column under different impact velocities.

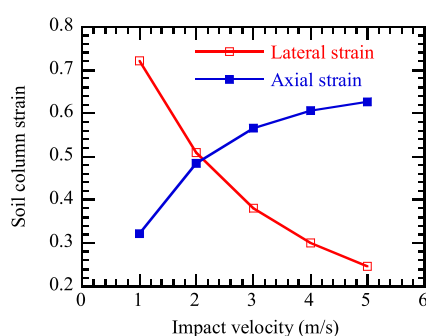| Group	Tamper initial velocity v_0 (m/s)	Axial plastic strain of soil column ε_1	Relative deformation at the end $\frac{d_0}{d}$
Group 1	1	0.322	0.721
Group 2	2	0.484	0.509
Group 3	3	0.565	0.380
Group 4	4	0.606	0.300
Group 5	5	0.626	0.246

FIGURE 2
Relationship between deformation of soil columns and impact velocity.
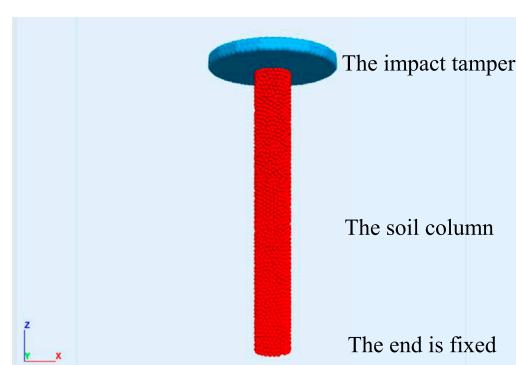

FIGURE 3
The schematic of the discrete element model.

the Finite Element Method (FEM) and the Discrete Element Method (DEM). Some scholars have also developed the Material Point Method and Boundary Element Method based on FEM concepts. However, FEM requires the initial assumption of the soil's constitutive model, which may not effectively serve the purpose of verifying the theoretical model. DEM divides the subject of study into independent units. Based on the interaction forces between these units and applying Newton's Second Law of Motion, iterative methods like static or dynamic relaxation techniques are used for repeated cyclic calculations. These methods determine the force and displacement state of each unit at every time step, continually updating the position of all units. This makes DEM very adaptable in dealing with large deformations and even destructive processes. By tracking and calculating the micro-movement characteristics of each unit, DEM allows for large deformations, rotations, sliding, and separation in the soil body, thus realistically simulating the nonlinear large deformation characteristics within the soil.

3.1 Construction of the discrete element model

When constructing the numerical model based on PFC, we first set the geometric boundary and determine the relevant properties of the particle material, and then determine the interaction law

of particle-particle and particle-boundary. As shown in Figure 3, in this numerical simulation, the cylindrical soil particle units are represented using standard spherical particles as the basic discrete elements. The rigid impactor is simulated with a clump, composed of multiple particles rigidly bound together. The parameters in the following table are chosen with due consideration of the actual situation of fine-grained soils and the fact that the deformation of soils under ramming is studied in this paper. The basic parameters of the materials for both are presented in Table 2.

To achieve a uniformly dense soil column, a stratified under-pressure method was employed, generating particles in five layers to simulate the soil body. In order to prevent the occurrence of uneven initial internal stress within the soil column, once the entire column reached its designed height, the "solve aratio" command in PFC3D was utilized to allow the particles to self-balance under the influence of gravity. This ensures that the unbalanced force on each soil particle is less than 10^{-5}N. Additionally, with a focus on computational efficiency of the model, 4,319 overlapping particles were collectively bound to simulate a rigid impact object, and 5,225 ball particles were used to model the soil column. Considering the mechanical characteristics of impact loading, a hysteresis damping model was adopted for the interactions between particles and between particles and the impact object. The model parameters were determined through extensive research and a comprehensive review of literature (as shown in Tables 2, 3).

TABLE 2 Basic parameters set of soil column and rigid impactor.

Material	Soil length (mm)	Radius (mm)	Density (kg/mm³)	Mass (kg)	Porosity	Particle size (mm)
Soil Column	150	10	1800	0.085	0.30	2
Rigid Plane	20	40		0.085		

TABLE 3 Contact model parameter values.

Parameter	emod	kratio	fric	dpn	dps	cbtenf	Cbshearf
Value	100	0.01	0.02	0.2	0.01	0.01	0

3.2 Impact process of the soil column

To test the applicability of the model, impact experiments were conducted using the established discrete element numerical model at five different initial velocities (respectively 1 m/s, 2 m/s, 3 m/s, 4 m/s, and 5 m/s). At the beginning of the experiment, the generated soil column was called upon and its lower end was fixed. The rigid impact object was positioned 5 cm above the top of the soil column and assigned a downward initial impact velocity. It's important to note that during the impact process, the acceleration due to gravity was zero, meaning that the effects of gravity were not considered. Throughout the impact, data such as the bulging at the ends of the soil column, changes in the length of the soil column, and other deformation data were recorded until the velocity of the rigid impact object reduced to zero, marking the completion of the impact process.

4 Results and analysis

4.1 Plastic deformation at the ends of the soil column

As shown in Figure 4, the deformation characteristics at the ends of the soil column, when subjected to impacts at various initial velocities, exhibit common features: The lateral deformation at the ends is greatest at the contact surface and gradually decreases further away. The deformed ends still maintain a circular shape, and the overall plastic deformation of the soil column presents a "mushroom shape" that is larger at the top and smaller at the bottom. More notably, there are differences in the deformation of the soil column ends under different impact velocities. Firstly, the axial plastic deformation of the soil column increases with the increase in impact velocity. In terms of lateral deformation, the deformation at the ends increases with increasing impact velocity. However, at excessively high velocities (v_0 = 4.0 m/s, v_0 = 5.0 m/s), a few particles at the impacted end of the soil column are observed to disintegrate, a phenomenon similar to the slight particle splashing observed in actual soil columns under impact.

4.2 The applicability of the theoretical model

To verify the applicability of the theoretical model, a comparative analysis was conducted from two perspectives: the axial plastic strain of the soil column and the lateral deformation at its ends. Figure 5 illustrates the axial plastic deformation of the soil after impacts at different velocities. It is observed that as the impact velocity increases, the axial deformation also increases, albeit at a decreasing rate. Comparing theoretical and experimental values reveals good consistency across the five impact velocities, with the largest discrepancy occurring at an impact velocity of 2 m/s, where the difference between the experimental and theoretical values of axial deformation is only 4.2 mm. Regarding the lateral deformation at the ends of the soil column (Figure 6), the theoretical and experimental values under different impact velocities still show good agreement. The greatest difference occurs at an impact velocity of 5 m/s, which can be attributed to the disintegration and farther scattering of individual particles at the ends of the soil column under high-velocity impacts. Considering both axial and lateral deformations, it can be concluded that the theoretical values aptly describe the deformation characteristics of the soil column under impact. This finding has significant implications for further research into the deformation characteristics of foundations and subgrades under impact compaction.

5 Conclusion

A simple theoretical model was presented to describe a soil column plastic deformation under impact load. Results showed that the end of the soil column was mushroom-shaped after impact load. The lateral deformation at the end of the soil column is the biggest. Both the axial and lateral deformation increased with the impacting velocity. However, the axial deformation increment of the soil column decreases gradually, while the lateral deformation increment changes less. The good agreement between the theoretical estimated and experimental measured deformation verified the characteristics of the complex deformation for a soil column under impact load. This can help us to better understand the behavior of soil, prevent and mitigate the effects of geohazards
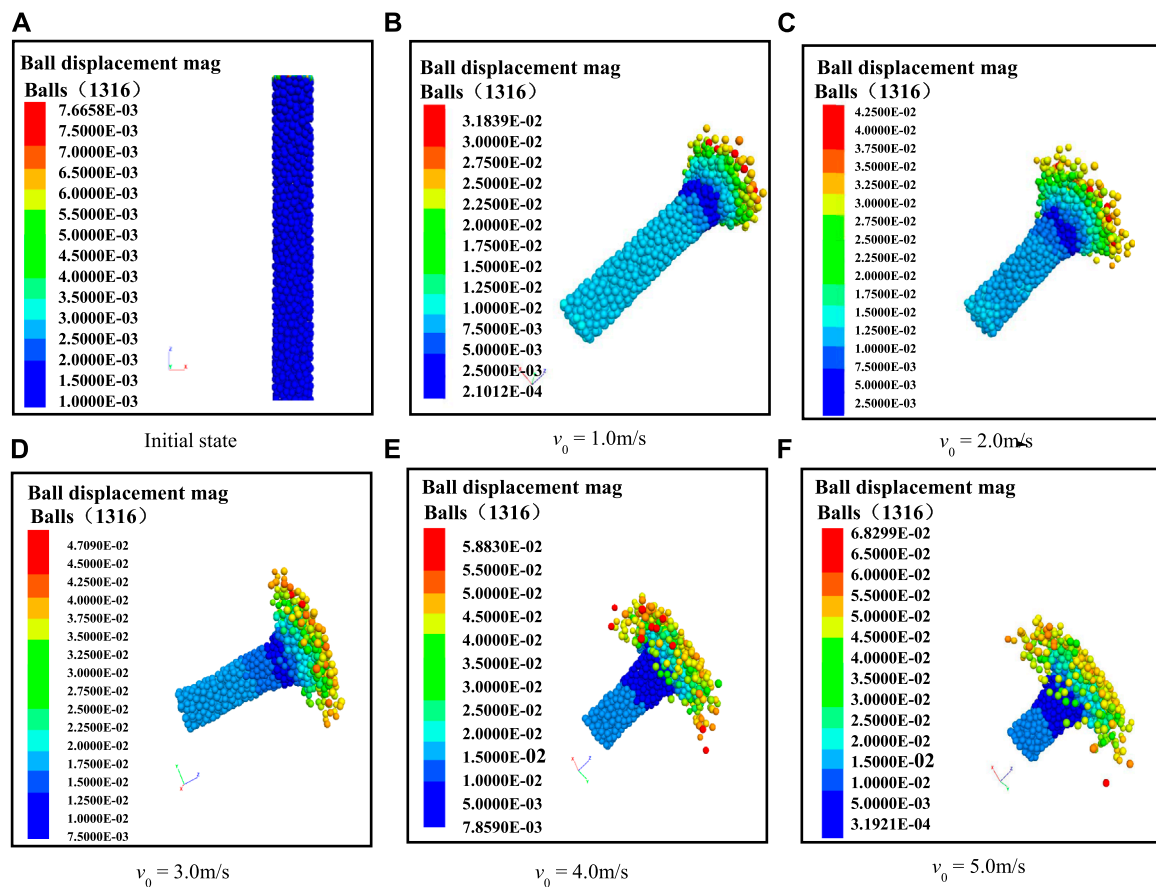
FIGURE 4
Deformation of the soil column under different impact velocity.
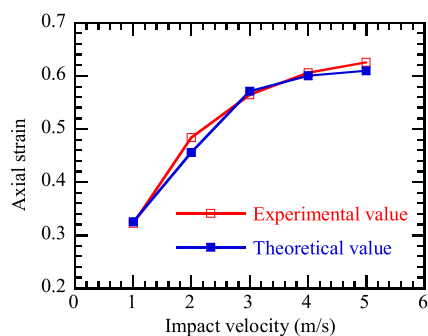
FIGURE 5
Axial plastic deformation of the soil column under different impact velocities.
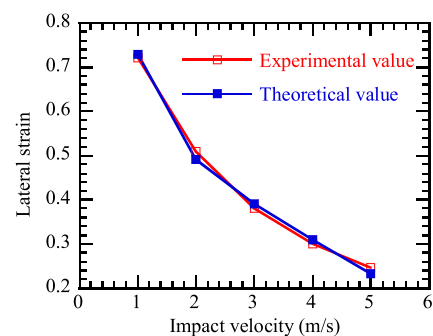
FIGURE 6
Lateral deformation at the ends of the soil column under different impact velocities.

and thus improve the quality and safety of our engineering design and construction. Future study can be carried out on the factors that affect the value of parameters of Duncan-Zhang model, including particle breakage, moisture content, particle size distribution.

Data availability statement

The original contributions presented in the study are included in the article/Supplementary Material, further inquiries can be directed to the corresponding authors.

Author contributions

HJ: Investigation, Methodology, Writing–original draft. JZ: Formal Analysis, Investigation, Software, Validation, Writing–original draft. WH: Investigation, Methodology, Resources, Writing–original draft. LT: Conceptualization, Formal Analysis, Methodology, Software, Writing–original draft. PX: Resources, Validation, Visualization, Writing–original draft. TY: Data curation, Methodology, Resources, Writing–review and editing. LQ: Data curation, Formal Analysis, Writing–review and editing. LX: Funding acquisition, Supervision, Writing–review and editing.

Funding

Conflict of interest

Authors HJ, WH, LT, PX, TY, and LQ were employed by China Railway Wuju Group the First Engineering Co., Ltd.

The remaining authors declare that the research was conducted in the absence of any commercial or financial relationships that could be construed as a potential conflict of interest.

Publisher's note

All claims expressed in this article are solely those of the authors and do not necessarily represent those of their affiliated organizations, or those of the publisher, the editors and the reviewers. Any product that may be evaluated in this article, or claim that may be made by its manufacturer, is not guaranteed or endorsed by the publisher.

References

Dou, J. Z., Chen, J. J., and Wang, W. (2019). Method for estimating the degree of improvement in soil between adjacent tamping locations under dynamic compaction. *Int. J. Geomechanics* 19, 04019134. doi:10.1061/(ASCE)GM.1943-5622.0001530

Jia, M. C., Liu, B., Xue, J. F., and Ma, G. Q. (2021). Coupled three-dimensional discrete element–finite difference simulation of dynamic compaction. *Acta Geotech.* 16, 731–747. doi:10.1007/s11440-020-01055-y

Kong, L. W., and Yuan, J. X. (1999). Study on surface contact stress distribution properties for multi-layered foundation during dynamic consolidation. *Chin. J. Theor. Appl. Mech.* 31, 250. doi:10.6052/0459-1879-1999-2-1995-026

Li, X., Li, J., Ma, X. Y., Teng, J. D., and Zhang, S. (2018). Numerical study of the dynamic compaction process considering the phenomenon of particle breakage. *Adv. Civ. Eng.* 2018, 1–10. doi:10.1155/2018/1838370

Li, X., Lu, Y., Cui, Y., Qian, G., Zhang, J., and Wang, H. (2024). Experimental investigation into the effects of tamper weight and drop distance on dynamic soil compaction. *Acta Geotech.* 19, 2563–2578. doi:10.1007/s11440-023-02198-4

Li, X., Lu, Y. B., Qian, G. P., Yu, H. N., Zhang, J., Wang, H., et al. (2023). A new index for estimating the improved depth of dynamic compaction. *Int. J. Geomechanics* 24. Available at SSRN 4128740. doi:10.1061/ijgnai.gmeng-8705

Li, X., Yang, H., Zhang, J. Y., Qian, G. P., Yu, H. N., and Cai, Y. (2021). Time-domain analysis of tamper displacement during dynamic compaction based on automatic control. *Coatings* 11, 1092. doi:10.3390/coatings11091092

Li, X., Zhang, K. F., Ma, X. Y., Teng, J. D., and Zhang, S. (2020). New method to evaluate strengthen efficiency by dynamic compaction. *Int. J. Geomechanics* 20, 04020024. doi:10.1061/(ASCE)GM.1943-5622.0001586

Valliappan, S., Yazdi, J. T., and Zhao, C. (1995). Analytical solution for two-dimensional dynamic consolidation in frequency domain. *Int. J. Numer. Anal. Methods Geomechanics* 19, 663–682. doi:10.1002/nag.1610191002

Wu, S. F., Wei, Y. Q., Zhang, Y. Q., Cai, H., Du, J. F., Wang, D., et al. (2020). Dynamic compaction of a thick soil-stone fill: dynamic response and strengthening mechanisms. *Soil Dyn. Earthq. Eng.* 129, 105944. doi:10.1016/j.soildyn.2019.105944

Xu, P., Zhu, X., Qiao, S. F., Wang, G., and Yu, P. K. (2022). Field study of compaction quality control parameters and compaction mechanism of large particle size stone-filled embankment. *Rock Mech. Rock Eng.* 55, 3687–3702. doi:10.1007/s00603-022-02811-0

Yao, Z. Y., Zhou, C., Lin, Q. Q., Yao, K., Satchithananthan, U., Lee, F. H., et al. (2022). Effect of dynamic compaction by multi-point tamping on the densification of sandy soil. *Comput. Geotechnics* 151, 104949. doi:10.1016/j.compgeo.2022.104949

Ye, X. Y., Wang, S. Y., Zhang, S., Xiao, X., and Xu, F. (2020). The compaction effect on the performance of a compaction-grouted soil nail in sand. *Acta Geotech.* 15, 2983–2995. doi:10.1007/s11440-020-01017-4

Zhang, R. Y., Sun, Y. J., and Song, E. X. (2019). Simulation of dynamic compaction and analysis of its efficiency with the material point method. *Comput. Geotechnics* 116, 103218. doi:10.1016/j.compgeo.2019.103218

Zhang, S., Li, X., Teng, J. D., Ma, X. Y., and Sheng, D. C. (2017). A theoretical method for determining sample mass in a sieving test. *Comput. Geotechnics* 91, 12–16. doi:10.1016/j.compgeo.2017.06.004

Zhang, T. W., Cui, Y. J., Lamas-Lopez, F., Calon, N., and D'Aguiar, S. C. (2018). Compacted soil behaviour through changes of density, suction, and stiffness of soils with remoulding water content. *Can. Geotechnical J.* 55, 182–190. doi:10.1139/cgj-2016-0628

Zhou, C., Jiang, H. G., Yao, Z. Y., Li, H., Yang, C. Y., Chen, L. C., et al. (2020). Evaluation of dynamic compaction to improve saturated foundation based on the fluid-solid coupled method with soil cap model. *Comput. Geotechnics* 125, 103686. doi:10.1016/j.compgeo.2020.103686

Zhou, C., Yao, K., Rong, Y., Lee, F. H., Zhang, D. M., Jiang, H. G., et al. (2022). Numerical investigation on zone of improvement for dynamic compaction of sandy ground with high groundwater table. *Acta Geotech.* 18, 695–709. doi:10.1007/s11440-022-01638-x

The flexural mechanical properties and mesoscopic mechanisms of fracture failure of HPC with ASR inhibition measures under prolonged alkaline solution immersion

Juan Guo[1,2], Weifeng Liu[1], Jianbo Guo[1], Hongfa Yu[1]*,
Haiyan Ma[1]*, Jun Yan[3], Qinghua Tao[1], Weiquan Gao[1],
Meng Zhang[1] and Fang Wang[1,2]

[1]Department of Civil and Airport Engineering, Civil Aviation College, Nanjing University of Aeronautics
and Astronautics, Nanjing, China, [2]Xinjiang Vocational and Technical College of Transportation,
Xinjiang, China, [3]School of Civil Engineering, Wuhan University, Wuhan, China

The harsh geological conditions in the northwest region of China, characterized by widespread saline-alkali soil rich in alkali ions, pose a high risk of Alkali-Silica reaction (ASR) in concrete, particularly due to the presence of ASR-active natural river sands. To address ASR hazards, locally applied concrete often employs High-Performance concrete (HPC) prepared with high proportions of mineral admixtures. In this paper, the alkali content is controlled by adding mixed water with NaOH to the initial configuration of concrete, and three different alkali content states are set up. A 1 mol/L NaOH solution was used to simulate alkaline conditions, and HPC specimens were immersed for an extended period to investigate the effects of equivalent alkali content, immersion time, concrete strength, and admixture on the flexural mechanical properties of HPC under the condition of long-term alkali immersion. Results indicate that, the strength grade was positively correlated with the flexural strength of HPC, but the alkali content was negatively. Initial immersion significantly enhances strength, followed by a gradual decline after long-term immersion. Among three types of admixture addition methods, the impact on flexural strength of HPC immersed in alkaline solution for 10 years follows the order: Double doped air entraining agent and rust inhibitor is greater than single doped air entraining agent is greater than single doped rust inhibitor. In the process of macroscopic test, it is difficult to observe the variation rule of stress and strain in detail, only the final aggregate failure mode can be analyzed. In order to analyze the strain change of the specimen and the failure process of the aggregates more accurately, a three-dimensional random aggregate concrete mesoscopic model was established, and equations relating microhardness to the mechanical properties of concrete components were derived from statistical analysis, providing a basis for parameter selection in the model. Results demonstrate that with increasing strength, the occurrence time of initial cracks is delayed, and the ratio of cracks bypassing aggregates (cracks develop along the ITZ between

aggregate and mortar until complete failure) decreases, and the ratio of cracks penetrating aggregates (cracks develop directly through aggregates in an almost vertical direction) increases.

1 Introduction

In the northwest region of China, salt lakes and saline-alkali soils contain high concentrations of chlorides, sulfates, and alkali metal ions, which greatly predispose concrete to alkali-aggregate reaction (AAR). Aggregates, serving as the framework of concrete, typically consist of minerals containing silica dioxide such as chalcedony, quartz, and chert. These mineral components are prone to undergo ASR with alkalis (Na2O, K2O) in cement, resulting in the formation of expansive alkali-silicate gel, thus leading to concrete deterioration (Zhou, 2011).

Over the past half-century, more than 20 countries have incurred significant losses due to the damage inflicted on buildings by ASR (Tang et al., 2022; Mong et al., 2002; E Grattan-Bellew et al., 1998). Numerous experiments have been conducted to investigate the impact of ASR on concrete strength. Cavalcanti (Cavalcanti, 1986) studied the extent of strength, durability, and harmful cracking effects of concrete under long-term ASR. Sanchez et al. (Crouch and Wood, 1990; Kubo and Nakata, 2012; Sanchez, 2014) found that the tensile strength and elastic modulus of concrete are more affected by ASR than compressive strength. Nixon et al. (Nixon and Bollinghaus, 1985; Smaoui et al., 2004) demonstrated that high expansion levels have a significant impact on compressive strength. At low expansion levels (0.05%) and high expansion levels (0.2–0.3%), the tensile strength decreased by 12%–70% and 50%–70%, respectively.

Currently, the main methods to suppress ASR include the use of inactive aggregates, controlling moisture, managing total alkali content in concrete, and adding inhibitory materials and chemical admixtures (Ding et al., 2008; Jan et al., 2013; Liu et al., 2015). According to Qian's research (Qian et al., 1994), as the content of slag and fly ash in concrete increases, the expansion decreases, and the inhibition effect on ASR strengthens. The optimal inhibition effect on ASR is achieved when the addition reaches 30%. Moreover, studies have pointed out that the key role of fly ash lies in alleviating or preventing the chemical reaction of reactive aggregates. Chen's research (Chen et al., 1993) indicates that the effective addition of silica fume is about 10%–15%, but it can only delay the occurrence of ASR without complete inhibition. Duyhai et al. (Choi and Choi, 2015; Vo et al., 2020) explored the effect of slag content on inhibiting ASR in highly alkaline reactive aggregates and found a positive correlation. The use of admixtures to suppress ASR can be traced back to as early as 1951 (McCoy and Caldwell, 1951). Due to not requiring changes in construction conditions and even possibly improving the performance of concrete, this method has received considerable attention. Shayan and Ivanusec (Shayan and Ivanusec, 1989) explored the influence of adding NaOH on the mechanical properties of mortar containing non-reactive and reactive aggregates and ultimately found that adding NaOH led to a decrease in mortar

strength, with similar trends observed in both types of concrete. This is because the addition of NaOH undergoes significant chemical reactions with cement, affecting the performance of concrete. In general, high alkaline conditions are detrimental to the strength of concrete (Qian, 1996).

Wu Z et al. (Wu, 2000) summarized the definition of HPC. In addition to cement, aggregate and water, low water-binder ratio, sufficient mineral admixtures and high-efficiency admixtures were used, and stricter quality management was adopted. Concrete with excellent mechanical properties, durability and good impact resistance can be called High-Performance Concrete (HPC).

HPC inherently exhibits a suppression effect on ASR due to its internal incorporation of large quantities of mineral admixtures such as slag, fly ash (FA), and silica fume (SF). Marzouk and Langdon (Marzouk and Langdon, 2003), in their exploration of the influence of alkaline aggregates on the mechanical properties of HPC and Ordinary Portland Cement (OPC), immersed concrete specimens separately in NaOH solution at 80°C or distilled water for 12 weeks. They found that high alkaline environments significantly affected the strength of OPC but had minimal impact on both low and high alkali-reactive HPC. Fares and Khan (Fares and Khan, 2013) investigated the inhibitory effects of two-phase and three-phase blended materials on ASR, including FA and SF. The results indicated that the inhibitory effect of single addition SF (15% content) or single addition FA (45% content) on ASR was not as good as the combined addition of FA + SF (10% FA and 10% SF).

Yu et al. (Yu et al., 2003) investigated the compressive strength of OPC20 and OPC30 after 270 days of exposure in the saline soil environment of Qinghai Chaerhan Salt Lake, and found that they were reduced by 41%–65% and 18%–23%.

Wang et al. (Wang, 1993) found that the compressive strength of high-strength and high-density concrete with a water-binder ratio of 0.22–0.26 and a strength grade of C50 mixed with 10% silica fume increased by 18.5%–27.3% after immersion in salt lake alkaline solution for 3 years, indicating that HPC showed better corrosion resistance in the face of long-term corrosion.

Zhang et al. (Zhang, 2014) found that the relative dynamic elastic modulus of OPC30 and OPC50 increased to 110% and 109% after 550 days immersion in salt lake alkaline solution, and decreased to 90% and 104% respectively after 1,550 days of immersion in salt lake alkaline solution. The relative dynamic elastic modulus of HPC with strength grade of C65 (10% silica fume +45% slag), C70 (10% silica fume +27% fly ash) and C80 (10% silica fume) were still in the growth stage at 1,550 days, and increased by about 110%–120%.

Gao et al. (Gao et al., 2019) studied the compressive strength of HPC exposed to salt lake alkaline solution for 1 year and 1.5 years. It was found that the compressive strength of HPC with the strength

grade C50 (12% fly ash +20% slag +3% silica fume) increased by 35% and 27%.

At present, the research on the mechanical properties of HPC in salt lake alkali corrosion environment has not been more than 5 years, so it is urgent to study its durability and long-term strength change in a longer time span, which has important scientific value for the technical development and engineering application of HPC in salt lake environment.

With the continuous progress of computer technology, the strict requirements of traditional tests and high cost have prompted researchers to start exploring in the direction of numerical simulation. At present, breakthrough progress has been made in many fields, for example, Xiang et al. (Xiang and Liew, 2013) proposed a computational framework for transverse compression of microtubules using Cauchy-Born rules, and used atomistic-continuum simulation and mesh-free method to calculate the high-order gradient continuum theory format, and deeply studied the elastic properties and mechanical response of microtubules under transverse compression.

In the field of concrete, it has been widely used to analyze the mechanical response of concrete under load, such as cracking and failure mode. Compared with the test, numerical simulation has many advantages, which can more intuitively observe the stress and strain changes of the specimen, the specific failure process of aggregate, the crack propagation and damage mechanism. It has important research value and significance.

Xu et al. (Xu et al., 2011) employed a novel algorithm to determine the stacking problem between ellipsoidal and ellipsoidal aggregate models and investigated the influence of aggregate shape on aggregate packing behavior in concrete. Fang et al. (Fang et al., 2013) proposed an efficient three-dimensional aggregate growth and determination algorithm based on vector growth and judgment criteria. They generated spatial octahedral aggregate models with random shape characteristics and successfully applied them to static and dynamic microscopic mechanical simulation of concrete.

Zhang et al. (Zhang et al., 2021) discussed the influence of porosity characteristics on the compressive strength of coral aggregates and developed a series of algorithms considering the real mesoscopic characteristics of coral aggregates based on two-dimensional XCT images. Wu (Wu et al., 2021a; Wu et al., 2022) established particle generation algorithms and vector growth algorithms that can generate three-dimensional particle systems assembled from irregularly shaped and sized particles. They obtained convex-concave particles with different shapes and sizes, which are more in line with engineering reality compared to previous simulations that could only model regular geometric shapes or simple polyhedra particles. To address the issue of particle volume fraction in the model being smaller than the actual fraction, they proposed using the gravity compaction algorithm in the PFC3D program and a spatial translation/rotation algorithm from literature to analyze the distribution of aggregates in concrete models.

Wu et al. (Wu et al., 2021b), through numerical simulation and comparison with experimental results, found that coral aggregate concrete (CAC) with larger aggregate volumes and smaller MAS values experienced faster failure processes. They also demonstrated that the proposed three-dimensional random mesoscopic modeling method, considering the random characteristics of aggregate shape and spatial distribution, exhibits high reliability in simulating and

analyzing the compression performance of CAC. This method can provide further insights into the mixture design, performance research, and prediction of CAC. Li (Li et al., 2023) utilized the 3D random aggregate concrete mesoscopic model to simulate the uniaxial compressive mechanical properties of HPC specimens under long-term corrosion conditions and found that the failure morphology was in good agreement with the compressive strength.

Chen (Chen et al., 2023) studied the change of bearing capacity of reinforced cage specimens and ordinary specimens with different eccentricity and width-thickness ratio, and discussed the law of reinforcement effect of reinforced cage using the finite element analysis method. And found that when the width-thickness ratio is 22.5 and the eccentricity is small, the reinforcement cage greatly improves the ultimate bearing capacity of the CFSST column, however, this enhancement decreases with the increase of eccentricity.

Currently, there is a lack of research on the mechanical properties of HPC containing alkali-reactive aggregates and high proportions of mineral admixtures under prolonged exposure to alkaline solution environments. Therefore, this study aims to investigate the flexural mechanical properties of HPC with ASR inhibition measures under prolonged immersion in alkaline solution and analyze the mesoscopic mechanisms of fracture failure.

2 Experiment

2.1 Raw materials

The cement used is P.II 52.5 cement and P.O 42.5 cement produced by Gansu Qilianshan Cement Group Co., Ltd. The main physical and mechanical properties of this type of cement are shown in Table 1. The chemical composition and alkali content of the main raw materials are shown in Tables 2 and 3, respectively. Fly ash is produced by Gansu Yongdeng Liandian Fly Ash Co., Ltd. Ground granulated blast furnace slag: S95 grade product from Gansu Xiangyang Trading Co., Ltd.'s slag mill, with a specific surface area of 330 m^2/kg. Silica fume: Product from Qinghai Blue Sky Environmental Protection Technology Co., Ltd., with a SiO2 content of 90.51% and a specific surface area of 26,200 m^2/kg. Fine aggregate: River sand from Ledu, Qinghai, with a bulk density of 1,639 kg/m^3, fineness modulus of 2.87, and classified as medium sand with specific parameter indexes shown in Table 4. The coarse aggregate for C40~45 consists of granite crushed stone from Xining, with a maximum particle size of 31.5 mm. It contains 2.9% needle-like particles, and it has a continuous grading from 5mm to 31.5 mm. The SO_4^{2-} content is 0.02%, and the Cl^- content is 0.0063%. For C50~60, the coarse aggregate also comprises granite crushed stone from Xining, with a maximum particle size of 20 mm. It contains 2.6% needle-like particles, and it has a continuous grading from 5mm to 20 mm. The SO_4^{2-} content is 0.02%, and the Cl^- content is 0.0057%. For specific parameter details, please refer to Table 4. High-efficiency water reducer: PJ-FDN polycarboxylate-based high-efficiency water reducer from Xining Yangjian Waterproofing Additives Co., Ltd., liquid form, recommended dosage of 1.5%, water reduction rate of over 25%, K2O content of 0.000562%, Na$_2$O content of 0.427518%, solid content greater than 9.5%, and Cl^- content of 0.037909%. Air-entraining agent: Product from Xining

TABLE 1 Physical mechanical properties of cement (Yan et al., 2022).

No.	Fitness/%	Specific surface area/m²·kg⁻¹	Water requirement for normal consistency/%	Setting time/h		Flexural strength/MPa		Compression strength/MPa	
				Initial set	Final set	3 d	28 d	3 d	28 d
P.II 52.5	0.8	412	25	1.6	2.4	5.6	9.3	26.8	57.2
P.O 42.5	0.8	348	26	2.4	3.7	5.5	7.6	21.6	48.7

TABLE 2 Chemical composition of main materials/%.

Materials	SiO_2	Al_2O_3	CaO	MgO	SO_3	Fe_2O_3	MnO	TiO_2	Na_2O	K_2O	I.L	Cl^-
P.II 52.5	19.56	3.78	65.88	2.42	2.41	3.69	–	–	0.50	0.82	0.94	0.022
P.O 42.5	20.98	9.38	59.45	2.00	2.44	3.64	–	–	0.24	0.59	1.28	0.023
SF	90.51	0.96	0.50	2.10	-	0.64	–	–	1.03	2.00	2.26	0.26
FA	52.68	32.42	2.94	1.21	0.74	7.47	–	–	0.74	1.46	0.34	0.0012
Slag	26.09	26.88	37.38	5.6	1.75	0.67	–	–	0.49	0.83	0.31	0.014

TABLE 3 Alkali active ingredients of main materials (Yan et al., 2022).

Materials	Na_2O/%	K_2O/%	Na_2O+0.658 K_2O/%
PO42.5 cement	0.24	0.59	0.63
PII52.5 cement	0.50	0.82	1.04
SF	1.03	2.00	2.35
FA	0.63	1.35	1.52
Slag	0.27	0.40	0.53

Yangjian Waterproofing Additives Co., Ltd., with K_2O content of 0.000562%, Na_2O content of 0.390312%, SO_4^{2-} content less than 0.105%, and Cl^- content of 0.016994%. FDN steel anti-corrosion agent: Product from Xining Yangjian Waterproofing Additives Co., Ltd., with a solid content of 30%, K_2O content of 0.131472%, Na_2O content of 0.080336%, SO_4^{2-} content less than 0.1145%, and Cl^- content of 0.648371%. Water: Drinking water that meets national standards.

According to the CECS53: 93 standard, the alkali content of concrete raw materials refers to the content of equivalent sodium oxide in raw materials, measured as a percentage of weight. Equivalent sodium oxide content refers to the sum of sodium oxide and 0.658 times of potassium oxide. When calculating the alkali content (kg/m³) of concrete, the equivalent alkali content of cement is counted as 100% of the equivalent alkali content, the equivalent alkali content of mineral admixture = 15% of the equivalent alkali of fly ash +50% of the equivalent alkali of slag +50% of the equivalent alkali of silica fume, the equivalent alkali content of admixture = 100% of the equivalent alkali of admixture. The equivalent alkali content of each component including mixed water multiplied by the

corresponding amount (kg/m³), and then all the alkali content of each components are added as the alkali content of concrete (kg/m³). The equivalent alkali content of concrete refers to the percentage of the alkali content of concrete divided by the mass of unit volume concrete.

2.2 Mixture design

The paper presents four different concrete mix designs for varying strength grades, and for the C50 strength grade, three types of admixture addition methods are employed. To investigate the influence of total alkali content in concrete on its physical mechanical properties under high-concentration alkali exposure, various equivalent alkali contents are designed based on the aforementioned six concrete mixtures. Specifically, specimens labeled as −0 represent the original equivalent alkali content of the materials, termed as low alkali state; whereas specimens labeled as −1 and −2 have NaOH added to the mixing water to increase the equivalent alkali content, referred to as medium alkali state and high alkali state, respectively. The detailed information regarding the equivalent alkali content and material usage for each mix design can be found in Table 5. Additionally, Table 6 provides detailed specifications of important indicators such as slump, water-cement ratio, expansion degree, and air content for each mix design.

2.3 Corrosion medium

The corrosion medium used in this experiment is a standard alkaline solution, specifically employed for ASR testing. Following ASTM standards, a solution of 1 mol/L NaOH concentration is utilized, and all concrete specimens are fully immersed in the

TABLE 4 Basic parameters of aggregate (Yan et al., 2022).

Type of aggregate		Apparent density/(kg/m^3)	Bulk density/(kg/m^3)	Soil content/%	Porosity/%	Crush index/%
Fine aggregate	-	2,650	1,470	5.6	38.1	–
Coarse aggregate	C40-C45	2,780	1,525	0.8	41	8.2
	C50-C60		1,530			

solution. Figure 1 illustrates the preparation process of concrete specimens 10 years ago.

2.4 Test method

2.4.1 The flexural test

The concrete specimens immersed in alkaline solution for 10 years are highly valuable, and it is crucial to ensure adequate spacing between specimens in the immersion environment. To fully utilize the immersion space and obtain as many different mechanical properties as possible, the specimens used in this experiment have dimensions of 515 mm × 100 mm × 100 mm. All the specimens were made in the same batch and began to immerse. They are all immersed in standard alkaline solution (1 mol/L NaOH) for durations of 0 days, 28 days, 182 days, 365 days and 3,650 days. When the required immersion time was reached, some specimens were taken out for testing and the rest continued to immerse. The flexural test is conducted using four-point loading, with the loading points illustrated in Figure 2. After completing the flexural test, the remaining portions of the specimens are subjected to other mechanical property tests.

2.4.2 Flexural test data processing

According to the Standard for Testing Methods of Physical and Mechanical Properties of Concrete (Ministry of Housing and Urban-Rural Development of the OPeople's Republic of China, 2019), the flexural strength of concrete specimens can be calculated by Eq. 1:

$$f_{t,m} = \frac{FL}{bh^2} \tag{1}$$

Where, $f_{t,m}$ is the flexural strength (MPa), L is the span between the supports (mm), h and b are the section height and width (mm) of the specimen. In addition, the strength values measured by non-standard specimens should be multiplied by the size conversion coefficient of 0.85 (Ministry of Housing and Urban-Rural Development of the OPeople's Republic of China, 2019).

2.4.3 Preparation and measurement instruments for microhardness testing

During the specimen preparation process, the specimens were first cut into approximately 3 mm thick slices using a precision automatic cutting machine. Subsequently, they were polished using 240-grit and 600-grit sandpaper. During the polishing process, a figure "8" motion was used to pre-polish, aiming to remove any damage zones that could cause polishing errors. Next, the specimens were embedded in epoxy resin within a metallographic

mold. The epoxy resin mixture was injected into the mold using a vacuum drying oven to ensure complete sealing of the specimens. After sealing, the back of the specimens was polished to ensure uniform force application during polishing. Manual pre-polishing was performed to remove the resin layer from the front surface, ensuring a resin impregnation depth of 0.1 mm and avoiding excessive resin thickness during pre-polishing. Ultrasonic cleaning with anhydrous ethanol was then conducted, followed by formal polishing using a UNIPOL-12000M automatic pressure grinding and polishing machine (as shown in Figure 3A). Diamond polishing compounds of varying particle sizes were used for polishing, ranging from large to small. The final polished samples retained a thin layer of resin protection on the surface, exhibiting a mirror-like finish. The polished samples were dried in a vacuum drying oven for more than 48 h to evaporate the anhydrous ethanol and prevent contamination of the hardness tester. Microhardness testing was performed using an HVS-1000MZ hardness tester (as shown in Figure 3B), employing a 136° inverted pyramid diamond indenter. Indentations were made on the specimen surface under the applied test load, and Vickers hardness values were calculated accordingly.

2.4.4 Vickers hardness calculation

After applying a certain test load with the diamond indenter, the length of the indentation diagonal is calculated using the arithmetic mean method. Based on this, the indentation surface area is calculated, and subsequently, the Vickers hardness value is determined. The specific calculation formula is shown as Eq. 2:

$$HV = 0.102 \frac{F}{S} \times 2F \frac{\left(\frac{\theta}{2}\right)}{d^2} = 0.1891 \frac{F}{d^2} \tag{2}$$

Where, HV is the Vickers hardness (MPa), F is the test load (N) (the test load is determined based on the clarity of the indentation, typically ranging from 20 μm to 60μm, and in this study, a test load of 0.490N was used under a ×400 magnification), S is the surface area of the indentation (mm^2), d is the arithmetic mean of the diagonals of the indentation (mm), θ is the included angle of the diamond indenter (°), which is 136° in this study.

3 Results and discussion

The long-term immersion of HPC in standard alkali solution can lead to changes in its strength, which is a key indicator for assessing its durability. Systematic studies on the strength variation of HPC specimens at different immersion ages provide valuable insights into their performance under various environmental conditions. This research helps to determine the corrosion resistance of HPC in harsh

TABLE 5 The mix proportion and material consumption of concrete/kg (YAN et al., 2022).

No.	Binding materials	Cement	FA	Slag	SF	Sand	Stone	Corrosion inhibitor	Water reducer	Air entraining agent	Water	Equivalent alkali content/%
Ca40-0	460	405	55	–	–	714	1,165	–	8.64	0.23	161	0.6
Ca40-1	460	405	55	–	–	714	1,165	–	8.64	0.23	161	1.4
Ca40-2	460	405	55	–	–	714	1,165	–	8.64	0.23	161	1.9
Ca45-0	480	336	48	96	–	722	1,130	–	9.6	0.24	168	0.5
Ca45-1	480	336	48	96	–	722	1,130	–	9.6	0.24	168	1.4
Ca45-2	480	336	48	96	–	722	1,130	–	9.6	0.24	168	1.9
C50Z-0	500	325	60	100	15	741	1,159	33	10	–	127	0.8
C50Z-1	500	325	60	100	15	741	1,159	33	10	–	127	1.2
C50Z-2	500	325	60	100	15	741	1,159	33	10	–	127	1.6
Ca50-0	500	325	60	100	15	741	1,159	-	10	0.25	150	0.8
Ca50-1	500	325	60	100	15	741	1,159	-	10	0.25	150	1.3
Ca50-2	500	325	60	100	15	741	1,159	-	10	0.25	150	1.8
Ca50Z-0	500	325	60	100	15	741	1,159	33	10	0.25	127	0.8
Ca50Z-1	500	325	60	100	15	741	1,159	33	10	0.25	127	1.2
Ca50Z-2	500	325	60	100	15	741	1,159	33	10	0.25	127	1.6
Ca60Z-0	536	322	80	118	16	739	1,155	33	13.4	0.268	127	0.7
Ca60Z-1	536	322	80	118	16	739	1,155	33	13.4	0.268	127	1.1
Ca60Z-2	536	322	80	118	16	739	1,155	33	13.4	0.268	127	1.6

Note: Because of the different admixtures and admixtures added in concrete, the significance of different specimens in this paper is as follows: a represents the addition of air-entraining agent, Z represents the addition of rust inhibitor.

TABLE 6 The performance of HPC with different strength grades.

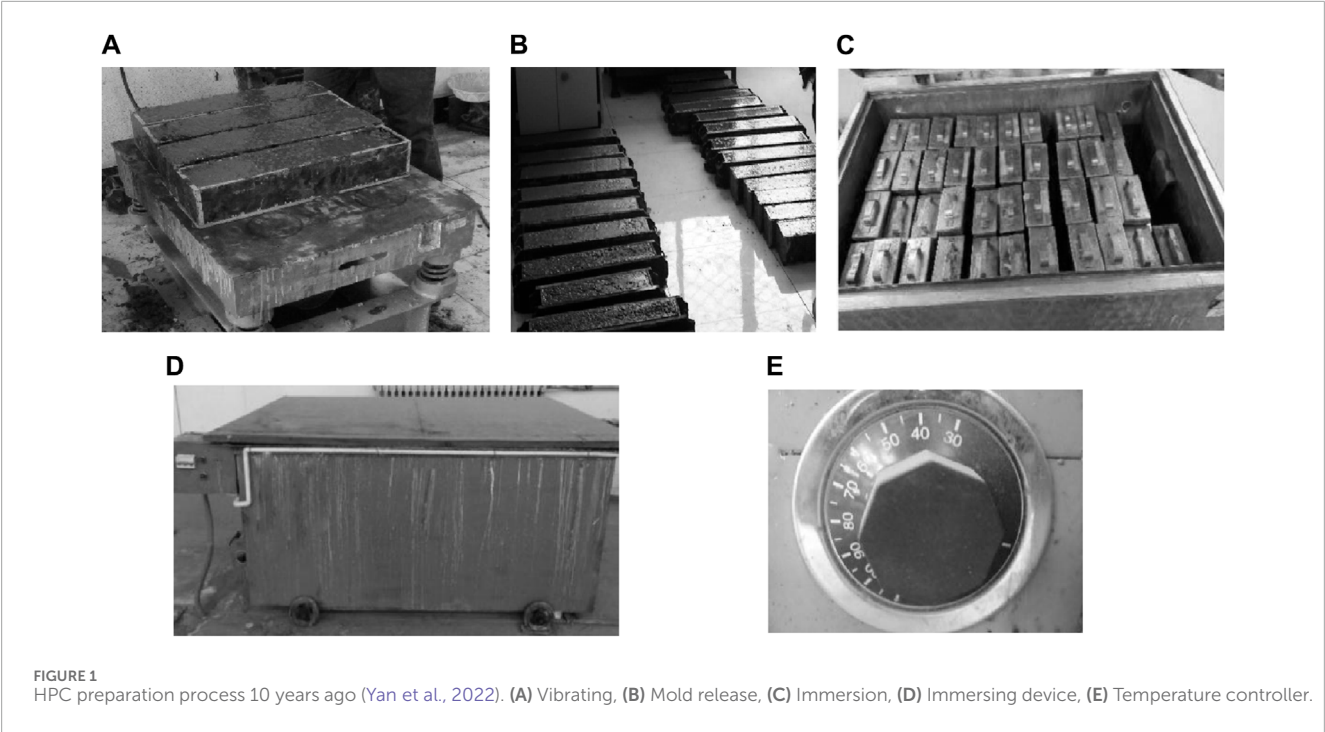|	W/C	Slump (mm)	Expansion degree (mm)	Gas content (%)
Ca40	0.35	210	580	5.2
Ca45	0.35	235	600	5.7
Ca50	0.30	215	500	5.1
C50Z	0.25	190	400	1.9
Ca50Z	0.25	220	570	4
Ca60Z	0.24	235	600	5.6

FIGURE 1
HPC preparation process 10 years ago (Yan et al., 2022). **(A)** Vibrating, **(B)** Mold release, **(C)** Immersion, **(D)** Immersing device, **(E)** Temperature controller.
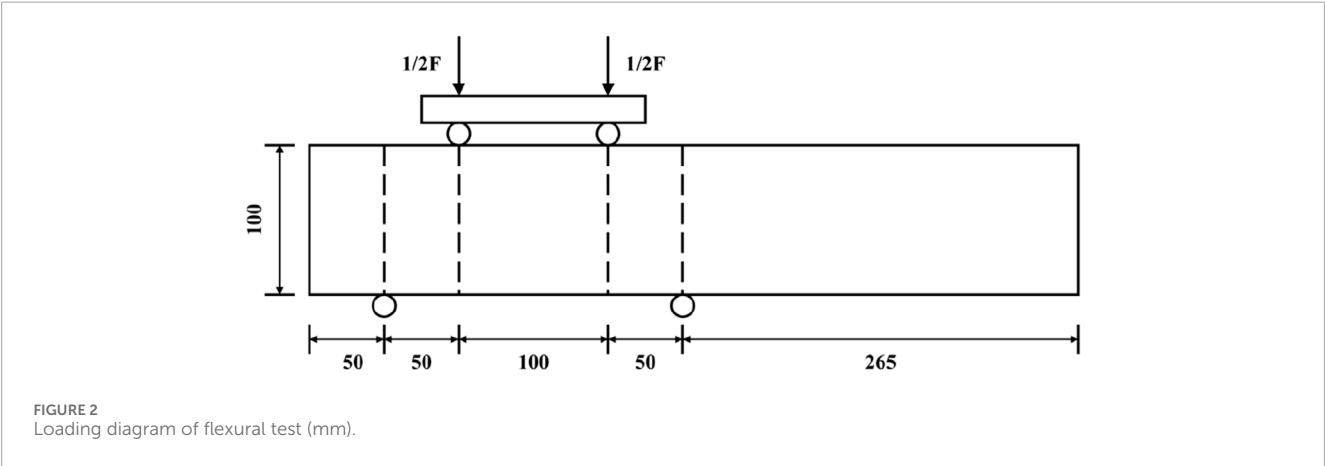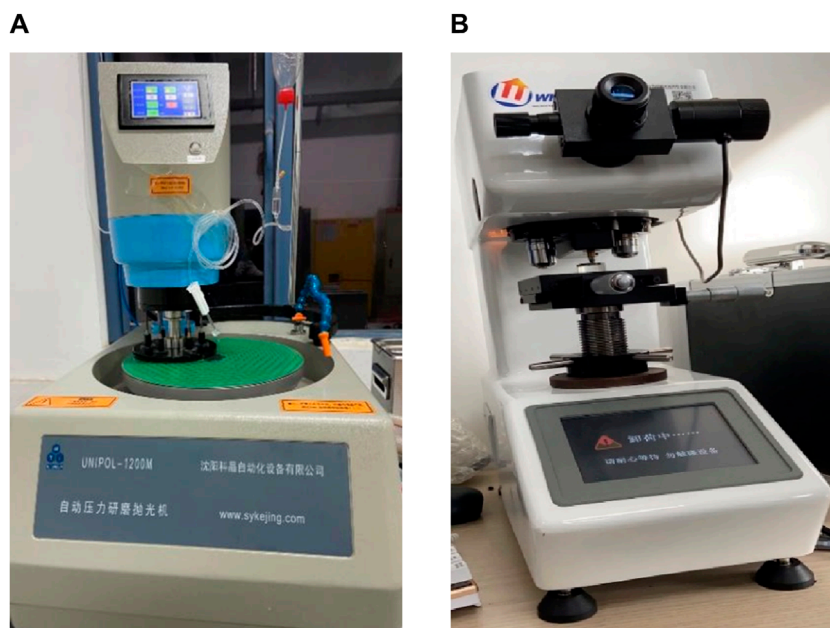

FIGURE 2
Loading diagram of flexural test (mm).

FIGURE 3
Microhardness specimen preparation and testing equipment. **(A)** UNIPOL-12000M automatic pressure grinding and polishing machine, **(B)** HVS-1000MZ hardness tester.

environments such as brine, providing comprehensive information and basis for evaluating its durability.

3.1 The effect of immersing in standard alkali solution for 10 years on the flexural strength of HPC

The flexural strength of HPC immersed in 38°C standard alkali solution for 10 years was tested, and the flexural strength of 0 days and 3,650 days was recorded. The resistance coefficient proposed in reference (Gao, 2018) can effectively assess the strength changes of HPC after long-term immersion, thus providing a more comprehensive and accurate evaluation of the material's durability. The specific calculation formula is shown as Eq. 3:

$$K_s = \frac{R_{st}}{R_{s0}} \qquad (3)$$

Where, K_s is the corrosion resistance coefficient, R_{st} is the strength of the specimen when the immersing time in the standard alkali solution is t, R_{s0} is the strength of the specimen before immersing (the age before immersion is 28 days).

Table 7 summarizes the initial strength, strength after 10 years immersion, and corresponding corrosion resistance coefficients of specimens with different strength levels under low alkali and medium alkali conditions. For HPC with varying alkali content, the flexural strength generally exhibits an increasing trend with higher strength grades. Furthermore, comparison between HPC specimens with different admixture at C50 strength level reveals that air-entraining agent and corrosion inhibitor can enhance the flexural strength of HPC. It is noteworthy that although both air-entraining

agent and corrosion inhibitor improve the flexural performance of HPC, after 10 years of immersion, the HPC with air-entraining agent demonstrates superior flexural performance.

Furthermore, the corrosion resistance coefficients in Table 7 are generally greater than 1, indicating a widespread increase in flexural strength of HPC under long-term ASR inhibition. A comparison of corrosion resistance coefficients between low alkali and medium alkali states of HPC reveals that the corrosion resistance coefficient under low alkali conditions is typically greater than that under medium alkali conditions. The corrosion resistance coefficient under low alkali conditions is around 1.2, while that under medium alkali conditions is slightly higher than 1. Further analysis indicates that before immersion in alkali solution, the difference in flexural strength between low alkali and medium alkali states of HPC is small, and the flexural strength of HPC under medium alkali conditions is relatively higher. However, after 10 years of immersion in alkali solution, the flexural strength of HPC under medium alkali conditions is affected by factors such as expansion rate and damage, resulting in slightly lower strength of specimens under medium alkali conditions. Additionally, long-term immersion of HPC in standard alkali solution leads to the formation of ASR corrosion products, which fill and divide cracks. Although this increases the porosity, the corrosion products fill the pores, resulting in a reduction in crack size, thereby improving the flexural strength of HPC to some extent.

3.2 Effect of immersing time in standard alkali solution on flexural strength of HPC

This study conducted experimental tests on the flexural strength of HPC under medium alkali conditions immersed in alkali solution

TABLE 7 Comparison of initial flexural strength and flexural strength immersed in standard alkali solution for 10 years of HPC (MPa).

| Specimen	0 d	3650 d	Corrosion resistance coefficient K_s	Specimen	0 d	3650 d	Corrosion resistance coefficient K_s
Ca40-0	5.19	6.68	1.29	Ca40-1	5.59	6.1	1.09
Ca45-0	3.96	6.28	1.59	Ca45-1	6.44	6.03	0.94
C50Z-0	5.71	7.35	1.29	C50Z-1	6.87	6.96	1.01
Ca50-0	6.13	7.45	1.22	Ca50-1	6.38	7.13	1.12
Ca50Z-0	6.57	7.49	1.14	Ca50Z-1	6.76	7.26	1.07
Ca60Z-0	7.26	8.85	1.22	Ca60Z-1	8.06	8.18	1.01

Note: a represents the addition of air entraining agent, Z represents the addition of corrosion inhibitor.

TABLE 8 The change of flexural strength of HPC in medium alkali state with the immersing time (MPa).

Specimen	0 d	28 d	182 d	365 d	3650 d
Ca40-1	5.59	6.94	7.13	6.55	6.1
Ca45-1	6.44	7.25	7.42	7.06	6.03
C50Z-1	6.87	7.89	7.64	7.41	6.96
Ca50-1	6.38	8.03	8.33	8.15	7.13
Ca50Z-1	6.76	8.04	8.2	7.85	7.26
Ca60Z-1	8.06	9.12	8.96	8.64	8.18

FIGURE 4
The change of flexural strength of HPC in medium alkali state with the immersing time of alkali solution.

for 0 days, 28 days, 182 days, 365 days, and 3650 days, and the results are shown in Table 8.

Based on the experimental data in Table 8, curves depicting the flexural strength and relative flexural strength of HPC under medium alkali conditions over time of alkali immersion were plotted as shown in Figures 4, 5. From the observations in Figure 4, it can be inferred that the flexural strength of HPC under medium alkali conditions generally increases with increasing strength grade during different immersion periods. With prolonged immersion time, the flexural strength of HPC exhibits a trend of initially increasing and then decreasing: at 28 days of immersion, the flexural strength of HPC is generally higher compared to the initial strength, during the period from 28 days to 182 days of immersion, the flexural strength of most strength grades of HPC continues to increase but gradually levels off, after 365 days of immersion, the flexural strength of HPC is lower than that at 182 days, however, between 365 days and 3650 days of immersion, the flexural strength of HPC continues to decrease but remains higher than the initial flexural strength before immersion. This indicates that during prolonged alkali immersion, HPC with ASR inhibition measures experiences a significant increase in flexural strength at the initial stage of immersion, followed by corrosion-induced damage. Nonetheless, the ultimate flexural
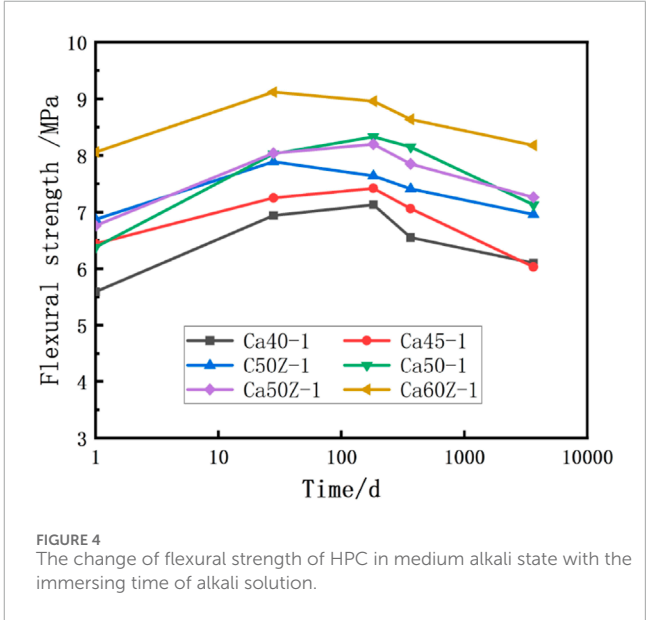
mechanical performance still exhibits an improvement in durability characteristics.

By comparing the flexural strengths of C50Z-1, Ca50-1, and Ca50Z-1 at different time intervals, it was found that the addition of air-entraining agent and corrosion inhibitor can improve the flexural performance of HPC. During the immersion period of 28 days to 365 days in alkali solution, the HPC with only air-entraining agent showed higher flexural strength compared to that with only corrosion inhibitor. After immersion for 3650 days, HPC with both additives maintained higher long-term flexural performance, indicating that the combination of air-entraining agent and corrosion inhibitor can synergistically enhance the stability of long-term flexural performance in alkali solution immersion.

In Figure 5, the relative flexural strength of Ca50-1 specimens is significantly higher than other mix proportions at each time interval, demonstrating a notable performance advantage. This also suggests that the effect of air-entraining agent on resisting ASR in HPC is stronger than that of corrosion inhibitor. Additionally, the relative

FIGURE 5
The change of the relative flexural strength of HPC in alkali state with the immersion time of alkali solution.
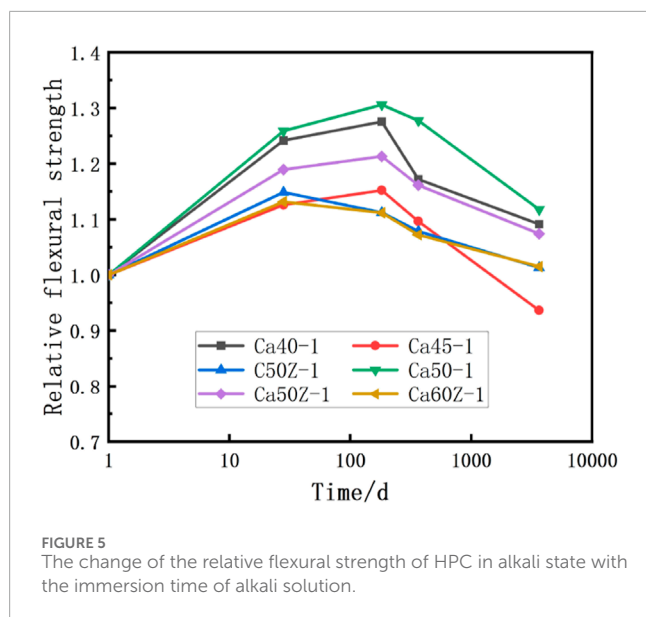
flexural strength of Ca60Z-1 remains relatively stable over time, indicating that long-term immersion in alkali solution has the least impact on its flexural mechanical performance.

3.3 The effect of alkali content on the flexural strength of HPC immersed in standard alkali solution for 10 years

This study analyzed the flexural strength of specimens with different alkali contents immersed in standard alkali solution for 10 years, and the relevant data were summarized in Table 9. The relative residual flexural strength represents the ratio of the flexural strength of HPC under medium and high alkali conditions to that under low alkali conditions.

According to the relevant data from Table 9 and Figure 6 is plotted below. In the graph, the horizontal axis labels 0, 1, and two represent the HPC specimens under low, medium, and high alkali conditions, respectively. By observing the data in the graph, it facilitates a better analysis of the trends and characteristics of the experimental results, thereby gaining deeper insights into the tendencies and features of the experiment.

Based on the observation of Figure 6, it is evident that HPC under different alkali content states generally exhibits an increasing trend in flexural strength as their respective strength grades increase. However, with the increase in alkali content, the flexural strength of HPC gradually decreases. Under medium alkali conditions, the relationship between flexural strength and strength grade is not significant, with a decrease ranging from 3.07% to 8.68%. Specifically, the Ca40 specimens show the highest decrease in flexural strength at 8.68%, while the Ca50Z specimens exhibit the lowest decrease at only 3.07%. Conversely, under high alkali conditions, the relative residual flexural strength of specimens across different strength grades remains at around 92%. This indicates that although the flexural strength of HPC generally increases with the increase in concrete strength grade, excessively high alkali content also leads to a certain degree of performance reduction.

3.4 The failure mode and crack propagation characteristics of HPC flexural test

The flexural strength is an important index to measure the flexural failure resistance of materials, which can be used to evaluate the performance of concrete beam-column members. At the same time, the actual flexural failure of concrete is also closely related to its seismic and other properties (Chen et al., 2019). Therefore, it is of great engineering significance to study the flexural strength of concrete. Figure 7 illustrates the flexural failure modes of Ca40 specimens with different alkali contents. In the early stages of the test, tensile deformation was observed at the bottom of the specimen, while compressive deformation was evident at the top. Due to the excellent performance of high-performance concrete, cracks typically exhibited small extension trends during the test. As the load continued to increase, cracks at the center of the specimen gradually expanded, forming distinct tensile failure characteristics. The expansion of cracks led to gradual loss of connection among the concrete inside the specimen, ultimately resulting in its failure. Upon reaching the failure point, noticeable fragmentation and collapse occurred at the center of the specimen, with cracks extending across the entire cross-section, exhibiting clear brittle failure characteristics.

Furthermore, HPC specimens with different alkali contents exhibited similar characteristics in the flexural test: there were distinct nearly vertical main cracks near the center of the specimen, causing the concrete to fracture into two parts. Upon studying the cross-section of the HPC specimens, it was observed that the fracture surface was relatively smooth. Statistical analysis of the damage to the aggregates revealed (yellow circles in Figure 7 represent cracks bypassing the aggregates, while red circles represent cracks penetrating the aggregates) that the alkali content had minimal influence on the damage pattern of the aggregates within the specimens. Approximately 64.9% of the cracks in Ca40 specimens penetrated the aggregates (there is a relatively smooth section of the aggregate in the final failure surface). This is mainly due to the excellent mix design of HPC and the tight bond between aggregates and mortar induced by various admixtures. As a result, cracks directly penetrated through them, leading to a relatively smooth fracture surface.
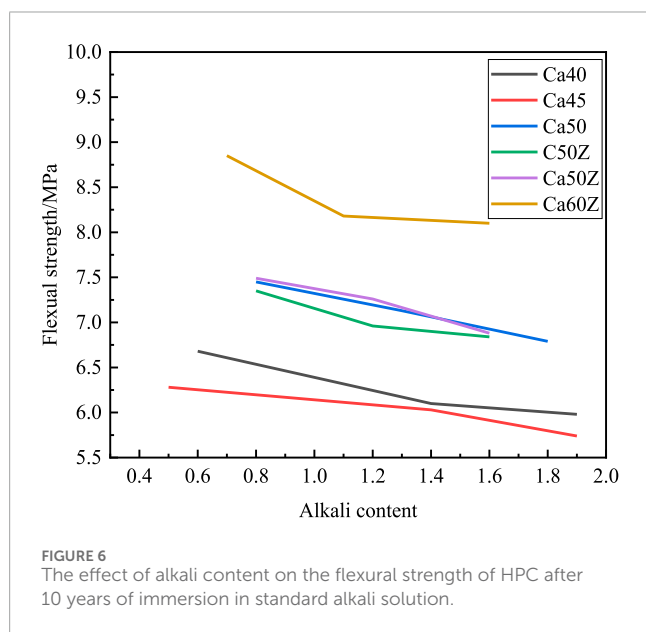
Figure 8 illustrates the failure modes of HPC specimens with different strength grades under low alkali conditions. There were no significant differences in the overall failure modes of specimens with different strength grades, which still exhibited a single main crack near the center of the specimen. Some specimens experienced slight damage during immersion in the alkali solution, resulting in minor spalling of the concrete surface during the loading test. However, the overall fracture surfaces appeared relatively smooth.

Compared to admixtures, the strength has a significant influence on the internal crack propagation characteristics of HPC. With the increase in strength grade, the probability of interface failure between aggregate and mortar decreases. Consequently, the proportion of cracks bypassing aggregates (there are grooves or protrusions of aggregate in the final failure surface) and causing aggregate detachment gradually reduces. When the strength grade reaches C50 and C60, the proportion of cracks penetrating

TABLE 9 The effect of alkali content on the flexural strength of HPC after immersing in standard alkali solution for 10 years.

Specimen	Flexural strength/MPa	Relative residual flexural strength/%	Specimen	Flexural strength/MPa	Relative residual flexural strength/%
Ca40-0	6.68	100.00	Ca45-0	6.28	100.00
Ca40-1	6.10	91.32	Ca45-1	6.03	96.02
Ca40-2	5.98	89.52	Ca45-2	5.74	91.40
C50Z-0	7.35	100.00	Ca50-0	7.45	100.00
C50Z-1	6.96	94.69	Ca50-1	7.13	95.70
C50Z-2	6.84	93.06	Ca50-2	6.79	91.14
Ca50Z-0	7.49	100.00	Ca60Z-0	8.85	100.00
Ca50Z-1	7.26	96.93	Ca60Z-1	8.18	92.43
Ca50Z-2	6.88	91.86	Ca60Z-2	8.1	91.53

FIGURE 6
The effect of alkali content on the flexural strength of HPC after 10 years of immersion in standard alkali solution.

aggregates is 80.4% and 83.3% respectively, with the majority of aggregates being directly split, resulting in smooth fracture surfaces.

4 Mesoscopic simulation of the flexural failure process of HPC and the propagation path of fracture cracks

4.1 Establishment of 3D random aggregate concrete mesoscopic model

With the advancement of computer technology, scholars have established various random aggregate models of different shapes and dimensions to simulate the distribution of coarse aggregates in concrete. Since Wittmann's pioneering work (Wittmann et al.,

1985) using 2D circular aggregate models to study the influence of coarse aggregates on the micro-mechanical properties of concrete, the understanding of aggregate shapes has deepened. As a result, random aggregate models have gradually evolved from regular geometric bodies to random-shaped particles, transitioning from two-dimensional planes to three-dimensional space. Common random aggregate models include two-dimensional spheres, ellipses, and polygons, as well as three-dimensional spheres, ellipsoids, and regular polyhedra [(Häfner et al., 2006; Wriggers and Moftah, 2006; Lu et al., 2010)]. In this study, based on random quadrilaterals in a plane, a spatial random octahedra matrix is generated. Then, a 3D random convex polyhedron aggregate model with controllable shape and size is obtained by using the random growth algorithm. The modeling process is described in the following text.

(1) Generating Planar Random Quadrilaterals

To ensure the randomness of the aggregate model shapes, a random quadrilateral is established in the plane as the projection surface of the aggregate model. Specifically, a circle with a radius of R = 0.5D is generated in the XOY plane, where D is the determined aggregate diameter. Within this circle, a random quadrilateral ABCD is determined as the inscribed shape, roughly as shown in Figure 9A.

(2) The spatial random octahedron matrix generates a 3D random convex polyhedron by growth algorithm.

An appropriate aggregate center point O is determined in the XOY plane, and a spatial random octahedron is established as the base of the aggregate model. After that, a random growth algorithm is used to obtain 3D random convex polyhedron aggregate model with controllable shape and size. As seen in Figure 9B, the three-dimensional random model closely resembles real aggregates in terms of edge and corner features, demonstrating the authenticity and reliability of this aggregate model.

(3) Aggregate Placement

FIGURE 7
The flexural failure modes of Ca40 with different alkali contents.
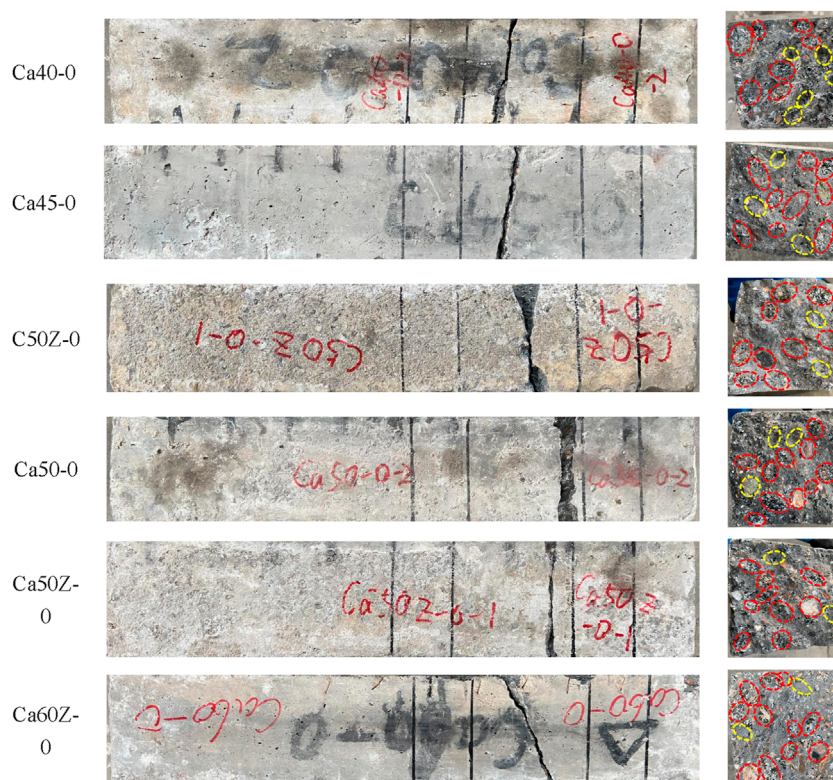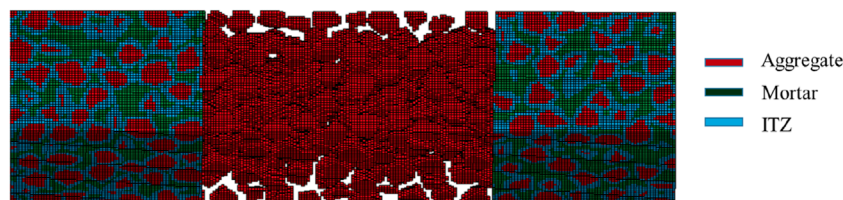

FIGURE 8
Failure modes of HPC with different strength grades under low alkali state.

During aggregate placement, the Fuller grading curve is used to determine the gradation relationship of random polyhedral aggregates in the mesoscopic model of concrete to meet the gradation requirements of coarse aggregates. An aggregate library is established based on the grading curve, and random center coordinates for aggregates are determined. Aggregates are then selected from the library based on these coordinates and placed within the designated area. Subsequently, the coordinates of the placed aggregates are checked against the boundary: if all vertexes of the aggregates are within the area, the placement is valid; if any vertexes are outside the area, indicating invalid placement, the aggregates are removed, and new center coordinates are determined for re-placement. During aggregate placement, the spatial "limited translation" and "random placement" algorithms proposed in reference (Fang et al., 2013) are utilized, combined with criteria for aggregate intersection and boundary intrusion, to adjust the spatial positions of aggregates. This process ultimately yields a three-dimensional random aggregate model that meets the desired aggregate volume fraction.
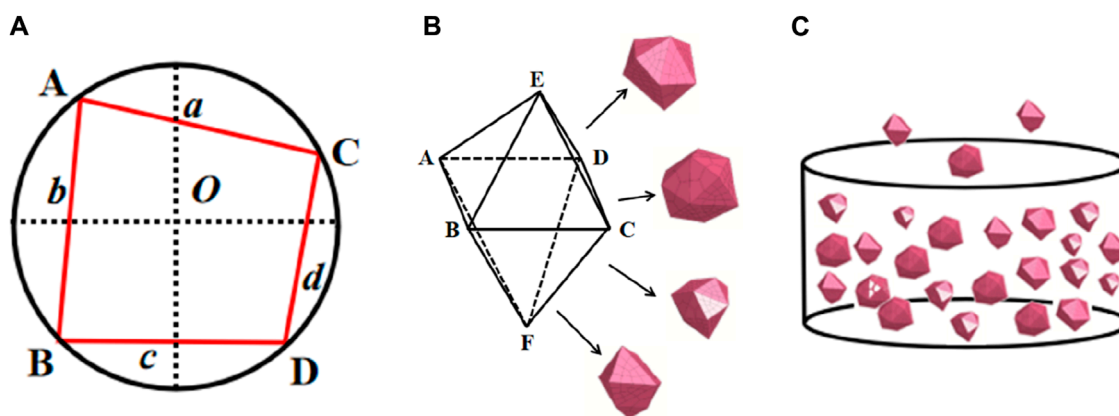
FIGURE 9
Modeling process of three-dimensional random aggregate concrete meso-model. **(A)** Generating Planar Random Quadrilaterals, **(B)** The spatial random octahedron generates a 3D random convex polyhedron by growth algorithm, **(C)** Aggregate Placement.

FIGURE 10
Three-dimensional random aggregate concrete model.

After completing the aggregate placement, referring to the mesoscopic model established by Wu et al. (Wu et al., 2021c) based on the finite element method, the ITZ is treated as a continuum damage-plasticity model. The material identification algorithm [(Fang and Zhang, 2012; Fang et al., 2016; Mao et al., 2019)] is used to identify coarse aggregates, mortar, and ITZ in the three-dimensional mesoscopic model. Subsequently, the mapping algorithm [(Fang and Zhang, 2012; Fang et al., 2016; Mao et al., 2019)] is employed to mesh the model, generating finite element meshes for different components, the mesh type is hexahedral mesh, the characteristic mesh size is 2mm, and the element number is 643,750, as shown in Figure 10. From the figure, it can be observed that after concealing the mortar and ITZ in the central part of the specimen, the distribution of aggregates appears completely random.

In this paper, the model of aggregate is selected as HJC model, and the model of mortar and ITZ is selected as K&C model. The HJC model needs to obtain the elastic modulus, mass density, Poisson's ratio and compressive strength of the aggregate. Because this paper uses the REL3 version of the K&C model, compared with other versions, it has the function of automatically determining the material parameters. It only needs to input the initial parameters such as uniaxial compressive strength, uniaxial tensile strength and elastic modulus, other parameters of concrete can be automatically calculated.

In this paper, the parameters of the model are determined by the microhardness as the medium, and the relationship between the microhardness and the meso-components of the concrete is acquired by means of statistics. The microhardness of each component of HPC required in this paper is obtained through experiments, and finally the mechanical parameters of each component of HPC are obtained. Details are shown in Section 4.2.

4.2 Mechanical properties of HPC meso-components and determination of model parameters

In order to obtain the mechanical parameters of each mesoscopic component of HPC, the microhardness test was carried out in this paper. According to the calculation formula for microhardness in Section 2.4.4, the microhardness variation with position near the coarse aggregate can be obtained (Figure 11). In the figure, the initial phase with relatively high microhardness corresponds to the aggregate, the lowest point in the curve represents the microhardness of the ITZ, and the subsequent relatively flat segment corresponds to the microhardness of the matrix. By conducting parallel measurements of 10 sets of data near the same aggregate and taking the average, the specific microhardness values for Ca40-0, Ca50-0, and Ca60Z-0 components are presented in Table 10.
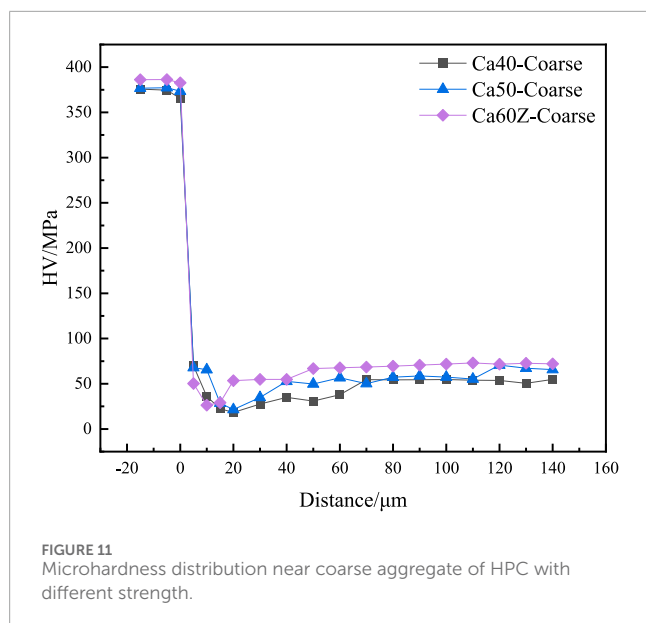
FIGURE 11
Microhardness distribution near coarse aggregate of HPC with different strength.

TABLE 10 Microhardness of HPC components with different strength.

	Coarse aggregate/MPa	ITZ/MPa	Matrix/MPa
Ca40-0	376.5	18.1	53.75
Ca50-0	370.8	21.7	64.07
Ca60-0	386.2	24.6	69.71

Due to limitations in size and testing conditions, the mechanical properties of mortar and the interface transition zone (ITZ) have not been accurately determined. Therefore, this study first obtained the microhardness values of various components inside concrete, including the matrix, aggregate, and ITZ, through experiments. Then, based on the work of Diao et al. (Diao, 2021) and Liu et al. (Liu and Jia, 1995), relationships between the macroscopic mechanical properties such as compressive strength fc, splitting tensile strength fst, and elastic modulus Ec of concrete and microhardness were established.

Through data fitting analysis, it was found that there is a linear relationship between the microhardness HV of the matrix and the splitting tensile strength fst-mor of mortar, and a quadratic function relationship between the compressive strength fc of the matrix and its microhardness. The relationship between the compressive strength fc and the static modulus of elasticity Ec of the matrix is linear. The static modulus of elasticity Ec of the matrix has a power function relationship with the elastic modulus Ec-mor of mortar, and the elastic modulus Ec-mor of mortar has a power function relationship with the compressive strength fc-mor of mortar, as shown in Figure 12. By using the experimentally measured microhardness of the matrix, the mechanical properties of the mortar components can be subsequently determined.

Figure 13 illustrates the relationship between the microhardness of the ITZ and its mechanical properties. From the graph, it is

evident that the microhardness of the ITZ exhibits an exponential relationship with its splitting tensile strength, and the splitting tensile strength of the ITZ has an exponential relationship with its compressive strength. Since the ITZ can be considered as the weaker mortar component, the relationship between Ec-ITZ and fc can be referenced from Figure 12C.

In this study, the mortar and ITZ are modeled using the K&C model, which includes three strength failure surfaces: the initial yield surface, the ultimate strength surface, and the residual strength surface. This model can simulate the changes of the strengthening surface between the initial yield surface and the ultimate strength surface, as well as the softening surface between the ultimate strength surface and the residual strength surface (Liu and Jia, 1995). By utilizing the aforementioned relationships between microhardness and the mechanical properties of each component, the material parameters of mortar and ITZ can be calculated, as detailed in Table 11.

The aggregate is modeled using the HJC model, which comprises a state equation, a yield surface equation, and a damage evolution model, as illustrated in Figure 14. Specific material parameters are selected based on references (Li et al., 2023), with an elastic modulus E = 66GPa, mass density ρ = 2780 kg/m^3, Poisson's ratio μ = 0.15, and compressive strength fc = 50 MPa.

4.3 Verification of model parameters of 3D concrete mesoscopic model in HPC flexural test

Based on the modeling method and process described in Section 4.1, a 515 mm × 100 mm × 100 mm prismatic concrete specimen model was established with a mesh size of 2mm, resulting in a total of 645,060 elements. The aggregate volume fraction is 46%. Distributed displacement loads were applied along the Z-axis to simulate the mesofailure mechanism of HPC in flexural experiments (Figure 15). From the simulated results, stress is concentrated between the two loading points, and cracks gradually propagate upwards in this region. Eventually, the overall failure process is consistent with the simulation results, with most of the aggregates along the failure surface being split, forming relatively smooth fracture surfaces.

By referring to the relevant articles (Liu et al., 2021; Guo et al., 2022; Li et al., 2023), it can be found that the simulation effect is better when the error between the experiment and the simulation results is less than 10%.

Table 12 summarizes the experimental and simulated flexural strengths, the error is within 10%, indicating that this model can effectively simulate the flexural mechanical properties of HPC containing ASR inhibitors under long-term alkali immersion.

Figure 16 depicts the failure process of three different strength HPC specimens, Ca40-0, Ca50-0, and Ca60Z-0. The maximum effective strain was adjusted to 0.003. From the figure, it can be observed that cracks in all specimens generally develop from bottom to top. Cracks first appear in Ca40-0 at 0.002 s, then propagate rapidly upwards, bypassing the bottom aggregates and directly penetrating some aggregates in the middle of the specimen by
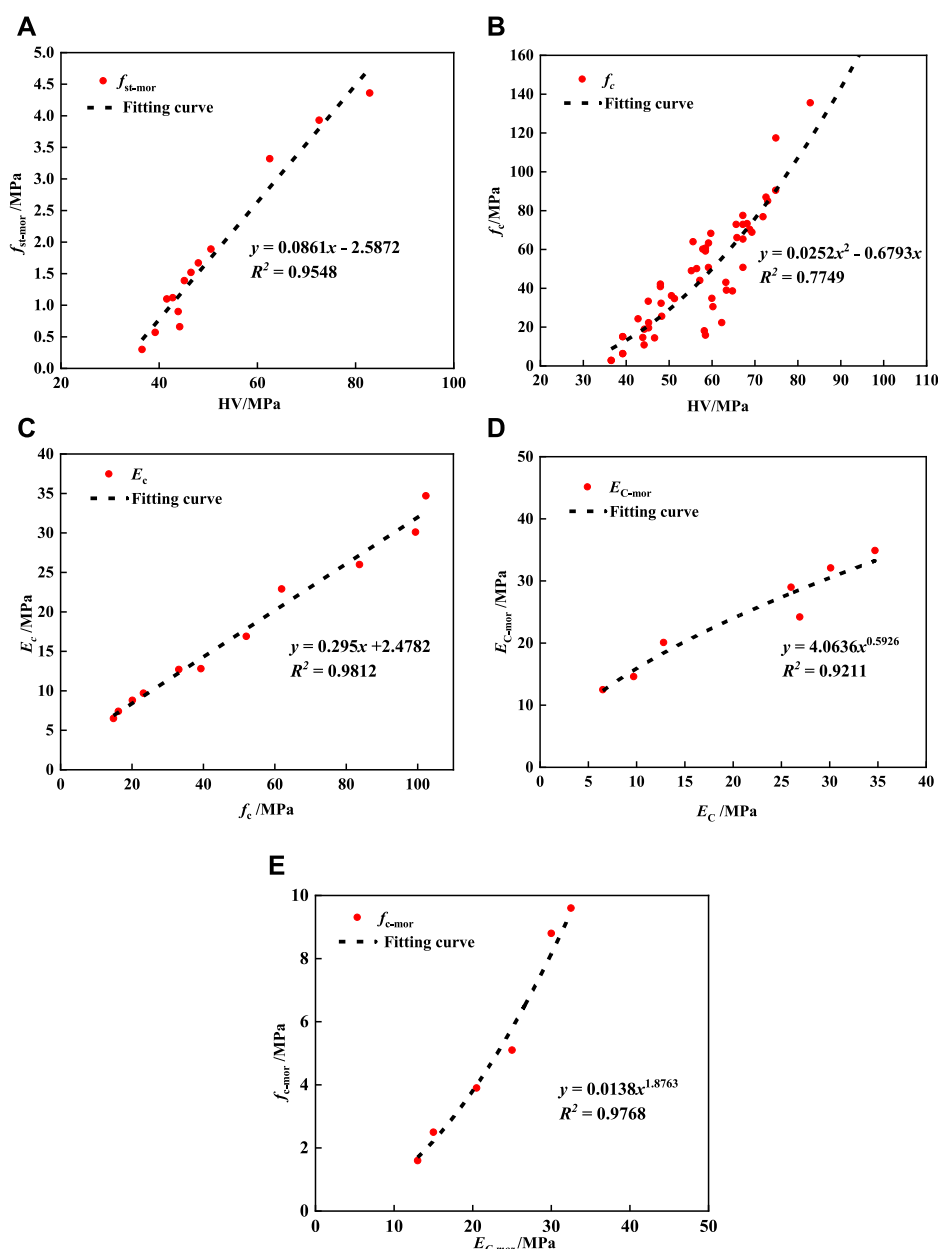
FIGURE 12
Relationship between the macroscopic mechanical properties of mortar and HV of matrix. **(A)** Relationship between HV and f_{st-mor} of matrix, **(B)** Relationship between HV and f_c of matrix, **(C)** The relationship between f_c and E_c of matrix, **(D)** The relationship between E_c and E_{c-mor}, **(E)** Relationship between E_{c-mor} and f_{c-mor}.

0.008s, forming the main crack. In contrast, cracks in Ca50-0 and Ca60Z-0 form later due to directly penetrating the bottom aggregates, but the main cracks also form at 0.008 s. With subsequent loading, the cracks gradually widen, leading to the final failure mode consistent with the actual scenario. Specifically, with increasing strength, the proportion of cracks penetrating aggregates increases. Almost no cracks bypassing aggregates were observed in Ca50-0 and Ca60Z, indicating that using the three-dimensional random aggregate mesoscopic model and associating microhardness with the mechanical parameters of concrete components to obtain model parameters can effectively simulate the flexural failure mode of HPC.

4.4 Numerical simulation of mesoscopic failure mechanism in HPC flexural test

Figure 17 illustrates the failure process of coarse aggregates in the Ca40-0 model, where most aggregates exhibit splitting failure. As shown in the figure, as the loading time progresses, cracks make contact with the aggregates at 0.002s, followed by the appearance of fine cracks in the aggregates at 0.004 s. With further loading, the cracks continue to expand, penetrating the aggregates almost vertically, widening the cracks on both sides, and squeezing the aggregates sideways, ultimately resulting in a relatively smooth fracture surface. A small portion of
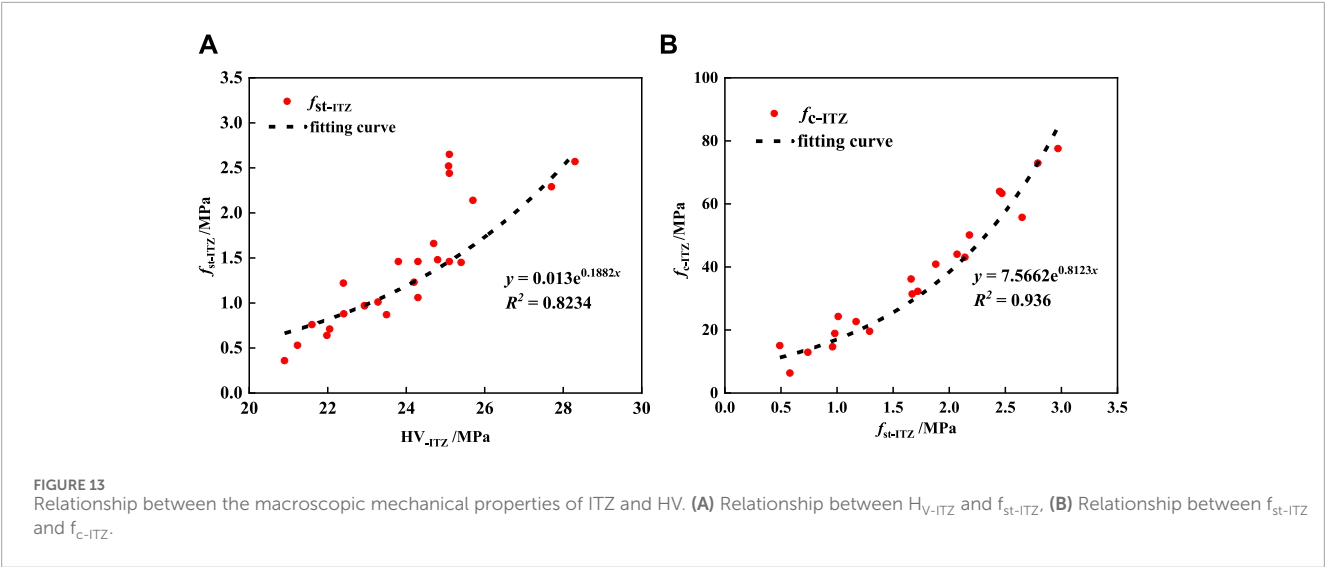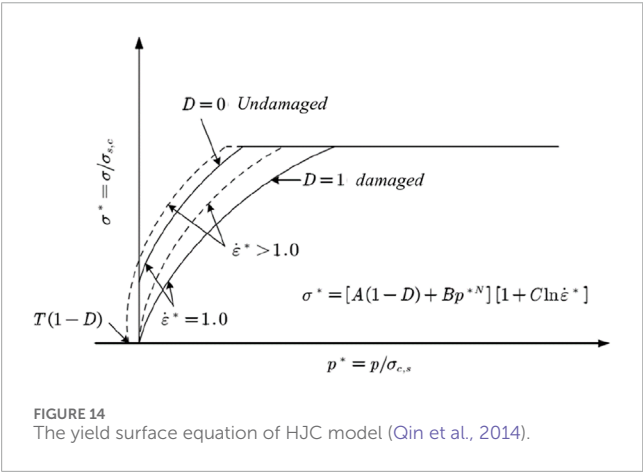
FIGURE 13
Relationship between the macroscopic mechanical properties of ITZ and HV. **(A)** Relationship between H_{V-ITZ} and f_{st-ITZ}, **(B)** Relationship between f_{st-ITZ} and f_{c-ITZ}.

TABLE 11 Model parameters of mortar and ITZ material.

Model parameters	Mortar			ITZ		
	Ca40-0	Ca50-0	Ca60Z-0	Ca40-0	Ca50-0	Ca60Z-0
fc/MPa	36.3	59.9	75.1	10.4	14.7	27.7
fst/MPa	2.04	2.93	3.41	0.39	0.77	1.33
Ec/GPa	13.2	20.2	24.6	5.5	6.8	10.7

FIGURE 14
The yield surface equation of HJC model (Qin et al., 2014).

FIGURE 15
Failure mode of Ca50-0 specimen in flexural test.

cracks bypassing the aggregates can be observed. At 0.004s, the crack penetrates the ITZ and reaches the aggregates. Subsequently, instead of continuing to propagate in the original direction, the crack propagates along the ITZ between the aggregates and the mortar until complete failure occurs, causing the detachment of the aggregates from the mortar. The final failure surface exhibits protruding aggregates or retained aggregate voids.
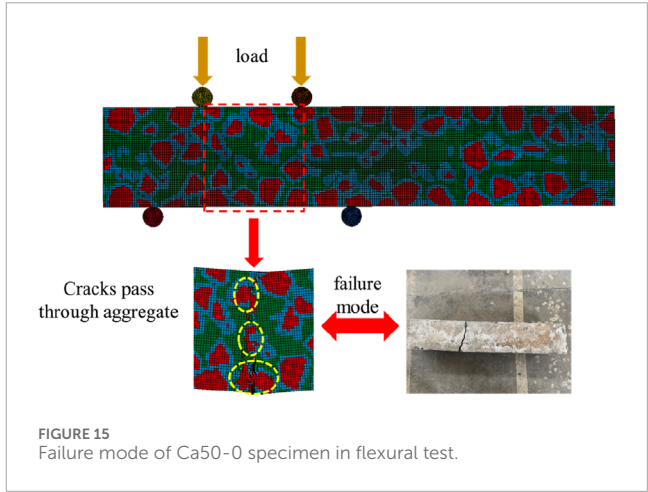
TABLE 12 Comparison of different strength HPC test and simulated flexural strength.

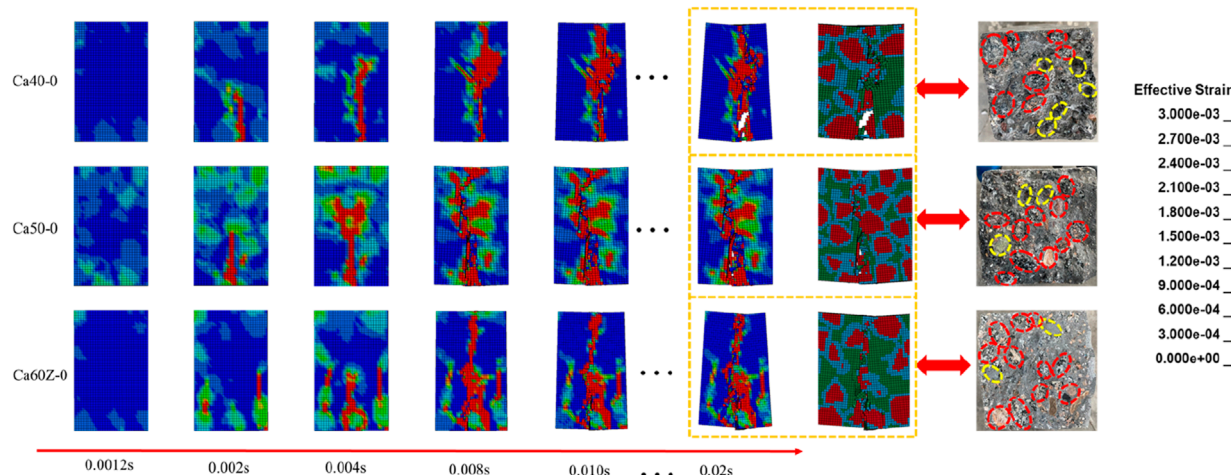|	Test/MPa	Simulation/MPa	Error (%)
Ca40-0	6.68	6.23	−6.73
Ca50-0	7.45	7.11	−4.56
Ca60Z-0	8.65	8.83	+2.08

FIGURE 16
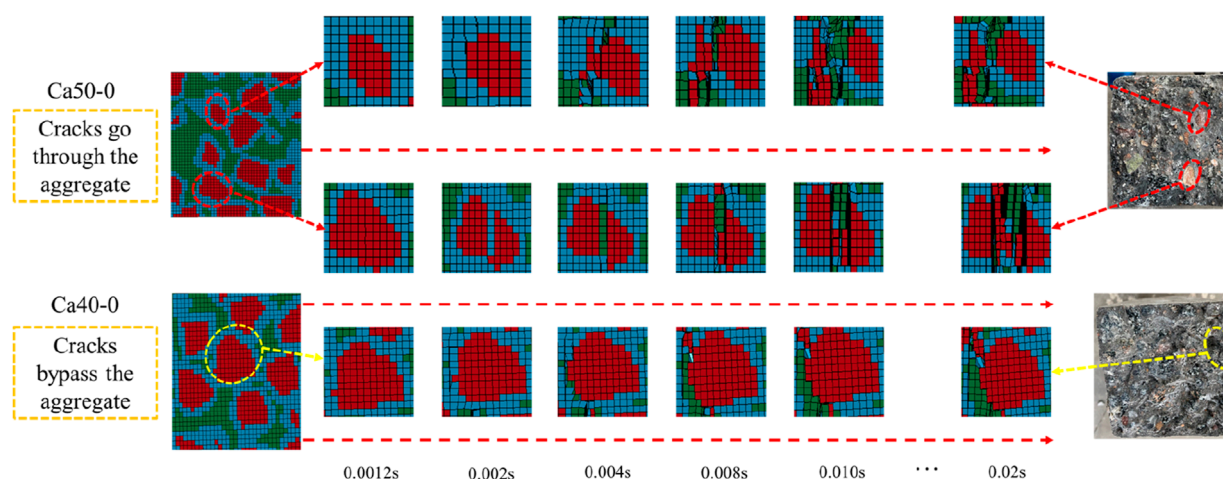Analysis of failure process of HPC with different strength grades.

FIGURE 17
Different failure processes of coarse aggregate.

5 Conclusion

Based on the investigation of the mechanical properties and microfailure mechanisms of HPC containing ASR inhibition measures under long-term alkali immersion, the specific conclusions are as follows.

(1) With the increase in strength grade, the flexural strength of HPC generally shows an increasing trend, but as the alkali content rises, the flexural strength gradually decreases. Air-entraining agents perform better in resisting ASR under long-term alkali immersion compared to corrosion inhibitor.

(2) In standard alkali solution, the flexural strength of HPC in the middle alkali state generally increases with the increase in strength grade during different immersion periods. The immersion time has an impact on the flexural strength of HPC with different strength grades. Initially, immersion can

significantly enhance the flexural strength, but prolonged immersion leads to a gradual decrease in strength, albeit still maintained at a relatively high level.

(3) HPC specimens of different strength grades and alkali contents exhibit similar fracture characteristics in flexural tests, mainly characterized by a single primary crack formed between loading points and eventually extending to the specimen section.

(4) The three-dimensional random aggregate mesoscopic concrete model was used to simulate the flexural failure mode of HPC. Results demonstrate that with increasing strength, the occurrence time of initial cracks is delayed, and the ratio of cracks bypassing aggregates (cracks develop along the ITZ between aggregate and mortar until complete failure) decreases, and the ratio of cracks penetrating aggregates (cracks develop directly through the aggregates in an almost vertical direction) increases.

Data availability statement

Author contributions

Funding

Conflict of interest

Publisher's note

References

Cavalcanti, A. J. C. T. (1986). "Alkali-aggregate reaction at moxoto dam, Brazil," in *Proceedings of the 7th international conference on alkali-aggregate reaction in concrete* (Canada: Noyes Publication), 168–172. doi:10.1016/S0963-8695(97)88915-3

Chen, H., Soles, J. A., and Malhotra, V. M. (1993). Investigations of supplementary cementing materials for reducing alkali-aggregate reactions. *Cem. Concr. Compos.* 15 (1-2), 75–84. doi:10.1016/0958-9465(93)90039-C

Chen, J., Shi, H., Li, J., Guo, M., Ding, F., Shao, Z., et al. (2023). Mechanical properties of CFSST with steel reinforcement cage under biaxial eccentric compression. *J. Constr. Steel Res.* 204, 107853. doi:10.1016/j.jcsr.2023.107853

Chen, J., Zhao, C., Ding, F., and Xiang, P. (2019). Experimental study on the seismic behavior of precast concrete column with grouted corrugated sleeves and debonded longitudinal reinforcements. *Adv. Struct. Eng.*, 1369–4332.

Choi, Y. C., and Choi, S. (2015). Alkali–silica reactivity of cementitious materials using ferro-nickel slag fine aggregates produced in different cooling conditions. *Constr. Build. Mater.* 99, 279–287. doi:10.1016/j.conbuildmat.2015.09.039

Crouch, R. S., and Wood, J. G. M. (1990). Damage evolution in AAR affected concretes. *Eng. Fract. Mech.* 35, 211–218. doi:10.1016/0013-7944(90)90199-q

Diao, Y. (2021). Research on macroscopic mechanical properties of concrete interfacial transition zone and its relationship with microstructure. *Nanjing Univ. Aeronautics Astronautics*.

Ding, J., Bai, Y., and Cai, Y. (2008). Suppressing effect of lithium slag on alkalisilica reaction and separation of its self-expansion. *J. Hohai Univ. Nat. Sci.* 36 (6), 824–827.

E Grattan-Bellew, P., J Beaudoin, J., and Vallée, V.-G. (1998). Effect of aggregate particle size and composition on expansion of mortar bars due to delayed ettringite formation. *Cem. Concr. Res.* 28 (8), 1147–1156. doi:10.1016/S0008-8846(98)00084-2

Fang, Q., and Zhang, J. (2012). "Three-dimensional numerical modelling of concrete-like materials subjected to dynamic loadings," in *Advances in protective structures* (Boca Raton: CRC Press), 33–64.

Fang, Q., Zhang, J., Huan, Y., et al. (2013). The investigation into three-dimensional mesoscale modelling of fully-graded concrete. *Eng. Mech.* 30 (1), 14–30. (in Chinese).

Fang, Q., Zhang, J., Zhang, Y., Gong, Z., Chen, L., and Liu, J. (2016). 3D numerical investigation of cement mortar with microscopic defects at high strain rates. *J. Mater Civ. Eng. ASCE28* 28 (3), 1–10. doi:10.1061/(asce)mt.1943-5533.0001436

Fares, G., and Khan, M. I. (2013). HPC composites formulated to counteract early ASR expansion. *J. ofF Mater. Civ. Eng.* 25 (12), 1951–1958. doi:10.1061/(asce)mt.1943-5533.0000790

Gao, P. (2018). Study on durability of subway concrete structures under high salty soil in high altitude region of northwest China. *Nanjing Univ. Aeronautics Astronautics*.

Gao, P., Yu, H., Wen, J., et al. (2019). Effect of air-entraining agent on mitigating alkali-silica reactions under high-altitude alkaline environment. *J. Chin. Ceram. Soc.* 47 (5), 625–631.

Guo, J., Zhang, J., Yu, H., Ma, H., and Wu, Z. (2022). Experimental and 3D mesoscopic investigation of uniaxial compression performance on basic magnesium sulfate cement-coral aggregate concrete (BMSC-CAC). *Compos. Part B Eng.* 236, 109760. doi:10.1016/J.COMPOSITESB.2022.109760

Häfner, S., Eckardt, S., Luther, T., and Könke, C. (2006). Mesoscale modeling of concrete: geometry and numerics. *Comput. Struct.* 84 (7), 450–461. doi:10.1016/j.compstruc.2005.10.003

Jan, L., Thomas, M. D. A., Sellevold, E. J., Pedersen, B., Andiç-Çakır, Ö., Justnes, H., et al. (2013). Alkali-silica reaction (ASR)-performance testing: influence of specimen pre-treatment, exposure conditions and prism size on alkali leaching and prism expansion. *Cem. Concr. Res.* 53 (11), 68–90. doi:10.1016/j.cemconres.2013.05.017

Kubo, Y., and Nakata, M. (2012). "Effect of reactive aggregate on mechanical properties of concrete affected by alkali-silica reaction," in Proceedings of the 14th International Conference on Alkali–Aggregate Reaction in Concrete, Austin, May 20–25th 2012. (electronic).

Li, L., Ma, H., Yu, H., Zhang, J., Cheng, M., Wu, Z., et al. (2023). Attack resistance mechanism, uniaxial compressive mechanical properties and meso-simulation of high-performance concrete exposed to brine in salt lake for 10 years. *Constr. Build. Mater.* 407, 133520. doi:10.1016/j.conbuildmat.2023.133520

Liu, S. H., Bracci, J. M., Mander, J. B., and Hurlebaus, S. (2015). Performance of D-regions affected by alkali-silica reaction: experimental and analytical study. *ACI Mater. J.* 4 (112), 501–511. doi:10.1061/(ASCE)ST.1943-541X.0001847

Liu, H., and Jia, F. (1995). Effect of fine aggregate on elastic modulus of mortar and concrete. *concrete* (1), 12–18.

Liu, T., Ma, H., Wu, Z., et al. (2021). Study on impact compressive properties of basic magnesium sulfate cement concrete. *J. Build. Mater.* 24 (03), 562–570.

Lu, Y., Song, Z., and Tu, Z. (2010). Analysis of dynamic response of concrete using a mesoscale model incorporating 3D effects. *Int. J. Prot. Struct.* 1 (2), 197–217. doi:10.1260/2041-4196.1.2.197

Ma, H., Xu, W., and Li, Y. (2016). Random aggregate model for mesoscopic structures and mechanical analysis of fully-graded concrete. *Comput. Struct.* 177, 103–113. doi:10.1016/j.compstruc.2016.09.005

Mao, L., Hu, Z., Xia, J., Feng, G. l., Azim, I., Yang, J., et al. (2019). Multi-phase modelling of electrochemical rehabilitation for ASR and chloride affected concrete composites. *Compos. Struct.* 207, 176–189. doi:10.1016/j.compstruct.2018.09.063

Marzouk, H., and Langdon, S. (2003). The effect of alkali -aggregate reactivity on the mechanical properties of high and normal strength concrete. *Cem. Concr. Compos.* 25 (4-5), 549–556. doi:10.1016/s0958-9465(02)00094-x

McCoy, W. J., and Caldwell, A. G. New approach to inhibiting alkali-aggregate reaction expansion, A. C. I, 1951,22(9):693- 706.

Ministry of Housing and Urban-Rural Development of the OPeople's Republic of China (2019). *GB/T 50081-2019 Standard for test methods of concrete physical and mechanical properties*. Beijing: China Architecture and Building Press.

Mong, X., Xu, Z., and Tang, M. (2002). Review of alkali-aggregate reaction and its research progress. *J. Mater. Sci. Eng.* (01), 128–132. (in Chinese).

Nixon, P. J., and Bollinghaus, R. (1985). The effect of alkali aggregate reaction on the tensile strength of concrete, Durab. *Build. Mater.* 2 (3), 243–248.

Qian, C. X., Guo, H. D., and Tang, M. S. (1994). Mechanism of mineral admixture suppressing alkali-silica reaction: Part I, Corrosion degree of reactive aggregate in blended cement pastes and its correlations with expansion value and electric resistance change. *Cem. Concr. Res.* 24 (16), 1111–1120. doi:10.1016/0008-8846(94)90035-3

Qian, C. (1996). Effect of alkali on the performance of concrete. *Ind. Constr.* (12), 38–42.

Qin, F., Kong, X. Z., and Wu, H. (2014). Determination of HOLMQUIST-JOHNSON-COOK CONSITIUTIVE model parameters of rock. *Eng. Mech.* 31 (03), 197–204. doi:10.6052/j.issn.1000-4750.2012.10.0780

Sanchez, L. F. M. (2014). *Contribution to the assessment of damage in aging concrete infrastructures affected by alkali-aggregate reaction* (Québec: Department of Geology and Geological Engineering, Université Laval). PhD thesis.

Shayan, A., and Ivanusec, I. (1989). "Influence of NaOH on mechanical properties of cement paste and mortar with and without reactive aggregate," in *Proceedings of the8th intonational conference on alkali-aggregate reaction in concrete* (Japan: Kyoto).

Smaoui, N., Bérubé, M. A., Fournier, B., and Bissonnette, B. (2004). Influence of specimen geometry, orientation of casting plane, and mode of concrete consolidation on expansion due to ASR. *Cem. Concr. Aggreg.* 26 (2), 1–13. doi:10.1520/cca11927

Tang, M., Xu, Z., Deng, M., Lv, Y., Han, S., and Lan, X. (2022) Alkali aggregate reaction of concrete in China. *J. Build. Mater.* 1998 (01), 10–16. (in Chinese).

Vo, D., Hwang, C., Tran Thi, K. D., Yehualaw, M. D., and Chen, W. C. (2020). Effect of fly ash and reactive MgO on the engineering properties and durability of high-performance concrete produced with alkali-activated slag and recycled aggregate. *J. Mater. Civ. Eng.* 32 (11). doi:10.1061/(ASCE)MT.1943-5533.0003420

Wang, F. (1993). "A Study on corrosion and destruction of concrete under natural condition of Caerhan," in *Proc. 3rd Beijing Int. Symp. On cem. And concr* (Beijing: IEEE), 811–815.

Wittmann, F. H., Roelfstra, P. E., and Sadouki, H. (1985). Simulationin and analysis of composite structures. *Mater. Sci. Eng.* 68 (2), 239–248. doi:10.1016/0025-5416(85)90413-6

Wriggers, P., and Moftah, S. O. (2006). Mesoscale models for concrete: homogenisation and damage behaviour. *Finite Elem. Analysis Des.* 42 (7), 623–636. doi:10.1016/j.finel.2005.11.008

Wu, Z. (2000). High performance concrete–green high performance concrete. *China Concr. Cem. Prod.* (01), 3–6.

Wu, Z., Zhang, J., Fang, Q., Yu, H., and Ma, H. (2021a). Mesoscopic modelling of concret-e material under static and dynamic loadings: a review. *Constr. Build. Mater.* 278, 122419. doi:10.1016/j.conbuildmat.2021.122419

Wu, Z., Zhang, J., and Yu, H. (2021c). Three-dimensional mesoscopic investigation on quasi-static compressive properties of coral aggregate concrete. *ACI Mater. J.* 118 (4), 121–132.

Wu, Z., Zhang, J., and Yu, H. (2022). Mesoscopic particulate system assembled from three-dimensional irregular particles. *Adv. Powder Technol.* 33 (5), 103580. doi:10.1016/j.apt.2022.103580

Wu, Z., Zhang, J., Yu, H., Ma, H., and Fang, Q. (2021b). 3D mesoscopic analysis on the compressive behavior of coral aggregate concrete accounting for coarse aggregate volume and maximum aggregate size. *Compos. Struct.* 273, 114271. doi:10.1016/j.compstruct.2021.114271

Xiang, P., and Liew, K. M. (2013). A computational framework for transverse compression of microtubules based on a higher-order Cauchy–Born rule. *Comput. Methods Appl. Mech. Eng.* 254, 14–30. doi:10.1016/j.cma.2012.10.013

Xu, W., Chen, H., and Lv, Z. (2011). An overlapping detection algorithm for random sequential packing of elliptical particles. *Phys. A Stat. Mech. its Appl.* 390 (13), 2452–2467. doi:10.1016/j.physa.2011.02.048

Yan, J., Yu, H., Zhang, W., Zahng, L., Ma, H., Gong, X., et al. (2022). Expansion and mechanical properties of high-performance concrete with ASR inhibition measures exposed to alkaline solution at 38°C for 10 years. *Constr. Build. Mater.* 353, 129044. doi:10.1016/j.conbuildmat.2022.129044

Yu, H., Hua, P., Qu, W., Sun, W., and Yan, L. (2003). Field exposure experiment of anti-corrosion concrete pole in northwest salt lake area. *China Concr. Cem. Prod.* (6), 23–26. (in chinese).

Zhang, J., Wu, Z., Zhang, Y., Fang, Q., Yu, H., and Jiang, C. (2021). Mesoscopic characteristics and macroscopic mechanical properties of coral aggregates. *Constr. Build. Mater.* 309, 125125. doi:10.1016/j.conbuildmat.2021.125125

Zhang, L. (2014). *Research on durability of reinforced concrete structure based on the correlation between field exposure test and indoor durability test*. Nanjing: Nanjing University of Aeronautics and Astronautics.

Zhou, L. (2011). Research on influences of alkali-aggregate reactions on durability of concrete. *Ind. Constr.* 41 (S1), 759–762+749. doi:10.13204/j.gyjz2011.s1.028

Compression behaviour of Q355 steel angles with local defect at bolt holes

Jinglu Zhang[1], An He[2,3], Yu Liu[2,3]* and Shao-Bo Kang[4]

[1]SWJTU-Leeds Joint School, Southwest Jiaotong University, Chengdu, China, [2]School of Civil Engineering, Southwest Jiaotong University, Chengdu, China, [3]MOE Key Laboratory of High-speed Railway Engineering, Southwest Jiaotong University, Chengdu, China, [4]School of Civil Engineering, Chongqing University, Chongqing, China

This paper presents experimental and numerical studies on compression behaviour of equal-leg steel angles with bolted connection and subjected to local defect at the bolt hole. To simulate corrosion, a mechanical cutting method was used in the experimental test to increase the diameter of bolt holes, and a total of 18 steel angles were investigated in the study. The parameters considered included the slenderness and the diameter of bolt holes. The slendernesses of steel angles were 80 and 140, and the diameter of bolt holes ranged from 21.5 to 27.5 mm. Additionally, numerical models were established for the steel angles. The accuracy of the numerical model was verified by comparing experimental data with numerical results. Based on the validated numerical model, a parametric analysis was conducted to quantitatively assess the influences of the slenderness and the diameter of bolt holes on the load capacity of specimens against global buckling. Experimental and numerical results showed that the defect at the bolt hole affected the load capacity of specimens when the diameter of the bolt hole was increased to 27.5 mm and the slenderness was not greater than 100.

1 Introduction

Equal-leg steel angles are widely used in the structures of transmission towers due to their diverse sectional dimensions, ease of fabrication, and convenient connection options. In the towers, steel angles connected with bolts at one leg are often used as inclined compression or tension members. The overall buckling behaviour of these steel angles has become the focus of research studies (Adluri and Madugula, 1996; Bathon et al., 1993; Shi et al., 2011; Wakabayashi and Nonaka, 1965; Cao et al., 2017; Chen, 2012; Liu et al., 2021).

Since transmission towers operate outdoors in the service life and they are frequently subjected to various weathering conditions, making the steel angle highly susceptible to varying degrees of corrosion (Huang et al., 2023). Corrosion alters the chemical and physical properties of steel, thereby reducing the behaviour and resistance of components. For corroded steel angles, it is essential to carefully assess their residual load capacities to ensure safety. Researchers have conducted various compression tests to quantify the overall buckling load of steel angles with

corrosion. Beaulieu et al. (2010) considered the corrosion of 16 steel angles by immersing them in saturated copper sulphate solution, followed by compression testing. They investigated the influence of slenderness, width-to-thickness ratio, and degree of corrosion on the compressive behaviour of steel angles. Zhang et al. (2014) investigated the influence of acid rain corrosion models on the seismic behaviour of Q355 equal-leg steel angle through quasi-static tests and established corresponding degradation models. Gao et al. (2020) quantitatively analysed the effects of four common types of corrosion, including uniform corrosion, pitting corrosion, localized corrosion, and corrosion at the edge, on the performance of steel angles by numerical modelling. Additionally, researchers have developed calculation methods to predict the load capacity of steel angles. Ye et al. (2016) established a conversion relationship between artificial accelerated corrosion tests and the corrosion status of Q235 steel components under marine atmospheric conditions. They also proposed a practical calculation method to analyse the mechanical behaviour degradation of pitted steel components. Oszvald et al. (2016) simulated corrosion by reducing the thickness of steel angles using mechanical cutting. They conducted compression tests and numerical simulations on corroded equal-leg steel angles and developed a simplified design method to predict the residual compressive resistance of corroded components. Wang (2021) studied the influence of pit thickness, corrosion range, corrosion location, and slenderness of components on the mechanical properties of Q420 locally corroded steel angles through numerical simulations. Based on the research results, they proposed calculation formulae to evaluate the ultimate tensile and compressive load-bearing capacities. In summary, most studies have focused on the influence of corrosion on the mechanical properties of steel or a single component in specific environments. However, there is a lack of sufficient experimental data regarding the residual compression resistance of steel angles with bolted connections on one leg after corrosion.

This study aims to provide experimental and numerical data on the compression load capacity of equal-leg steel angles with bolted connections after simulated corrosion. The corrosion of steel angles was simulated using mechanical cutting methods and the diameter of bolt holes and slenderness was varied in the experimental tests and numerical study. The influences of slenderness and bolt hole diameter on its buckling behaviour of steel angles were quantified in the experimental and numerical results.

2 Experimental programme for steel angles in compression

2.1 Specimen design

Q355 steel angles with equal legs were selected for compression tests. Figure 1 displays an image of steel angles. The steel angles had a cross-sectional dimension of 75 mm × 6 mm, with total lengths of 1,092 mm and 1,986 mm respectively. Based on the distance between the top and bottom hinged supports (measured as 2,086 mm for long angle steel and 1,192 mm for short angle steel), the slendernesses of steel angles with regard to its minor axis were calculated to be 80 and 140, respectively. Figure 2 shows the detailed dimension of specimens. A steel plate was connected to one leg

FIGURE 1
Steel angles used in the experimental tests.

of each angle using three bolts at each end, representing a typical form of connection in transmission towers. To simulate corrosion, mechanical cutting can be adopted to reduce the thickness of steel plates (Oszvald et al., 2016). Site investigations before testing showed that the connection of steel angles might be subjected to severe corrosion. To simulate the corrosion, the diameter of bolt holes was enlarged by mechanical cutting, but the thickness of steel angles remained unchanged. It should be pointed out that mechanical cutting would not affect the compression behaviour of steel angles, as the compression capacity of steel angles is only sensitive to changes in the cross-sectional area of steel angles rather than the different levels of stress concentration. However, the residual stress distribution may be affected due to the heat generated in the cutting process. In this study, a total of 6 sets of steel angles were tested in compression, with three steel angles with the same parameter in each set. Table 1 lists the specific parameter of steel angles. In the table, the symbols are defined as follows: L and S represent the long and short steel angles, respectively; H indicates the defect at the bolt hole. For example, L-H23.5 indicates that the bolt hole diameter of the long angle steel is 23.5 mm. The steel angles used in the compression tests could be categorized into two groups. The first group consisted of 2 sets of control specimens without damage (Huang et al., 2024). The second group included 4 sets of specimens with enlarged bolt holes, namely, the diameter of the bolt hole was increased from 21.5 mm to 23.5 and 27.5 mm, respectively. The cross-section and slenderness of steel angles were selected based on the widely used dimension of steel angles in transmission towers in China. Note that the diameter of bolt holes was affected by the service life and environmental conditions of transmission towers.

2.2 Mechanical properties of steel angles

According to GB/T 228.1-2010 (Management Committee for National Standards, 2010), three samples were cut from the steel angle and tested in tension. The sample thickness was 6 mm, the same as the steel angle, and the gauge length was 96 mm. Figure 3 shows the stress-strain curve obtained from the tension test (Huang et al., 2024). It is evident that the curves for all three samples were close to one another, each consisting of an elastic stage, a yield plateau and a hardening stage. Experimental data showed that the elastic modulus of the steel angle was 201,172 MPa, the yield strength was 380.3 MPa, and the ultimate strength was 555.9 MPa.
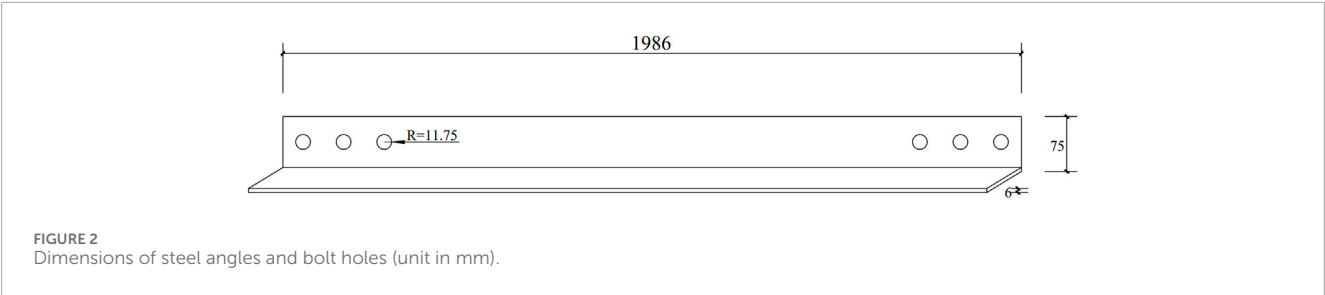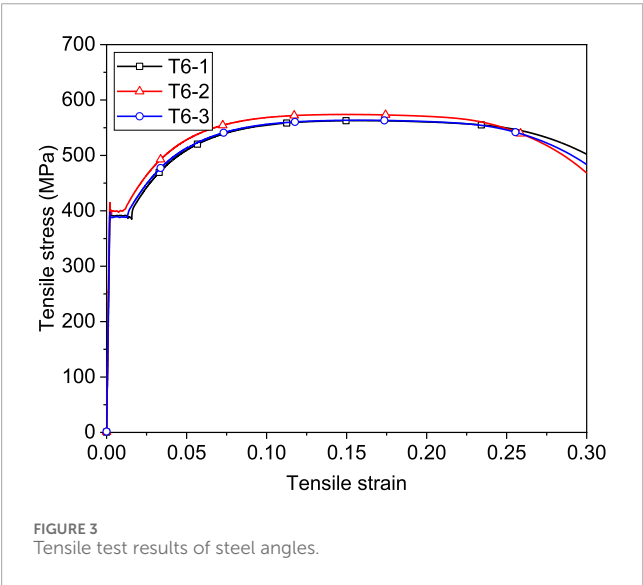
FIGURE 2
Dimensions of steel angles and bolt holes (unit in mm).

TABLE 1 Summary of geometric dimensions of steel angles.

Steel angles	Section of steel angles (mm)	Slenderness about the minor axis	Type of defect	Design length (mm)
SCN		80	--	1,092
LCN		140	--	1,986
SC-H23.5		80	Bolt hole of 23.5 mm	1,092
LC-H23.5	L75 × 6	140	Bolt hole of 23.5 mm	1,986
SC-H27.5		80	Bolt hole of 27.5 mm	1,092
LC-H27.5		140	Bolt hole of 27.5 mm	1,986

FIGURE 3
Tensile test results of steel angles.

2.3 Testing method

A compression machine was used to load the steel angle in compression, as illustrated in Figure 4. In the test setup, each end of the loaded leg was connected to a hinge using three Grade R8.8 high-strength steel bolts. In practice, the steel angle is subjected to an eccentric compressive load. Thus, a unidirectional knife-edge support was used for the hinge to ensure that the steel angle would bend about its weak axis in compression. A 50-tonne load cell was installed between the end plate and the support. In the testing process, the top of the testing machine remained fixed, while the bottom support moved upwards to apply the vertical load.

During loading, the compressive load was measured using the load cell. Two linear variable differential transducers (LVDTs) were installed at the bottom of the testing device to measure the vertical displacement of the steel angle. Additionally, two more LVDTs were erected in the middle of specimens to measure its lateral deformation perpendicular to the two legs. To further analyse the strain development across different sections of the steel angle under vertical loads, strain gauges with a gauge length of 5 mm were attached on the face at the mid-height and ends of the steel angle. These strain gauges could measure the variation of strain when buckling occurred during testing.

According to the DL/T 5486-2020 (Management Committee for National Standards, 2020b), a vertical load was applied at a loading rate of 2 kN/s up to 80% of the calculated theoretical ultimate load. When the applied load exceeded 80% of the theoretical ultimate load, the loading rate was adjusted to 1 kN/s. The loading was stopped when the load decreased to 70% of the peak value after the failure of specimens.

3 Discussions on test results

3.1 Load-deflection relationship of steel angles

Figure 5 plots the typical load-in-plane deflection curve for steel angle without local defects (Huang et al., 2024). The measured deflection represents that of steel angles about the minor axis.
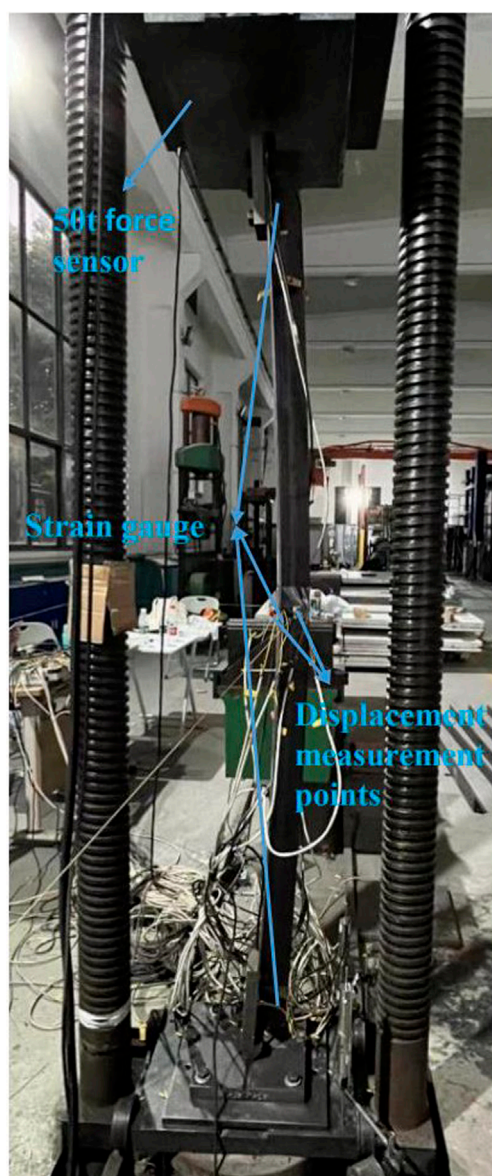
It can be observed from Figure 5A that when the load was less than 120 kN, the curves of SCN-2 and SCN-3 were almost the same, without any lateral deflections measured. However, the curve of SCN-1 differed from the other two. As the load increased to 120 kN, the deflection of SCN-1 continued to increase linearly with the applied load. The differences in the curves during the initial loading phase might originate from different initial geometric imperfections of the steel angles in the same group. SCN-2 and SCN-3 had smaller geometric imperfections, resulting in a slower increase in the in-plane deflection upon loading. In contrast, SCN-1 had larger initial geometric imperfections, leading to the rapidly increasing deflection during the initial loading phase. As the load approached the peak value, the load-deflection curve became flatter, with the rapid increasing in the deflection. It should be noted

that SCN-1 developed the same load capacity with SCN-2 and SCN-3. As the length of steel angles increased, the associated compression capacity reduced significantly, but the overall trend of the load-deflection curves remained consistent, as shown in Figure 5B.
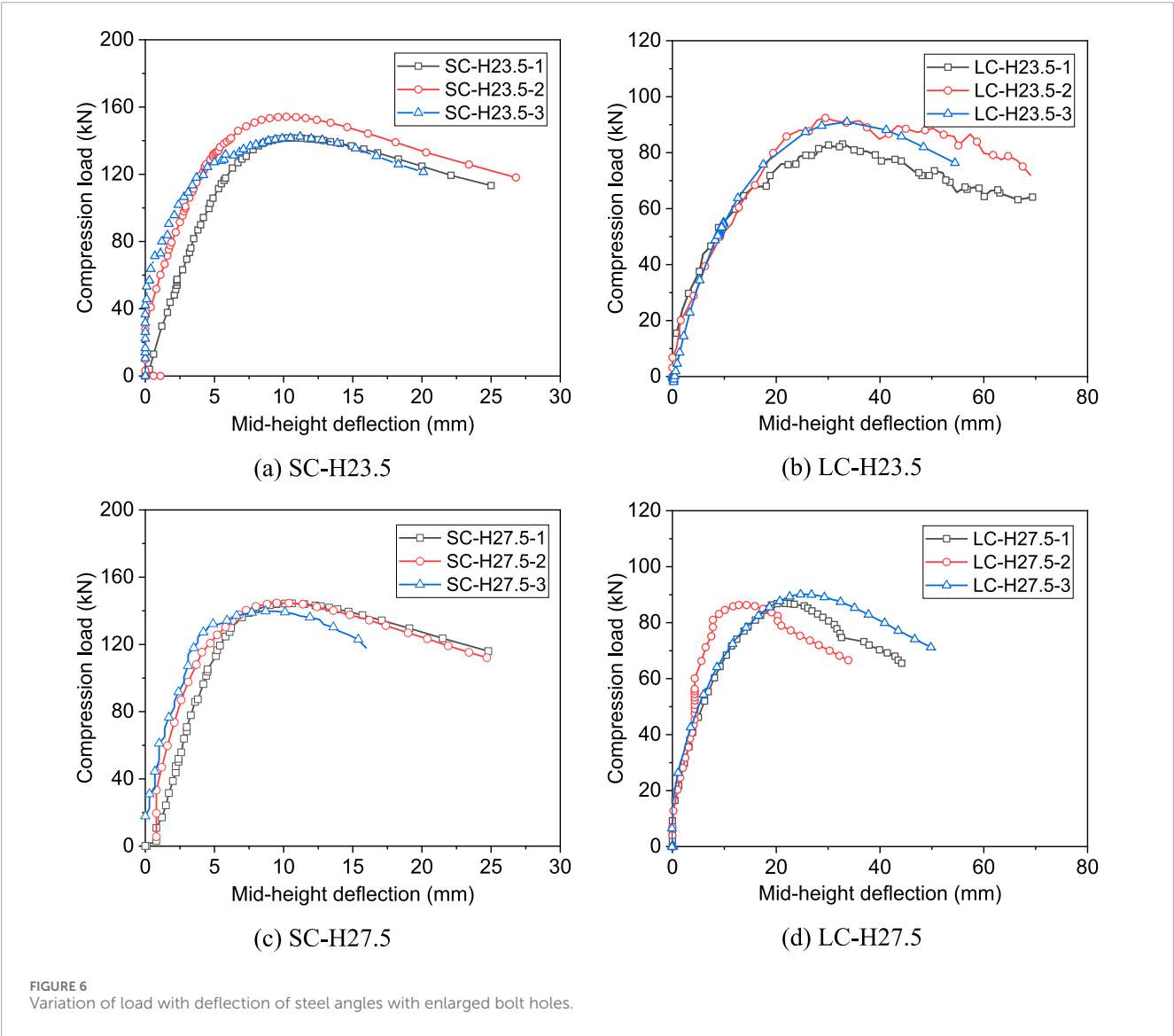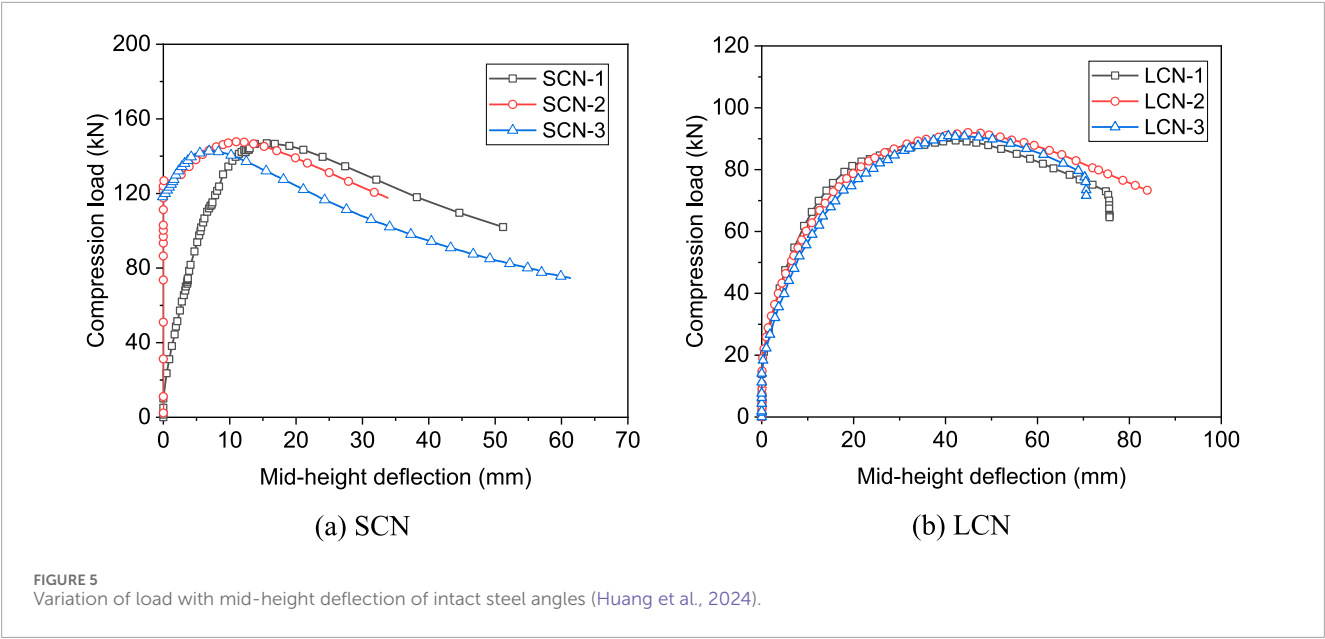
Figure 6 shows the curves of steel angles with enlarged bolt holes. The curves in general were similar to those without local defects. The compression capacity decreased with increasing bolt holes. However, the reduction of the compression capacity was insignificant when the diameter of the bolt hole was increased from 21.5 mm to 27.5 mm. It can also be observed from the figure that the deflection associated with the compression capacity decreased with the increasing diameter of the bolt hole.

3.2 Failure modes of steel angles

Figure 7 illustrates the typical failure modes of steel angles under compression. In the initial phase of loading, the steel angle underwent deflection about its weak axis, which rapidly increased after the attainment of the peak load and was accompanied by torsion. As a result of the similarity in the failure mode of specimens, only those of SC-H27.5 and LC-H27.5 are displayed in the figure. The final modes of failure of specimens were global buckling, displaying a clear sinusoidal half-wave form along the longitudinal axis. Besides, noticeable torsional deformations were observed for both long and short steel angles. Therefore, the actual failure mode observed in the tests was combined flexural and torsional buckling.

3.3 Load-strain curves

Figures 8, 9 present the typical load-strain curves of steel angles in compression. To clearly show the variation of strains at the end and middle of steel angles, curves from two specimens SC-H27.5 and LC-H27.5 were analysed in the study. Figure 8A shows the load-strain curve of the steel angle SC-H27.5. The strains at positions T-3, T-4, and T-5 near the loading leg developed compressive values, while positions T-1 and T-2 on the unloaded leg showed tensile strains. Notably, the strain at position T-4 exceeded that at positions T-3 and T-5 with increasing compression, and the strain at position T-3 started decreasing, suggesting that the specimen might have experienced twisting at the end. At the attainment of the load capacity, the strains at positions T-3 and T-4 were significantly greater than the yield strain measured in the coupon test. Figure 8B plots the load-strain curve at the mid-height of SC-H27.5. It is visible that strains at M-3 and M-4 remained compressive during the whole loading phase and gradually increased. Particularly, at positions M-5 and M-6, the strain varied from compressive to tensile after the steel angle reached its ultimate load. Meanwhile, positions M-1 and M-2 at the unloaded leg consistently generated tensile strains, with M-1 almost the same as M-2. This observation suggested that noticeable twisting also occurred at the end of the steel angle during compression. The peak strains exceeded the yield stress measured
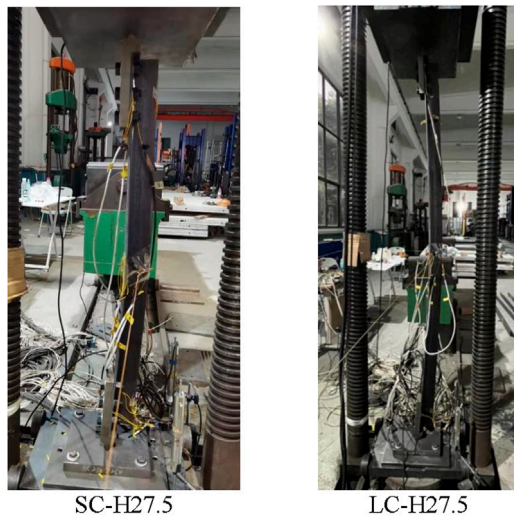
FIGURE 5
Variation of load with mid-height deflection of intact steel angles (Huang et al., 2024).

FIGURE 6
Variation of load with deflection of steel angles with enlarged bolt holes.

FIGURE 7
Typical modes of failure of specimens in compression.

in the coupon test, indicating that inelastic buckling occurred for specimens.

Figure 9A provides a detailed view of the load-strain curves at the top end of steel angle LC-H27.5 with defect at the bolt hole. Similar to the undamaged specimen LC-H23.5, positions T-1 and T-2 on LC-H27.5 consistently exhibited tensile strains throughout the compression process, while positions T-3 to T-5 developed compressive strains. However, compared to LC-H23.5, the compressive strains of LC-H27.5 at T-3 and T-5 showed a clear decreasing trend after the specimen reached the compression capacity, and the peak value of compressive strains at these points were also significantly lower than those at T-4. This phenomenon indicated that twisting occurred at the upper end of the steel angle. Figure 9B displays the strain development in the middle of LC-H27.5. There were no significant differences between the strains at positions M-1 and M-2 in the middle of LC-H27.5, suggesting that no significant torsional deformations occurred in the middle. This observation indicated that even though LC-H27.5 showed twisting at the top end, it did not significantly affect the strain measured in the middle.

3.4 Discussions on test results

Figure 10 shows the influence of bolt hole diameters on the compression capacity of steel angles under compression. Experimental results indicated that, despite an increase in the bolt hole diameter, the change in the load capacity was minimal, typically within 3%, for specimens with the same slenderness. However, the increase in the bolt hole diameter might change the strain variation in the middle. When the diameter of the bolt hole increased, the strain measured in the middle did not indicate significant torsional deformations, as the steel section at the end was significantly

reduced which eventually led to localised torsional deformation at the end.

4 Finite element simulations of steel angles in compression

4.1 Development of finite element models

To study the influence of defect at the bolt hole on the compressive behaviour of steel angles, numerical models were developed using finite element software ABAQUS. In the model, bolts, steel angle, connection plates, and end plates were all modelled using C3D8R (eight-node linear hexahedral, reduced integration elements) solid elements, as shown in Figure 11. To optimize computational efficiency while ensuring the accuracy of the numerical model, a mesh sensitivity analysis was conducted to investigate the influence of mesh size on the compressive behaviour of steel angles. Preliminary results showed that when the mesh sizes in longitudinal, width and thickness directions were determined to be 10, 5 and 2 mm, respectively, the influence of mesh size on the ultimate load could be neglected. Therefore, the mesh size was set to 10 mm × 5 mm×2 mm. Additionally, global and local seeds were appropriately placed within the model to optimize the distribution of the mesh.

In this study, a point-to-surface restraint was defined to couple the loading end plate with the reference point RP1. Considering the experimental conditions of the steel angle and the use of a hinge connection at the edge of the connection plate, the boundary conditions for reference point RP-1 were set to U1 = U2 = U3 = 0 and UR2 = UR3 = 0. As the bottom end plate was fixed, its restraints were set to U1 = U2 = U3 = UR1 = UR2 = UR3 = 0. Moreover, seven types of surface-to-surface contact interactions were defined between the steel angle, connection plates, bolts, and end plates in the model. A bolt preload was applied by defining the bolt load; then, the bolt load was adjusted to keep the present length constant, and the boundary conditions for reference point RP1 were reset. A Load was applied along the longitudinal axis through a displacement-control method.

4.2 Mechanical properties of steel

In this numerical model, the material properties of the steel, such as elastic modulus, yield strength, and ultimate strength, were determined based on the results of tensile tests on steel coupons. A Poisson's ratio of 0.3 was used, and the mechanical properties were averaged across three test specimens. The stress-strain curve obtained from the experiments showed a distinct yield plateau, and thus the model employed an elastic-plastic model that incorporates the yield plateau and hardening stage, as depicted in the Figure 12 (Huang et al., 2024). The model also assumed that the materials of the connection plates, end plates, and bolts remain elastic. Their elastic properties were consistent with those of the steel angle.
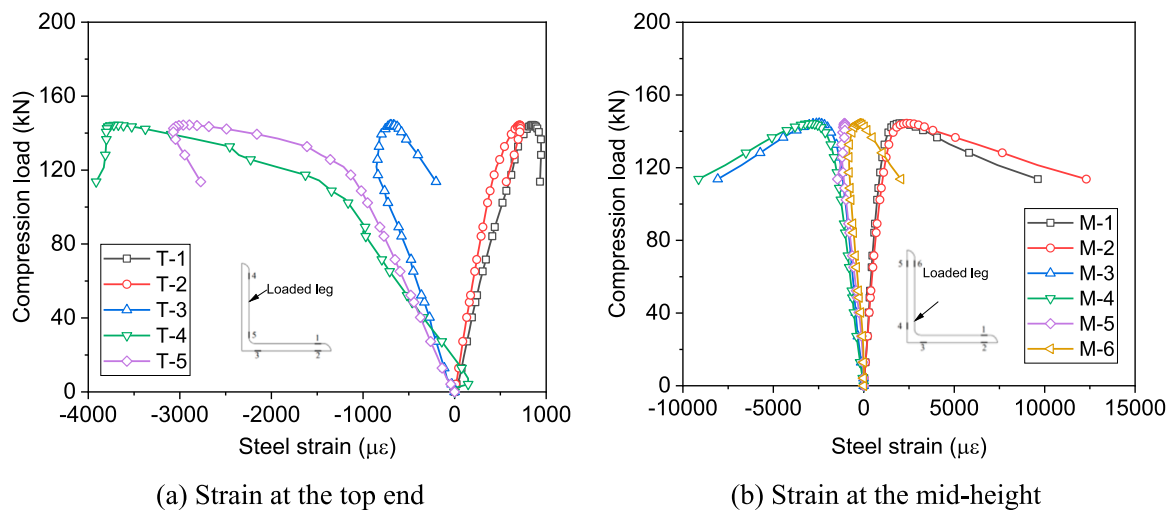
FIGURE 8
Variation of steel strain with compression for angle SC-H27.5.
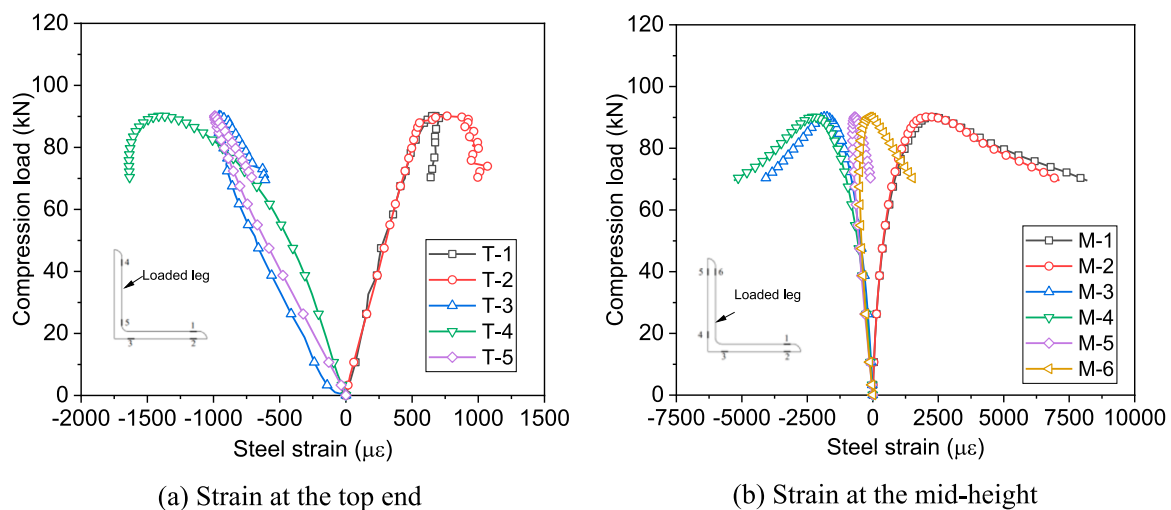

FIGURE 9
Variation of steel strain with compression for angle LC-H27.5.

The residual stress in the steel angle was not measured before testing, but the simplified distribution proposed by Wang (Wang, 1981a; Wang, 1981b) was defined in the finite element model. Note that even though the residual stress may be affected by mechanical cutting, it was not considered in the numerical model due to the lack of test data. Residual stresses were applied longitudinally to the steel angle model through a prestress field. Based on the recommendation of GB50017-2017 (Management Committee for National Standards, 2020a), the initial bending of the steel angle in the model was set at 1/1,000 of its length to simulate the geometric imperfection.

4.3 Validation of finite element models

In this study, finite element analyses were conducted for all specimens in compression, and typical specimens, including SC-23.5, LC-23.5, SC-H27.5 and LC-27.5, were selected to analyse and compare the load-deflection curves obtained from experiments and numerical simulations. In general, the trends obtained in the numerical simulations closely match the curves obtained from the experimental tests, as shown in Figure 13. During the initial loading phase, the numerical simulation shows a rapid increase in the deflection of the steel angle. When the steel angle is close to buckling, the experimental and simulation curves match well.
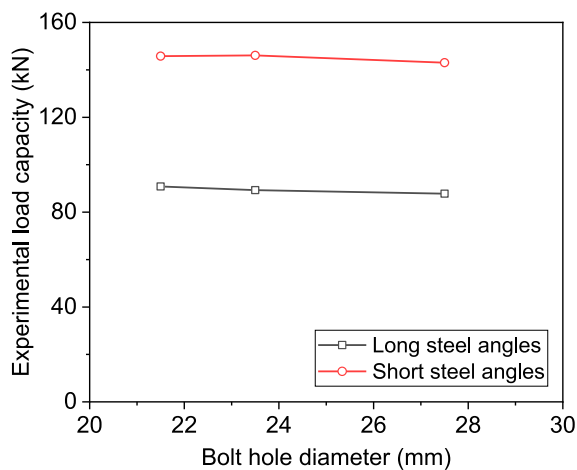
FIGURE 10
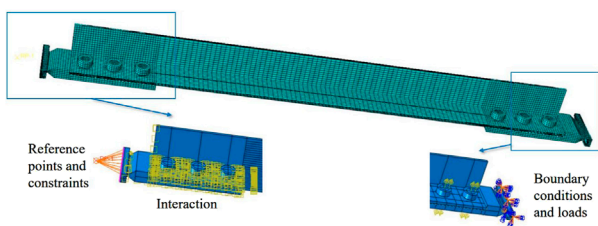Effect of bolt hole diameters on compression capacity of long and short steel angles.

FIGURE 11
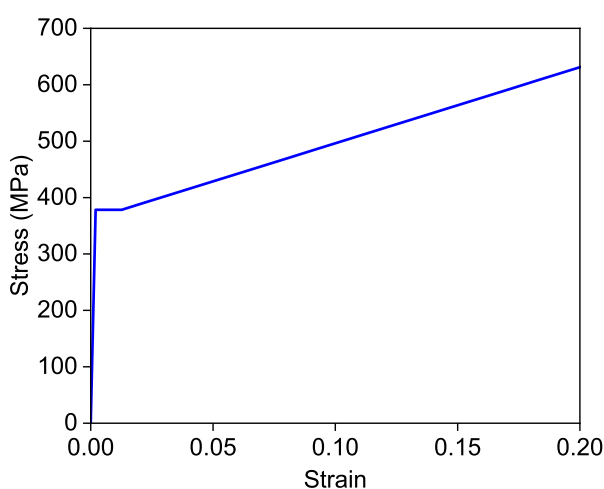Numerical models for steel angles in compression.

FIGURE 12
Stress-strain model for steel angles in the finite element model.

The difference between the experimental and numerical curves may be due to that the initial bending of the steel angle in the experiments was not 1/1,000 of the angle length as assumed in the model.

In addition to the load-deflection curve, the peak loads obtained from numerical simulations and experimental tests were also compared, as shown in the Table 2. The average numerical to experimental load ratio is 0.92, with a coefficient of variation of 3.6%, indicating that the numerical model can accurately calculate the ultimate load of the specimens. For instance, the experimental value of SCN was 145.8 kN, while the simulated value is 140.9 kN, 3.4% less than the experimental value. This shows that the numerical value is generally lower than the experimental value. The underestimation of the load capacity might result from the neglecting of the friction between the hinge and the end plate and the assumed residual stress and initial bending in the numerical model.

Figure 14 shows the deflection and stress distribution in the numerical simulation when the steel angle reaches yielding and compare with the failure modes observed in the experimental tests. It can be observed that the simulation and experimental results exhibit good agreement in terms of the failure mode, displaying combined bending and torsional buckling. The maximum stress in SC-H27.5 is primarily concentrated at the middle of the unloaded leg, with a value of 459.8 MPa. However, when the slenderness is increased to 140, the maximum stress occurs at the end of the steel angle, with a value of 537.5 MPa. The increase in the stress at the end is mainly induced by the increased diameter of bolt holes and the associated reduced net section area of the steel angle.

5 Parametric study

In accordance with the verified finite element model, a parametric study was performed to study the effects of slenderness on the compression capacity of specimens with different diameters of bolt holes, as shown in Figure 15. In the parametric study, three different bolt hole diameters, namely, 21.5, 23.5 and 27.5 mm, are determined based on the experimental result. Steel angles with various slendernesses, namely, 80, 100, 120, and 140, are selected to investigate the combined effect of bolt hole diameter and slenderness. It can be observed that the ultimate load of steel angles with the same diameter of bolt holes decreases with the increasing slenderness. For example, when the bolt hole diameter is 23.5 mm, the load capacity of the steel angle with a slenderness of 80 is 136.9 kN, but the value decreases by 40.5%–81.5 kN when the slenderness increases to 140. The figure also shows the influences of the diameter of bolt holes on the compression capacity of specimens. It is apparent the diameter of bolt holes on the compression capacity is significant if the bolt hole diameter is 27.5 mm and the slenderness of specimens does not exceed 100. Otherwise, the reduction in the ultimate load induced by the bolt hole is less than 4% as compared with the undamaged steel angle. Thus, numerical results imply that under certain conditions, the influence of the bolt hole diameter on the load capacity of steel angles can be neglected, even though the presence of the bolt hole can reduce the restraint stiffness provided by the end plate and lead to localised twisting at the end.

FIGURE 13
Comparisons of numerical load–deflection curves with experimental results.
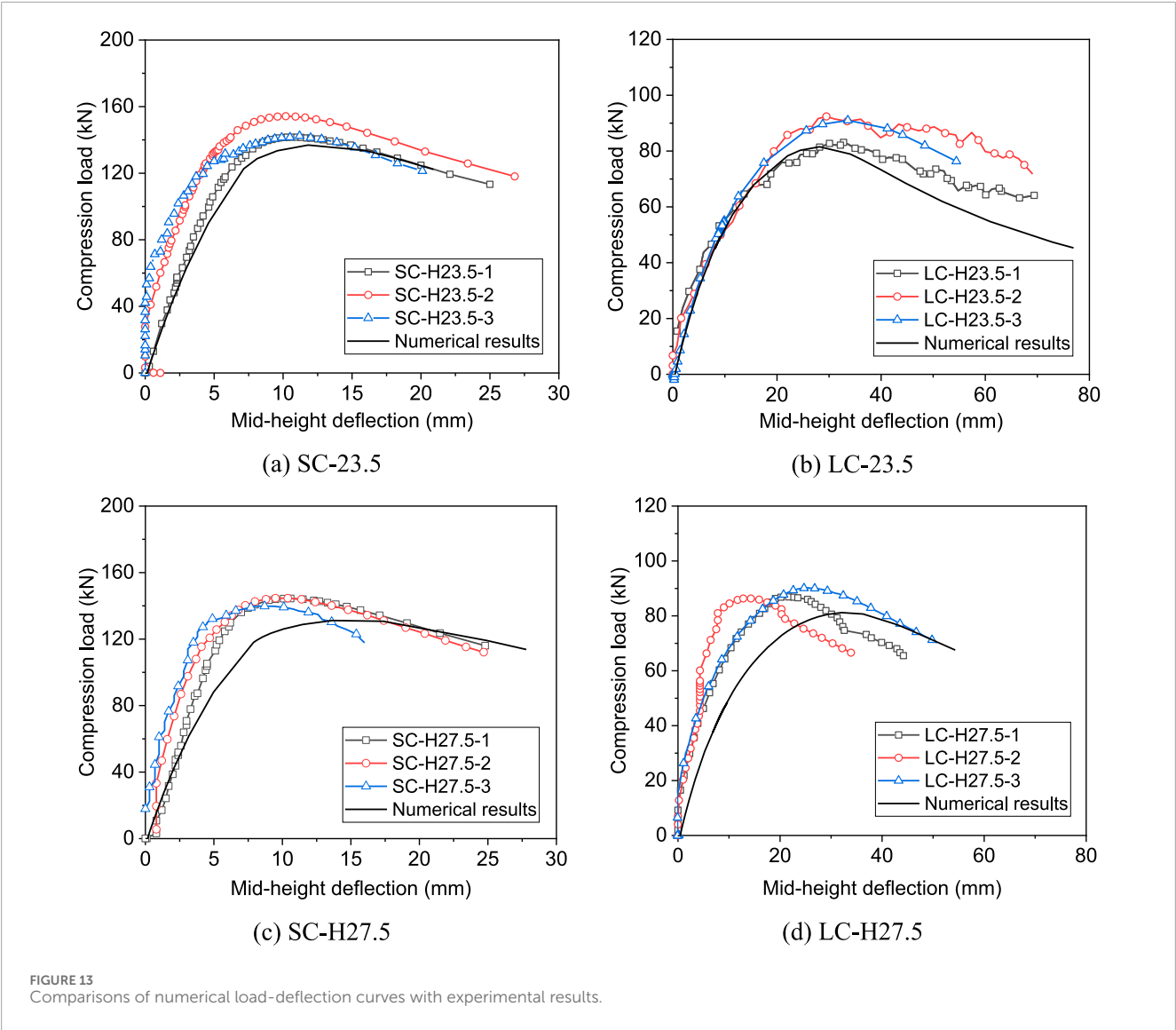
TABLE 2 Comparison of numerical ultimate loads with experimental values.

Specimens	Experimental ultimate load P_E (kN)	Numerical load ultimate load P_N (kN)	$\frac{P_N}{P_E}$
SCN	145.8	140.9	0.97
LCN	90.8	81.3	0.90
SC-H23.5	146.1	136.9	0.94
SC-H27.5	143.0	131.2	0.92
LC-H23.5	89.3	81.5	0.91
LC-H27.5	87.8	81.2	0.92
Mean ratio			0.92
Coefficient of variation			3.6%
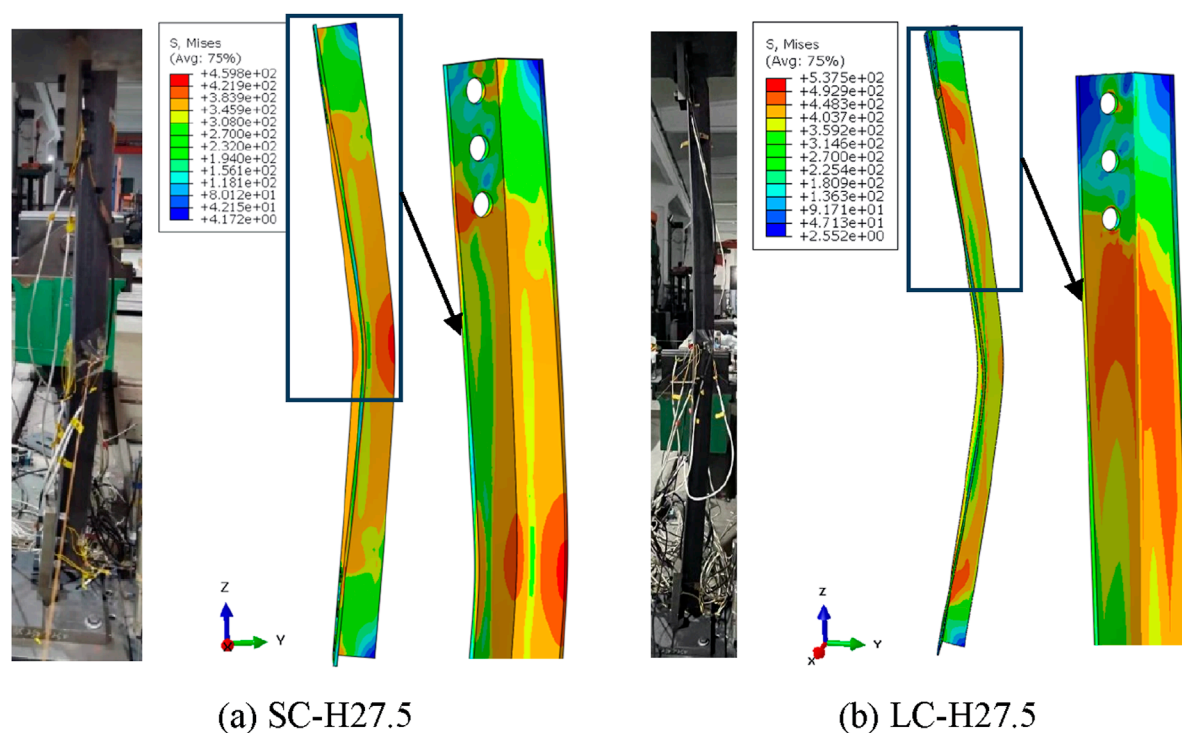
FIGURE 14
Comparisons of numerical and experimental failure modes of specimens.
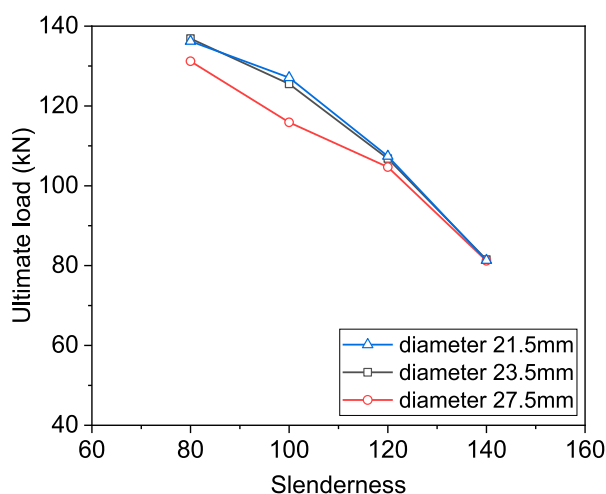
FIGURE 15
Influence of bolt hole diameters and slenderness on the compression capacity of specimens.

6 Conclusion

This paper presents experimental and finite element studies on the global buckling behaviour of steel angles with defect at the bolt hole and subjected to compression. The compression capacity and global buckling failure of steel angles were examined through compression tests and numerical modelling. The influences of the slenderness and bolt hole diameter on the buckling load of specimens were also analysed in the parametric study. The following conclusions can be found as follows.

(1) When the diameter of the bolt hole was increased from 21.5 to 27.5 mm, the compression capacity of specimens with a slenderness of 80 was slightly reduced by 3.0%, whereas that with a slenderness of 120 remained almost unchanged. The effects of the diameter of bolt holes were insignificant for steel angles with a slenderness greater than 120 and can be neglected in design.

(2) Steel angles developed combined bending and twisting failure when they were loaded in compression on one leg. The presence of bolt holes led to localised twisting of steel angles near the end, but the twisting effect in the middle became insignificant.

(3) Parametric analysis through the numerical model indicates that as the slenderness ratio increases, the load-bearing capacity of steel angles with different diameters of bolt holes decreases, but the effect is only significant when the diameter of bolt holes is 27.5 mm and the slenderness is not greater than 100. Thus, when the slenderness of steel angles is less than 100, the effect of enlarged bolt holes on the compression capacity of steel angles should be reduced in design.

It should also be pointed out that the present study only focuses on the effect of corrosion at the bolt hole. In fact, corrosion may occur at the bolt hole and the connection at the same time. In that case, the conclusion of the present study is not applicable, and further experimental tests or numerical simulations are necessary to evaluate the influence of corrosion at the connection.

Data availability statement

The raw data supporting the conclusions of this article will be made available by the authors, without undue reservation.

Author contributions

JZ: Formal Analysis, Investigation, Writing–original draft. AH: Methodology, Writing–review and editing. YL: Funding acquisition, Supervision, Writing–review and editing. S-BK: Supervision, Writing–review and editing.

Conflict of interest

The authors declare that the research was conducted in the absence of any commercial or financial relationships that could be construed as a potential conflict of interest.

Publisher's note

All claims expressed in this article are solely those of the authors and do not necessarily represent those of their affiliated organizations, or those of the publisher, the editors and the reviewers. Any product that may be evaluated in this article, or claim that may be made by its manufacturer, is not guaranteed or endorsed by the publisher.

References

Adluri, S. M. R., and Madugula, M. K. S. (1996). Flexural buckling of steel angles: experimental investigation. *J. Struct. Eng.* 122 (3), 309–317. doi:10.1061/(asce)0733-9445(1996)122:3(309)

Bathon, L., Mueller, W. H., and Kempner, L. (1993). Ultimate load capacity of single steel angles. *J. Struct. Eng.* 119 (1), 279–300. doi:10.1061/(asce)0733-9445(1993)119:1(279)

Beaulieu, L. V., Legeron, F., and Langlois, S. (2010). Compression strength of corroded steel angle members. *J. Constr. Steel Res.* 66 (11), 1366–1373. doi:10.1016/j.jcsr.2010.05.006

Cao, S. S., Zhang, D. C., and Gao, Z. P. (2017). Experiemental and analytical research on axial bearing capacity of single steel angles. *J. NANJING TECH Univ. Nat. Sci. Ed.* 39 (03), 108–113.

Chen, S. F. (2012). Elastic and inelastic stability capacity of single angle under axial compression. *J. Build. Struct.* 33 (10), 134–141.

Gao, C., Liu, J., Zheng, Y., Wu, B., and Chu, Z. (2020). Effect of corrosion on mechanical properties of transmission tower angle steel. *Corros. and Prot.* 41 (8), 32–38.

Huang, X., He, S.-Y., Liu, X.-Y., Han, D.-G., Pu, F., Yan, H.-Q., et al. (2024). Compression behaviour of Q355 steel equal-leg angles with simulated local defects at the mid-height. *J. Constr. Steel Res.* 217, 108673. doi:10.1016/j.jcsr.2024.108673

Huang, Y., Su, Z. G., Zhu, B. R., Chen, Y. X., Wan, T., and Tuo, Z. X. (2023). The influence of corrosion on the bearing capacity characteristics of overhead transmission line tower. *Nonferrous Metals Sci. Eng.*, 1–11.

Liu, H. Y., Li, Z. L., and Huang, Z. L. (2021). A study on the bearing capacity of angle steel members in transmission towers. *Prog. Steel Build. Struct.* 23 (12), 47–55.

Management Committee for National Standards, Metallic materials-Tensile testing Part 1: method of test at room temperature,GB/T 228.1-2010, Beijing, 2010.

Management Committee for National Standards, Standard for design of steel structures, GB50017-2017, Beijing, 2020a.

Management Committee for National Standards (2020b). *Technical specification for the design of steel supporting structures of overhead transmission line.* Beijing. DL/T5486-2020.

Oszvald, K., Tomka, P., and Dunai, L. (2016). The remaining load-bearing capacity of corroded steel angle compression members. *J. Constr. Steel Res.* 120, 188–198. doi:10.1016/j.jcsr.2016.01.003

Shi, G., Liu, Z., Zhang, Y., Shi, Y. J., and Wang, Y. Q. (2011). Study on the local buckling behavior of steel equal angle members under axial compression with the steel strength variation. *Adv. Mater. Res.* 374-377, 2430–2436. doi:10.4028/www.scientific.net/amr.374-377.2430

Wakabayashi, M., and Nonaka, T. J. B. o.t.D. P. R. I. (1965) *On the buckling strength of angles in transmission towers*, 15, 1–18.

Wang, G. Z. (1981a). The influence of residual stress on the bearing capacity of steel tie rods: overview and theoretical analysis(1). *Metall. Constr.* 8, 15–19.

Wang, G. Z. (1981b). The influence of residual stress on the bearing capacity of steel tie rods: overview and theoretical analysis(2). *Metall. Constr.* 9, 31–36.

Wang, X. (2021). *Study on the bearing performance of Q420 equal angle steel subjected to local corrosion*. Wuhan, Hubei: Wuhan University.

Ye, J. H., Shen, H. Q., and Xue, S. D. (2016). Simplified analytical method of mechanical property degradation for steel members with pitting corrosion. *J. Harbin Inst. Technol.* 48 (12), 70–75.

Zhang, C. T., Fan, W. L., and Li, Z. L. (2014). Quasi-static test of Q345 equal-angles in corrosion environment. *Eng. Mech.* 31 (11), 53–62.

Study on increasing load capacity of wooden arch bridge by CFRP strengthening: experimental and numerical Verification

Liping Li[1], Yan Wang[2]*, Yafei Zhang[3]*, Xu Wang[4], Guangyao Ji[1] and Xuping Li[1]

[1]Department of Civil Engineering, Faculty of Engineering, Lishui University, Lishui, China, [2]Lishui Science and Technology Innovation Service Center, Lishui, China, [3]School of Civil Engineering, Tianjin University, Tianjin, China, [4]China Academy of Building Research, Beijing Glory PKPM Technology Company Limited, Beijing, China

The wooden arch corridor bridge is a typical representative of Chinese wooden bridges, holding significant historical research value. Currently, these bridges face issues of severe component deformation and insufficient load-bearing capacity. To address these problems, this study employs CFRP reinforcement on the components of wooden arch corridor bridges to reduce deformation and enhance load-bearing capacity. Experimental research on CFRP reinforcement has yielded the elastic modulus of the bonding interface. Given the lack of an accurate numerical model for wooden arch corridor bridges, this study establishes a precise numerical model by setting parameters based on load test data from wooden arch corridor bridges. The elastic modulus obtained from the experiments is input into the numerical model for analysis. The results indicate that CFRP exhibits excellent reinforcement performance, with the load-bearing capacity of the reinforced damaged components still reaching 75%−85% of their original capacity, while the load-bearing capacity of the reinforced undamaged components increases to 130%−140% of their original capacity. The failure modes of the CFRP-reinforced wooden components suggest that allowing for some gaps in the bonding of CFRP can enhance overall ductility. The application of CFRP to wooden arch corridor bridges also demonstrates favorable reinforcement effects, increasing the load-bearing capacity of the arch surface by approximately 20%, thereby providing a theoretical basis for the reinforcement of wooden arch bridge frameworks.

KEYWORDS

CFRP, wooden arch bridge, elastic modulus of bonding interface, experimental study, reinforce

1 Introduction

The wooden arch bridge is a quintessential example of timber bridges, characterized by its interlocking mortise and tenon woven arch structure. This structure primarily consists of the "Sanjiao Miao" (three-section sprout), "Wujiao Miao" (five-section sprout), and "Niu Tou" (ox head). The main load-bearing capacity is found in the "Sanjiao Miao," which combines the side sprouts of the three or five-section sprouts with the central flat

sprout. Currently, wooden arch bridges can be classified into two styles: "Sanjiao Miao" and "Sanjiao" or "Wujiao Miao." For instance, the "Sanjiao Miao" style is exemplified by Puji Bridge, located in Fucun Natural Village, Hejin Prefecture, Xiandu Township, Liandu District. This bridge was constructed in the 17th year of the Republic of China (1928 AD) and has a total length of 22.1 m, a width of 3.2 m, a clear span of 13.7 m, and a height of 5.00 m. In contrast, the "Wujiao Miao" style is represented by Long Bridge, situated in Yueshan Village, Jushui Township, Qingyuan County, Zhejiang Province. Constructed in the fifth year of Ming Rixing (1625 AD), it features a total length of 28.2 m, an arch span of 14.1 m, a clear span of 19.5 m, and a width of 6 m. Both Puji Bridge and Long Bridge fully preserve the architectural styles of "Sanjiao Miao" and "Sanjiao" or "Wujiao Miao" wooden arch bridges. They serve as important references for the study of ancient bridge history in China and possess significant historical, artistic, and scientific value.

The existing wooden arch bridges have a long history and are often classified as national treasures due to their cultural significance. Overall, these bridges are well-preserved; however, some local components have experienced a noticeable reduction in load-bearing capacity, attributed to various material choices made during construction or surface corrosion caused by moisture. Furthermore, increased bridge loads during the flood season, aimed at preventing scouring and accommodating the high volume of tourists during peak seasons, can lead to significant deformation of components or insufficient load-bearing capacity, resulting in the bridge tilting to one side. Therefore, reinforcing the original components of the wooden arch bridge *in situ* to maintain its original appearance is of great importance.

From Figures 1, 2, it is evident that the main load-bearing points of the components of the wooden arch bridge are in the middle section of the central components. The existing wooden arch bridge components, mostly the central components, suffer from insufficient load-bearing capacity. Currently, there is no satisfactory solution for reinforcing the central components of the wooden arch bridge. Typically, the central components are either completely replaced after being dismantled from the frame or partially removed and connected to the pier platform, followed by reinforcement using nails, steel plates, and rivets. This approach is costly and demands high construction technology requirements. Additionally, nails and steel plates are used to strengthen the mortise and tenon connections. Many studies have shown that this method can enhance their load-bearing capacity to some extent (Jin et al., 2022; Wang et al., 2021; Guo et al., 2020; Zhou et al., 2016; Xue et al., 2015). However, it has a short aging time, is prone to corrosion and detachment, leading to a significant decline in reinforcement effectiveness.

Currently, there is an urgent need for a new reinforcement scheme for the central components of wooden arch bridges. Li et al. (2019) analyzed and prospected the restoration and reinforcement techniques of Chinese ancient wooden structures. They suggested that, based on inheriting and exploring traditional techniques, there should be active introduction of new materials and technologies to compensate for traditional deficiencies. There have been some studies on the application of CFRP in glued laminated timber beams. Klaudia et al. (2021) found that the failure mode of CFRP-reinforced glued laminated timber beams has changed. İşleyen et al. (2021) and Vahedian et al. (2019) demonstrated

FIGURE 1
Puji bridge.

FIGURE 2
Rulong bridge.

that CFRP applied to composite timber beams can improve their ultimate load-carrying capacity. Siha et al. (Zhou et al., 2020; A et al., 2021) investigated CFRP and near-surface reinforcement of circular wooden columns, showing improved axial load-carrying capacity and good deformation coordination for all three materials. Ghanbari Ghazijahani et al. (Tohid et al., 2020) enhanced the load-carrying capacity and ductility of CFRP-reinforced I-beams. Brol and Agnieszka (2019) and Bashandy et al. (2018) used various composite materials to reinforce aged wood, with CFRP showing the best reinforcement effect. CFRP reinforcement also has a good effect on defective or extended wooden beams (Rescalvo et al., 2018a; Rescalvo et al., 2018b; Zhang et al., 2018; Yuan et al., 2014; Zhu et al., 2005; Lin et al., 2016). Buell and Saadatmanesh (2005) applied composite materials in the form of fabric wrapping or laminates to enhance the load-bearing capacity of wooden bridges, and the results indicated that the carbon fiber fabric significantly improved the bending and shear strength of the wooden beams. Gentile et al. (2000) utilized CFRP for the reinforcement of wooden bridges, studying its bending capacity, and found that the bending strength increased by 18%–46%. Dagher and Lindyberg (2004) bonded FRP to the tension side of wooden bridges, repairing and upgrading existing wooden structures, and their results demonstrated good reinforcement performance. Qiu et al. (2021) applied three different CFRP reinforcement methods to laminated bamboo arches, and the experimental results indicated that the peak load can be increased by 26.54%.

TABLE 1 Physical and mechanical properties of timber-arched lounge bridge members.

Material name	Tensile strength along grain/ (MPa)	Compressive strength along grain/ (MPa)	Elastic modulus/ (MPa)
Lishui fir wood	80.12	36.95	13,020

CFRP demonstrates excellent reinforcement effectiveness in wooden structures, including both building structures and bridges. Currently, most research on CFRP reinforcement has focused on beam-column structures, with relatively little attention given to arched wooden bridges, particularly woven arch bridges like the wooden arch corridor bridge. The wooden components of the wooden arch corridor bridge not only resist bending and shear forces, but some of these components also bear compressive loads while simultaneously resisting bending. The main objectives of this study can be summarized as follows: Section 2 introduces the components of the wooden arch bridge and the preparation for the experiments, and provides theoretical derivation of the elastic modulus of the bonding interface between CFRP and the components. Section 3 presents the load tests on the main components of the wooden arch bridge, and obtains the elastic modulus of the bonding interface between CFRP and the components through experimental and theoretical analysis. Section 4 investigates the arches of the wooden arch bridge through experimental studies, conducts numerical modeling using SAP2000 for comparative analysis, and performs numerical simulations of CFRP-reinforced wooden arch bridge arches. Section 5 presents the conclusions drawn from the study.

2 Experimental study

2.1 Component selection and fabrication

The wood selected for this experiment is Shandong cedar from Lishui City, chosen to closely match practical conditions, as this type of wood is commonly used in the construction of wooden arch corridor bridges. The physical and mechanical properties determined by wood testing methods are shown in Table 1. Six middle-section seedlings were fabricated for the three-segment arch bridge, consisting of three unreinforced components and three reinforced components, each illustrated in Figure 3. Figure 4 presents the moisture content of the wooden components reinforced with CFRP and those that are unreinforced. The selected moisture content reflects the levels typically encountered in the environmental conditions to which the wood is exposed, simulating the performance of CFRP reinforcement under normal drying conditions.

The moisture content of the wooden arch bridge components was measured using the ZTW1601a wood moisture tester produced by Zhengtai Network Technology Co., Ltd. The CFRP used in the experiment was carbon fiber cloth produced by Shanghai Zhinuo

FIGURE 3
Timber-arched lounge bridge members.

Decoration Materials Co., Ltd., with a model specification of Grade I 58,788 (200 g); the adhesive was epoxy resin impregnated adhesive produced by Shanghai Zhino Decoration Materials Co., Ltd., with a model of ZN-700. It consists of two components, A and B, mixed in a ratio of A:B = 2:1. The mechanical properties of CFRP and adhesive were tested by the National Building Materials Testing Center on behalf of the company. The test results are shown in Table 2.

2.2 Loading scheme and measurement scheme

The experiments were performed using a 5000 kN hydraulic testing machine at the Structural Laboratory of Lishui University. The loading process entailed concentrated loading at two points on the beam, with preliminary loading of the specimen to mitigate local voids and minimize their impact on the test results. Subsequently, graded loading was applied until failure ensued.

During the experiment, measurements primarily encompassed the mid-span displacement of the wooden arch bridge components, strain at mid-span cross-sections, and strain at adjacent points of CFRP bonding termination. Observations and records of damage to the wooden arch bridge components during loading were also conducted. The arrangement of the loading device and measurement points is depicted in Figure 5.

2.3 Theoretical analysis of elastic modulus of bonding interface

The components of the wooden arch bridge were reinforced using carbon fiber cloth. This paper conducted theoretical analysis on the small range of the two end points, as shown in Figure 6 (unit: mm).

For the small cross-sectional analysis around adjacent measurement points, it is assumed that after CFRP reinforcement of the wooden arch bridge components, the strain between the adjacent measurement points exhibits linear variation, meaning that the shear stress at the bonding interface between adjacent measurement points remains constant. The shear stress within this range can be obtained through the equilibrium relationship between adjacent CFRP points,

(a) Moisture content of reinforced members   (b) moisture content of unreinforced members

FIGURE 4
Moisture content of components of timber-arched lounge bridge. **(A)** moisture content of reinforced members. **(B)** moisture content of unreinforced members.

TABLE 2 Performance indexes of CFRP and binder.

Material name	Tensile strength/(MPa)	Elastic modulus/(MPa)	Bond tensile strength/ (MPa)	Thickness/ (mm)	Poisson's ratio	Elongation/(%)
CFRP	3450	2.61×10^5	—	0.111	—	1.65
Binder	57	2690	42	—	0.25	2.66
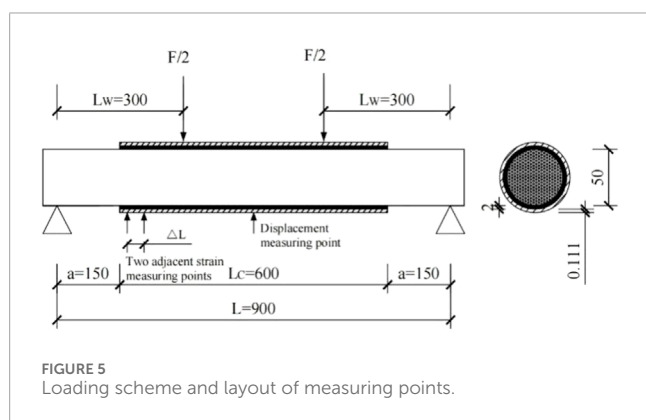
FIGURE 5
Loading scheme and layout of measuring points.

namely, the average bonding interface shear stress τ. Assuming the distance between the two points is ΔL, and the strains at the two measurement points are ε_1 and ε_2, respectively, the equilibrium relationship can be expressed as follows (Dai et al., 2015):

$$F_{N1} + F_{Nb} = F_{N2} \tag{1}$$

$$\begin{cases} F_{N1} = b_C \delta_C E_C \varepsilon_1 \\ F_{N2} = b_C \delta_C E_C \varepsilon_2 \\ F_{Nb} = b_C \triangle L \tau \end{cases} \tag{2}$$

Where F_{N1} and F_{N2} are the axial forces of adjacent measuring points respectively; F_{Nb} is the axial force of the bonding interface layer.

According to Equations 1, 2, order $\Delta\varepsilon = \varepsilon_2 - \varepsilon_1$, the average shear stress τ between the two measuring points of CFRP and wooden arch corridor bridge members in ΔL section is:

$$\tau = E_C \delta_C \triangle \varepsilon / \triangle L \tag{3}$$

Where E_C is the elastic modulus of CFRP; $\Delta\varepsilon$ is the strain difference of CFRP between two measuring points in ΔL section, that is, the relative strain between the two measuring points.

According to Equation 3, the shear stress of the bonding interface of the member under different loads can be calculated.

The components of wooden arch corridor bridge are strengthened with CFRP, and the micro elements of two adjacent measuring points dx are taken, then the shear strain γ of the bonding layer is:

$$\gamma = \frac{di(x,y)}{dy} + \frac{dj(x,y)}{dx} \tag{4}$$

where $i(x,y)$ and $j(x,y)$ are the horizontal and vertical displacement of the bonding layer respectively. According to Equation 3, the shear stress $\tau(x)$ at the bonding interface is:

$$\tau(x) = G_A \left[\frac{di(x,y)}{dy} + \frac{dj(x,y)}{dx} \right] \tag{5}$$

where G_A is the shear modulus of the bonding layer. It is assumed that the horizontal displacement of the bonding layer is linearly distributed along the vertical, that is:

$$\frac{di(x,y)}{dy} = \frac{1}{\delta_A} \left[i_C(x) - i_W(x) \right] \tag{6}$$
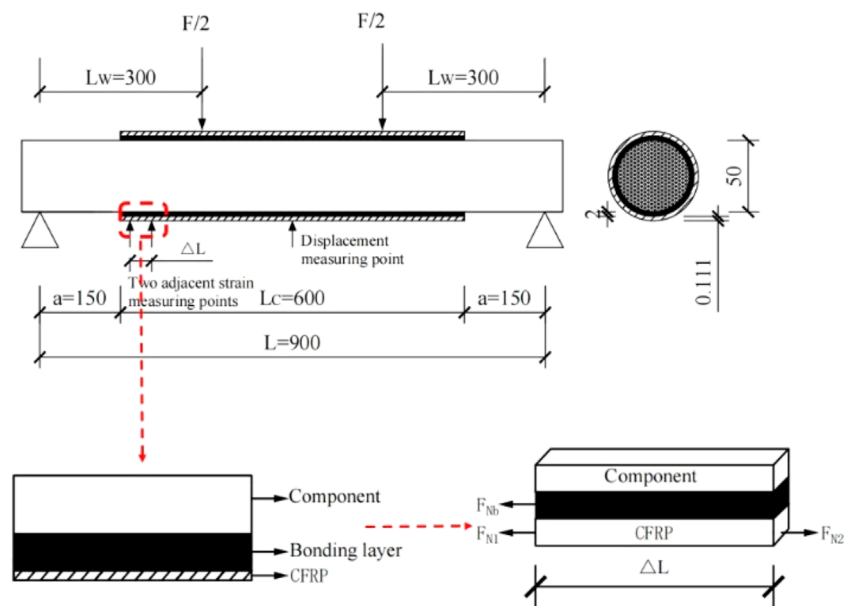
FIGURE 6
Mechanical analysis of CFRP wood bonding interface.

where $i_C(x)$ and $J_W(x)$ are the horizontal displacement of the outer surface and inner surface of the bonding layer respectively, that is, the horizontal displacement of the inner surface of CFRP and the outer surface of wood beam respectively; δ_A is the thickness of the tack coat. Substituting Equation 6 into Equation 5 and deriving, it obtains:

$$\frac{d\tau(x)}{dx} = G_A \left\{ \frac{1}{\delta_A} \left[\frac{di_C(x)}{dx} - \frac{di_W(x)}{dx} \right] + \frac{d^2 j(x,y)}{dx^2} \right\} \quad (7)$$

Since the influence of shear deformation is very small, the shear deformation of single member of wooden arch corridor bridge and CFRP is ignored, then:

$$\frac{di_C(x)}{dx} = \frac{F_{NC}(x)}{E_C A_C} - \frac{M_C(x)\delta_C}{2E_C I_C} \quad (8)$$

$$\frac{di_W(x)}{dx} = \frac{M_W(x)(d/2 + \delta_A + \delta_C)}{E_W I_W} - \frac{F_{NW}(x)}{E_W A_W} \quad (9)$$

where $F_{NC}(x)$ and $F_{NW}(x)$ are the axial forces of CFRP and wooden arch corridor bridge components respectively; $M_C(x)$ and $M_W(x)$ are the bending moments of CFRP and wooden arch corridor bridge members respectively; E_C and E_W are the elastic modulus of CFRP and timber-arched lounge bridge members respectively; A_C and A_W are the sectional areas of CFRP and wooden arch corridor bridge components respectively; I_C and I_W are the section moment of inertia of CFRP and timber-arched lounge bridge components respectively; δ_C and δ_A are the thickness of CFRP and bonding layer respectively, and δ is the diameter of the member.

Because the stiffness and shear capacity of CFRP are very small, the bending moment and shear force borne by CFRP are ignored, that is:

$$F_{SC}(x) = 0; \ F_{SW}(x) = F_S(x); \ M_C(x) = 0 \quad (10)$$

$$M_W(x) = M(x) - F_{NC}(x)(d/2 + \delta_A + \delta_C) \quad (11)$$

According to the relationship between curvature and bending moment in material mechanics:

$$\frac{d^2 j(x,y)}{dx^2} = -\frac{M(x)}{EI} \quad (12)$$

$$EI = E_C I_C + E_A I_A + E_W I_W \quad (13)$$

The equation for EI represents the total section bending stiffness, where E_C, E_A and E_W denote the elastic modulus of CFRP, the elastic modulus of the bonding layer, and the elastic modulus of the wooden arch corridor bridge components, respectively; I_A signifies the cross-sectional moment of inertia of the bonding layer. By substituting Equation 8–13 into Equation 7, we can obtain:

$$\frac{d\tau(x)}{dx} = \frac{G_A}{\delta_A} \left\{ \frac{F_{NW}(x)}{E_W A_W} - \left(\frac{d/2}{E_W I_W} + \frac{\delta_A}{EI} \right) M(x) \right.$$
$$\left. + \left[\frac{1}{E_C A_C} + \frac{(d/2 + \delta_A + \delta_C)d/2}{E_C I_C} \right] F_{NC}(x) \right\} \quad (14)$$

By deriving from both sides of Equation 14:

$$\frac{d^2\tau(x)}{dx^2} = \frac{G_A}{\delta_A} \left\{ \frac{1}{E_W A_W} \frac{dF_{NW}(x)}{dx} - \left(\frac{d/2}{E_W I_W} + \frac{\delta_A}{EI} \right) \frac{dM(x)}{dx} \right.$$
$$\left. + \left[\frac{1}{E_C A_C} + \frac{(d/2 + \delta_A + \delta_C)d/2}{E_C I_C} \right] \frac{dF_{NC}(x)}{dx} \right\} \quad (15)$$

Considering the balance of micro elements, it can be obtained that:

$$\frac{dF_{NC}(x)}{dx} = \frac{dF_{NW}(x)}{dx} = b_C \tau(x) \quad (16)$$

(a) Loading failure form of unreinforced members

(b) Loading failure form of members after reinforcement failure

FIGURE 7
Failure mode of member. **(A)** loading failure form of unreinforced members. **(B)** loading failure form of members after reinforcement failure.

(a)Failure forms of reinforced undamaged members

(b) Detailed failure forms of reinforced undamaged members

FIGURE 8
Failure mode of CFRP strengthened members. **(A)** failure forms of reinforced undamaged members. **(B)** detailed failure forms of reinforced undamaged members.

$$\frac{d^2\tau(x)}{dx^2} = \frac{G_A}{\delta_A} \left\{ -\left(\frac{d/2}{E_W I_W} + \frac{\delta_A}{EI} \right) \right.$$

$$F_S(x) + \left[\frac{1}{E_C A_C} + \frac{1}{E_W A_W} \right]$$

$$\left. b_C\tau(x) + \frac{(d/2 + \delta_A + \delta_C)d/2}{E_W I_W} b_C\tau(x) \right\} \qquad (17)$$

Order:

$$\lambda^2 = \frac{G_A b_C}{\delta_A} \left[\frac{1}{E_C A_C} + \frac{1}{E_W A_W} + \frac{(d/2 + \delta_A + \delta_C)d/2}{E_W A_W} \right] \qquad (18)$$

$$m_1 = \frac{G_A}{\delta_A \lambda^2} \left(\frac{d/2}{E_W I_W} + \frac{\delta_A}{EI} \right) \qquad (19)$$

According to Equations 15–19, can be obtained:

$$\frac{d^2\tau(x)}{dx^2} - \lambda\tau(x) + m_1\lambda^2 F_S(x) = 0 \qquad (20)$$

Equation 20 is the governing differential equation of shear stress at the bonding interface, and its solution is:

$$\tau(x) = C_1 e^{\lambda x} + C_2 e^{-\lambda x} + m_1 F_S(x) \qquad (21)$$

where C_1 and C_2 are coefficients, which can be obtained according to the two-point centralized loading, and the two-point centralized loading of wooden arch corridor bridge components as shown in Figure 6. In the shear span, $q(x) = 0$, $F_S(x) = F/2$; In the pure bending section, $q(x) = 0$, $F_S(x) = 0$. Substituting it into Equation 21, the interfacial shear stress is:

$$\tau(x) = \begin{cases} \tau_1(x) = C_1 e^{\lambda x} + C_2 e^{-\lambda x} + m_1 F/2, 0 \le x \le L_W - a \\ \tau_2(x) = C_3 e^{\lambda x} + C_4 e^{-\lambda x}, L_W - a \le x \le L_C/2 \end{cases} \qquad (22)$$

The boundary conditions are:$x = L_C/2$; $\tau(L_C/2) = 0$; $x = L_W$-a;

$$\tau_1(x)|_{x=L_W-a} = \tau_2(x)|_{x=L_W-a}; \left. \frac{d\tau_1(x)}{dx} \right|_{x=L_W-a} = \left. \frac{d\tau_2(x)}{dx} \right|_{x=L_W-a}$$

Order: $m_2 = \frac{G_A}{\delta_A} \left(\frac{d/2}{E_W I_W} + \frac{\delta_A}{EI} \right)$,

Obtain: $\left. \frac{d\tau_1(x)}{dx} \right|_{x=0} = -m_2 M(0)$

According to the boundary conditions:

$$C_1 = -\frac{m_1 F}{4\left(1 + e^{\lambda L_C}\right)} \left[e^{\lambda(L_C - L_W + a)} + e^{\lambda(L_W - a)} \right] - \frac{m_2 Fa}{2\lambda\left(1 + e^{\lambda L_C}\right)},$$
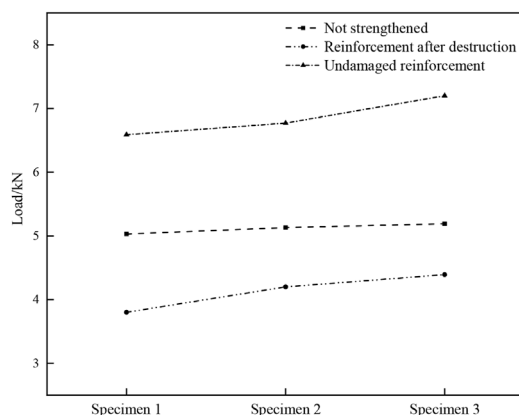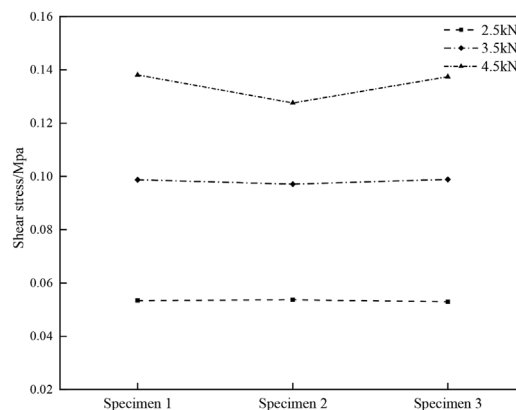
FIGURE 9
Ultimate load value of member.
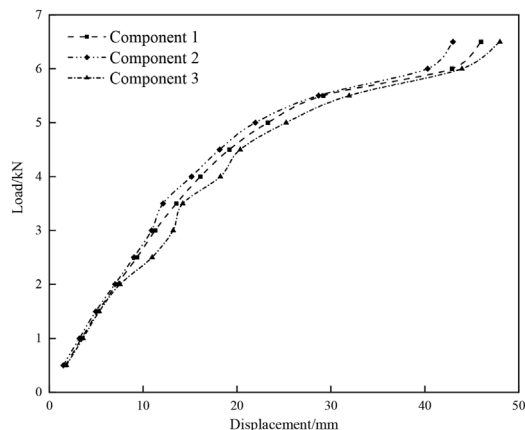

FIGURE 12
Shear stress at bonding interface.
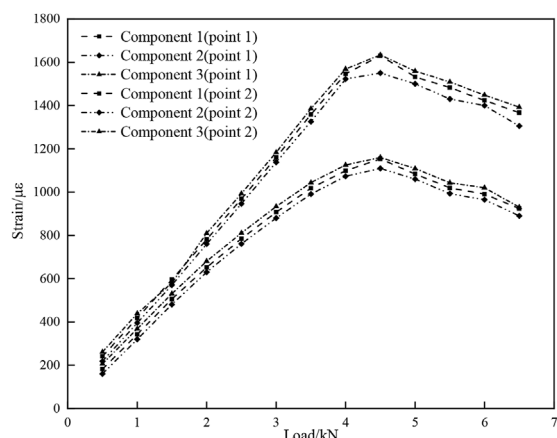

FIGURE 10
Load displacement curve.

FIGURE 11
Strain-load curve of two adjacent measuring points at the end.

$$C_2 = -\frac{m_2 Fa}{2\lambda\left(1+e^{\lambda L_C}\right)}e^{\lambda L_C} - \frac{m_1 F}{4\left(1+e^{\lambda L_C}\right)}\left[e^{\lambda(L_C-L_W+a)} + e^{\lambda(L_W-a)}\right],$$

$$C_3 = \frac{m_1 F}{4\left(1+e^{\lambda L_C}\right)}\left[e^{-\lambda(L_W-a)} - e^{\lambda(L_W-a)}\right] - \frac{m_2 Fa}{2\lambda\left(1+e^{\lambda L_C}\right)},$$

$$C_4 = \frac{m_2 Fa}{2\lambda\left(1+e^{\lambda L_C}\right)}e^{\lambda L_C} + \frac{m_1 F}{4\left(1+e^{\lambda L_C}\right)}\left[e^{\lambda(L_C+L_W-a)} - e^{\lambda(L_C-L_W+a)}\right]$$

Where a is the distance from the end of CFRP to the support; L_W is the distance from the action point of concentrated load to the support; L_C is the length of the CFRP.

3 Test results and analysis

When selecting components for the wooden arch corridor bridge, those without decay, nodes, or surface damage exhibit consistent test results. Hence, this paper analyzes the test outcomes of unreinforced component 1 and reinforced component 1. Figure 7A illustrates the failure mode of the member not strengthened with CFRP under load, while Figure 7B depicts the failure mode of the member reinforced with CFRP under load.

From Figure 7, it is evident that the failure mode of the wooden arch corridor bridge members under load is characteristic shear bending failure, with the members exhibiting longitudinal fiber fracture. The failure mode of the members after CFRP reinforcement is similar to that before reinforcement, as they are destroyed along the original section. During the test process, the members exhibit significant deflection under load before failure. However, after failure, the deflection produced by CFRP reinforcement under load is smaller than that of the former.

The failure form of undamaged members strengthened with CFRP under load is shown in Figure 8.

As observed in Figure 8, undamaged members of the wooden arch bridge, reinforced with CFRP, exhibit fracture in the middle under load. The upper part experiences shear failure, while the lower part undergoes tensile failure. Upon loading to a certain extent, a brittle crack sound of CFRP extrusion failure is audible, followed by the sound of wood cracking after continuous loading.
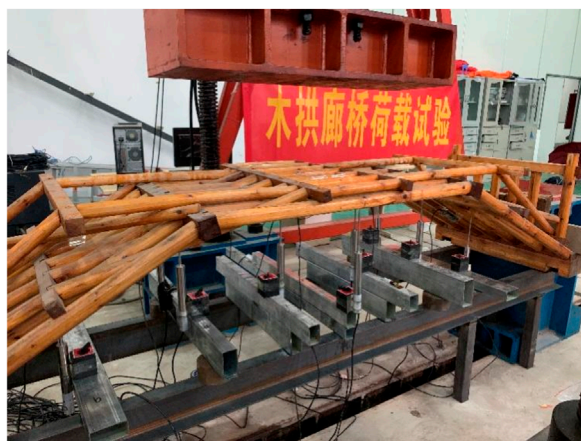
(a) Test diagram
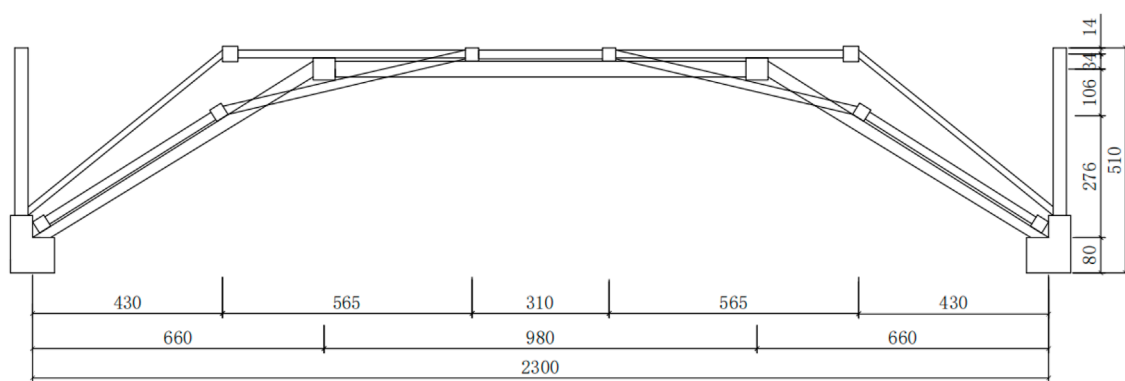
(b) Specimen size drawing

FIGURE 13
Load test of the wooden arch bridge arches. **(A)** test diagram. **(B)** specimen size drawing.
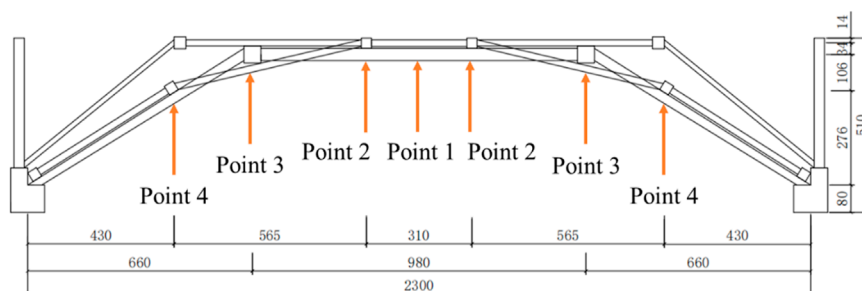
FIGURE 14
Load test measurement points of the wooden arch bridge arches.

From the comparison of Figures 7, 8, it can be observed that the CFRP-reinforced damaged wooden components exhibit different failure modes compared to the unreinforced wooden components. For the CFRP-reinforced damaged wooden components, the failure mode resembles that of the original wooden components, characterized by a distinct ductile failure, with minimal differences in ductility under loading when compared to the unreinforced wooden components. In contrast, the CFRP-reinforced undamaged wooden components display a failure mode similar to brittle fracture, indicating that the incorporation of CFRP reduces the ductility of the wooden components. The difference between these two failure modes lies in the presence of gaps in the CFRP-reinforced damaged components, which results in less secure wrapping of the CFRP and allows for some degree of deformation. For the undamaged wooden components reinforced with CFRP, there are essentially no gaps, and since the ductility of CFRP is lower than that of wood, the deformation range

FIGURE 15
Displacement of measurement points in the load test of the wooden arch bridge arches.
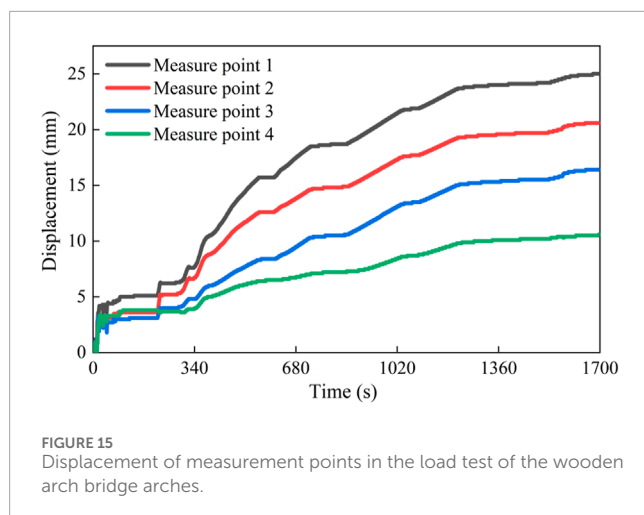
after reinforcement is smaller, exhibiting a brittle failure pattern. When applying CFRP reinforcement to the components of wooden arch corridor bridges, it is not necessary to achieve a tight wrap, allowing for the retention of certain gaps.

The comparison of Figures 7–9 reveals significant reinforcement of the timber-arched lounge bridge members with CFRP. After being strengthened with CFRP, the bearing capacity of completely damaged members can reach 75%–85%, while that of undamaged members can reach 130%–140%.

The load displacement curve of undamaged members of CFRP strengthened wooden arch bridge is shown in Figure 10.

From Figure 10, it is evident that the wood arch bridge, reinforced with CFRP, exhibits no damaged members. In the initial loading phase, displacement changes linearly, indicating strong adhesion between CFRP and the members. As loading progresses, the rate of displacement increase slows down until the undamaged member reinforced with CFRP fails upon reaching the ultimate load.

The strain load curves of two adjacent measuring points at the end of undamaged members of CFRP strengthened wood arch bridge are shown in Figure 11.

Figure 11 illustrates that the change trends of the two measurement points remain largely consistent throughout the entire loading process. Initially, the load strain of both measuring points changes linearly, indicating effective bonding performance between CFRP and the undamaged member. However, as the load continues to increase, the rate of CFRP strain growth slows down, lagging behind the load increase rate. This suggests shear deformation occurring in the bonding layer, leading to slip between CFRP and the undamaged members. The shear stress at the bonding interface between CFRP and undamaged members can be computed based on the strain of adjacent measuring points of undamaged members reinforced with CFRP under the same load.

The shear stress of bond interface of undamaged members of wood arch bridge strengthened with CFRP under different loads is shown in Figure 12.

The shear stress values in Figure 12 are computed based on Formula 3 in the text. The shear stress at the bonding interface of three undamaged members reinforced with CFRP under identical loads remains consistent. However, the bonding interface shear

stress of these members varies under different loads, increasing with higher loads. The test results indicate minimal discrepancies among the bonding interface shear stresses of the three undamaged members reinforced with CFRP, suggesting the measured values in this test are reasonably feasible.

The interface bonding layer is applied twice. By measuring the thickness of the bonding layer δ_A = 2mm, the average elastic modulus of the bonding interface of timber-arched lounge bridge members strengthened with CFRP E_A = 1852.5 MPa is calculated according to Equation 22 and experimental results.

4 The application of CFRP in reinforcing wooden arch bridge

4.1 Experimental testing of wooden arch bridge arches

The 1:5 scale model of the wooden arch bridge was placed under the MTS hydraulic testing machine for load testing, as shown in Figure 13. The displacement measurement points for the load test of the wooden arch bridge arches are illustrated in Figure 14.

Static load test was conducted on the wooden arch bridge arches, and the displacements at each measurement point are shown in Figure 15.

From Figure 15, it can be observed that the displacement curves at each measurement point exhibit a similar trend under static loading. The maximum displacement occurs at the mid-span of the wooden arch bridge arches under static loading, gradually decreasing towards the sides. This trend indicates that during flood periods when additional loads are applied to prevent the bridge from being washed away, reducing the load at the mid-span while distributing it towards the sides may be advisable.

4.2 CFRP reinforcement of the wooden arch bridge arches

A numerical model of the wooden arch bridge was established using SAP 2000, as shown in Figure 16A. The established numerical model was compared with the experimental results to validate its accuracy, and the obtained displacements are illustrated in Figure 16B.

As shown in Figure 16A, during the numerical modeling of the wooden arch corridor bridge using SAP 2000, the deck beams were modeled; however, since there were no deck beams in the experiments, the deck beams were assumed to bear no loads during the numerical calculations. Additionally, each node was subject to a relaxation of constraints, allowing for a limited movement of 5 mm in all six degrees of freedom, changing the constraints from fixed to movable. The current model is suitable for the performance of the specimens tested; however, its generalizability needs to be enhanced through additional experiments with different specimens for parameter calibration. As indicated in Figure 16B, the numerical model of the wooden arch bridge framework established using SAP2000 demonstrates a close agreement in mid-span displacement under static loading, indicating a certain level of accuracy in the model.
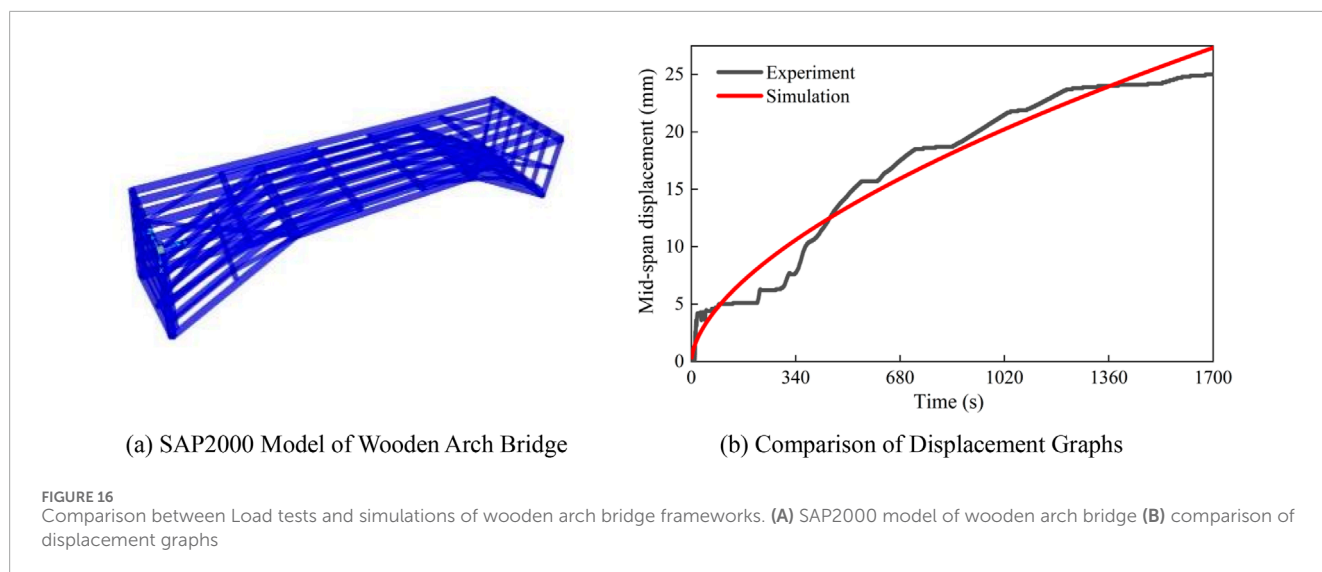
FIGURE 16
Comparison between Load tests and simulations of wooden arch bridge frameworks. **(A)** SAP2000 model of wooden arch bridge **(B)** comparison of displacement graphs
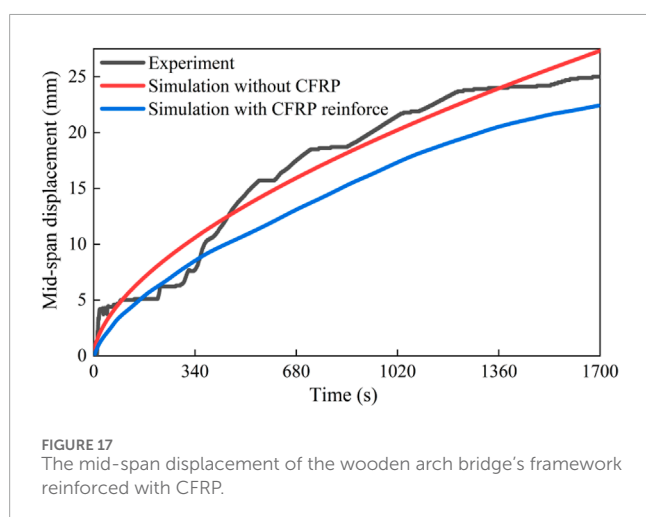

FIGURE 17
The mid-span displacement of the wooden arch bridge's framework reinforced with CFRP.

Using the data obtained from the CFRP reinforcement of components in Section 2, the spring elements representing CFRP are attached to the mid-span nodes of the wooden arch bridge framework and subjected to load simulation, with results shown in Figure 17.

From Figure 17, it is evident that the application of CFRP reinforcement significantly enhances the load-bearing capacity of the wooden arch bridge, resulting in a substantial reduction in mid-span displacement under the same load conditions. CFRP reinforcement of the wooden arch bridge's framework can increase its load-bearing capacity by 20%. When subjected to flood periods, CFRP reinforcement of the wooden arch bridge's framework ensures its structural integrity under applied loads.

5 Conclusion

Based on the experimental research and theoretical analysis of timber-arched lounge bridge members reinforced with CFRP, the following conclusions are drawn:

(1) Based on the comparison between the test results and theoretical research, the elastic modulus of the bonding interface is determined, providing an accurate value for subsequent establishment of the finite element model of local damage of timber-arched lounge bridge components and the setting of component interface parameters for CFRP reinforcement E_A = 1852.5 MPa.

(2) The failure modes of CFRP-reinforced damaged wooden components and undamaged wooden components exhibit significant differences. Given that CFRP has lower ductility compared to wood, when reinforcing the components of wooden arch corridor bridges with CFRP, it is advisable to leave small gaps. This approach allows the reinforced components to retain a certain degree of ductility, thereby preventing failure modes resembling brittle fracture and providing practical guidance for application.

(3) The local components of the wooden arch corridor bridge are damaged and can be reinforced with CFRP to restore their load-bearing capacity. It exhibits excellent reinforcement performance, allowing the components to retain 75%–85% of their original load-bearing capacity after reinforcement. During flood periods, when the load on the wooden arch corridor bridge increases, local members may experience insufficient load-bearing capacity and excessive deformation. CFRP reinforcement can address this issue, increasing the load-bearing capacity to 130%–140% of the original level.

(4) The application of CFRP to the framework of wooden arch bridges has shown promising reinforcement effects, capable of enhancing the load-bearing capacity of the wooden arch bridge framework by approximately 20%, thus providing a theoretical basis for the reinforcement of wooden arch bridge frameworks.

For ancient wooden bridges, the use of CFRP for reinforcement and the reinstallation of components after replacement hold significant value in preserving their original appearance and maintaining their integrity. Additionally, given that wooden bridges are situated above rivers, the durability of CFRP reinforcement in moist environments also requires urgent investigation.

Data availability statement

The original contributions presented in the study are included in the article/supplementary material, further inquiries can be directed to the corresponding authors.

Author contributions

LL: Data curation, Formal Analysis, Project administration, Supervision, Validation, Writing–original draft, Writing–review and editing. YW: Funding acquisition, Methodology, Visualization, Writing–original draft, Writing–review and editing. YZ: Formal Analysis, Methodology, Writing–original draft, Writing–review and editing. XW: Data curation, Formal Analysis, Validation, Writing–original draft. GJ: Data curation, Formal Analysis, Methodology, Project administration, Supervision, Validation, Writing–original draft. XL: Conceptualization, Data curation, Formal Analysis, Investigation, Methodology, Project administration, Resources, Supervision, Validation, Writing–original draft.

Funding

Conflict of interests

Author XW was employed by Beijing Glory PKPM Technology Company Limited.

The remaining authors declare that the research was conducted in the absence of any commercial or financial relationships that could be construed as a potential conflict of interest.

Publisher's note

All claims expressed in this article are solely those of the authors and do not necessarily represent those of their affiliated organizations, or those of the publisher, the editors and the reviewers. Any product that may be evaluated in this article, or claim that may be made by its manufacturer, is not guaranteed or endorsed by the publisher.

References

A, S. H., Zhou, C. D., and Yang, L. G. (2021). Experimental study on axial compression behavior on circular timber columns strengthened with CFRP strips and near-surface mounted steel bars. *J. Struct. Eng.* 147 (3), 1–12. doi:10.1061/(asce)st.1943-541x.0002931

Bashandy, A. A., El-Habashi, A. E., and Dewdar, A. K. (2018). Repair and strengthening of timber cantilever beams. *Wood Material Sci. & Eng.* 13 (4), 241–253. doi:10.1080/17480272.2017.1366944

Brol, J., and Agnieszka, W. P. (2019). Old timber reinforcement with FRPs. *Materials* 12 (24), 4197. doi:10.3390/ma12244197

Buell, T. W., and Saadatmanesh, H. (2005). Strengthening timber bridge beams using carbon fiber. *J. Struct. Eng.* 131 (1), 173–187. doi:10.1061/(asce)0733-9445(2005)131:1(173)

Dagher, H. J., and Lindyberg, R. (2004). FRP-wood hybrids for bridges: a comparison of E-glass and carbon reinforcements. *Adv. Technol. Struct. Eng.*, 1–8. doi:10.1061/40492(2000)191

Dai, T. W., Ji, T., Zhang, Y., and Zhuang, Y. Z. (2015). Experimental study on the effect of the number of layers of carbon fiber cloth on the flexural performance of mortise and tenon timber beams. *J. Fuzhou Univ. Nat. Sci. Ed.* 43 (02), 225–230. doi:10.7631/issn.1000-2243.2015.02.0225

Gentile, C. J. (2000). Flexural strengthening of timber bridge beams using FRP.

Guo, Y., Liu, R. J., Song, Y., Li, Y. H., and Yao, L. H. (2020). Research progress on seismic performance and post earthquake reinforcement and repair of tenon and mortise joints of wood structures. *For. Prod. Ind.* 57 (04), 25–28. doi:10.19531/j.issn1001-5299.202004005

İşleyen, K. U., Ghoroubi, R., Mercimek, Ö., Anıl, Ö., Togay, A., and Erdem, R. T. (2021). Effect of anchorage number and CFRP strips length on behavior of strengthened glulam timber beam for flexural loading. *Adv. Struct. Eng.* 24 (9), 1869–1882. doi:10.1177/1369433220988622

Jin, Y. C., Su, H. X., Pan, W., He, Y. C., Du, J. W., and Fu, G. P. (2022). Experimental research on seismic performance and reinforcement comparison of mortise-tenon and joints in timber structures. *J. Civ. Environ. Eng.* 44 (02), , 138–147. doi:10.11835/j.issn.2096-6717.2021.095

Klaudia, S. W., Adam, O. K., Justyna, J. L., and Karolak, A. (2021). The influence of CFRP sheets on the load-bearing capacity of the glued laminated timber beams under bending test. *Materials* 14 (14), 4019. doi:10.3390/ma14144019

Li, A. Q., Zhou, K. P., Wang, C. C., and Xie, L. L. (2019). Analysis and Prospect of wood structure repair and reinforcement technology of Chinese ancient buildings. *J. Southeast Univ. Nat. Sci. Ed.* 49 (01), 195–206. doi:10.3969/j.issn.1001-0505.2019.01.027

Lin, H. Y., Ji, T., Dai, T. W., Lin, X. J., and Zhang, Y. (2016). Experimental study for the effect of dovetail style on the flexural behavior of timber beams extended by a mortise-tenon joint and strengthened by CFRP sheets. *J. Fuzhou Univ. Nat. Sci. Ed.* 44 (04), 524–530. doi:10.7631/issn.1000-2243.2016.04.0524

Qiu, Z., Yan, M., Yang, Y., Li, J., Zhu, W., and Fan, H. (2021). Flexural behaviors of CFRP strengthened laminated bamboo arches. *Constr. Build. Mater.* 305, 124759. doi:10.1016/j.conbuildmat.2021.124759

Rescalvo, F. J., Valverde-Palaacios, I., Elisabet, S., and Gallego, A. (2018b). Experimental and analytical analysis for bending load capacity of old timber beams with defects when reinforced with carbon fiber strips. *Compos. Struct.* 186, 29–38. doi:10.1016/j.compstruct.2017.11.078

Rescalvo, F. J., Valverde-Palacios, I., Elisabet, S., Roldán, A., and Gallego, A. (2018a). Monitoring of carbon fiber-reinforced old timber beams via strain and multiresonant acoustic emission sensors. *Sensors* 18 (4), 1224. doi:10.3390/s18041224

Tohid, G. G., Russo, T., and Valipoue, H. R. (2020). Lightweight timber I-beams reinforced by composite materials. *Compos. Struct.* 233, 111579. doi:10.1016/j.compstruct.2019.111579

Vahedian, A., Shrestha, R., and Crews, K. (2019). Experimental and analytical investigation on CFRP strengthened glulam laminated timber beams: full-scale experiments. *Compos. Part B* 164, 377–389. doi:10.1016/j.compositesb.2018.12.007

Wang, S. Y., Guo, T., Deng, H., and Zhou, H. B. (2021). Study on seismic performance of mortise and tenon joint reinforcement of bucket type wood structure. *Wood Sci. Technol.* 35 (01), 36–41. doi:10.12326/j.2096-9694.2020026

Xie, Q. F., Zhao, H. T., Xie, J. Y., Wu, J. B., and Sui, Y. (2008). Experimental study and theoretical analysis on interfacial bond stress of timber beams strengthened with CFRP sheets. *Eng. Mech.* (07), 229–234+240.

Xue, J. Y., Zhai, L., Zhang, F. L., and Li, Y. Z. (2015). Performance analysis and design method of damaged joints of wood structures of ancient buildings strengthened with flat steel. *J. Xi'an Univ. Archit. Technol. Nat. Sci. Ed.* 47 (05), 621–625. doi:10.15986/j.1006-7930.2015.05.002

Yuan, S. C., Dong, J. F., Wang, Q. Y., and Zhu, Y. M. (2014). Calculation and analysis on load carrying capacity of damaged timber beams strengthened with CFRP. *Appl. Math. Mech.* 35 (S1), 261–265.

Zhang, L., Zhou, A. P., Sheng, B. L., Shen, Y. R., and Xu, J. N. (2018). Experimental study on wood beams with defects strengthened with carbon fiber composites. *J. For. Eng.* 3 (03), 128–135. doi:10.13360/j.issn.2096-1359.2018.03.021

Zhou, C. D., Liang, L. C. A. S. H., Zhang, Y., and Yang, L. G. (2020). Experimental study on axial compression performance of rectangular section wood columns strengthened with embedded reinforcement and wrapped CFRP. *J. Build. Struct.* 41 (07), 173–181. doi:10.14006/j.jzjgxb.2018.0517

Zhou, T. G., Zhu, R. Z., Zhu, L. X., Yu, W., and Zuo, D. L. (2016). Shaking table test study on seismic reinforcement of adobe retaining wall wood structure residential buildings. *J. Xi'an Univ. Archit. Technol. Nat. Sci. Ed.* 48 (03), 346–350 + 370. doi:10.15986/j.1006-7930.2016.03.007

Zhu, J. B., Wang, B. S., and Wang, J. B. (2005). Experimental study on Strengthening Damaged wood beams with CFRP. *Ind. Archit.* 4 (10), 86–89. doi:10.13204/j.gyjz2005.10.026

*CORRESPONDENCE
Jinrui Zhang,
✉ 335257@whut.edu.cn

Characteristics of dynamic mechanics and energy loss in reef limestone concrete during dry-wet carbonation periods

Jian Li[1], Fei Li[2], Mingju Mao[3], Jinrui Zhang[3]* and Ran Fan[3]

[1]Department of Architecture Engineering and Design, Wuhan Institute of Shipbuilding Technology, Wuhan, China, [2]Department of Road and Bridge Engineering, Guizhou Communications Polytechnic University, Guiyang, China, [3]Wuhan University of Technology, Wuhan, China

Coral reef limestone is a unique type of rock and soil body characterized by high porosity. Its dynamic mechanical properties under impact loads differ significantly from those of conventional land-sourced aggregate concrete.This study utilizes coral reef limestone as both coarse and fine aggregates to prepare C40 strength concrete. The research investigates the effects of dry-wet carbonation cycles on its dynamic mechanical behavior and energy evolution characteristics using a Split Hopkinson Pressure Bar (SHPB) mechanical testing system.The findings reveal that increasing the number of dry-wet carbonation cycles leads to a significant weakening of the internal structural bonding in coral reef limestone concrete. Notably, the degree of phenolphthalein color change diminishes, while uniaxial compressive strength and tensile strength demonstrate an overall downward trend. The reduction in tensile strength is less pronounced than the decrease in compressive strength. Additionally, the relative dynamic elastic modulus gradually decreases, and a size effect is noted, with a rapid acceleration in mass loss. As the number of dry-wet carbonation cycles increases, dynamic compressive strength declines, and failure modes shift from surface cracking to crush-type failure.The dynamic increase factor (DIF) of the coral reef limestone concrete indicates a high sensitivity to strain rate, with a significant rise in DIF value as the strain rate increases. Various energies generated under impact load exhibit clear strain rate effects. Furthermore, the effects of dry-wet carbonation cycling enhance energy dissipation, especially at 30 cycles, where energy dissipation increases sharply, while a hindering effect on transmitted energy is observed.

KEYWORDS

reef limestone concrete, dry-wet carbonation cycle, dynamic fragmentation, strain rate, energy dissipation

1 Introduction

The engineering projects on the coral reefs in Western Pacific Ocean waters are far from the mainland, leading to a severe scarcity of mainland-sourced mechanized sand aggregates and freshwater resources. Transporting sand, gravel, and other concrete materials from the mainland not only increases construction costs but also impacts the construction schedule. Utilizing local materials by preparing concrete from reef limestone for the construction of island reef projects alleviates the issue of raw material shortages

FIGURE 1
Grading curve of reef limestone aggregates.
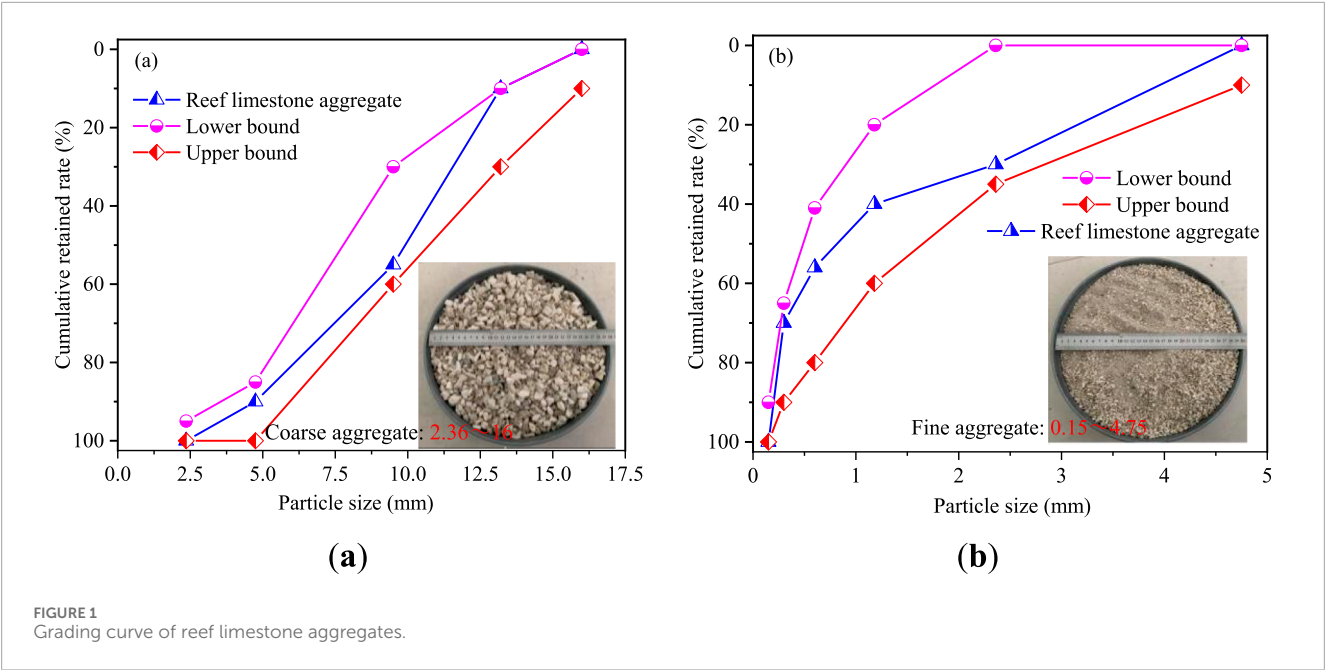
TABLE 1 Mix proportions of reef limestone concrete (kg/m³).

Name	Ordinary portland cement	Reef limestone	Reef limestone	Seawater	Fly ash	Slag	Crack-resistant waterproofing agent
Amount	780	700	300	250	70	150	15

FIGURE 2
Dry-wet carbonation cycle experimental procedure.
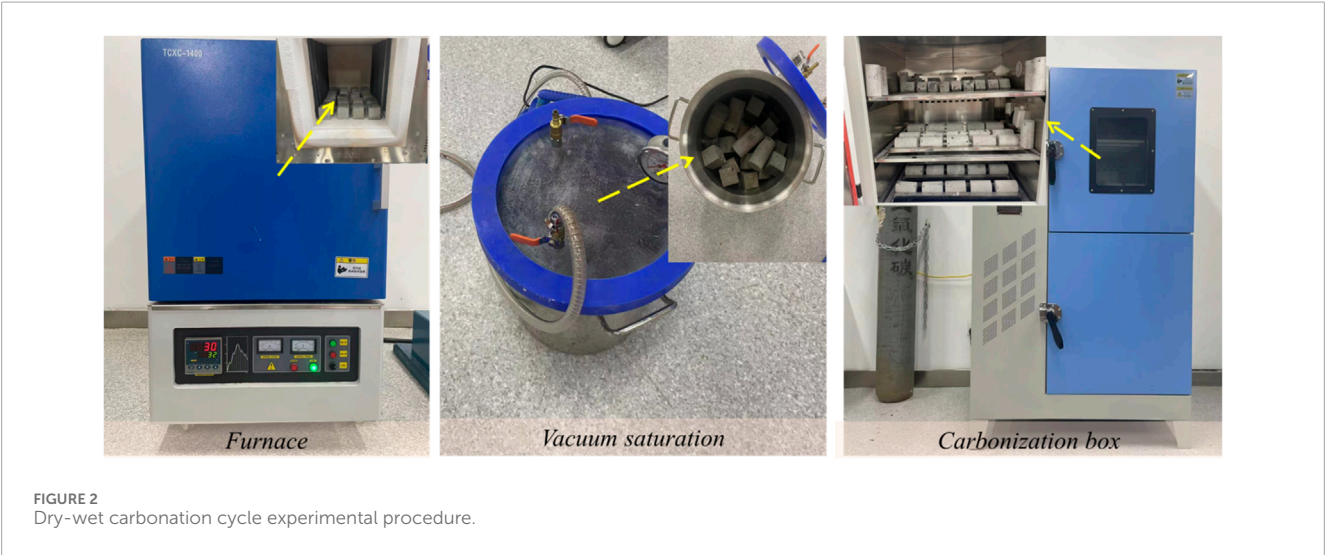
in marine engineering and allows for the reasonable development and use of marine resources according to local conditions (Deng et al., 2022; Zhou et al., 2020). Furthermore, the structural designs of coral reefs in Western Pacific Ocean waters are designed to endure not just static forces but also diverse dynamic forces, including earthquakes, tsunamis, and unintended blasts. This places strict requirements on the selection and design

of building materials for their impact resistance (Lahiri et al., 2022). At the same time, the structures on the reefs inevitably face the harsh service environment affected by long-term dry-wet carbonation cycles (Liu et al., 2023), This leads to the deterioration of concrete structural performance and a reduction in service life, which severely threatens the long-term stability of reef projects. Consequently, researching the dynamic mechanical efficiency of
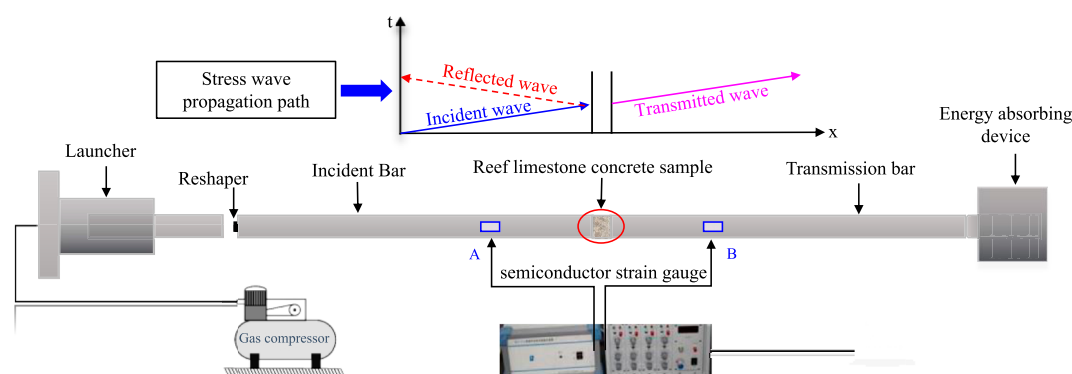
FIGURE 3
Hopkinson pressure bar setup.
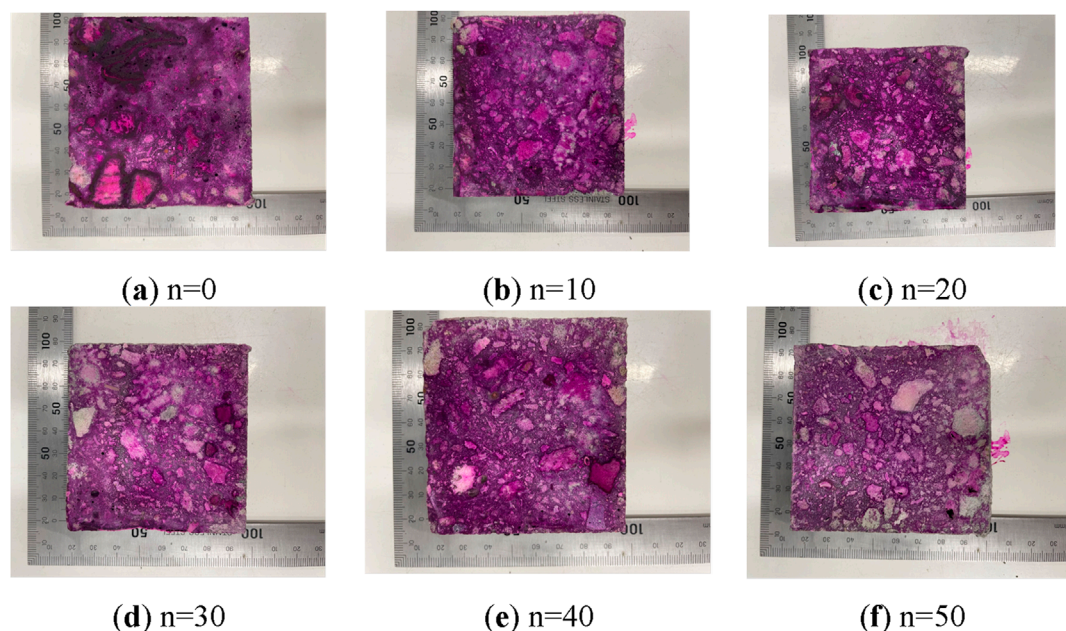
FIGURE 4
Phenolphthalein Color Reaction for the Degree of Carbonation of Reef limestone Concrete. **(A)** n = 0, **(B)** n = 10, **(C)** n = 20, **(D)** n = 30, **(E)** n = 40, **(F)** n = 50.

reef limestone concrete in response to dry-wet carbonation cycles is crucial.

As a unique geomaterial, coral reef limestone is extensively found across Western Pacific Ocean waters (Zhang et al., 2023). In the 1940s, some marine infrastructure construction projects began to involve coral reef limestone concrete (Fu et al., 2021). Concrete, a tripartite medium made up of aggregates, the interface transition zone, and cement paste, plays a significant role in determining its performance (Meddah et al., 2010; Uddin et al., 2017). Research indicates that fissures in light aggregate concrete mainly infiltrate the aggregates, in contrast to traditional aggregate concrete where cracks predominantly emerge at the junction of the aggregates and the paste (Sim et al., 2013), Reef limestone aggregates fall into the category of typical lightweight aggregates, and the surfaces of reef

limestone coarse aggregates are porous and rough. Consequently, the way reef limestone concrete fails when subjected to external loads is markedly distinct compared to other light aggregates and standard concrete. Wu et al. (2020) discovered that reef limestone concrete's dynamic compressive strength, when subjected to impact loads, surpasses that of standard concrete of identical quality, yet falls marginally short of other light aggregate concretes. Wu et al. (2019); Ma et al. (2020) discovered that reef limestone aggregate concrete, maintaining identical strength and minimal strain rates, shows reduced static and dynamic compressive strengths compared to traditional aggregate concrete, yet its dynamic increase factor (DIF) demonstrates a more pronounced strain rate impact. It was found that the primary formation of cracks in reef limestone concrete occurs via the aggregates of reef limestone, rather than at the
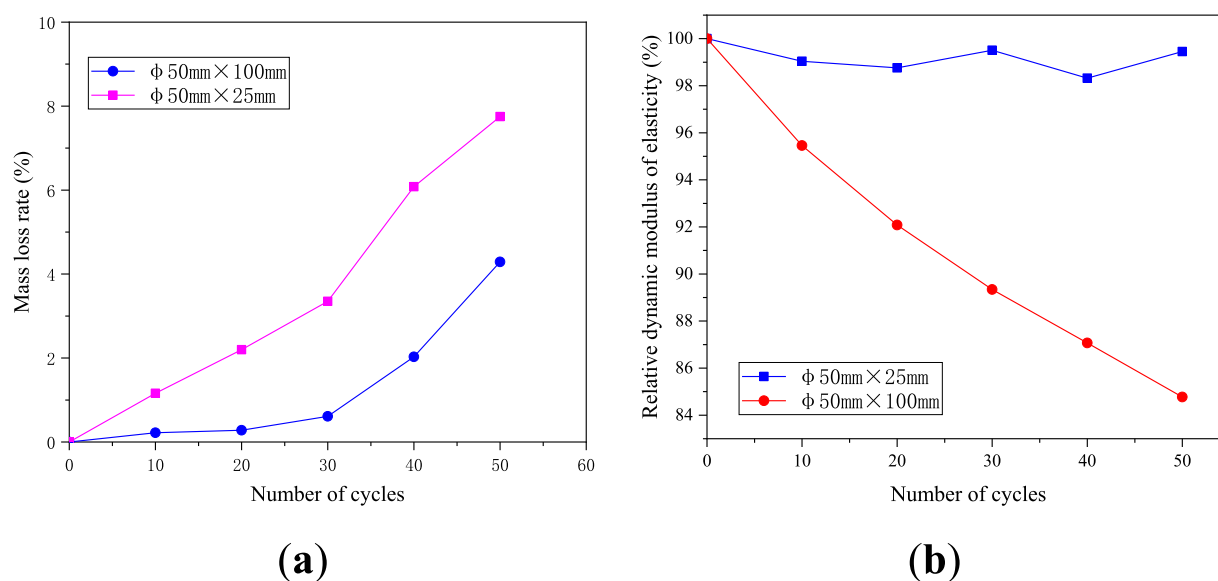
FIGURE 5
Mass loss rate and relative elastic modulus.

junction of these aggregates and the paste (Ma et al., 2019). Qin et al. (2023) examined the evolving properties, patterns of energy development, modes of fractures, and damage processes in coral reef sand concrete when subjected to impact forces.

Concrete structures inevitably face various harsh environmental challenges during their service life, including extreme weather changes, chemical corrosion, water infiltration, and physical impacts. Mumenya et al. (2010) found that concrete materials exposed to specific environments, such as dry-wet cycles, for extended periods experience certain changes in mechanical properties. Donnini (2019) investigated the mechanical characteristics of two varieties of concrete in solutions varying in temperature and pH, discovering that the mechanical attributes of standard concrete show minimal sensitivity to changes in temperature and pH; however, there is a notable impact on the tensile strength of glass fiber concrete. Li et al. (2021); Yin et al. (2019) studied to understand the deterioration trends of mechanical properties in recycled concrete under freeze-thaw cycles in both salt solutions and dry-wet conditions. Zhang et al. (2024) used waste glass instead of sand as fine aggregate to study the performance change of concrete after dry-wet cycle. Xu et al. (2021) investigated the combined impact of hybrid fibers on concrete's longevity and additionally forecasted the durability of fiber-reinforced concrete under carbonation and chloride ion corrosion conditions.

The evaluation of reef limestone concrete's bearing capacity and durability, a novel deep-sea island reef construction material, is still in its initial stages of exploration and verification, facing notable limitations in its adaptability studies in severe marine conditions. Coral reef limestone aggregates are naturally characterized by their loose and porous properties, making them highly susceptible to corrosion from marine gaseous environments. Previous studies have focused more on the static mechanical properties of coral reef limestone concrete in harsh marine environments, while research on its durability under dynamic impact loads has

been insufficient. Consequently, this research utilizes a divided Hopkinson pressure bar for performing impact assessments on reef limestone concrete samples undergoing dry-wet carbonation processes. This study explores how dry-wet carbonation cycles impact the dynamic compressive strength, modes of failure, and energy development traits of reef limestone concrete, and delves into the inherent connections among loading speeds, fracturing traits, and energy loss properties when dry-wet carbonation is combined. The results offer theoretical backing for the creation and advancement of novel concrete frameworks in the field of island reef engineering.

2 Materials and methods

2.1 Preparation of reef limestone concrete samples

Limestone samples from a reef on an island in Western Pacific Ocean waters were synthetically pulverized into particles, each not exceeding 16 mm in size. Particles measuring 4.75–16 mm in size were processed as coarse aggreagte, whereas those ranging from 0.15 to 4.75 mm were selected for fine aggreagte (Fan et al., 2023; Liu et al., 2018). Figure 1 elaborates on the ongoing categorization of both coarse and fine aggregates of coral reef limestone.

Contrasting with traditional land-based sand and gravel, fragments of reef limestone display features like suboptimal particle form, uneven particle shapes, coarse surfaces, significant porosity, extensive specific surface area, and reduced strength (Luo et al., 2023). Therefore, more cement paste is required to enhance workability when mixing concrete, making it less suitable for high-strength concrete applications. This research involved blending both coarse and fine reef limestone aggregates with standard Portland cement, seawater, fly ash, slag, and various additives, as

FIGURE 6
Compressive strength and tensile strength (disc shape for uniaxial tension test, cylindrical shape for uniaxial compression test).
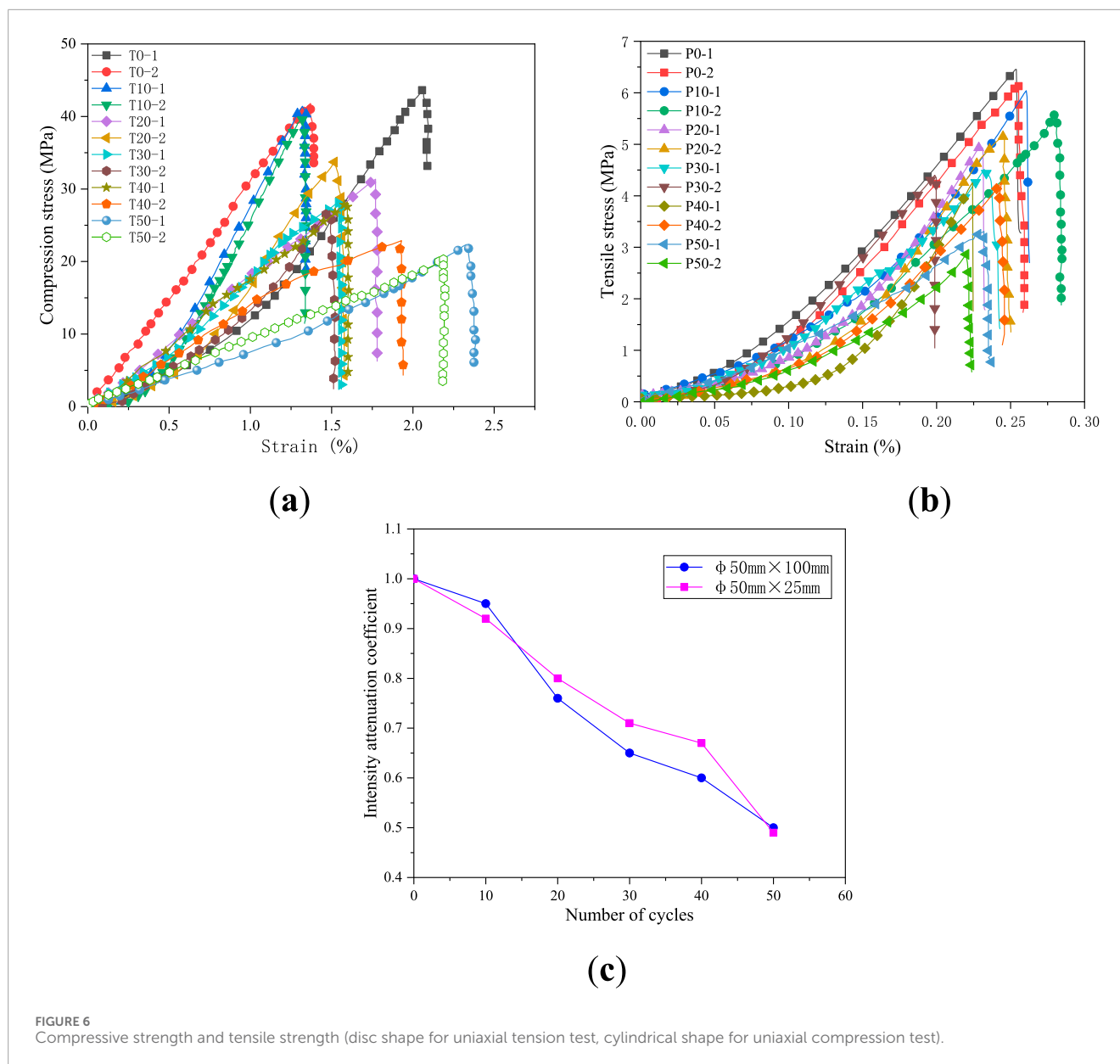
detailed in Table 1, to create concrete with a C40 strength. Notably, the aggregates of reef limestone underwent water immersion before being mixed to eliminate detrimental ions and contaminants. After processes such as mixing, vibrating, and curing, cylindrical specimens with height-to-diameter ratios of 1:2 (φ50 mm × 25 mm) and 2:1 (φ50 mm × 100 mm) were prepared.

2.2 Dry-wet carbonation

Figure 2 illustrates the entire process of the dry-wet carbonation cycle that the reef limestone concrete samples underwent. Before the experiments, the samples were subjected to a drying pretreatment (assessed by changes in mass to determine whether they reached a dry state). In order to ensure the rationality of the dry-wet carbonation cycle pretreatment scheme, the existing research results

are referred to Wang et al. (2018); Jiang et al. (2017); Zhang and Shao (2016). First, the dried samples were placed in a vacuum saturation container filled with seawater (soaked in a vacuum state for 12 h). Subsequently, the samples, once saturated, underwent a drying phase in an oven maintained at a steady 60°C for 12 h. Ultimately, the specimens were positioned in a carbonation chamber to undergo carbonation treatment, characterized by a carbon dioxide level of 20% ± 3%, a humidity of 70% ± 5%, a temperature maintained at 20°C ± 5°C, and a 24-h period. The trio of stages forms a single cycle, with the count of dry-wet carbonation cycles adjusted to 0, 10, 20, 30, 40, and 50 cycles.

Micro-fissures in the reef limestone concrete samples will progressively widen and enlarge due to dry-wet carbonation cycles, resulting in the unavoidable seepage of internal elements. Initially, the specimens have relatively high density and stronger resistance to dry-wet cycles and carbonation. However, with the rise in cycle
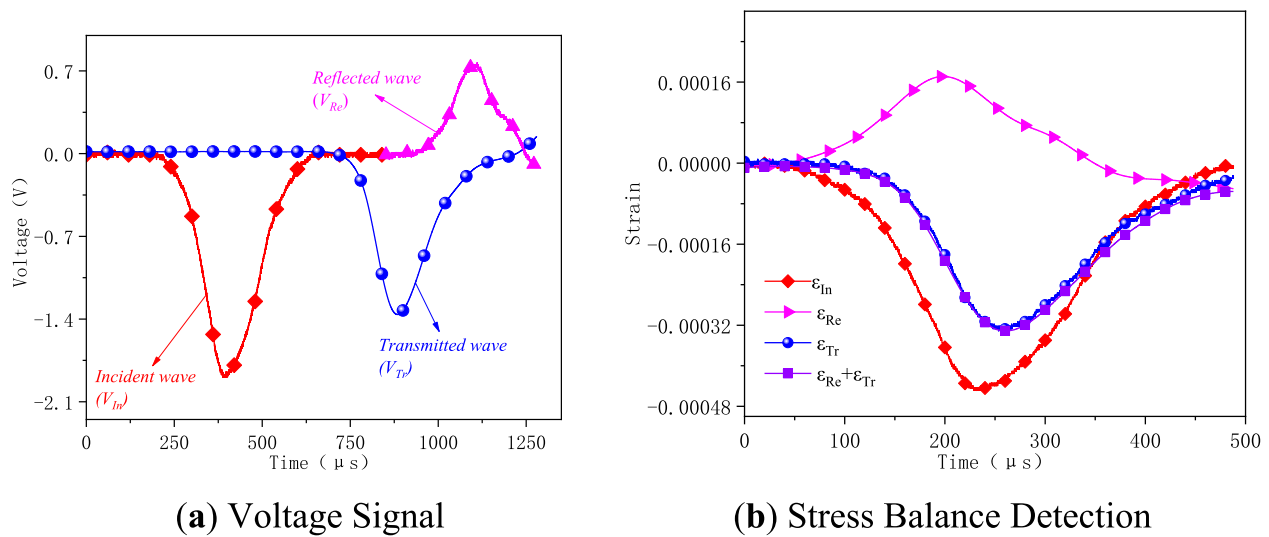
FIGURE 7
Typical dynamic stress wave time history curve. **(A)** Voltage signal, **(B)** stress balance detection.
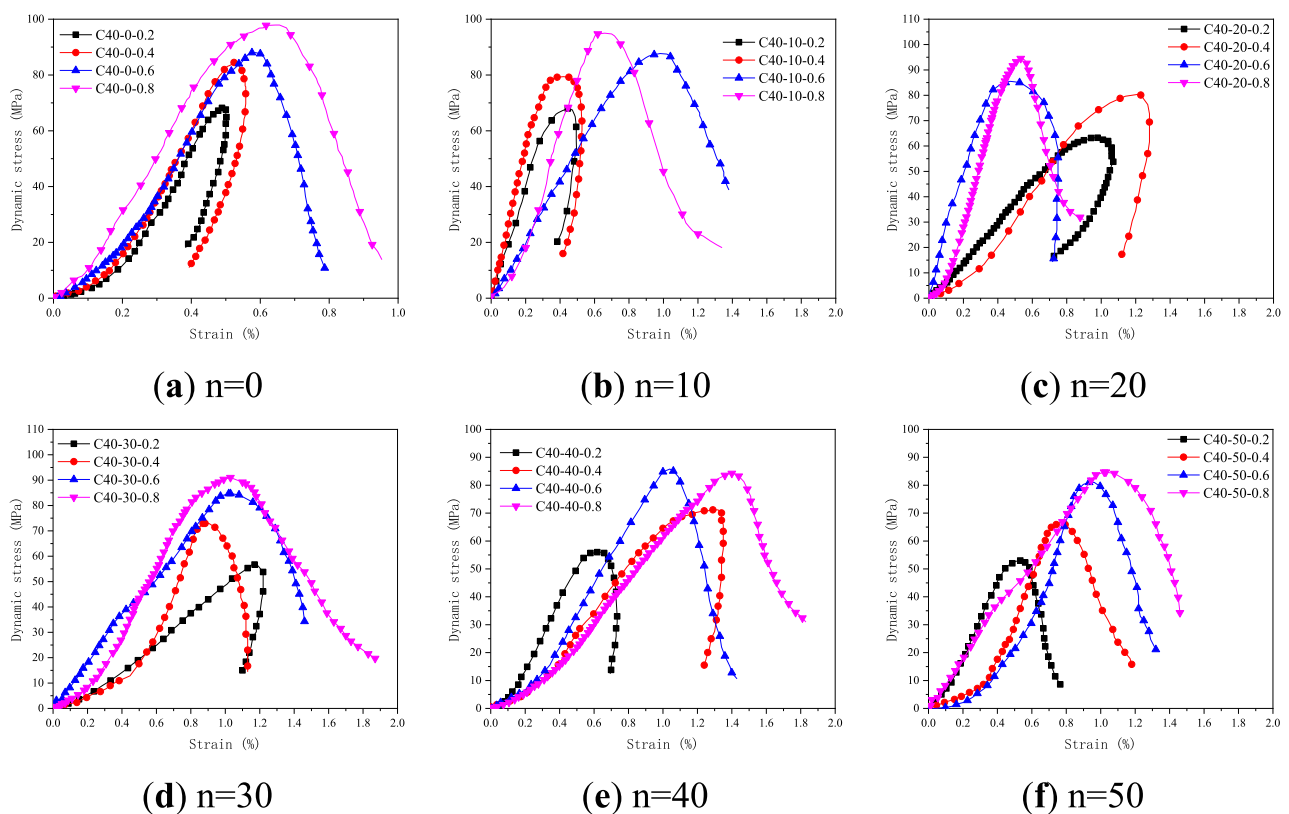
FIGURE 8
Dynamic Stress-Strain Curves. **(A)** n = 0, **(B)** n = 10, **(C)** n = 20, **(D)** n = 30, **(E)** n = 40, **(F)** n = 50.

count, there will be a noticeable alteration in the ultimate weight of the samples. Consequently, the rate at which mass is lost serves as an indicator of the extent of damage and degradation. The method and procedure for calculating the mass loss rate are as follows:

1) Dry the specimens after completing the dry-wet carbonation cycles, and wrap them in plastic wrap to prevent moisture from causing errors, then weigh each specimen three times and take the average value as its initial mass; 2) Place the specimens

TABLE 2 Overview of characteristic parameters under impact load.

Number of deterioration cycles	Impact Load/MPa	Strain rate/s-1	Dynamic peak Strength/MPa	Peak strain/%	DIF
0	0.2	54.65	68.20	0.489	1.60
	0.4	83.88	84.48	0.524	1.98
	0.6	106.57	88	0.576	2.06
	0.8	124.60	97.90	0.644	2.29
10	0.2	62.80	68.00	0.45	1.59
	0.4	83.37	79.40	0.42	1.86
	0.6	116.31	87.70	0.98	2.05
	0.8	132.91	95.00	0.66	2.22
20	0.2	66.75	63.25	0.956	1.48
	0.4	90.91	80.34	1.21	1.88
	0.6	111.36	85.50	0.47	2.00
	0.8	144.17	94.5	0.53	2.21
30	0.2	77.16	56.70	1.2	1.33
	0.4	91.63	72.93	0.87	1.71
	0.6	118.66	84.7	1.02	1.98
	0.8	144.56	91.00	1.03	2.13
40	0.2	76.19	56	0.619	1.31
	0.4	94.91	71.17	1.29	1.67
	0.6	129.31	85.80	1.04	2.01
	0.8	150.26	84.24	1.4	1.97
50	0.2	83.3	53.00	0.54	1.24
	0.4	106.17	66.70	0.77	1.56
	0.6	132.32	81.00	0.93	1.90
	0.8	158.33	84.70	1.02	1.98

into the corresponding equipment for the deterioration test according to the experimental protocol, and after undergoing the specified number of deterioration tests, remove the specimens, dry them, and weigh them; 3) Utilize the following formula to determine the rate at which the specimens lost mass following the nth deterioration test. Formula 1 is as follows:

$$\Delta m_n = \frac{m_0 - m_n}{m_0} \times 100\% \qquad (1)$$

In the equation, Δm_n represents the mass loss rate of the specimen (%); m_0 denotes the initial mass (g); and m_n represents the mass after undergoing n deterioration actions (g). Furthermore, the E_{rd} relative dynamic modulus of elasticity serves as a crucial measure for evaluating the specimens' damage and degradation. This refers to the proportion between the specimen's dynamic modulus of elasticity post the nth cycle and its initial dynamic modulus of elasticity. To prevent secondary damage during the testing process from causing experimental errors, the elastic modulus is
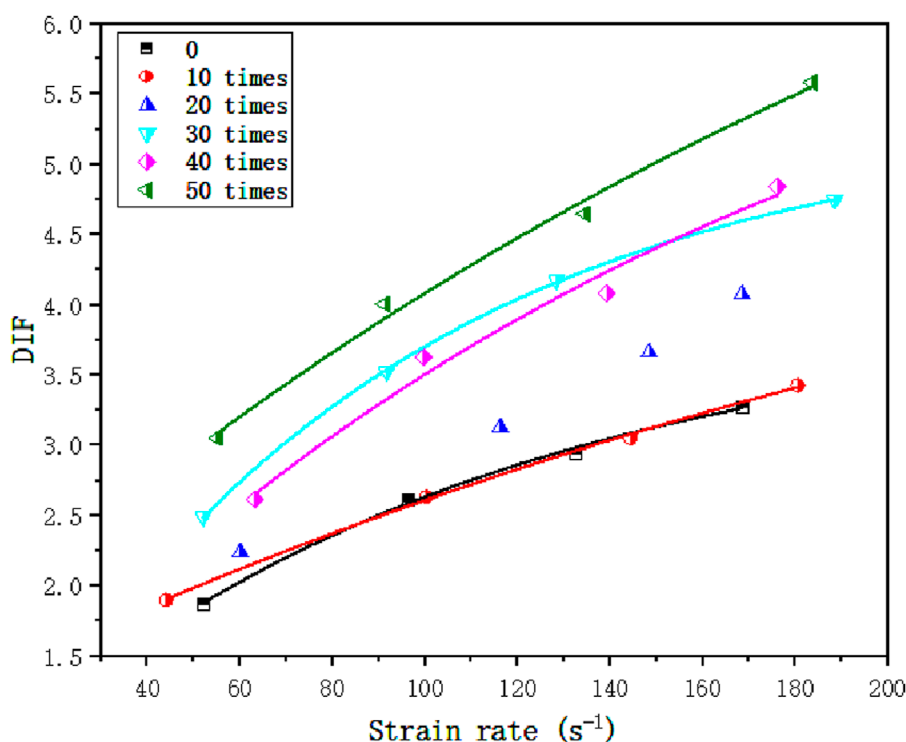
FIGURE 9
The fitting curves of DIF of specimens under different deterioration times.

calculated using parameters such as sound travel time and wave speed while ultrasonic waves propagate through the specimen. This method is completely non-destructive to the specimen, as shown in Equations 2, 3.

$$E_{rd} = \frac{E_{dn}}{E_{d0}} = \frac{V_n^2}{V_0^2} \qquad (2)$$

$$E_d = \frac{(1+v)(1-2v)\rho V^2}{1-v} \qquad (3)$$

In the equation, E_d represents the dynamic modulus of elasticity of the specimen (GPa); v represents the Poisson's ratio of the specimen; ρ represents the density of the specimen (kg/m³); V is the ultrasonic wave speed (m/s); E_{d0} is the initial dynamic modulus of elasticity of the specimen (GPa), and E_{dn} is the dynamic modulus of elasticity after undergoing n deterioration actions (GPa).

2.3 Impact testing equipment and testing principles

Using a divided Hopkinson pressure bar, dynamic compression experiments were performed on reef limestone concrete samples that had experienced cycles of dry and wet carbonation. The experimental setup is shown in Figure 3. The incident bar and the transmission bar are both 2,800 mm, the bar diameter is 50 mm, the elastic modulus is 210 GPa, and the density is 7,800 kg/m³. Introducing high-pressure gas into the emission chamber propels

the projectile at a specific speed, hitting the incident bar's end surface and creating a longitudinal compressive wave. Upon the arrival of this compressive wave at the specimen, a sequence of transmission and reflection events take place at the terminal surfaces of both the incident and transmission bars. Strain gauges affixed to both the incident and transmission bars record the incident strain ε_i, the reflected strain ε_r, and the transmitted strain ε_t. Ultimately, by presuming one-dimensional stress waves and uniformity, one can determine the specimen's stress-strain and loading rate data.

As per the principles of one-dimensional stress wave theory, the stress and strain of the specimen can be determined by the following Formula 4 (Dai et al., 2010):

$$\sigma_t = \frac{(\varepsilon_i(t) + \varepsilon_r(t) + \varepsilon_t(t))E_0 A}{2A_s}$$

$$\dot{\varepsilon}(t) = \frac{(\varepsilon_i(t) - \varepsilon_r(t) - \varepsilon_t(t))C_0}{L_s} \qquad (4)$$

$$\varepsilon(t) = \int_0^t \dot{\varepsilon}(t)dt$$

Within the formula, E_0, C_0, and A symbolize the velocity of the elastic wave within the bar, the elastic modulus, and the bar's cross-sectional area, in that order; A_S and L_S denote the specimen's cross-sectional area and length, respectively; and t denotes the stress wave's length.

In addition, the calculation Formula 5 of the incident energy W_I, reflected energy W_R and transmitted energy W_T on the pressure rod during the whole process from the beginning of loading to the failure

TABLE 3 Typical fracture modes of reef limestone concrete under impact load.

Load break Times	0.2 MPa	0.4 MPa	0.6 MPa	0.8 MPa
0				
10				
20				
30				
40				
50				

of the sample is as follows (Huang et al., 2014):

$$W_I = \frac{C_0 A}{E_0} \int \sigma_I^2(t)dt,$$
$$W_R = \frac{C_0 A}{E_0} \int \sigma_R^2(t)dt,   \quad (5)$$
$$W_T = \frac{C_0 A}{E_0} \int \sigma_T^2(t)dt$$

Given that the energy dissipation of the stress wave in both the bar and the specimen is deemed minimal, the aggregate energy the specimen absorbs and dissipates, denoted as W_L, is derivable from the subsequent Equation 6.

$$W_L = W_I - (W_R + W_T)   \quad (6)$$

3 Analysis of experimental results

3.1 Results of static mechanical properties tests

The primary cause of carbonation in reef limestone concrete lies in CO_2 penetrating its core, leading to a decrease in its alkalinity. Samples subjected to varying degrees of deterioration were cut and sprayed with a 1% phenolphthalein ethanol solution. The color reaction of the phenolphthalein ethanol solution is shown in Figure 4. After different numbers of deterioration cycles, the degree of carbonation represented by the phenolphthalein reagent varied. The undeteriorated samples showed a strong magenta color after treatment with phenolphthalein, while the degree of color change gradually weakened with an increasing number of deterioration cycles.

It is noteworthy that the reef limestone aggregate was also stained by the phenolphthalein reagent. This is because, after the aggregate underwent pre-absorption of water, more cement paste entered its interior during the mixing process, which increased the alkalinity of the aggregate. As the number of deterioration cycles increased, the cement content in the pores of the aggregate gradually decreased, resulting in a gradual reduction in the staining intensity under the phenolphthalein reagent. Further testing showed that the carbonation depth of reef limestone concrete at different deterioration levels increased by 1.5%, 1.58%, 2.87%, and 5.6% compared to the standard condition. Among them, the sample of reef limestone concrete with the deepest deterioration had a carbonation depth increase of 5.2 mm compared to the standard condition. He et al. research shows that cyclic dry-wet carbonation
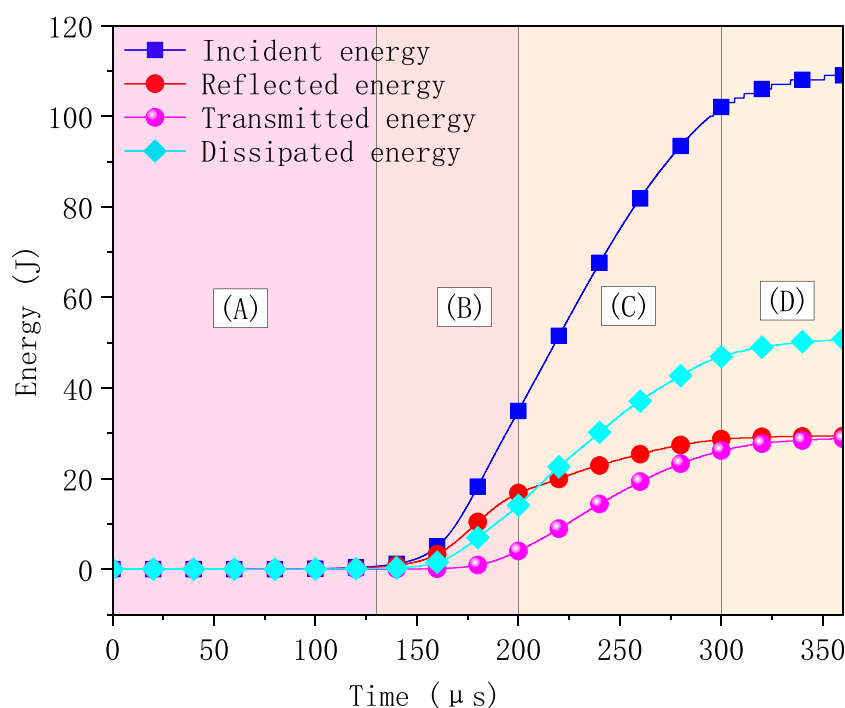
FIGURE 10
Energy-time curve under impact load.

can lead to changes in the pore structure of concrete and cause the reorganization of hydration products, affecting its structural strength. For example, some hydration products (such as C-S-H gel) may convert into lower-strength calcium carbonate, thereby weakening the overall strength and reducing its durability (He et al., 2022).

Figure 5 summarizes the mass loss rates and relative elastic moduli of reef limestone concrete specimens subjected to different numbers of deterioration cycles. When the mass loss rate reaches over 5%, the specimen can be deemed damaged. For cylindrical specimens (φ50 mm × 100 mm), the mass loss rate did not exceed 5% even after more than 40 deterioration cycles, while the disc specimens (φ50 mm × 25 mm) exhibited a high mass loss rate, indicating that the dry-wet carbonation cycles caused significant damage to the disc samples. Overall, although the shapes of the specimens differ, both types experienced an increase in mass loss rates with the growing number of deterioration cycles, although the trends in their growth were distinct. Furthermore, the relative dynamic elastic modulus displayed a significant size effect influenced by the number of dry-wet carbonation cycles. With the ongoing rise in deterioration cycles, there was an acceleration in the decrease rate of the cylindrical specimens' relative dynamic elastic modulus (φ50 mm × 100 mm), as evidenced by the reduced acoustic wave velocity. This suggests a swift escalation and ongoing spread of cracks within the specimens, thereby intensifying their damage severity. Conversely, the disc specimens' dynamic elastic modulus (φ50 mm × 25 mm) varied in tandem with the escalation of deterioration cycles. This difference reflects the varying internal structural responses of different specimens during the deterioration process; the cylindrical

specimens may exhibit better resistance to deterioration due to their structural characteristics compared to other types of specimens.

Furthermore, quasi-static compression and tension tests were conducted on reef limestone concrete samples subjected to varying degrees of deterioration, and the statistical results are shown in Figure 6. Despite variations in the data from uniaxial compression and tension tests, it's noticeable that the specimens' uniaxial compressive and tensile strengths exhibit a general downward trajectory after varying levels of degradation, with a direct relationship between the rise in peak strain and the frequency of these deterioration cycles.

Referring to Deng et al. (2020a); Deng et al. (2020b) research results, the ratio of strength is used as an increasing coefficient. The strength reduction coefficient is defined as the strength reduction coefficient is the ratio of uniaxial compressive strength of the sample after dry-wet carbonization cycle to that of the initial sample, to evaluate the degree of deterioration of reef limestone concrete specimens. When the number of deterioration cycles is less than 20, the strength attenuation is not significant, with the average compressive strength remaining above 40 MPa. However, once the count of degradation cycles surpasses 20, the reduction in strength becomes more noticeable, evidenced by the average compressive strength falling from 32.53 to 25.55 MPa. When samples undergo 40 cycles of decay, their uniaxial compressive strength drops to merely 60% of their original level, and upon reaching 50 cycles, the mean compressive strength drops to just 21.32 MPa. The maximum average tensile strength of the specimens is 6.31 MPa, but after 50 cycles of deterioration, the maximum tensile strength decreases to

TABLE 4 Energy characteristic values of reef limestone concrete under different impact loads and number of deterioration cycles.

Number of deterioration cycles	Impact Load/MPa	Strain Rate/s^{-1}	Incident Energy/J	Reflected Energy/J	Transmitted Energy/J	Dissipated energy
0	0.2	54.65	80.95	19.21	27.30	34.44
	0.4	83.88	108.11	35.45	36.03	26.63
	0.6	106.57	138.85	48.64	36.21	54.00
	0.8	124.60	171.22	57.67	26.99	86.56
10	0.2	62.80	76.08	15.27	25.69	35.13
	0.4	83.37	106.47	47.80	32.72	15.95
	0.6	116.31	139.61	35.74	45.26	58.61
	0.8	132.91	166.03	59.64	27.6	78.79
20	0.2	66.75	71.39	17.58	22.43	31.37
	0.4	90.91	105.75	42.45	30.39	22.91
	0.6	111.36	133.83	40.46	39.56	53.81
	0.8	144.17	160.69	54.19	27.86	78.64
30	0.2	77.16	72.10	15.47	14.66	41.97
	0.4	91.63	106.26	37.50	31.22	36.54
	0.6	118.66	133.77	37.5	39.89	56.38
	0.8	144.56	170.47	59.68	28.98	81.81
40	0.2	76.19	78.20	16.73	14.45	47.02
	0.4	94.91	106.11	33.63	32.51	29.97
	0.6	129.31	131.26	30.73	35.47	65.06
	0.8	150.26	165.12	57.55	20.01	87.56
50	0.2	83.3	79.36	16.20	12.73	50.42
	0.4	106.17	109.20	29.40	28.82	50.98
	0.6	132.5	132.5	25.39	26.49	80.62
	0.8	158.33	170.95	57.13	24.66	89.16

3.31 MPa, resulting in an overall tensile strength reduction of 49%. The reduction in tensile strength is lower than that of compressive strength.

3.2 Dynamic compression characteristic test results

3.2.1 Dynamic stress balance verification

The dynamic impact tests were conducted on coral reef limestone concrete specimens that had undergone 0, 10, 20, 30, 40,

and 50 cycles of wet-dry carbonation treatment. The impact loads considered were 0.2, 0.4, 0.6, and 0.8 MPa, respectively. As per the ISRM (International Society for Rock Mechanics) guidelines for dynamic analysis of rock-like substances, conducting a preliminary test prior to the official experiment is essential to verify the experiment's accuracy and reduce errors in the process. In the initial testing phase, semiconductor strain gauges were employed to measure three wave signals, and the uniformity of stress in the samples was confirmed through the three-wave technique. A test is deemed legitimate if the stress exerted at either end of the specimen is evenly distributed.
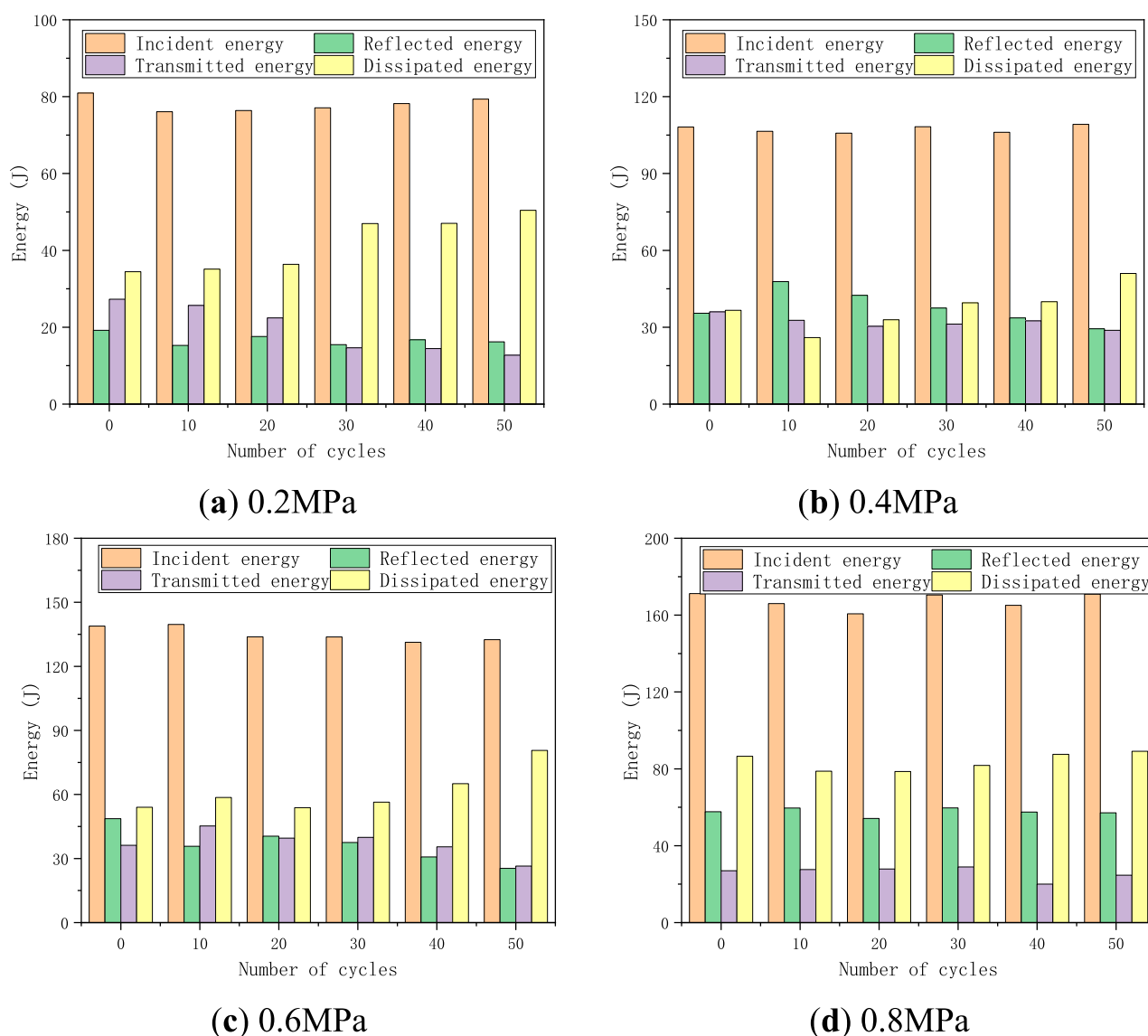
FIGURE 11
Impact of dry-wet-cycling carbonation cycles and impact load magnitude on energy distribution. **(A)** 0.2 MPa, **(B)** 0.4 MPa, **(C)** 0.6 MPa, **(D)** 0.8 MPa.

Figure 7A shows the voltage signals of the incident wave, reflected wave, and transmitted wave collected by the strain gauges during a single impact test, Incident Strain $\varepsilon_{In(t)}$, Reflected Strain $\varepsilon_{Re(t)}$ and Transmitted Strain $\varepsilon_{Tr(t)}$. The three-wave method was used for illustration and analysis, as shown in Figure 7B, the incident strain $\varepsilon_{In(t)}$ and the reflected strain $\varepsilon Re(t)$ roughly coincide with the transmitted strain $\varepsilon_{Tr(t)}$ after superposition ($\varepsilon_{In(t)}$ + $\varepsilon_{Re(t)}$ ≈ $\varepsilon_{Tr(t)}$). This indicates that dynamic stress uniformity was achieved in the reef limestone concrete sample during the impact loading test.

3.2.2 Dynamic strength and deformation characteristics

Figure 8 depicts the dynamic stress-strain curves of reef limestone concrete under different impact load conditions (after experiencing varying degrees of deterioration treatment). Both the number of deterioration cycles and the magnitude of the impact load

significantly influence the dynamic stress-strain response of the reef limestone concrete. The characteristic parameters of each test result are shown in Table 2. Among these, dynamic compressive strength is an important indicator of the sample's impact resistance. By using the dynamic peak strength and uniaxial compressive strength, another indicator of impact resistance, the Dynamic Increase Factor (DIF), can be calculated.

An examination of Figure 8 and Table 2 reveals that in the condition lacking any degradation treatment (n = 0), as the impact load escalates from 0.2 MPa to 0.8 MPa, there's a rise in dynamic peak stress from 68.20 MPa to 88 MPa, with corresponding increases of 23.87%, 29.03%, and 43.5%, in contrast to outcomes not influenced by deterioration. This indicates that the dynamic strength of the material enhances strain rate. Furthermore, with a total of 50 degradation cycles, the maximum dynamic stress at a 0.2 MPa impact load reaches 53 MPa, while impact loads of 0.4, 0.6 MPa, and

0.8 MPa exhibit increases of 25.8%, 52.8%, and 58.49% respectively. This suggests that as the extent of deterioration increases, so does the susceptibility of the specimen's dynamic mechanical characteristics to the rate of strain. However, with the increase in the number of deterioration cycles, the peak stress exhibits a consistent downward trend. As an illustration, at an impact load of 0.2 MPa, following 50 cycles of dry-wet carbonation, the stress-strain curve's post-peak phase shifts from closed to open, experiencing a reduction in peak stress by about 10–20 MPa. It should be noted that due to issues such as uneven crushing of reef limestone aggregate during specimen preparation and uneven composition of aggregate and cementitious materials in the mold, some samples did not maintain good dependency between peak strain, number of deterioration cycles, and impact load under dynamic load conditions.

Perform a nonlinear fitting curve of the strain rate-DIF for reef limestone concrete specimens with different degrees of deterioration. The fitting curve model is $DIF = \ln(a + b\dot{\varepsilon})$. The correlation coefficients are all greater than 95%. Figure 9 illustrates that in conditions of elevated strain rates, as the specimen's degradation depth progressively deepens, there's a rising trend in the logarithmic-DIF curve's slope for strain rate, signifying a gradual escalation in the strain rate impact of reef limestone concrete.

3.2.3 Dynamic fracture mode

Table 3 summarizes the fracture conditions of reef limestone concrete under dynamic impact after different degrees of deterioration treatment. The impact load and the number of dry-wet carbonation cycles jointly determine the final failure mode of the specimen. Initially, by maintaining a steady count of dry-wet carbonation cycles, the extent of the specimen's fragmentation is intimately linked to the intensity of the impact load. When the impact load is 0.2 MPa, the surface of the specimen fractures, showing splitting failure with good overall integrity. However, as the impact force escalates to either 0.6 or 0.8 MPa, the sample is utterly obliterated, resulting in tinier fractured particles, predominantly in a powdery state. d particles are smaller, mainly in a powdery form. Additionally, maintaining a steady impact load, there's a positive relationship between the extent of the specimen's fragmentation and the frequency of dry-wet carbonation cycles. When subjected to an impact force of 0.2 MPa, the sample lacking dry-wet carbonation results in minimal surface debris, in contrast to the sample that undergoes 50 cycles of dry-wet carbonation, leading to significant fractures. When the impact load reaches 0.6 MPa, it is visually evident from the size of the fractured particles that the deterioration causes severe internal damage to the specimen, and the pulverization characteristic of the specimen becomes more significant compared to the specimen without dry-wet carbonation treatment.

The reasons for the above phenomenon can be roughly summarized into the following two points. Initially, the dry-wet carbonation cycles lead to the primary presence of free water between the cement mortar and its boundary, consequently diminishing the robustness of the cement matrix and the specimen's interface, thereby increasing the likelihood of dynamic failure, particularly evident in the more pronounced failure rate between these phases. Under the cyclic action of external factors, the internal cracks of concrete will change from micro to macro (Kuang et al., 2023). Secondly, following the combined effects of dry-wet cycles and carbonation, the internal stress of reef limestone concrete

transitions from equilibrium to imbalance under dynamic forces. In a very short period, the specimen cannot achieve internal stress rebalancing through elastic unloading, leading to the absorptin of energy by internal cracks, which begin to propagate and eventually cause extensive fracturing of the specimen.

3.2.4 Energy dissipation characteristics

The principal cause of the specimen's malfunction is the loss of energy during its dynamic fracturing. Under impact load, reef limestone concrete experiences irreversible deformation, leading to irreversible energy dissipation. The dimensions, amount, and spatial arrangement of the fragments created post dynamic compression failure represent a large-scale expression of energy loss. Illustrated in Figure 10, the energy-time graph of a reef limestone concrete sample, after undergoing 50 cycles of dry-wet carbonation with a 0.4 MPa impact load, can be broadly segmented into four distinct phases for analysis.

In region A (0–130 μs), the incident stress wave has not yet acted on the reef limestone concrete specimen. As the incident energy starts to rise, the procedure progresses to stage B (130–200 μs), during which the specimen's energy absorption curve shows a roughly linear increase. The rate of expansion exceeds that of the energy transmitted and closely mirrors the energy reflected. Throughout the 200–300 μs phase, there's a consistent linear increase in the absorbed energy timeline, mirroring the pattern of energy transmission and exhibiting a growth rate surpassing that of the reflected energy. The reason is that following the stress wave's impact on the specimen, there's a buildup and development of internal damage, resulting in a multitude of new microcracks in the specimen and a steady rise in the energy absorbed. During the 300–350 μs phase, there's a steady decline in the rate of energy absorption, with the incoming, reflected, and transmitted energy levels stabilizing, signifying the stress wave's completion of its dynamic compression impact on the sample. The energy characteristic values of reef limestone concrete specimens subjected to different degrees of deterioration under various impact loads are summarized in Table 4.

Figure 11 displays the ratios of incoming, reflected, transmitted, and dissipated energy in reef limestone concrete when subjected to impact forces of 0.2, 0.4, 0.6, and 0.8 MPa. Comprehensive examination reveals that the variance in incident energy from the experiments remains below 5% under an identical impact load, suggesting a uniform impact load across the experiment. With an increasing number of deterioration cycles, the energy dissipated during the fracturing of reef limestone concrete gradually increases, indicating that the dry-wet-carbonation cycling has a promoting effect on dissipated energy. If the count of dry-wet cycling-carbonation cycles surpasses 30, there's a notable increase in the expansion of energy that has dissipated. As an example, with an impact load of 0.2 MPa, there's a 46.39% rise in the amount of energy lost as the deterioration cycles escalate from 0 to 50. Conversely, the transmitted energy shows an overall declining trend with the increase in deterioration cycles. The main reason for this occurrence is the escalated internal harm to reef limestone concrete post-degradation. In the dynamic compression phase, increased energy is used to enlarge various cracks and move debris, causing a rise in energy dissipation and complicating the stress wave's journey through the specimen to the transmission rod, thereby diminishing the energy transmitted. Additionally, the reflected energy does

not show a clear trend, which may be attributed to the inherent discreteness of the specimen itself.

4 Conclusion

The SHPB impact tests explored how dry-wet-cycling carbonation cycles and the extent of impact load influence the dynamic failure traits and energy development in reef limestone concrete, culminating in these key findings:

(1) With the rise in dry-wet-cycling carbonation cycles, there's a shift in the phenolphthalein color indicator from a strong magenta hue to a slow decline, signifying a steady reduction in the bonding strength of the specimens' internal structure. There is a notable reduction in the relative dynamic elastic modulus, accompanied by a substantial effect of size and a marked acceleration in the rate of mass loss.

(2) After undergoing dry-wet-cycling treatment, the quasi-static compressive and tensile strengths of reef limestone concrete exhibit an overall decreasing trend, with the reduction in tensile strength being less pronounced than in compressive strength. As dynamic compressive strength diminishes, the frequency of dry-wet-cycling cycles intensifies the vulnerability of the DIF value to strain rates in reef limestone concrete.

(3) The total count of dry-wet-cycling cycles combined with the intensity of the impact load collectively dictate the ultimate mode of failure for the specimens. Both factors facilitate the failure, transitioning the fracture mode from surface splitting to catastrophic failure, indicating an increase in the fragility of the material's internal structure.

With the rise in dry-wet-cycling cycles, there's a gradual increase in the energy lost during reef limestone concrete fracturing, alongside a general decrease in the energy transmitted, and the reflected energy lacks a distinct pattern.

Data availability statement

The original contributions presented in the study are included in the article/supplementary material, further inquiries can be directed to the corresponding author.

Author contributions

JL: Project administration, Writing–review and editing, Funding acquisition, Supervision. FL: Writing–review and editing, Conceptualization, Resources, Validation, Visualization. MM: Investigation, Software, Writing–review and editing. JZ: Writing–review and editing, Methodology, Project administration, Writing–original draft. RF: Data curation, Resources, Software, Validation, Writing–original draft.

Funding

Conflict of interest

The authors declare that the research was conducted in the absence of any commercial or financial relationships that could be construed as a potential conflict of interest.

Publisher's note

All claims expressed in this article are solely those of the authors and do not necessarily represent those of their affiliated organizations, or those of the publisher, the editors and the reviewers. Any product that may be evaluated in this article, or claim that may be made by its manufacturer, is not guaranteed or endorsed by the publisher.

References

Dai, F., Huang, S., Xia, K. W., and Tan, Z. (2010). Some fundamental issues in dynamic compression and tension tests of rocks using split Hopkinson pressure bar. *Rock. Mech. Rock. Eng.* 43, 657–666. doi:10.1007/s00603-010-0091-8

Deng, Z. H., Huang, H. Q., Ye, B. L., Wang, H., and Xiang, P. (2020a). Investigation on recycled aggregate concretes exposed to high temperature by biaxial compressive tests. *Constr. Build. Mater.* 244, 118048. doi:10.1016/j.conbuildmat.2020.118048

Deng, Z. H., Huang, H. Q., Ye, B. L., and Xiang, P. (2020b). Mechanical performance of RAC under true-triaxial compression after high temperatures. *J. Mater. Civ. Eng.* 32 (8), 04020194. doi:10.1061/(ASCE)MT.1943-5533.0003231

Deng, Z. H., Wu, D., and Wang, Y. M. (2022). Mechanical properties and failure criteria of coral concrete under true triaxial compression. *J. Mater. Sci.* 57, 17622–17636. doi:10.1007/s10853-022-07728-1

Donnini, J. (2019). Durability of glass FRCM systems: effects of different environments on mechanical properties. *Compos. Part. B-Eng.* 174, 107047. doi:10.1016/j.compositesb.2019.107047

Fan, R., Gong, H. L., Luo, Y., Zhang, J., and Li, X. (2023). Experimental characterization of dynamic strength and failure behavior of saturated reef limestone concrete under biaxial stress constraint. *Constr. Build. Mater.* 403, 133116. doi:10.1016/j.conbuildmat.2023.133116

Fu, Q., Bu, M., Su, L., Guo, B., Chen, L., Song, H., et al. (2021). Dynamic triaxial compressive response and failure mechanism of basalt fibre-reinforced coral concrete. *Int. J. Impact. Eng.* 156, 103930. doi:10.1016/j.ijimpeng.2021.103930

He, R., Li, S., Fu, C., Zhou, K., and Dong, Z. (2022). Influence of cyclic drying–wetting and carbonation on oxygen diffusity of cementitious materials: interpretation from the perspective of microstructure. *J. Mater. Civil. Eng.* 34 (10), 04022256.

Huang, S., Liu, H., and Xia, K. (2014). A dynamic ball compression test for understanding rock crushing. *Rev. Sci. Instrum.* 85, 123902. doi:10.1063/1.4902836

Jiang, C., Huang, Q., Gu, X. L., and Zhang, W. (2017). Experimental investigation on carbonation in fatigue-damaged concrete. *Cem. Concr. Res.* 99, 38–52. doi:10.1016/j.cemconres.2017.04.019

Kuang, Y., Wang, Y., Xiang, P., Tao, L., Wang, K., Fan, F., et al. (2023). Experimental and theoretical study on the fatigue crack propagation in stud shear connectors. *Materials* 16 (2), 701. doi:10.3390/ma16020701

Lahiri, S. K., Shaw, A., Ramachandra, L. S., and Maity, D. (2022). Fracture in concrete gravity dams under dynamic loading conditions. *Eng. Anal. Bound. Elem.* 143, 591–605. doi:10.1016/j.enganabound.2022.07.008

Li, Q. M., Li, X. X., Wang, Y. Z., Xie, T., and Zhou, S. (2021). Effects of coarse aggregate content and salt solution concentration on freeze-thaw damage in concrete. *J. Mater. Civ. Eng.* 33, 04021318. doi:10.1061/(ASCE)MT.1943-5533.0003940

Liu, J. M., Ou, Z. W., Peng, W., Guo, T., Deng, W., and Chen, Y. (2018). Literature review of coral concrete. *Arab. J. Sci. Eng.* 43, 1529–1541. doi:10.1007/s13369-017-2705-x

Liu, P. F., Liu, J., and Bi, J. (2023). Experimental and theoretical study of dynamic mechanical behavior of concrete subjected to triaxial confining and impact loads. *J. Build. Eng.* 64, 105715. doi:10.1016/j.jobe.2022.105715

Luo, Y., Gong, H. L., Wei, X. Q., Zheng, S., Pei, C., and Li, X. (2023). Dynamic compressive characteristics and damage constitutive model of coral reef limestone with different cementation degrees. *Constr. Build. Mater.* 362, 129783. doi:10.1016/j.conbuildmat.2022.129783

Ma, H., Yue, C., Yu, H., Mei, Q., Chen, L., Zhang, J., et al. (2020). Experimental study and numerical simulation of impact compression mechanical properties of high strength coral aggregate seawater concrete. *Int. J. Impact. Eng.* 137, 103466. doi:10.1016/j.ijimpeng.2019.103466

Ma, L., Li, Z., Liu, J., Duan, L., and Wu, J. (2019). Mechanical properties of coral concrete subjected to uniaxial dynamic compression. *Constr. Build. Mater.* 199, 244–255. doi:10.1016/j.conbuildmat.2018.12.032

Meddah, M. S., Zitouni, S., and Belaabes, S. (2010). Effect of content and particle size distribution of coarse aggregate on the compressive strength of concrete. *Constr. Build. Mater.* 24, 505–512. doi:10.1016/j.conbuildmat.2009.10.009

Mumenya, S. W., Tait, R. B., and Alexander, M. G. (2010). Mechanical behaviour of textile concrete under accelerated ageing conditions. *Cem. Concr. Res.* 32, 580–588. doi:10.1016/j.cemconcomp.2010.07.007

Qin, Q., Meng, Q., Mei, Q., Wu, K., Wang, C., and Zhang, J. (2023). Dynamic response characteristics of coral reef sand concrete under impact loading. *J. Build. Eng.* 66, 105847. doi:10.1016/j.jobe.2023.105847

Sim, J. I., Yang, K. H., and Jeon, J. K. (2013). Influence of aggregate size on the compressive size effect according to different concrete types. *Constr. Build. Mater.* 44, 716–725. doi:10.1016/j.conbuildmat.2013.03.066

Uddin, M. T., Mahmood, A. H., Kamal, M. R. I., Yashin, S., and Zihan, Z. U. A. (2017). Effects of maximum size of brick aggregate on properties of concrete. *Constr. Build. Mater.* 134, 713–726. doi:10.1016/j.conbuildmat.2016.12.164

Wang, J., Su, H., and Du, J. (2018). Influence of coupled effects between flexural tensile stress and carbonation time on the carbonation depth of concrete. *Constr. Build. Mater.* 190, 439–451. doi:10.1016/j.conbuildmat.2018.09.117

Wu, J. W., Ma, L. J., Kong, X. L., Luo, Z. M., and Duan, L. Q. (2020). Dynamic properties of coral concrete under impact load. *J. Build. Mater.* 23, 581–588. (in Chinese). doi:10.3969/j.issn.1007-9629.2020.03.014

Wu, W. J., Wang, R., Zhu, C. Q., Meng, Q., and Liu, H. (2019). Experimental study on dynamic compression performance of coral aggregate concrete. *J. Build. Mater.* 22, 7–14. (in Chinese). doi:10.3969/j.issn.1007-9629.2019.01.002

Xu, H., Wang, Z., Shao, Z., Cai, L., Jin, H., Zhang, Z., et al. (2021). Experimental study on durability of fiber reinforced concrete: effect of cellulose fiber, polyvinyl alcohol fiber and polyolefin fiber. *Constr. Build. Mater.* 306, 124867. doi:10.1016/j.conbuildmat.2021.124867

Yin, S., Jing, L., Yin, M., and Wang, B. (2019). Mechanical properties of textile reinforced concrete under chloride wet-dry and freeze-thaw cycle environments. *Cem. Concr. Res.* 96, 118–127. doi:10.1016/j.cemconcomp.2018.11.020

Zhang, D., and Shao, Y. (2016). Early age carbonation curing for precast reinforced concretes. *Constr. Build. Mater.* 113, 134–143. doi:10.1016/j.conbuildmat.2016.03.048

Zhang, M. C., Luo, Y., Gong, H. L., Zhu, Y., and Li, X. (2023). Fine characterization of pore structures in coral reef limestones based on three-dimensional geometrical reconstruction. *Mar. Georesour. Geotec.* 42, 721–735. doi:10.1080/1064119X.2023.2215246

Zhang, X. B., Quan, Y., Cao, G. H., Tang, S., Ou, W., Cao, J., et al. (2024). Influence of waste glass on concrete strength and permeability during dry-wet cycles. *Eur. J. Environ. Civ. En.*, 1–22. doi:10.1080/19648189.2024.2365960

Zhou, W., Feng, P., and Lin, H. W. (2020). Constitutive relations of coral aggregate concrete under uniaxial and triaxial compression. *Constr. Build. Mater.* 251, 118957. doi:10.1016/j.conbuildmat.2020.118957

Check for updates

Fatigue damage analysis of plain and steel fiber-reinforced concrete material based on a stiffness degradation microplane model

Changjin Qin[1,2], Xiaogang Dong[2], Biao Wu[2], Lidong Cai[2], Shaohua Wang[2] and Qing Xia[1]*

[1]School of Civil Engineering and Transportation, South China University of Technology, Guangzhou, China, [2]China Construction Third Bureau First Engineering Co., Ltd., Wuhan, Hubei, China

Steel fiber-reinforced concrete material has garnered significant attention in structure design due to its excellent resistance to fatigue damage. The application of the plain concrete microplane model is extended to steel fiber-reinforced concrete by modifying the stress-strain boundary conditions on the microplane and then extended to fatigue damage analysis by considering fatigue-related material stiffness, mainly concerned with tensile damage, mainly concerned with tensile damage. The normal positive strain on the micro-plane is regarded as the fatigue variable, and the fatigue history variable is the accumulation of the fatigue variable during the loading. The relationship between the fatigue history variable and the material stiffness fatigue degradation function is established. In the numerical implementation, the crack band model is combined to reduce the mesh sensitivity caused by strain localization. During the numerical simulation, the parameters of plain concrete, steel fiber-reinforced concrete, and the material fatigue degradation function can be calibrated sequentially, requiring only a few benchmark tests for accurate parameter calibration. The numerical results show that this model can be used for the fatigue damage analysis of plain concrete and steel fiber-reinforced concrete material. It is expected to be used for the refined analysis of concrete structures under complex loading conditions and structural forms in the future, providing convenience to engineering design, evaluation, and optimization.

KEYWORDS

material stiffness degradation, fatigue damage, plain concrete, steel fiber-reinforced concrete, microplane model

1 Introduction

Concrete material has a wide range of applications in infrastructure, including bridges, roads, high-rise buildings, and the foundations of power machinery. However, concrete structures are often subjected to cyclic loads, such as traffic (Zhang et al., 2024) and wind, which can lead to material fatigue stiffness degradation (Riyar et al., 2023). This can gradually deteriorate the structural performance, potentially leading to structural failure. Fiber-reinforced concrete material has emerged as a promising

solution to improve the durability and safety of concrete structures. Incorporating short fibers, including steel or polypropylene fibers, into fiber-reinforced concrete results in a composite material that exhibits enhanced resistance to cracking, improved toughness, and fatigue properties (Carlesso et al., 2019). It is imperative to investigate the fatigue characteristics of plain and fiber-reinforced concrete and their damage evolution patterns. This is crucial for precisely predicting and assessing the service life of concrete structures and developing adequate maintenance and reinforcement strategies.

As early as the late 19th century, engineers established the S-N curve (Aas-Jakobsen, 1970; Cornelissen, 1984; Miarka et al., 2022) based on experimental data to reflect the fatigue life of concrete at different stress levels. The S-N curve also applies to fiber-reinforced concrete, but it is necessary to consider the fiber type, volume fraction, and orientation effects on fatigue life. The S-N curve is a reasonable method for estimating the anticipated lifespan under disparate stress levels. However, it requires a substantial corpus of experimental data and may not accurately reflect the intricate stress conditions. With the advent of fracture mechanics, the Paris law (Paris and Erdogan, 1963) was introduced to describe the crack propagation rate in plain concrete under constant load. For fiber-reinforced concrete material, the parameters in the Paris law must be adjusted to reflect the hindering effect of fibers on crack propagation. The Paris law is suitable for single crack extension analysis under simple loading conditions, but its application is limited under complex or variable loading. Hillerborg et al. considered a virtual crack in front of a visible crack in concrete and cohesive stress between the interfaces of the virtual crack (Hillerborg et al., 1976). The cohesive zone model simulates the nonlinear fracture behavior of concrete by defining the relationship between the cohesive stress between the crack interfaces and the crack opening displacement and extends the model to fatigue loading by correcting the relationship between the cohesive stress and the crack opening displacement (Gylltoft, 1984). For fiber-reinforced concrete, the cohesive zone model needs to consider further the bridging effect of fibers, which can increase the cohesive stress at the crack surface and thus slow down the crack extension. The damage constitutive model (Marigo, 1985), on the other hand, describes the degradation of the mechanical properties of concrete under repetitive loading from a material microscopic point of view by introducing damage variables, which can be extended to fatigue loading by introducing fatigue history variables and adjusting the damage evolution conditions. This model considers the emergence and expansion of microcracks within concrete and their effect on the overall material properties. For fiber-reinforced concrete, the damage constitutive model needs to consider the effect of fibers on the damage evolution, including the reinforcing and toughening effects of fibers (Li et al., 2024).

In addition to the macro-mechanical modeling of concrete, researchers began to seek breakthroughs in micro-mechanical theories to study concrete constitutive relationships, such as the microplane damage model (Caner and Bažant, 2013a; Caner and Bazant, 2013b). The microplane, which represents a plane perpendicular to any direction at a material point, can describe the interactions between weak planes, cracks, and different defects on microstructures in all directions and can be used to model the inelastic behavior of quasi-brittle materials (e.g., concrete), and has been developed into its seventh version up to the present day.

Subsequently, Caner et al. (2013) extended the normal concrete microplane model to fiber concrete by improving the stress-strain boundary conditions on the microplane to describe the pullout and fracture behavior of fibers in fiber-reinforced concrete. Kirane and Bažant (2015) incorporated the fatigue effect into the normal concrete microplane model by introducing a fatigue history variable to quantify the cyclic damage accumulation of the material. However, there is still a lack of microplane models applicable to fatigue damage studies of fiber-reinforced concrete. Although the performance of Engineered Cementitious Composites (ECC) (Lu et al., 2017; Huang et al., 2022; Zhu et al., 2022) and Ultra High-Performance Fiber Reinforced Concrete (UHPFRC) (Wille et al., 2014; Yoo et al., 2017; Nguyen et al., 2023) is higher than that of ordinary fiber-reinforced concrete. However, considering the cost and construction conditions, steel fiber-reinforced concrete specimen (SFRC) (Li et al., 2018; Chu et al., 2023) is still one of the most common FRCs used in engineering. Although compression also leads to fatigue-related material stiffness degradation, this paper will focus on the tensile fatigue damage of SFRC, considering the significant difference between concrete's tensile and compressive properties.

In the following study, Section 2 presents the basic framework of the microplane damage model for plain concrete, including the three processes of projecting macrostrain to micro-strain, establishing the stress-strain relationship on the microplane, and homogenizing microstress to macro-stress. Section 3 describes how to extend the microplane model from plain concrete to steel fiber-reinforced concrete and how to consider fatigue effects in the microplane damage model. Section 4 summarises the numerical algorithm for the microplane model, parameter calibration, and validation of the concrete microplane damage model. Section 5 compares the fatigue damage analysis of plain and steel fiber-reinforced concrete with experimental results. Section 6 summarises the further research focus. Finally, Section 7 summarises the main conclusions of the paper.

2 Microplane damage model for plain concrete

2.1 A framework for microplane theory

The concrete microplane damage model (Caner and Bažant, 2013a; Caner and Bazant, 2013b) consists of three parts: physical mapping of "macro to micro physical variables," establishment of constitutive relationship at the micro scale, and homogenization of "micro to macro physical variables," as shown in Figure 1.

2.2 Macroscale to microscale strain decomposition

The microplane model portrays the mechanical behavior of concrete materials at the microscopic level in terms of stresses and strains in vector form, so it is necessary to transform the stresses or strains at the macroscopic level into the stresses or strains at the microscopic level. According to the treatment of the relationship between the macroscopic stress tensor or macroscopic
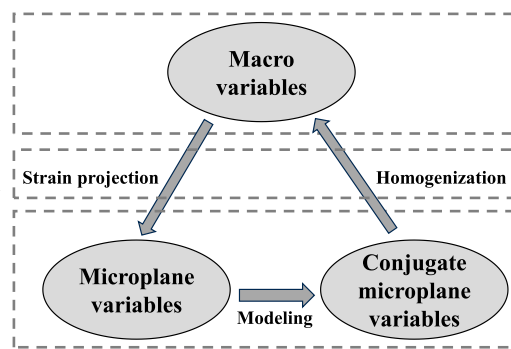
FIGURE 1
Framework for microplane theory.
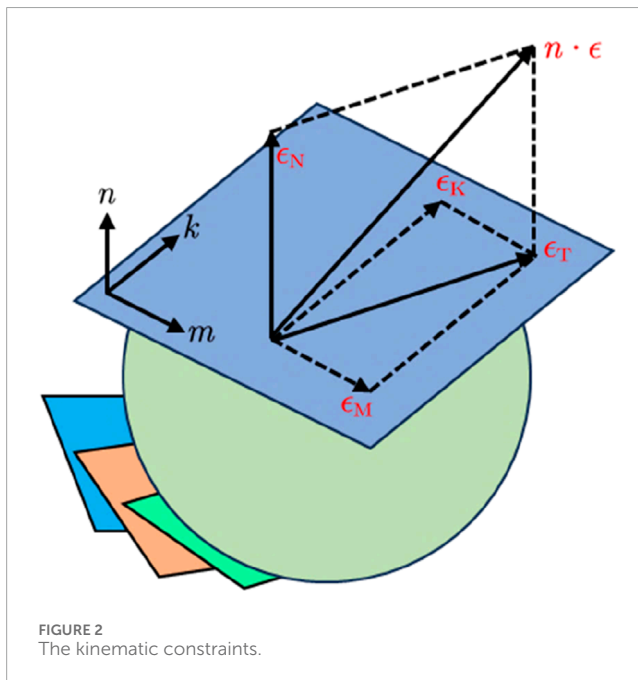
FIGURE 2
The kinematic constraints.

strain tensor and the stress or strain vector on the microplane, they are usually categorized into static and kinematic constraints. They can be understood as the projection of the macroscopic stress tensor on the microplane to obtain the corresponding stress vector and the projection of the macroscopic strain tensor on the microplane to obtain the corresponding strain vector, respectively. Due to the strain-softening behavior of quasi-brittle materials such as concrete, the kinematic constraints shown in Figure 2 are used in the concrete microplane damage model to ensure the stability of the model when analyzing strain softening.

As shown in Figure 2, the strain vector e on the microplane i (normal vector is denoted as n) is expressed as the projection of the macroscopic strain vector ϵ by Equation 1.

$$e = n \cdot \epsilon = e_N n + e_T \tag{1}$$

where $e_N = \epsilon_N = N{:}\epsilon$ is the normal strain component on the microplane, $e_T = \epsilon_T = T \cdot \epsilon$ is the tangential shear strain vector on

the microplane, $|e_T| = \sqrt{\epsilon_K^2 + \epsilon_M^2}$; N and T are the corresponding projection operators. Further, the tangential strain e_T in the microplane is used to characterize plasticity and friction; the normal strain e_N is distinguished into the tensile strain (i.e., the part where $e_N > 0$) to characterize the tensile ability, and the compressive strain (i.e., the part where $e_N < 0$) to characterize the compressive ability, while the compressive strain can be decomposed into the volume component e_V and the deviatoric component e_D by Equation 2.

$$e_N = e_V + e_D = V{:}\epsilon + D{:}\epsilon \tag{2}$$

where $V = \frac{1}{3}I$ is the volume component, $D = n \otimes n - \frac{1}{3}I$ denotes the bias obtained by subtracting the volume component from the total strain, and I is the third-order unit tensor.

2.3 Stress-strain relationships on microplane

2.3.1 Elastic response and stiffness degradation

Unlike the traditional tensor-type constitutive model, the microplane model defines constitutive relations on a general plane (microplane) in any direction at a material point. If the strain component on the microplane has been obtained from kinematic constraints, the general expression for the stress on the microplane is given by Equation 3.

$$
\begin{aligned}
\sigma_N(t) &= \mathcal{F}_{\tau=0}^t [\varepsilon_N(\tau), \varepsilon_T(\tau)], \\
\sigma_L(t) &= \mathcal{G}_{\tau=0}^t [\varepsilon_N(\tau), \varepsilon_T(\tau)], \\
\sigma_M(t) &= \mathcal{H}_{\tau=0}^t [\varepsilon_N(\tau), \varepsilon_T(\tau)].
\end{aligned}
\tag{3}
$$

where $\mathcal{F}, \mathcal{G}, \mathcal{H}$ is the history functional of the microplane strain at moment t.

When the stress on the microplane develops in the elastic range, the normal strain is not decomposed into its volume component e_V and bias component e_D, and the modulus of elasticity, shear modulus, and normal strain e_N are used directly to solve for the stress on the microplane. The elasticity modulus E_N and shear modulus E_T on the microplane can be defined as

$$E_N = \frac{E}{1-2\nu}, E_T = E_N \frac{1-4\nu}{1+\nu}, \tag{4}$$

where E is the macroscopic level modulus of elasticity, v is Poisson's ratio, $E_N = K/3$, and K is the bulk modulus. Since E_N and E_T are required to be non-negative, Equation 4 holds for Poisson's ratio $v \in [-1, 0.25]$, and the Poisson's ratio v of concrete (about 0.18) is satisfied. Starting from the microplane model M3 (Bažant et al., 1996), the concept of a stress-strain boundary is introduced, within which the response is considered to be elastic with constant microplane elastic stiffness E_N and E_T.

In addition, when the material is in the elastic stage, the modulus of elasticity is gradually degraded due to the progression of damage. The evolution of the microplane normal elastic modulus needs to be considered in the damage variables. Here the current value of the microplane normal elastic modulus damage is calculated by retrieving the largest magnitude of positive and negative normal strains $\epsilon_N^{0+}, \epsilon_N^{0-}$ stored so far. For the case of $\sigma_N^0 \geqslant 0$, it is calculated using Equation 5.

$$E_N = E_{N0}e^{-c_{13}\epsilon_N^{0+}}f(\mathcal{F}) \, \text{but}, E_N = E_{N0}, \text{if}, \sigma_N^0 > E_{N0}\epsilon_N \, \text{and} \, \sigma_N^0 \Delta \epsilon_N < 0 \tag{5}$$

and in the case of $\sigma_N^0 < 0$, it is calculated using Equation 6.

$$E_N = E_{N0}\left(e^{-c_{14}|\epsilon_N^{0-}|/(1+c_{15}\epsilon_e)} + c_{16}\epsilon_e\right). \tag{6}$$

In Equation 5, the fatigue degradation function $f(\mathcal{F})$ and the meaning of the parameters will be described later. At this point the stress in the normal direction of the microplane elastic stage is given by Equation 7.

$$\sigma_N^e = \sigma_N^0 + E_N\Delta\epsilon_N, \tag{7}$$

It is worth noting that Equation 5 is used in order to ensure that the unloading moves towards the origin along the initial elastic slope after intersection, rather than continuing along the original unloading path after intersection.

2.3.2 Stress-strain boundaries on microplanes

As shown in Figure 2, the strain on the microplane is divided into normal strain and tangential strain, and normal strain can be divided into tensile strain and compressive strain. For normal tensile strain, the tensile normal stress-strain boundary is introduced to characterize the inelastic response on the microplane. For normal compression strain, the key innovation of M7 that significantly improves it is that when the microplane is under pressure, it no longer separately determines whether the volume stress and deviator stress exceed the boundary, but calculates the two boundary values separately and then sums them up, i.e., $\sigma_N^b = \sigma_V^b + \sigma_D^b$. Then it is compared with the normal stress σ_N^e calculated using the elastic increment method to determine the normal stress value on the microplane. The study found this improvement is also logically consistent with elastic and damage potential energy. It effectively avoids problems such as excessive lateral expansion during tensile response and normal stress self-locking in the softening section. In addition, in M7, the boundary function about the shear resultant force σ_τ is defined, which solves the problem of direction dependence of the results due to the arbitrary selection of shear component coordinates. Therefore, in the microplane model

M7 (Caner and Bažant, 2013a; Caner and Bazant, 2013b), the boundary functions that characterize the inelastic response on the microplane are normal tensile stress-strain boundary, compressive deviatoric stress-strain boundary, compressive volume stress-strain boundary and plastic-friction stress-strain boundary (shear boundary).

2.3.2.1 Normal tensile stress-strain boundary

Figure 3A shows that the normal tensile stress-strain boundary controls the tensile fracture behavior, calculated by Equation 8.

$$\sigma_N^b = Ek_1\beta_1 e^{-\langle \epsilon_N - \beta_1 c_2 k_1 \rangle / (c_4 \epsilon_e \text{sgn}(\epsilon_e) + k_1 c_3)}. \tag{8}$$

where $\beta_1 = -c_1 + c_{17}e^{-c_{19}\langle \epsilon_e - c_{18}\rangle}$. The recommended values of the parameters and their significance in this section will be described in detail later.

2.3.2.2 Compressive deviatoric stress-strain boundary

Figure 3B shows that the compression deviatoric stress-strain boundary is used to model the damage evolution under compression conditions, calculated by Equation 9.

$$\sigma_D^b = -\frac{Ek_1\beta_3}{1 + \left[\langle -\epsilon_D\rangle / (k_1\beta_2)\right]^2}. \tag{9}$$

where $\gamma_0 = f_{c0}'/E_0 - f_c'/E$, $\gamma_1 = e^{\gamma_0}\tanh\left(c_9\langle -\epsilon_V\rangle / k_1\right)$, $\beta_2 = c_5\gamma_1 + c_7$, $\beta_3 = c_6\gamma_1 + c_8$. f_c' denotes the compressive strength of the concrete material, and f_{c0}' is the reference value of compressive strength for model calibration.

2.3.2.3 Compressive volume stress-strain boundary

As shown in Figure 3C, the compressive volumetric stress-strain boundary is used to model pore collapse and expansion rupture of the material, calculated by Equation 10.

$$\sigma_V^b = -Ek_1k_3e^{-\frac{\epsilon_V}{k_1\alpha}}, \tag{10}$$

where $\alpha = \frac{k_5}{1+\epsilon_e}\left(\frac{\epsilon_I^0 - \epsilon_{III}^0}{k_1}\right)^{c_{20}} + k_4$. $\epsilon_I^0, \epsilon_{III}^0$ are the maximum and minimum principal strains at the beginning of the step, and $\epsilon_e = \langle -\sigma_V^0/E_{N0}\rangle$, where $\langle x \rangle = \max(x, 0)$.

2.3.2.4 Plastic-friction stress-strain boundary (shear boundary)

As shown in Figure 3D, the plastic-friction boundary is used to model the shear behavior of the material, calculated by Equation 11.

$$\sigma_T^b = F_T(-\sigma_N) = \frac{E_T k_1 k_2 c_{10}\langle -\sigma_N + \sigma_N^0\rangle}{E_T k_1 k_2 + c_{10}\langle -\sigma_N + \sigma_N^0\rangle}. \tag{11}$$

where $\sigma_N^0 = \langle E_T k_1 c_{11} - c_{12}\langle \epsilon_V\rangle\rangle$.

2.3.3 Yielding and plastic flow criteria on microplane

The yield condition and plastic flow criterion on the microplane are defined as follows: when the stress on the microplane lies within the stress-strain boundary, the stress-strain on the microplane is in the elastic phase. At this time, the stress is
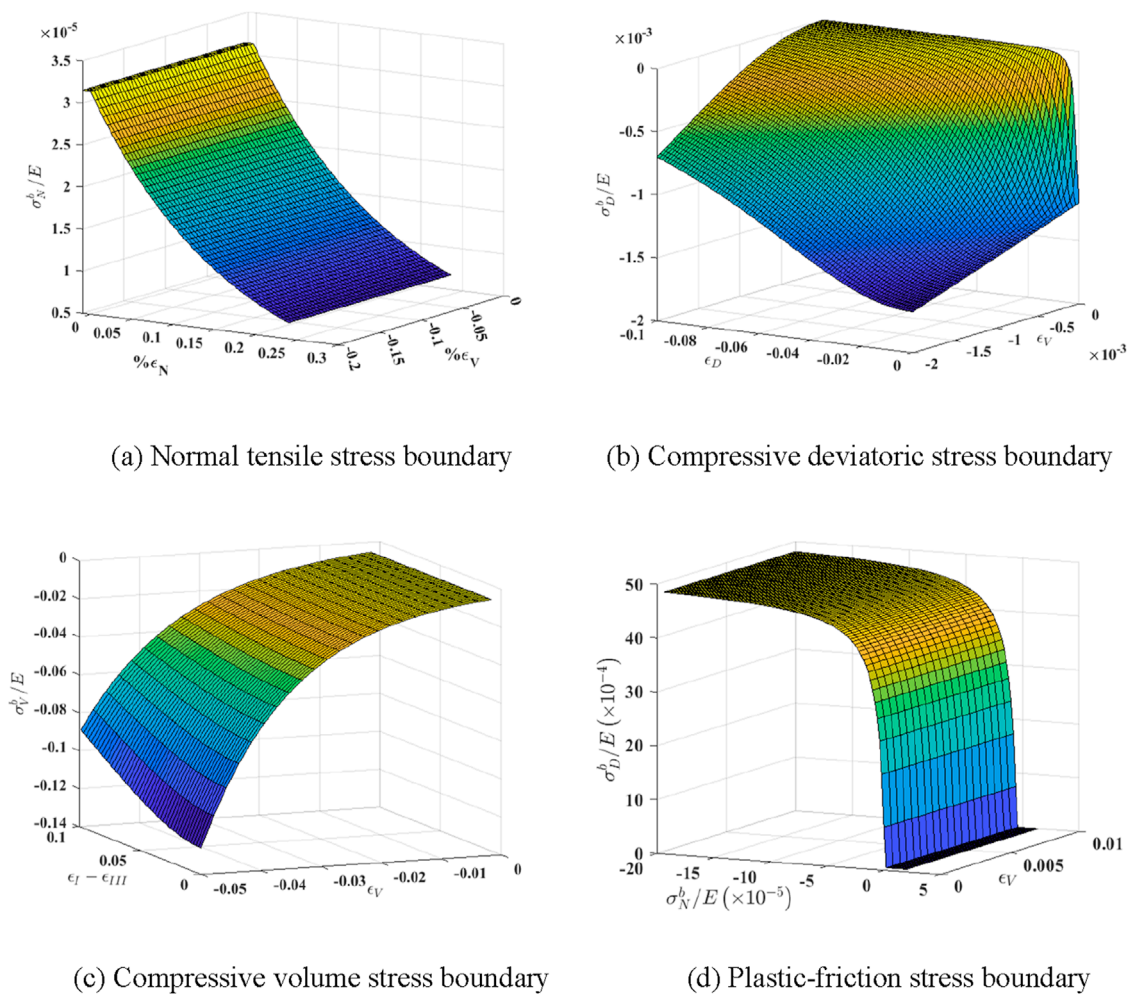
FIGURE 3
Stress-strain boundaries on the microplane. **(A)** Normal tensile stress boundary. **(B)** Compressive deviatoric stress boundary. **(C)** Compressive volume stress boundary. **(D)** Plastic-friction stress boundary.

given by σ_N^e in Equation 7. When the stress on the microplane exceeds the stress-strain boundary, the strain remains, and the stress falls back to the boundary. The normal stress is evaluated using Equation 12.

$$\sigma_N = \max\left[\min\left(\sigma_N^e, \sigma_N^b\right), \sigma_V^b + \sigma_D^b\right]. \tag{12}$$

The shear stress on the microplane is given by Equation 13.

$$\sigma_\tau = \min\left(|\sigma_\tau^e|, \sigma_\tau^b\right). \tag{13}$$

Where the incremental, cumulative form of the formula for calculating the shear stress in the elastic phase on the microplane is given by Equations 14–16.

$$\sigma_\tau^e = \sqrt{\left(\sigma_M^0 + E_T \Delta \epsilon_M\right)^2 + \left(\sigma_L^0 + E_T \Delta \epsilon_L\right)^2}, \tag{14}$$

$$\sigma_M = \sigma_M^0 + \Delta \sigma_M, \sigma_L = \sigma_L^0 + \Delta \sigma_L, \tag{15}$$

$$\Delta \sigma_M = E_T \Delta \epsilon_M \frac{\sigma_\tau}{\sigma_\tau^e}, \Delta \sigma_L = E_T \Delta \epsilon_L \frac{\sigma_\tau}{\sigma_\tau^e}. \tag{16}$$

2.4 Homogenization from microscale to macroscale

After defining the stress-strain relationship on the microplane, the principle of virtual work is applied to establish the equation between the microplane stress vector and the macroscopic stress tensor, from which the macroscopic stress tensor σ_{ij} satisfies Equation 17.

$$\frac{2\pi}{3} \sigma_{ij} \delta \epsilon_{ij} = \int_\Omega (\sigma_N \delta \epsilon_N + \sigma_L \delta \epsilon_L + \sigma_M \delta \epsilon_M) d\Omega \tag{17}$$

where Ω is the surface of the unit hemisphere and $2\pi/3$ is the volume of the hemisphere, the integral is regarded as a homogenization of the microplane contributions in different directions within the material. Due to $\delta \epsilon_N = N_{ij} \delta \epsilon_{ij}, \delta \epsilon_L = L_{ij} \delta \epsilon_{ij}$ and $\delta \epsilon_M = M_{ij} \delta \epsilon_{ij}$, from the arbitrariness of the variation $\delta \epsilon_{ij}$, the equilibrium relation can be obtained as Equations 18, 19.

$$\sigma_{ij} = \frac{3}{2\pi} \int_\Omega s_{ij} d\Omega \approx 6 \sum_{\mu=1}^{N_m} w_\mu s_{ij}^{(\mu)} \tag{18}$$

$$s_{ij} = \sigma_N N_{ij} + \sigma_L L_{ij} + \sigma_M M_{ij}, \qquad (19)$$

The integral is approximated by the optimal Gaussian integral formula for the sphere, denoting the weighted sum of microplane in the direction $\boldsymbol{n}_\mu$, with the weight w_μ normalized, so $\sum_\mu w_\mu = 1/2$. For better accuracy in the far-peak post-softening, 37 microplane are recommended to be preferred.

3 Microplane model extend to steel fiber-reinforced concrete and fatigue damage

3.1 Extend to fiber-reinforced concrete

The simplest way to extend the plain concrete microplane model to make it applicable to SFRC containing materials such as steel fibers is to adjust the stress-strain boundary conditions on the microplane (Caner et al., 2013). First, fibers usually increase the tensile capacity of the concrete material (Jiang et al., 2023; Lakavath et al., 2024), so the effect of steel fiber reinforcement needs to be introduced on the normal tensile stress-strain boundary. The contribution of fiber reinforcement is given by a simplified form of the Kholmyansky equation (Kholmyansky, 2002), as Equation 20.

$$\sigma_N^f = \begin{cases} Ep_1 k_1 \langle \epsilon_N/k_1 \rangle e^{-p_2 \langle \epsilon_N/k_1 \rangle}, \text{if} \epsilon_N/k_1 < 1/p_2 + p_4. \\ Ep_1 k_1/p_2 e^{-1}, \text{if} 1/p_2 + p_4 \leqslant \epsilon_N/k_1 < p_3. \\ Ep_1 k_1 \langle \epsilon_N/k_1 - p_3 + 1/p_2 \rangle e^{-p_2 \langle \epsilon_N/k_1 - p_3 + 1/p_2 \rangle}, \text{if} p_3 \leqslant \epsilon_N/k_1. \end{cases} \qquad (20)$$

This contribution is obtained by the gradual activation of the bridging of the fibers during the development of the crack, as shown in Figure 4. Assuming parallel coupling of the fibers and the matrix, the normal stress on the microplane is Equation 21.

$$\sigma_N^{bf} = \sigma_N^b + \sigma_N^f. \qquad (21)$$

where σ_N^{bf} is the total normal stress of the fiber-reinforced concrete, σ_N^b is the normal stress of the plain concrete matrix, and σ_N^f is the normal stress of steel fiber contribution given by Equation 20. Therefore, in the microplane model of fiber-reinforced concrete, Equation 12 is modified as Equation 22.

$$\sigma_N = \max\left[\min\left(\sigma_N^e, \sigma_N^{bf}\right), \sigma_V^b + \sigma_D^b\right]. \qquad (22)$$

In addition, the tensile capacity that steel fiber-reinforced concrete can withstand changes (increases or decreases) before cracks develop. Therefore, the normal tensile stress-strain boundary Equation 8 of the plain concrete matrix needs to be adjusted to Equation 23.

$$\beta_1 = -c_1 + c_{17} e^{-c_{19}\langle \epsilon_e - c_{18} \rangle} + p_0\left(V_f\right). \qquad (23)$$

Secondly, the addition of steel fibers changes the compressive capacity of the concrete material, especially the shear expansion deformation, so the compressive deviatoric stress-strain boundary condition Equation 9 needs to be adjusted to Equation 24.

$$\beta_2 = c_5 \gamma_1 + c_7\left(V_f\right). \qquad (24)$$
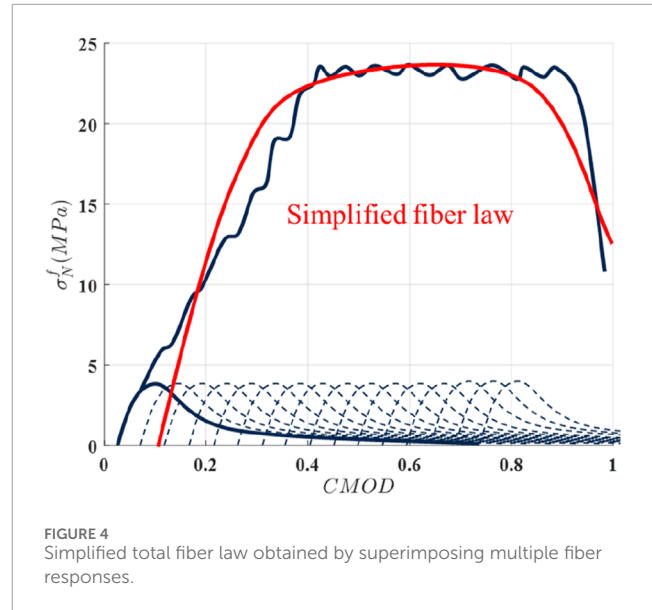
FIGURE 4
Simplified total fiber law obtained by superimposing multiple fiber responses.

Finally, steel fibers change the mechanical behavior of concrete in triaxial compression, so the plastic-friction boundary Equation 11 needs to be adjusted to Equation 25.

$$\sigma_T^b = F_T(-\sigma_N) = \frac{E_T k_1 k_2\left(V_f\right) c_{10}\left(V_f\right)\left\langle -\sigma_N + \sigma_N^0 \right\rangle}{E_T k_1 k_2\left(V_f\right) + c_{10}\left(V_f\right)\left\langle -\sigma_N + \sigma_N^0 \right\rangle}, \qquad (25)$$

where $\sigma_N^0 = \left\langle E_T k_1 c_{11}\left(V_f\right) - c_{12}\left(V_f\right)\langle \epsilon_V \rangle \right\rangle$.

The microplane model of steel fiber-reinforced concrete is based on the microplane model of plain concrete. Therefore to calibrate its parameters, it is necessary to calibrate the parameters of plain concrete first. Then from the uniaxial tensile data of SFRC, $p_0\left(V_f\right)$, $p_1\left(V_f\right)$, $p_2\left(V_f\right)$, $p_3\left(V_f\right)$, $p_4\left(V_f\right)$ can be identified. From Equation 23, it can be found that the parameter $p_0\left(V_f\right)$ determines whether the fibers in the concrete matrix are bonded or not. The parameter $p_1\left(V_f\right)$ controls the proportion of steel fiber contribution, while $p_2\left(V_f\right)$ controls the pullout of fibers connecting the open cracks. Parameters $p_3\left(V_f\right)$, $p_4\left(V_f\right)$ determine the length of the plastic plateau in the stress-strain relationship (shown in Figure 4). $c_7\left(V_f\right), c_{12}\left(V_f\right)$ can be determined from the uniaxial compression data and $k_2\left(V_f\right), c_{10}\left(V_f\right), c_{11}\left(V_f\right)$ can be determined from triaxial compression data. In many practical applications, fewer triaxial compression problems are involved. Therefore, it is mostly sufficient to study the uniaxial compression and uniaxial tension of fiber concrete. If uniaxial tension tests are difficult to perform, the parameters can be calibrated indirectly by means of the notched three-point loaded bending concrete beam test.

3.2 Extend to fatigue damage

In the concrete microplane damage model, taking the stretch shown in Equation 5 as an example, the damage behavior of concrete under several cycles can be described by assuming that the elastic modulus E_N in the μ-th microplane will undergo damage by

Equation 26.

$$\frac{E_N(\mu)}{E_{N0}} = \exp\left(-A\epsilon_N^{0+}(\mu)\right). \tag{26}$$

where E_{N0} is the undamaged modulus, A is the material parameter which is called c_{13} in Equation 5, and $\epsilon_N^{0+}(\mu)$ is the maximum strain reached so far in the μ-th microplane. This approach can characterize the damage to the concrete for a few cycles or so, but it does not capture fatigue. It is worth noting that once damage begins to occur in the material, strain localization occurs, and strain calculations at this point are affected by the finite element mesh size in a way that is difficult to ignore. Therefore, it is necessary to analyze the microplane model in conjunction with nonlocal theory or the crack band model (Bažant and Oh, 1983) (used here). In order to effectively predict the fatigue response, it is necessary to introduce a variable that measures the fatigue damage history paths (Kirane and Bažant, 2015; Baktheer et al., 2021; Aguilar et al., 2022).

3.2.1 Fatigue history variable

The fatigue damage variable is denoted as ζ. $\mathcal{F}$ is the fatigue history variable obtained from the accumulation of fatigue damage variables, and because fatigue damage is irreversible, $\mathcal{F}$ never decreases. For simplicity, in this paper, only the cyclic cumulative damage under tension is considered,and the cyclic cumulative damage under compression is ignored. The normal positive strain $\epsilon_N^+(\mu)$ reached on the microplane is adopted as the fatigue variable. Then the fatigue damage history variable at the end of the increment is given by Equation 27.

$$\mathcal{F} = \mathcal{F}_0 + d\zeta, d\zeta = |d\epsilon_N^+|. \tag{27}$$

The fatigue damage behavior of concrete under compressive loading can be used as a fatigue variable for compressive fatigue damage by using the normal negative strain, $\epsilon_N^-(\mu)$, as the fatigue variable for compressive fatigue damage. At this time the elastic model of fatigue damage occurring on the microplane should be calculated using Equation 6.

3.2.2 Fatigue damage estimation

Next, the stiffness degradation of the material is related to the fatigue damage history variables. A model is obtained that is suitable for both fatigue damage analyses without affecting the calibration of the parameters of the original microplane model. The material stiffness degradation on the microplane is represented by the damage parameter $\omega = E_N/E_{N0}$, in for the intact material $\omega = 1$, and $\omega = 0$ for the fully damaged material. Equation 26 is further written as Equation 28.

$$\frac{E_N}{E_{N0}} = \omega = \exp\left(-A\epsilon_N^{0+}\right). \tag{28}$$

Then, introduce $\omega = \omega_{cyc} = f(\mathcal{F})$ as the material stiffness degradation due to cyclic loading. To obtain the dependence of the damage parameter ω on the fatigue history variable $\mathcal{F}$, in analogy with Paris law, the following successively increasing damage accumulation rates are introduced,

$$\frac{d\omega_{cyc}}{d\mathcal{F}} = -s\mathcal{F}^p. \tag{29}$$
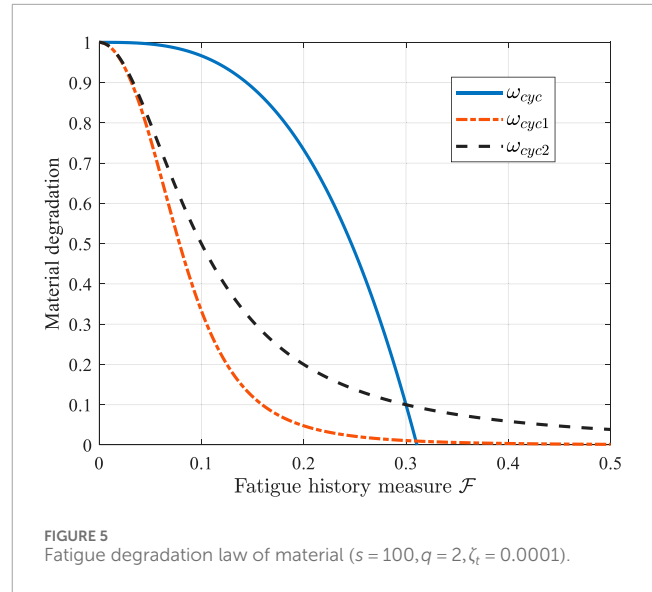
where s and p are material parameters. Integration of Equation (29), taking into account $\mathcal{F} = 0$ at $\omega_{cyc} = 1$, yields

$$\omega_{cyc} = 1 - \frac{s}{p+1}\mathcal{F}^{p+1} \tag{30}$$

Usually taking $p \geq 1$, then Equation (30) becomes negative as the fatigue damage history variable increases. Therefore, the following alternatives are used

$$\omega_{cyc1} = \frac{1}{1 + (s\mathcal{F})^p + (s\mathcal{F})^{2p}} \tag{31}$$

$$\omega_{cyc2} = \frac{s\zeta_t}{\mathcal{F}^p + s\zeta_t} \tag{32}$$

Similarly, s and p are material parameters that characterize fatigue degradation. ζ_t is the reference strain for uniaxial tensile and $\zeta_t = f_t/E_0$ is suggested, where f_t is the material tensile strength. The degradation functions Equations 31, 32 both satisfy the conditions $\omega'_{cyc} \leqslant 0$, $\omega_{cyc} \geqslant 0$, and $\lim_{\zeta \to \infty} \omega_{cyc} = 0$. Equations 30–32 correspond to the material fatigue damage softening law as shown in Figure 5. It can be found that the fitting of the test data under monotonic loading is not affected by the degradation function $\omega_{cyc} \approx 1$, due to the small fatigue history variable $\mathcal{F}$, in the first one or two cycles.

4 Numerical implementation, parameter calibration and model validation

4.1 Numerical implementation

In the numerical implementation, it is necessary to incorporate the crack band model to reduce the mesh size sensitivity of the computed results (Bažant and Oh, 1983; Červenka et al., 2005). In ABAQUS commercial finite element software, VUMAT subroutine is written for numerical implementation. If the stress tried exceeds the stress-strain boundary, it is necessary to keep the strain and limit the stress to the stress-strain boundary. In the finite element method

TABLE 1 Default values of fixed parameters of microplane model and their meaning.

Parameter	Default value	Meanings
f'_{c0}	15.08 MPa	Reference compressive strength
E_0	20 GPa	Reference elastic modulus
c_1	0.089	Control uniaxial tensile strength
c_2	0.176	Control uniaxial tensile curve
c_3	4	Control uniaxial tensile curves
c_4	50	Control uniaxial compressive curves
c_5	3,500	Control compression volume expansion
c_6	20	Control compression volume expansion
c_7	1	Control uniaxial compression curves
c_8	8	Controls uniaxial compression strength
c_9	0.012	Control uniaxial compression curves
c_{10}	0.33	Effective coefficient of friction
c_{11}	0.5	Initial cohesive in frictional response
c_{12}	2.36	Cohesive changes with tensile volumetric strain
c_{13}	4,500	Control uniaxial tensile behavior
c_{14}	300	Unloading slope under low hydrostatic pressure
c_{15}	4,000	Unloading of high constraints to low constraints
c_{16}	60	Unloading slope under high hydrostatic pressure
c_{17}	1.4	Controls the uniaxial tensile strength
c_{18}	62.5 MPa	Tensile cracking in compression
c_{19}	1,000	Tensile softening due to compression
c_{20}	1.8	V-D component coupling at high pressures
c_{21}	250 MPa	Volumetric stress-strain boundary upper limit

program, if the strain increment $\Delta\varepsilon_{ij}$ at the current step is known, as well as the strain ε^0_{ij} and stress σ^0_{ij} at the end of the previous step, the new stress σ_{ij} is obtained at the end of the current step by the following steps:

Step 1: First, the strain and strain increment on the microplane are calculated by Equation 33 according to Equation 1,

$$\Delta\boldsymbol{\varepsilon_N} = \mathbf{N_{ij}}\Delta\boldsymbol{\varepsilon_{ij}}, \Delta\boldsymbol{\varepsilon_M} = \mathbf{M_{ij}}\Delta\boldsymbol{\varepsilon_{ij}}, \Delta\boldsymbol{\varepsilon_L} = L_{\mathbf{ij}}\Delta\boldsymbol{\varepsilon_{ij}}. \tag{33}$$

Step 2: Calculate the volumetric strain and its increment at the end of the previous and current steps, based on the given strain and its

increment by Equation 34.

$$\varepsilon^o_V = \varepsilon_{kk}/3, \Delta\varepsilon_V = \Delta\varepsilon_{kk}/3, \varepsilon_V = \varepsilon^o_V + \Delta\varepsilon_V. \tag{34}$$

Then, calculate $\varepsilon_e = \left\langle -\sigma^0_V/E_{N0} \right\rangle$, while the corresponding volumetric stress-strain boundaries σ^b_V are later calculated by Equation 10. The deviatoric strain can be obtained from total strain and volumetric strain by Equation 35.

$$\Delta\varepsilon_D = \Delta\varepsilon_N - \Delta\varepsilon_V, \varepsilon^0_D = \varepsilon_N - \varepsilon^0_V, \varepsilon_D = \varepsilon^0_D + \Delta\varepsilon_D, \tag{35}$$

and σ^b_D is calculated by Equation 9.

Step 3: Calculate the $\varepsilon_N = \varepsilon_V + \varepsilon_D$ retrieve the history variables $\varepsilon^{0+}_N, \varepsilon^{0-}_N$ of the largest magnitude stored so far. Next, the

Free parameter	Default value	Meaning
E	25000 MPa	Elastic modulus
ν	0.18	Poisson's ratio
k_1	1.5×10^{-4}	Proportionality parameter
k_2	110	Control plastic-friction stress boundary
k_3	30	Control stress-strain volumetric boundary
k_4	100	Control stress-strain volumetric boundary
k_5	1×10^{-4}	Control the V-D coupling at low pressure
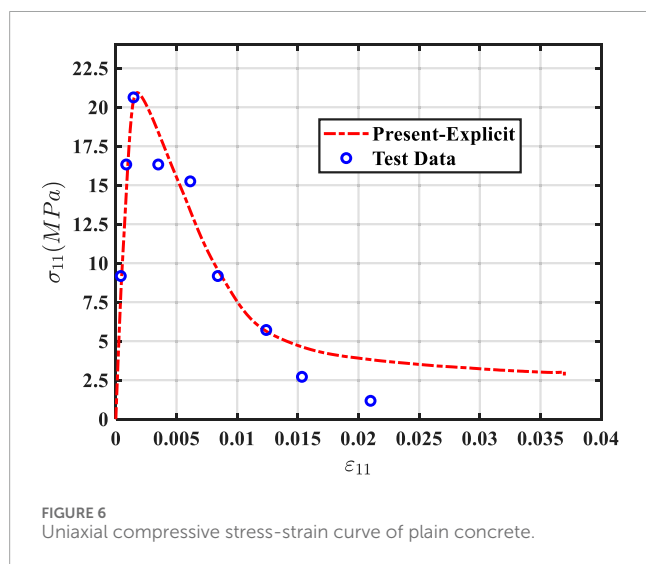
FIGURE 6
Uniaxial compressive stress–strain curve of plain concrete.

(a) Triaxial compression experiment and simulation with hydrostatic pressure

(b) Experimental and simulation of lateral limit uniaxial compression

FIGURE 7
Experimental and simulation of compression. **(A)** Triaxial compression experiment and simulation with hydrostatic pressure. **(B)** Experimental and simulation of lateral limit uniaxial compression.

current damage degree of the normal elastic modulus of the microplane is calculated according to $E_{N0} = E/(1-2\nu)$ by Equations 5, 6. Calculating the normal elastic stress of the microplane by Equation 36.

$$\sigma_N^e = \sigma_N^o + E_N \Delta \varepsilon_N \qquad (36)$$

Step 4: Calculate the normal tensile boundary σ_N^b of the microplane using Equation 8 when $\sigma_N^b > 0$.

Step 5: Holding the strain constant and allowing the stress to drop vertically to the normal tensile stress-strain boundary by Equation 37.

$$\sigma_N = \max\left[\min\left(\sigma_N^e, \sigma_N^b\right), \sigma_V^b + \sigma_D^b\right] \qquad (37)$$

Meanwhile, update the history maxima ε_N^{0+} and ε_N^{0+}.

Step 6: Calculate an approximation of the current volumetric stress by Equation 38.

$$\sigma_V \approx \frac{1}{2\pi} \sum_{\mu=1}^{N_m} w_\mu \sigma_N \qquad (38)$$

Retrieve the originally stored microplane shear stresses σ_L^o, σ_M^o, followed by estimating E_T according to Equation 4, and $\hat{\sigma}_N^0 = E_T \langle k_1 c_{11} - c_{12} \langle \varepsilon_V \rangle \rangle$. If we want to simulate cell failure, the recommended deletion criterion of the adopted cell is $\varepsilon_I \geq 0.5\%$. The shear boundary is then calculated by Equation 11.

Step 7: Calculate the shear response upon return to the stress-strain boundary by Equations 12–16.

Step 8: The stress σ_{ij} at the end of the current step is obtained by calculating the sum of stresses on all microplanes through Equations 18, 19, while recording the variables σ_V, σ_N, σ_L, σ_M, ε_N^{0+}, ε_N^{0-} at the end of the current step.

TABLE 3 Parameter calibration of carbon steel fiber reinforced concrete.

V_f	0%	1%	2%
p_0	-	0.0083	0.0165
p_1	-	0.178	0.357
p_2	-	0.266	0.234
p_3	-	4.22	5.09
p_4	-	3.75	3
c_7	1	1,000	1,000
k_2	100	110	120
c_{10}	0.33	0.43	0.43
c_{11}	0.5	3	6
c_{12}	2.36	0.236	0.0236

4.2 Parameter calibration

In the microplane model (M7), the shape of the response curve is determined by five free parameters and twenty-one fixed parameters. Tables 1, 2 provide a concise explanation of the meaning and default value of each parameter. The fixed parameters, as detailed in Table 1, are calibrated using the uniaxial compressive strength $f'_c = 36$MPa and the axial normal strain $\varepsilon_p = 0.0036$ at peak stress. The calibration of the uniaxial compressive strength f^*_c, and the corresponding strain ε^*_p, of a particular concrete using a microplane model requires only that the reference values of the free parameter k_1, and the elastic modulus E, be modified to,

$$k_1^* = k_1 \frac{\varepsilon^*_p}{\varepsilon_p}, E^* = E \frac{f^*_c}{f'_c} \frac{\varepsilon_p}{\varepsilon^*_p}. \tag{39}$$

To optimize the fitting of a large amount of experimental data, it is not necessary to change all five free parameters simultaneously in the actual microplane model (Caner and Bažant, 2013a; Caner and Bazant, 2013b). The elastic modulus E and Poisson's ratio v are determined through experimental measurement. First, all other parameters are assumed to be reference values, and subsequent parameter calibration is conducted. The parameter k_1 was calibrated based on the strain corresponding to the peak stress in the uniaxial compression experiment. If sufficient triaxial compression data are available, and the compression intensity is sufficiently strong to elicit an almost plastic response, the data are fitted by adjusting k_2. The parameters k_3 and k_4 are calibrated based on hydrostatic pressure experimental data. If sufficient uniaxial, biaxial, and triaxial compression data at low hydrostatic pressure are available, k_5 should be determined by fitting. Otherwise, the default values are retained.
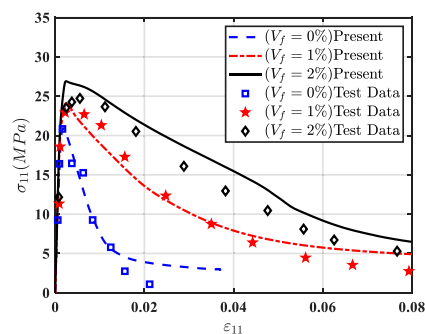
(a) Compression of carbon SFRC.
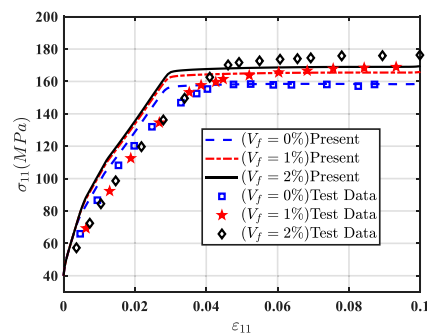
(b) Compression of carbon SFRC under 40 MPa hydrostatic pressure.
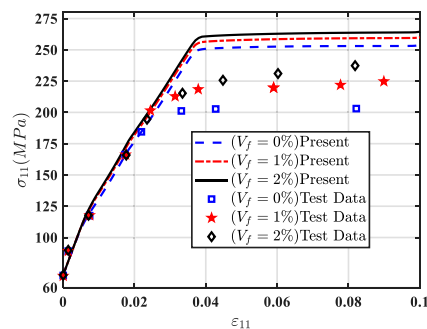
(c) Compression of carbon SFRC under 70 MPa hydrostatic pressure.

FIGURE 8
Experiment and simulation of carbon SFRC. **(A)** Compression of carbon SFRC. **(B)** Compression of carbon SFRC under 40 MPa hydrostatic pressure. **(C)** Compression of carbon SFRC under 70 MPa hydrostatic pressure.

4.3 Validation of representative examples

4.3.1 Plain concrete specimen

First, the uniaxial compression test of Chern et al. (1993) was fitted to the elastic modulus $E = 20$GPa, compressive strength $f'_c = 20.65$MPa, and Poisson's ratio $v = 0.18$ of plain concrete materials. The strain $\varepsilon^*_p = 0.001458$ corresponding to the peak load was obtained from the uniaxial compression experiment, and the free parameters $k_1 = 60$ were adjusted according to the prediction Equation 39 proposed by Bazant et al., with other parameters kept defaults. The calculated uniaxial compression stress-strain curve of plain concrete is shown in Figure 6, which is similar to the experimental results.

(a) Geometry of a concrete beam with notched three-point bending

(b) Load-displacement curve under monotonic loading

(c) Load-load point displacement curves under fatigue loading

FIGURE 9
Simulated load-displacement curve under monotonic and fatigue loading. **(A)** Geometry of a concrete beam with notched three-point bending. **(B)** Load-displacement curve under monotonic loading. **(C)** Load-load point displacement curves under fatigue loading.

TABLE 4 Parameter calibration of steel fiber reinforced concrete.

V_f	0%	0.5%	1.0%	1.5%
p_0	-	0.0042	0.0083	0.0125
p_1	-	0.089	0.178	0.267
p_2	-	0.282	0.266	0.260
p_3	-	3.79	4.22	4.65
p_4	-	4.12	3.75	3.38
k_1	140	140	140	140
k_2	100	110	115	120
c_7	1	50	100	500
c_{10}	0.33	0.38	0.43	0.48
c_{11}	0.5	1	2	4
c_{12}	2.36	1.52	0.438	0.152

41.369GPa, Poisson's ratio $v = 0.18$, free parameters $k_1 = 105 \times 10^{-6}$, $k_3 = 10$, $k_4 = 150$, and other parameters are kept default. The simulation results are shown in Present-1 in Figure 7B, which agrees with the tests. In literature (Caner and Bazant, 2013b), the free parameter $k_1 = 120 \times 10^{-6}$, corresponding to the computational results as shown in Present-2 in Figure 7B. When microplane model parameters are calibrated, it can be well used to capture plain concrete mechanical response.

4.3.2 Steel fiber-reinforced concrete specimen

In this section, the mechanical response of steel fiber-reinforced concrete is analyzed. The parameter calibration was performed for fiber reinforced, as shown in Table 3 (Caner et al., 2013). The experimental and simulation results of FRC containing carbon steel fibers (fiber volume admixture $V_f = 0\%$, 1%, 2%) at hydrostatic pressures of 0 MPa, 40 MPa, and 70 MPa are shown in Figure 8. Therefore, the microplane model can analyze the mechanical response of fiber-reinforced concrete when the parameters are calibrated.

5 Fatigue damage analysis

5.1 Plain concrete material

In this section, we consider a notched plain concrete beam of depth $D = 107.8$mm, span $S = 2.5D$, and a notch of length $a_0 = D/6$ situated at the center of the beam. The width of the beam is 38.1mm, as illustrated in Figure 9A. The parameters of plain concrete material: Young's modulus $E = 38.3$GPa, Poisson's ratio $v = 0.18$, compressive strength $f_c = 90.3$MPa, density $\rho = 2400$kg/m³. The free parameters $k_1 = 140 \times 10^{-6}$ are calibrated by matching the peak loads of monotonic load, and the default values are adopted for all other parameters. Two finite element mesh sizes were considered, i.e., $h_{size} = 3$mm and $h_{size} = 5$mm, and the predicted

Next, a triaxial compression experiment of concrete under hydrostatic pressure was fitted. Plain concrete material parameters (Chern et al., 1993): elastic modulus $E = 20$GPa, Poisson's ratio $v = 0.18$. The free parameter $k_1 = 60 \times 10^{-6}$ and other parameters are kept as default. The simulation and experimental results are shown in Figure 7A. The model is sufficient to capture concrete compression under low hydrostatic pressure conditions. Therefore, it is suitable for capturing the nonlinear behavior of concrete under conventional conditions.

Then, the mechanical behavior of plain concrete under side-limited uniaxial compression was fitted. The plain concrete material parameters (Caner and Bazant, 2013a): elastic modulus $E =$

TABLE 5 Experiments and simulations of monotonic and fatigue loading of steel fiber reinforced concrete.

Specimen	Peak load (kN)		Fatigue life		Fatigue law (s,q)
	Experimental	Simulation	Experimental	Simulation	
0%-PC	2.74	2.73	137	135	(3500,2)
0.5%-SFRC	2.83	2.86	2053	2,134	(850,2)
1.0%-SFRC	3.29	3.29	2,693	2,794	(750,2)
1.5%-SFRC	4.60	4.60	4,461	4,578	(700,2)
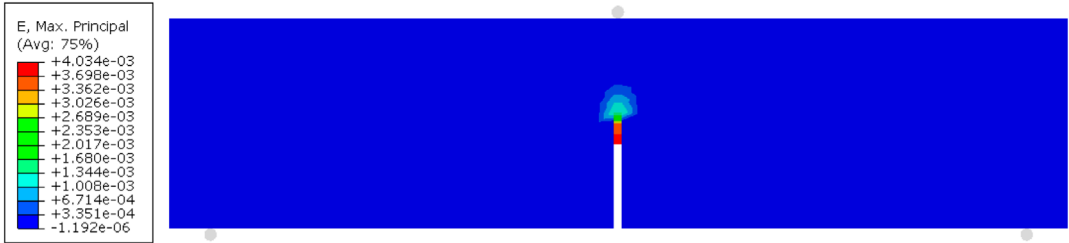
(a) The strain in a three-point bending beam one cycle before fatigue damage occurs.
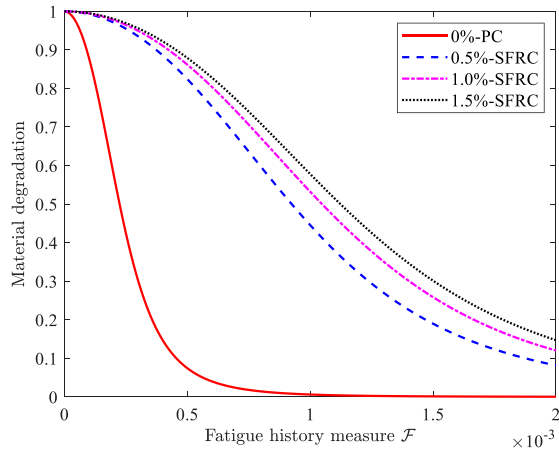
(b) Fatigue damage law of various fiber-reinforced concrete

FIGURE 10
The strain in a three-point bending beam and fatigue damage law. **(A)** The strain in a three-point bending beam one cycle before fatigue damage occurs. **(B)** Fatigue damage law of various fiber-reinforced concrete.
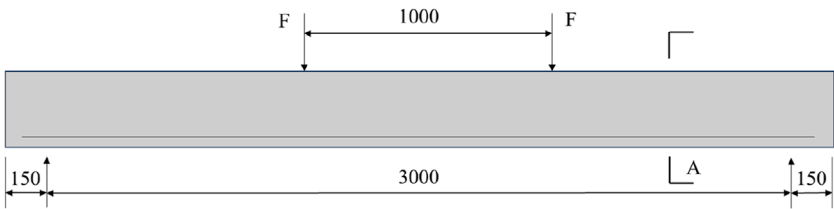
FIGURE 11
Geometry of reinforced concrete beams (mm) and its loaded conditions.

FIGURE 12
Load–displacement curves of reinforced concrete beams under monotonic loading (V_f = 0%, 0.5%, 1%, 1.5%).
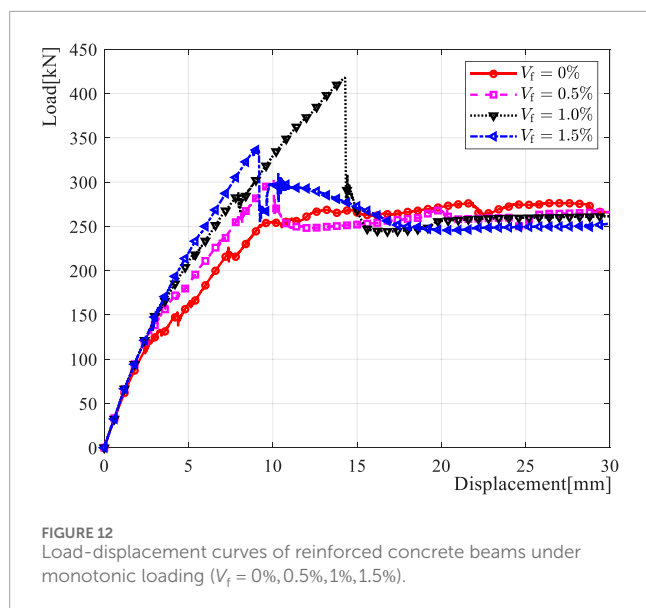
peak loads were 5.32MPa and 5.22MPa, which were in good agreement with the experimental results 5.4MPa (Bazant and Schell, 1993), as shown in Figure 9B. To reduce the computational cost, the finite element mesh size of the potential damage region was 5mm in the subsequent analysis.

Next, the fatigue simulation of a three-point bending beam was performed. Cyclic loading was applied up to 84% of the peak monotonic loading. The parameters of the fatigue damage law of the material are adjusted until the life prediction is satisfactorily close. The fatigue damage metric used was Equation 31, and with the adopted parameters s = 1800 and q = 2, the model predicted failure after 225 cycles in excellent agreement with the tested fatigue life of 212 cycles. In the last cycle, the failure is characterized by a sudden increase in the overall deformation, as shown in Figure 9C.

5.2 Steel fiber-reinforced concrete material

Then, the fatigue damage behavior of steel fiber-reinforced concrete is analyzed. A three-point bending beam (Qing et al., 2023) with notched specimen size $440 \times 100 \times 100 (\text{mm}^3)$, a notch of width 4mm is located at the bottom of the middle of the beam, the height of the notch is 40mm, and the span at the bottom of the beam is 400mm. Four groups of steel fiber-reinforced concrete (SFRC) with steel fiber volume admixture V_f = 0%, 0.5%, 1.0%, and 1.5% were used. Fiber-reinforced concrete material parameters: elastic modulus E_0 = 27.738GPa, Poisson's ratio v = 0.18, tensile strength f_t = 2.67MPa, compressive strength f_c = 34.39MPa. The model's free, fixed, and fiber parameters were calibrated, and the calibrated parameters are shown in Table 4. The peak monotonic loading predicted by the model is similar to the test, as shown in Table 5. The load capacity of the concrete beams was enhanced with the increase in the volume admixture of fiber-reinforced concrete.

Next, fatigue analysis of fiber-reinforced concrete three-point bending beams was performed. The maximum applied cyclic load was 85% of the monotonically loaded peak load. The fatigue

FIGURE 13
Strain in reinforced concrete beams under monotonic loading. **(A)** Displacement at load point 3 mm (V_f = 0%). **(B)** Displacement at load point 7.5 mm (V_f = 0%). **(C)** Displacement at load point 3 mm (V_f = 0.5%). **(D)** Displacement at load point 7.5 mm (V_f = 0.5%). **(E)** Displacement at load point 3 mm (V_f = 0.5%). **(F)** Displacement at load point 7.5 mm (V_f = 0.5%). **(G)** Displacement at load point 3 mm (V_f = 1.5%). **(H)** Displacement at load point 7.5 mm (V_f = 1.5%).

damage law parameters were adjusted until the life prediction was close enough. The strains of SFRC three-point bending beam with 0.5% volume steel fiber admixture for the one cycle before fatigue loading failure are shown in Figure 10A, and the strains for the remaining three groups are similar. The fatigue damage metric used is Equation 31, and the calibrated fatigue damage law parameters are shown in Table 5 for various fiber-reinforced concretes. The corresponding material fatigue damage law is shown in Figure 10B. The fatigue resistance of concrete is gradually improved with the increase of steel fiber mixing, and the fatigue resistance improvement is gradually slowed down when the steel fiber admixture is more than 1%. Therefore, the present
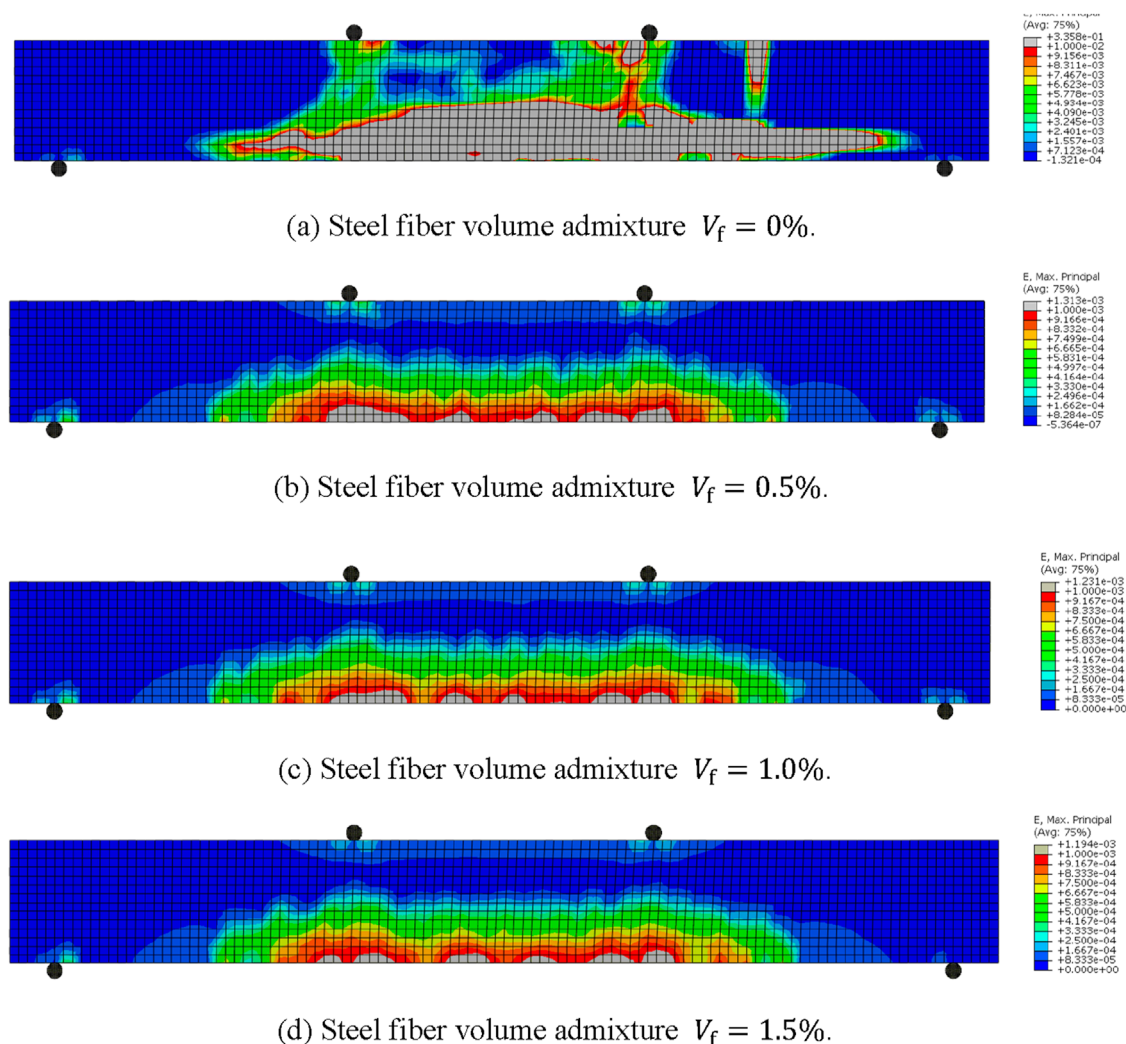
FIGURE 14
Reinforced concrete beam strains after fatigue loading. **(A)** Steel fiber volume admixture $V_f = 0\%$. **(B)** Steel fiber volume admixture $V_f = 0.5\%$. **(C)** Steel fiber volume admixture $V_f = 1.0\%$. **(D)** Steel fiber volume admixture $V_f = 1.5\%$.

model can be well used to analyze the mechanical response of fiber-reinforced concrete under monotonic and fatigue loading.
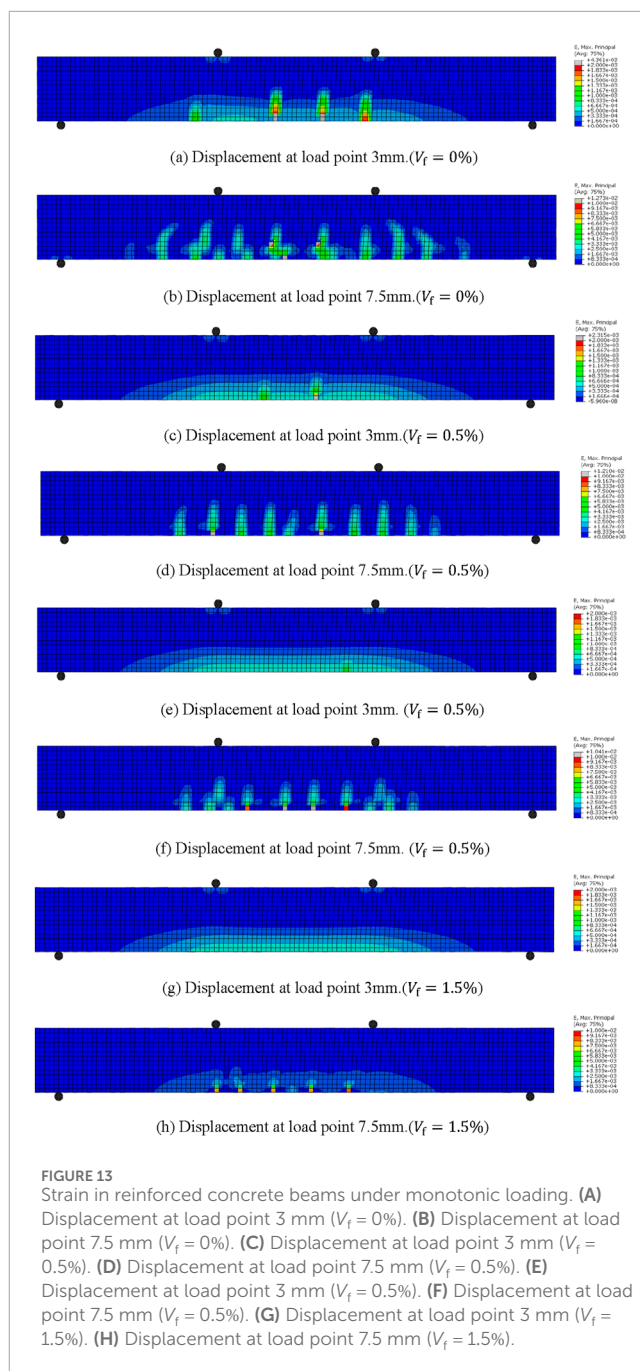
5.3 Plain and steel fiber-reinforced concrete beam

Fatigue damage modeling ultimately aims to fine-tune the analysis of the whole process of fatigue damage in concrete structures. This section simulates the fatigue damage of reinforced concrete beams using the proposed model as an illustrative study. The cross-section height of the concrete beam is $h = 400mm$, the cross-section width is $b = 300mm$, the protective layer thickness of the steel reinforcement is 40mm, and the cross-section reinforcement ratio of the longitudinal reinforcement $\rho \approx 1.26\%$. The geometry and loading of the concrete beam are shown in Figure 11. To show the potential of the model for capturing the fatigue damage behaviors of reinforced concrete

structures, the steel reinforcement is assumed to be ideally elastic-plastic with a yield strength of $f_y = 400MPa$, and the material parameters of the SFRC are the same as in the previous section.

First, a numerical simulation of the four-point bending of reinforced concrete beams ($V_f = 0\%, 0.5\%, 1.0\%, 1.5\%$) under monotonic loading is carried out. The load-displacement curves are shown in Figure 12. The ultimate load capacity of reinforced concrete increases gradually with the increase of fiber volume admixture, and the ultimate load capacity of reinforced concrete beams with a fiber volume admixture of 1% is the largest. Unlike the damage mechanics intrinsic model, the fatigue damage of a structure is usually accounted for by the development of strain in the microplane theory. It is worth noting that the bottom strain of plain reinforced concrete beams reaches up to 0.4361% at a displacement loading of 3 mm, and the stressed portion of the tensile zone gradually changes from concrete to steel reinforcement, as shown in Figure 13. With the increase in fiber volume admixture $V_f = 0.5\%, 1.0\%, 1.5\%$, the maximum strains of the resinforced

FIGURE 15
Displacement-loading number curves at loading point. (V_f = 0%, 0.5%, 1%, 1.5%).
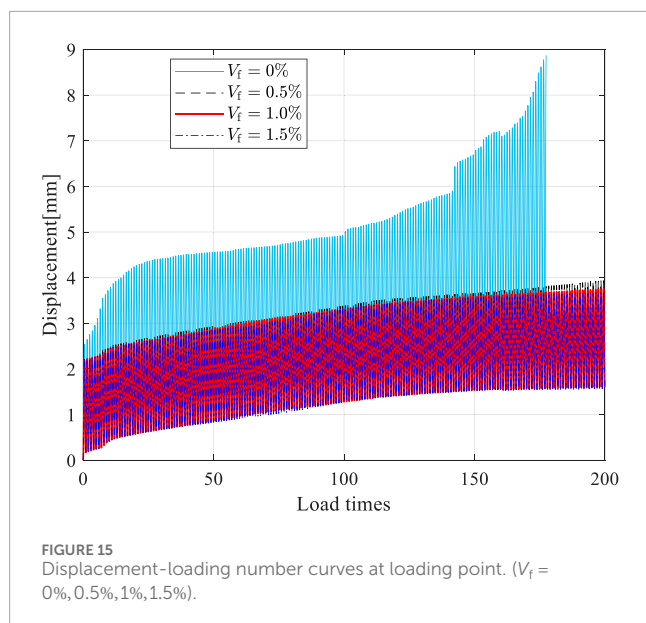
concrete beams were reduced to 0.2315%, 0.0927%, and 0.065% with displacement loading of 3 m. At a displacement loading of 7.5 mm, the steel reinforcement basically stressed the tensile zone of the concrete beams, and there were some areas where the strains were close to or more than 1%. However, the concrete structure would not be subjected to such large deformations under service conditions. Afterward, we will pay attention to the response of the concrete when cracked or just cracked. In this paper, the load capacity corresponding to a plain reinforced concrete beam subjected to a displacement loading of 3 mm is defined as F_u = 124.72kN, and the maximum value of the fatigue load magnitude is $0.9F_u$.

Next, fatigue damage simulations of reinforced concrete structures (V_f = 0%, 0.5%, 1%, 1.5%) under 200 cyclic loadings were performed. During cyclic loading, the fatigue history variables are gradually accumulated, resulting in gradual degradation of the material stiffness and gradual development of the strain in the concrete beams. The strain distribution after 200 loading cycles is shown in Figure 14. For a reinforced concrete beam composed of plain concrete with a fatigue life of 176 cyclic loadings, the strains at one time before structural failure are shown in Figure 14A. The strains at the bottom of the beam are more than 1% in most regions. With the increase in fiber dosage, the strain of the concrete structure improved during fatigue loading due to the improvement in tensile capacity, and the cracking pattern was transformed. The beam strain distribution after 200 loading cycles is shown in Figures 14B–D. The maximum strains of reinforced concrete beams with steel fiber volume admixture V_f = 0.5%, 1%, 1.5% are 0.1313%, 0.1231%, and 0.1194%, respectively. The displacements at the loading points also show a significant reduction trend, as shown in Figure 15. Therefore, the microplane model considering the material stiffness degradation can be used to reflect the fatigue damage behavior of plain and fiber-reinforced concrete materials.

It is worth noting that for the fatigue of reinforced concrete structures, to capture the various mechanical behaviors in the tests,

the slip between the concrete and the reinforcement also needs to be considered, and the degradation of the fatigue properties of materials such as reinforcement and fibers needs to be considered. However, this is not the focus of this study and will be illustrated in future studies. This model is expected to be used for the whole-process analysis of fatigue damage of plain concrete and steel fiber-reinforced concrete structures under complex loading conditions and structural forms, which will facilitate engineering design, evaluation, and optimization.

6 Further study

Despite the success in expanding the application of microplanar modeling of plain concrete, many issues need to be solved. In subsequent research, the following issues will be focused on:

(1) simplifying the extremely cumbersome parameters in M7 and developing user-friendly software tools or plug-ins.
(2) Consider the fatigue-related material stiffness under compression conditions and extend the model to compression fatigue analysis.
(3) Optimize the fiber toughening mechanism and expand the model to fatigue damage analysis of concrete materials such as ECC and UHPFRC.

7 Conclusion

This study successfully extends the microplane model for assessing fatigue damage in steel fiber-reinforced concrete (SFRC). The model combines material stiffness degradation, critical for analyzing fatigue damage, with fatigue history variables accumulated during cyclic loading. A more detailed prediction of the fatigue life and behavior of plain and steel fiber-reinforced concrete materials is possible. The following conclusions were obtained:

(1) The extended microplane model is suitable for mechanical response analysis of steel fiber-reinforced concrete materials. It provides an effective tool for predicting fatigue damage of concrete structures under cyclic loading by introducing fatigue history variables and establishing their relationship with material stiffness degradation.
(2) It is shown that steel fiber incorporation can substantially improve concrete's mechanical properties and fatigue resistance. The extended model can capture the reinforcing effect of fibers, which is consistent with the experiments.
(3) The model's parameters can be calibrated against benchmark experimental data. The model can be implemented numerically in ABAQUS commercial finite element software in conjunction with a crack band model for engineering analysis.
(4) The model can predict the fatigue life and mechanical behavior of plain and steel fiber-reinforced concrete materials, which helps in engineering design and optimization. Next, it is expected to be used for fatigue analysis of concrete structures under complex loading conditions and structural forms by considering the slip of reinforcement with concrete and the degradation of the fatigue performance of reinforcement.

Data availability statement

The original contributions presented in the study are included in the article/supplementary material, further inquiries can be directed to the corresponding author.

Author contributions

CQ: Methodology, Supervision, Writing–original draft, Writing–review and editing. XD: Funding acquisition, Resources, Writing–original draft. BW: Data curation, Investigation, Writing–original draft. LC: Validation, Visualization, Writing–original draft. SW: Formal Analysis, Project administration, Writing–original draft. QX: Conceptualization, Software, Writing–review and editing, Writing–original draft.

Funding

Conflict of interest

Authors CQ, XD, BW, LC, and SW were employed by China Construction Third Bureau First Engineering Co., Ltd.

The remaining author declares that the research was conducted in the absence of any commercial or financial relationships that could be construed as a potential conflict of interest.

The authors declare that this study received funding from China Construction Third Bureau First Engineering Co., Ltd. The funder had the following involvement in the study: study design, data collection, funding acquisition, preparation of the paper, and decision to submit it for publication.

Generative AI statement

The author(s) declare that no Generative AI was used in the creation of this manuscript.

Publisher's note

All claims expressed in this article are solely those of the authors and do not necessarily represent those of their affiliated organizations, or those of the publisher, the editors and the reviewers. Any product that may be evaluated in this article, or claim that may be made by its manufacturer, is not guaranteed or endorsed by the publisher.

References

Aas-Jakobsen, K. (1970). *Fatigue of concrete beams and columns*. Trondheim: University of Trondheim.

Aguilar, M., Baktheer, A., and Chudoba, R. (2022). "Numerical investigation of load sequence effect and energy dissipation in concrete due to compressive fatigue loading using the new microplane fatigue model MS1," in Presentations and videos to 16th International Conference on Computational Plasticity (COMPLAS 2021). IS17-Multiscale Modelling of Concrete and Concrete Structures. doi:10.23967/complas.2021.053

Baktheer, A., Aguilar, M., and Chudoba, R. (2021). Microplane fatigue model MS1 for plain concrete under compression with damage evolution driven by cumulative inelastic shear strain. *Int. J. Plasticity* 143, 102950. doi:10.1016/j.ijplas.2021.102950

Bažant, Z. P., and Oh, B. H. (1983). Crack band theory for fracture of concrete. *Mat. Constr.* 16, 155–177. doi:10.1007/BF02486267

Bazant, Z. P., and Schell, W. F. (1993). Fatigue fracture of high-strength concrete and size effect. *Mater. J.* 90, 472–478. doi:10.14359/3880

Bažant, Z. P., Xiang, Y., and Prat, P. C. (1996). Microplane model for concrete. I: stress-strain boundaries and finite strain. *J. Eng. Mech.* 122, 245–254. doi:10.1061/(ASCE)0733-9399(1996)122:3(245)

Caner, F. C., and Bažant, Z. P. (2013a). Microplane model M7 for plain concrete. I: formulation. *J. Eng. Mech.* 139, 1714–1723. doi:10.1061/(ASCE)EM.1943-7889.0000570

Caner, F. C., and Bazant, Z. P. (2013b). Microplane model M7 for plain concrete. II: calibration and verification. *J. Eng. Mech.* 139, 1724–1735. doi:10.1061/(ASCE)EM.1943-7889.0000571

Caner, F. C., Bažant, Z. P., and Wendner, R. (2013). Microplane model M7f for fiber reinforced concrete. *Eng. Fract. Mech.* 105, 41–57. doi:10.1016/j.engfracmech.2013.03.029

Carlesso, D. M., de la Fuente, A., and Cavalaro, S. H. P. (2019). Fatigue of cracked high performance fiber reinforced concrete subjected to bending. *Constr. Build. Mater.* 220, 444–455. doi:10.1016/j.conbuildmat.2019.06.038

Červenka, J., Bažant, Z. P., and Wierer, M. (2005). Equivalent localization element for crack band approach to mesh-sensitivity in microplane model. *Int. J. Numer. Methods Eng.* 62, 700–726. doi:10.1002/nme.1216

Chern, J., Yang, H., and Chen, H. (1993). Behavior of steel fiber reinforced concrete in multiaxial loading. *Mater. J.* 89. doi:10.14359/1242

Chu, S. H., Unluer, C., Yoo, D. Y., Sneed, L., and Kwan, A. K. H. (2023). Bond of steel reinforcing bars in self-prestressed hybrid steel fiber reinforced concrete. *Eng. Struct.* 291, 116390. doi:10.1016/j.engstruct.2023.116390

Cornelissen, H. A. W. (1984). Fatigue failure of concrete in tension. *HERON* 29 (4), 1–68. Available at: https://www.semanticscholar.org/paper/Fatigue-Failure-of-Concrete-in-Tension-Cornelissen/660b8ce20194711cb9477f0f6fc30503c637af43 (Accessed June 25, 2023).

Gylltoft, K. (1984). A fracture mechanics model for fatigue in concrete. *Mat. Constr.* 17, 55–58. doi:10.1007/BF02474057

Hillerborg, A., Modéer, M., and Petersson, P.-E. (1976). Analysis of crack formation and crack growth in concrete by means of fracture mechanics and finite elements. *Cem. Concr. Res.* 6, 773–781. doi:10.1016/0008-8846(76)90007-7

Huang, B.-T., Zhu, J.-X., Weng, K.-F., Li, V. C., and Dai, J.-G. (2022). Ultra-high-strength engineered/strain-hardening cementitious composites (ECC/SHCC): material design and effect of fiber hybridization. *Cem. Concr. Compos.* 129, 104464. doi:10.1016/j.cemconcomp.2022.104464

Jiang, J., Luo, Q., Wang, F., Sun, G., and Liu, Z. (2023). Uniaxial tensile constitutive model of fiber reinforced concrete considering bridging effect and its numerical algorithm. *J. Sustain. Cement-Based Mater.* 12, 207–217. doi:10.1080/21650373.2022.2034549

Kholmyansky, M. M. (2002). Mechanical resistance of steel fiber reinforced concrete to axial load. *J. Mater. Civ. Eng.* 14, 311–319. doi:10.1061/(ASCE)0899-1561(2002)14:4(311)

Kirane, K., and Bažant, Z. P. (2015). Microplane damage model for fatigue of quasibrittle materials: sub-critical crack growth, lifetime and residual strength. *Int. J. Fatigue* 70, 93–105. doi:10.1016/j.ijfatigue.2014.08.012

Lakavath, C., Prakash, S. S., and Allena, S. (2024). Tensile characteristics of ultra-high-performance fibre-reinforced concrete with and without longitudinal steel rebars. *Mag. Concr. Res.* 76, 738–754. doi:10.1680/jmacr.23.00181

Li, B., Chen, Z., Wang, S., and Xu, L. (2024). A review on the damage behavior and constitutive model of fiber reinforced concrete at ambient temperature. *Constr. Build. Mater.* 412, 134919. doi:10.1016/j.conbuildmat.2024.134919

Li, B., Chi, Y., Xu, L., Li, C., and Shi, Y. (2018). Cyclic tensile behavior of SFRC: experimental research and analytical model. *Constr. Build. Mater.* 190, 1236–1250. doi:10.1016/j.conbuildmat.2018.09.140

Lu, C., Leung, C. K. Y., and Li, V. C. (2017). Numerical model on the stress field and multiple cracking behavior of Engineered Cementitious Composites (ECC). *Constr. Build. Mater.* 133, 118–127. doi:10.1016/j.conbuildmat.2016.12.033

Marigo, J. J. (1985). Modelling of brittle and fatigue damage for elastic material by growth of microvoids. *Eng. Fract. Mech.* 21, 861–874. doi:10.1016/0013-7944(85)90093-1

Miarka, P., Seitl, S., Bílek, V., and Cifuentes, H. (2022). Assessment of fatigue resistance of concrete: S-N curves to the Paris' law curves. *Constr. Build. Mater.* 341, 127811. doi:10.1016/j.conbuildmat.2022.127811

Nguyen, D.-L., Le, H.-V., Vu, T.-B.-N., Nguyen, V.-T., and Tran, N.-T. (2023). Evaluating fracture characteristics of ultra-high-performance fiber-reinforced concrete in flexure and tension with size impact. *Constr. Build. Mater.* 382, 131224. doi:10.1016/j.conbuildmat.2023.131224

Paris, P., and Erdogan, F. (1963). A critical analysis of crack propagation laws. *J. Basic Eng.* 85, 528–533. doi:10.1115/1.3656900

Qing, L., Wang, Y., Li, M., and Mu, R. (2023). Fatigue life and fracture behaviors of aligned steel fiber reinforced cementitious composites (ASFRC). *Int. J. Fatigue* 172, 107643. doi:10.1016/j.ijfatigue.2023.107643

Riyar, R. L., Mansi, M., and Bhowmik, S. (2023). Fatigue behaviour of plain and reinforced concrete: a systematic review. *Theor. Appl. Fract. Mech.* 125, 103867. doi:10.1016/j.tafmec.2023.103867

Wille, K., El-Tawil, S., and Naaman, A. E. (2014). Properties of strain hardening ultra high performance fiber reinforced concrete (UHP-FRC) under direct tensile loading. *Cem. Concr. Compos.* 48, 53–66. doi:10.1016/j.cemconcomp.2013.12.015

Yoo, D.-Y., Kim, S., Park, G.-J., Park, J.-J., and Kim, S.-W. (2017). Effects of fiber shape, aspect ratio, and volume fraction on flexural behavior of ultra-high-performance fiber-reinforced cement composites. *Compos. Struct.* 174, 375–388. doi:10.1016/j.compstruct.2017.04.069

Zhang, H., Chen, S., Zhang, W., and Liu, X. (2024). Service life evaluation of curved intercity rail bridges based on fatigue failure. *Infrastructures* 9, 139. doi:10.3390/infrastructures9090139

Zhu, B., Pan, J., Zhang, M., and Leung, C. K. Y. (2022). Predicting the strain-hardening behaviour of polyethylene fibre reinforced engineered cementitious composites accounting for fibre-matrix interaction. *Cem. Concr. Compos.* 134, 104770. doi:10.1016/j.cemconcomp.2022.104770

frontiers | Frontiers in Materials

Cyclic testing of a steel-tube-enabled emulative precast column-to-column connection

Ming-Ming Ji[1,2], Wei Chen[1], Shi Zeng[2], Yan Xiong[2]* and Xin-Yu Zhao[2]*

[1]Guangzhou Engineering Contractor Group Co., Ltd., Guangzhou, China, [2]State Key Laboratory of Subtropical Building and Urban Science, South China University of Technology, Guangzhou, China

Precast systems are increasingly favored in modern construction to meet the growing demands for faster project delivery, cost control, and enhanced quality assurance. Yet, the feasibility of connections between precast elements remains a crucial factor affecting the overall structural performance of these systems. Considering the versatility and dimensional consistency of structural steel sections, this study introduces an emulative column-to-column hybrid connection achieved by using welding-spliced steel tubes, with a view to improving assembly efficiency and on-site quality control. Reversed cyclic loading tests were conducted on five near full-scale column specimens to assess the seismic performance of the proposed connection. Results indicated that this connection method could provide seismic performance comparable to that of the traditional cast-in-place counterpart. Nevertheless, the anchorage of the column longitudinal rebars played a critical role, as inadequate anchorages led to significant reductions in the columns' lateral capacity. For this reason, increasing the tube thickness was shown to be insufficient as a substitute for proper anchorage detailing. Moreover, it was found that the incorporation of the welded steel tubes shifted the plastic hinge region upward, resulting in a more extended damage zone—a consequence of the localized stiffening effect. Finally, existing equations and methods are employed to evaluate the lateral strength, load-displacement response, and plastic hinge length of the tested specimens.

1 Introduction

Precast concrete systems have become an integral part of modern construction, offering distinct advantages such as reduced labor demands, enhanced quality control, and improved environmental sustainability compared to traditional cast-in-place (CIP) methods (Englekirk, 2003; Hong et al., 2018; Wong and Loo, 2022). Off-site manufacturing enables higher precision and better material efficiency, while also

minimizing waste and environmental impact (Yee, 2001a; Yee, 2001b; Zhang X. et al., 2024). These benefits make precast systems ideal for applications ranging from buildings and industrial complexes to large-scale infrastructure projects. However, ensuring the reliability of connections between precast components remains a big challenge—especially in seismic regions, where these connections must accommodate large lateral deformations without compromising structural integrity (ACI 550R-96, 2001; Khaloo and Parastesh, 2003; Elliott and Jolly, 2013; Kurama et al., 2018; Ghayeb et al., 2020a; Hu et al., 2024; Zhang R. et al., 2024).

Currently, grouted sleeve connectors have been typically used in precast connections (Einea et al., 1995; Ameli et al., 2016; Tullini and Minghini, 2016; Fan et al., 2020; Liu et al., 2021; Xu et al., 2022; Zhang et al., 2023). While effective in load transfer and offering construction tolerances, they present notable drawbacks. For instance, the grouting process can be labor-intensive and time-consuming, with outcomes heavily influenced by site conditions (Yao et al., 2021; Li et al., 2021). Moreover, these connectors are concealed within concrete, making post-installation inspection and maintenance challenging (Henin and Morcous, 2015; Durgarian et al., 2022).

More critically, grouted sleeve connectors exhibit inherent seismic limitations, particularly in displacement ductility. Studies have reported reductions of up to 50% in ductility for precast columns with grouted sleeves compared to their monolithic counterparts (Haber et al., 2014; Tazarv, 2014; Ameli et al., 2015; 2016; Al-Jelawy et al., 2018). Liu et al. (2021) noted that while these connectors performed adequately under moderate axial loads, their energy dissipation and ductility significantly declined at higher axial loads. These findings emphasize the need for more robust and resilient connection systems capable of delivering reliable structural performance under seismic conditions.

To address these challenges, alternative connection methods have been widely investigated. A range of innovative solutions has been proposed to simplify construction processes, improve structural performance, and facilitate maintenance (as summarized in, e.g., Englekirk, 2003; Dal Lago et al., 2018; Ghayeb et al., 2020b; Guaygua et al., 2023). These strategies often involve mechanical connections using bolts, splices, or similar devices (Vidjeapriya and Jaya, 2013; Yekrangnia et al., 2016; Han et al., 2018; Baran et al., 2021; Nascimbene and Bianco, 2021; Qing et al., 2022; Zhou et al., 2022; Ahn et al., 2023), as well as prestressed or post-tensioning tendons, strands, rods, or reinforcing bars (Stone et al., 1995; Wang et al., 2018; Quiel et al., 2019; Kim et al., 2021; Kim et al., 2022). Welded connections have also been explored (Bhatt and Kirk, 1985; Ersoy and Tankut, 1993; Naito et al., 2012; Rodríguez and Torres-Matos, 2013; Girgin et al., 2017; Menegon et al., 2020; Dal Lago et al., 2022). Furthermore, the incorporation of high-performance materials has demonstrated potential for improving structural performance and ductility in precast connections (Xu et al., 2019; Ma et al., 2021; Zhang X. et al., 2024).

Among the emerging innovations, hybrid precast beam-to-column connections have shown significant promise. Ghayeb et al. (2023) conducted a comprehensive review of these systems, categorizing them into three types: Type I (dry and wet connections utilizing steel sections), Type II (composite material-based systems), and Type III (a combination of Type I and Type II). Their findings highlight the robustness and adaptability of steel sections integrated with the inherent advantages of precast concrete, effectively replicating the behavior of monolithic connections.

As early as the 1980s, Pillai and Kirk (1981) used steel plates to connect precast beam bars with reinforcing bars in the core of the joint through welding. They observed that all precast specimens endured an equal or greater number of lateral load cycles compared to their cast-in-place counterparts, achieving nearly twice the ultimate rotation. Since then, numerous studies have made use of the flexibility, dimensional precision, and availability of steel sections for precast joint detailing. For example, Korkmaz and Tankut (2005) explored a precast beam-to-beam connection using welded plates at the bottom and lap splices for the top steel, which exhibited satisfactory performance under testing. Later on, Li et al. (2009) employed steel angle sections to connect precast beams and columns, demonstrating adequate ductility and strength under cyclic loading, comparable to monolithic specimens. Their results also revealed that embedding steel sections in joint core greatly enhanced its strength, enabling specimens to carry story shears up to a drift ratio of 3.5. Choi et al. (2013) developed a wet precast connection with steel plates for joint continuity, achieving improved strength and ductility under cyclic loading. In a related effort, Ghayeb et al. (2017) introduced a dry precast connection combining steel plates and bolts, which delivered a superior seismic response compared to conventional CIP specimens, along with more stable load-displacement behavior and greater energy dissipation. Notably, the dry connection achieved drift ratios as high as 9.0%.

In recent years, research on hybrid precast connections has expanded significantly, offering valuable insights into the development of precast structures. Ghayeb et al. (2020a) proposed hybrid connections incorporating steel tubes, plates, and couplers, which demonstrated attainable drift ratios up to 50% higher than monolithic connections. Senturk et al. (2020) developed a monolithic-like precast connection with bolted plates, achieving a 34% improvement in both ductility and ultimate deformability. Zhang et al. (2020) advanced the field further by designing a precast connection system integrating highly ductile rods or steel shapes within the joint core. This approach significantly enhanced strength, reduced stiffness degradation, and improved energy dissipation, outperforming conventional monolithic designs. In addition, the addition of steel fiber concrete further boosted seismic performance. Ye et al. (2021) proposed a hybrid beam-to-column connection using an I-steel connector with high-strength bolts, which effectively mitigated stress concentrations while matching the performance of CIP connections. Albright et al. (2022) proposed the "New Performance System" (NPS®), a steel-concrete composite moment-resisting frame with superior strength, stiffness, ductility, and energy dissipation under simulated seismic conditions. More recently, Guan et al. (2023) developed a partially precast steel-reinforced concrete (PPSRC) beam-to-column connection, which shifted the plastic hinge away from the joint, resulting in enhanced strength, ductility, and energy dissipation compared to traditional connections.

Despite these advancements, challenges remain in optimizing these hybrid connections for practical application. Complex construction processes, high costs, and the need for specialized materials or workmanship continue to hinder wider adoption.
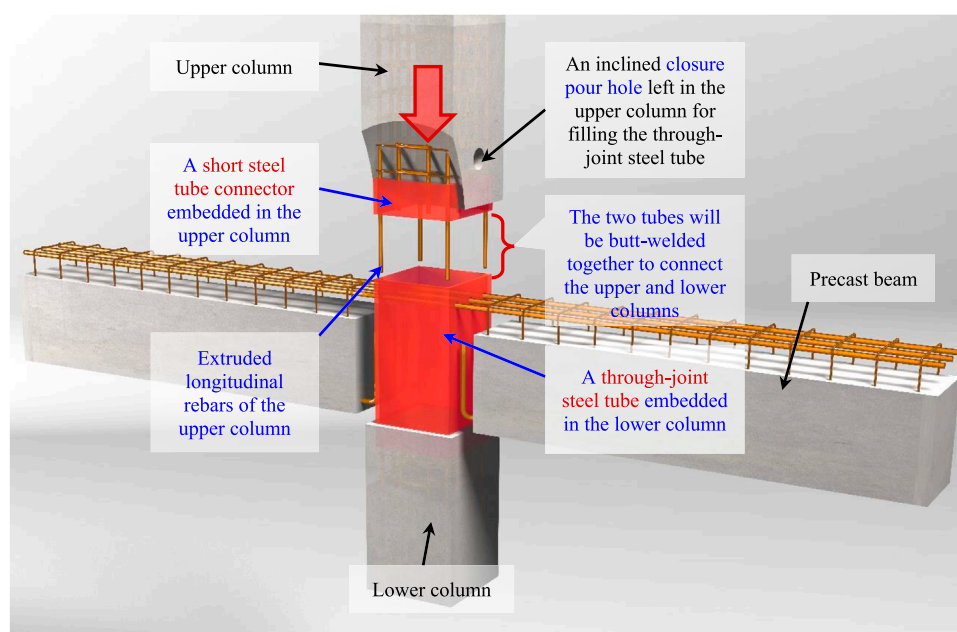
FIGURE 1
A emulative connection using butt-welded steel tubes embedded in precast columns.

Therefore, innovative solutions are still needed to balance structural performance with practical feasibility.

In response to these challenges, this study proposes a beam-to-column hybrid connection, as illustrated in Figure 1. This connection is achieved through welding-spliced steel tubes. The longitudinal rebars of the upper and lower precast columns are welded to the steel tubes embedded in the respective columns. The upper column includes a shorter steel tube connector, while the lower column features a longer steel tube extending through the joint core. The bottom longitudinal rebars of the precast beams are bent and anchored to a steel corbel extending from the lower column's steel tube (for clarity, this detail is omitted in Figure 1). The upper longitudinal rebars of the precast beams pass through pre-formed holes in the steel tube during construction. On-site, the steel tube connector of the upper column is welded to the steel tube of the lower column (Figure 1). Finally, the lower steel tube is filled with concrete through an inclined closure pour hole in the upper column, forming the proposed hybrid connection.

Compared to traditional grouted sleeve connections, this new connection eliminates the need for on-site grouting of the main reinforcement, thereby mitigating potential quality issues associated with grouting inconsistencies. Additionally, the welding-spliced steel tubes leverage the adaptability and dimensional precision of structural steel sections, which simplifies installation and improve alignment during assembly. Welding, a familiar practice for construction workers, enhances reliability compared to the complexities of sleeve grouting.

As noted by Alfred A. Yee over 60 years ago (Yee, 1962), maintaining dimensional accuracy in precast concrete production remains a significant challenge due to concrete's heterogeneity and the variability of materials and processes involved. Factors such as aggregate type, cement content, and curing methods contribute

to dimensional discrepancies, including length, camber, or twist. Human errors, such as misplacement of inserts or mismeasurement, exacerbate these issues, leading to costly errors in both field and factory. By incorporating the precision of structural steel sections, installation efficiency in precast systems can be greatly improved. This is the underlying rationale behind the development of the proposed hybrid connection.

Apparently, the column-to-column connection is a pivotal part of the proposed hybrid connection. To evaluate its efficiency and robustness, five large-scale specimens were tested to failure under lateral load reversals. The key experimental parameters included the anchorage conditions of column longitudinal rebars within the joint's steel tube (i.e., the steel tube extended from the lower column), as well as the thickness of the spliced steel tubes, both of which would significantly affect the connection's performance. The experiments assessed critical seismic behaviors, including hysteresis response, energy dissipation, and strength degradation. Additionally, this study explored how to predict the lateral strength, load-displacement response, and plastic hinge length of the column specimens. The outcomes of this study will serve as a basis for future research on the beam-to-column connection concerned.

2 Experimental program

2.1 Specimen design

The experimental program for this project included a total of five square column specimens: four precast columns (designated as PC-C1 to PC-C4) and one reference cast-in-place column (CIP-C0). The assembly process for the precast specimens is illustrated in Figure 2, while Figure 3 provides the structural details of all specimens. Key
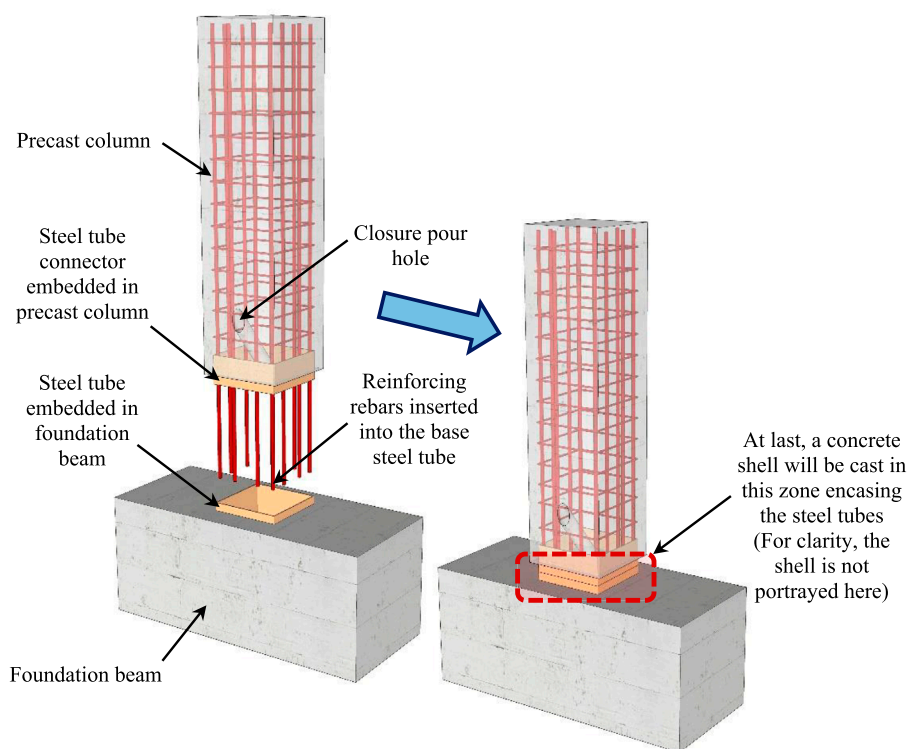
FIGURE 2
Schematic of assembly of the precast column model.

experimental parameters are summarized in Table 1. Each specimen was nearly full-scale, with a total height of 2,200 mm (including the foundation beam). The effective column shaft length (measured from the load point center to the foundation beam top) was thus 1,400 mm. The column shafts had a square cross-section measuring 400 mm × 400 mm.

The specimens were designed to investigate the influence of two primary parameters on the performance of the proposed connection:

(1) Anchorage ratio of column longitudinal rebars: This parameter was varied to examine how the degree of rebar engagement within the steel tube embedded in the foundation beam (referred to as the base steel tube or the foundation steel tube) affects the lateral load transfer mechanism and overall seismic performance. Specifically, these anchorage ratios were 0 (no rebar extended), 1/3 (only the four corner rebars extended), 1 (all rebars fully extended), and 0 for PC-C1, PC-C2, PC-C3 and PC-C4, respectively. These ratios chosen (0, 1/3, 1) represent typical configurations in practical precast design scenarios;

(2) Steel tube thickness: Two thickness levels (4 mm and 8 mm) were selected to study the effect of localized stiffening on the plastic hinge behavior and the distribution of damage. Specifically, the steel tube wall thickness was 4 mm for PC-C1 through PC-C3, while PC-C4 had a thicker tube of 8 mm. All the steel tubes had a uniform side length of 340 mm. From Figure 3, it can be observed that after the steel tube connector in the precast column was aligned and welded

to the extruded steel tube in the foundation beam, the exposed length of the steel tubes outside the concrete was 80 mm.

The above test parameters were chosen because they are critical to the performance of the proposed connection. The anchorage ratio directly influences the interaction between the longitudinal rebars and the steel tubes, while the steel tube thickness governs the tube's ability to resist local buckling and contribute to force transfer.

All specimens were subjected to a constant axial compression ratio of 0.3. The fabrication process for the precast specimens is detailed in Figure 4. Fabrication began with tying reinforcement for the column shaft and foundation beam. Each precast column had a 140-mm-tall steel tube connector embedded at its bottom end, with 40 mm extending beyond the concrete (Figure 4C). Inside the precast column, the longitudinal rebars were placed snugly against the inner surface of the tube connector. At the same time, the rebars and the connector were attached using 90-mm-long double-sided fillet welds (Figure 4A).

For the CIP-C0 specimen, a single continuous pour was employed. In contrast, the precast specimens were fabricated in two steps. First, the column shaft was cast and allowed to cure until the target strength was achieved. Next, the shaft was welded to the foundation's base steel tube via full penetration butt welds at their beveled ends. Concrete was then poured through a 70-mm-diameter inclined closure hole and thoroughly vibrated to ensure proper consolidation. Finally, a thin layer of concrete was applied around the welded steel tubes to protect them and provide a smooth surface for the precast column shaft (Figure 4F).
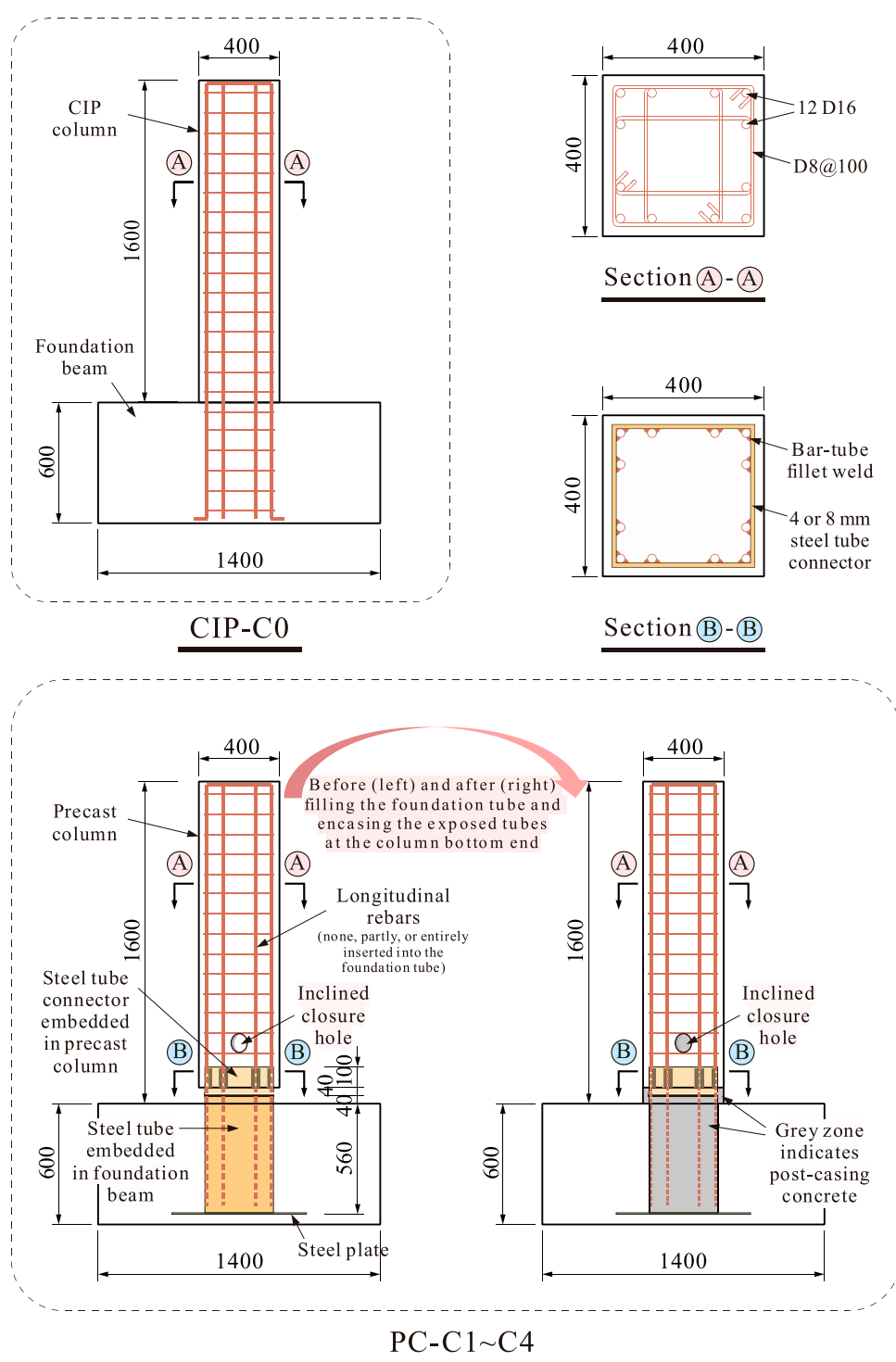
FIGURE 3
Design details of column specimens (unit: mm).

2.2 Materials

The column shafts and the foundation beams were cast using C30-grade concrete (30 MPa design strength). During testing, the measured compressive strength of the concrete was 37.5 MPa (150-mm cube samples), while the post-cast concrete poured through the

closure hole had a strength of 32.6 MPa. The reported strengths were averages based on at least three samples.

Both the steel tube connectors and foundation steel tubes were made of Q355-grade steel. For all of reinforcing bars used, the strength grade was HRB400. The columns were reinforced with twelve 16-mm-diameter longitudinal rebars, providing a

TABLE 1 Test matrix of specimens.

Specimen name	Steel tube thickness (mm)	Anchorage ratio *a*	Axial load ratio *n*
CIP-C0	0	1	0.3
PC-C1	4	0	0.3
PC-C2	4	1/3	0.3
PC-C3	4	1	0.3
PC-C4	8	0	0.3

(a) Welds between column longitudinal rebars and steel tube connector (STC)

(b) Installation of plastic pipe for forming inclined closure pour duct

(c) Completion of casting of precast columns with extruded rebars and STCs

(f) The final appearance of precast column specimens erected outside the lab

(e) Filling foundation steel tube with concrete (through inclined closure pour hole)

(d) Installing a precast column by aligning and welding exposed steel tubes

FIGURE 4
Casting and assembly process of specimens. **(A)** Welds between column longitudinal rebars and steel tube connector (STC) **(B)** Installation of plastic pipe for forming inclined closure pour duct **(C)** Completion of casting of precast columns with extruded rebars and STCs **(D)** Installing a precast column by aligning and welding exposed steel tubes **(E)** Filling foundation steel tube with concrete (through inclined closure pour hole) **(F)** The final appearance of precast column specimens erected outside the lab.

reinforcement ratio of 1.51%. Stirrups were 8-mm-diameter four-legged ties, spaced at 100 mm. The actual tensile properties of the rebars and steel tubes were measured, with details provided in Table 2.

2.3 Loading protocol and instrumentation

The experiments were conducted at the Structural Engineering Laboratory of South China University of Technology. Each

specimens was anchored to the lab's strong floor using a restraint system. Lateral loads were applied incrementally using an MTS electro-hydraulic actuator in a low-cycle push-pull manner. Additionally, a jack with roller supports was used to apply axial load to each specimen. The axial load was managed to keep constant at 1,400 kN, corresponding to an axial compression ratio of 0.3. The complete loading setup is shown in Figure 5.

An array of linear variable displacement transducers (LVDTs) was mounted on the lower part of the specimens to monitor curvature changes and slip rotations there (Figure 6). Strain gauges

TABLE 2 Measured tensile strengths of steels used in the tests.

Steel type	Diameter or thickness (mm)	Yield strength (MPa)	Ultimate strength (MPa)
Rebar	8	406.8	616.3
	16	451.1	642.9
Tube	4 mm (actual: 3.78 mm)	372.3	504.6
	8 mm (actual: 7.76 mm)	407.1	538.2

FIGURE 5
Test setup.
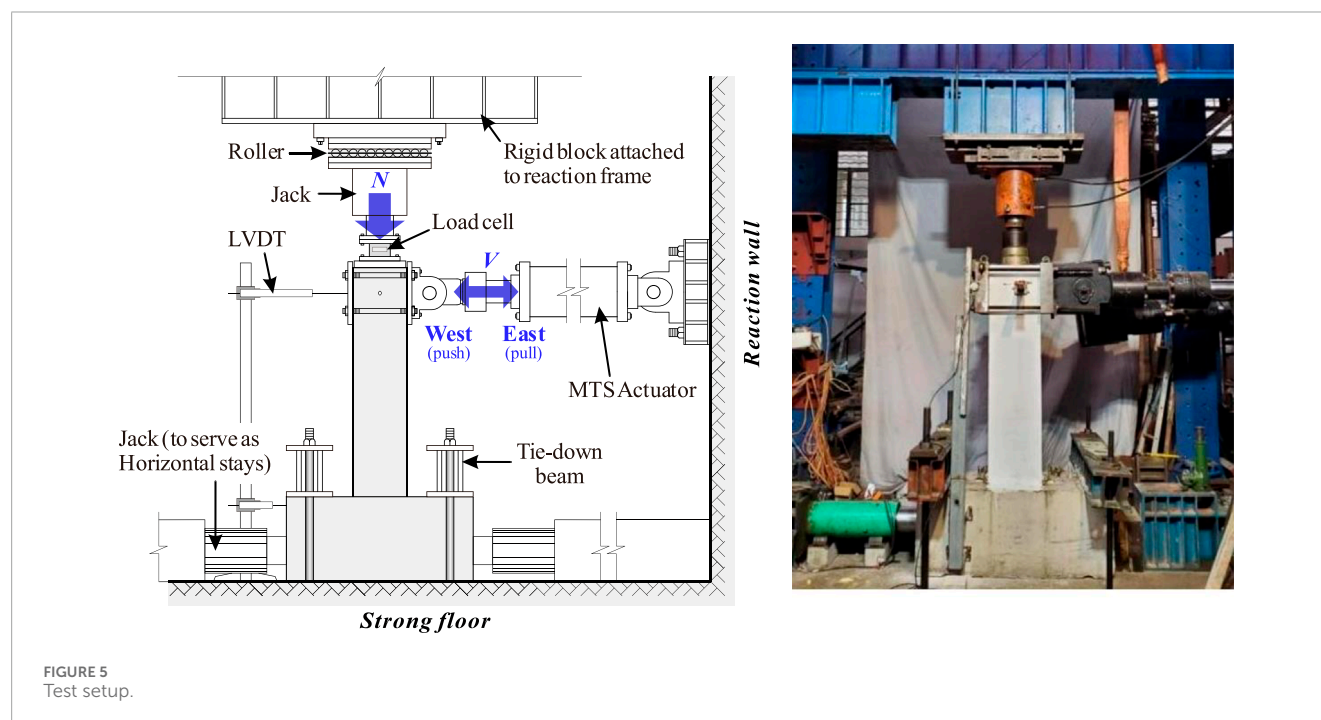
were attached to key locations on the rebars and steel tubes within the columns and foundations. All instrument readings were automatically collected by a computer system. To better observe concrete cracking, each specimen was coated with whitewash.

According to ACI 374.1-05, (2005) guidelines, the cyclic loading was run in a displacement-controlled mode, with drift ratios stepping up as follows (±%): 0.1, 0.25, 0.50, 0.75, 1.0, 1.5, 2.0, 2.5, 3.0, 3.5, and 4.0. Each drift level was cycled three times. For safety, testing was terminated when the lateral load dropped to 80–85% of its peak value.

3 Test results

3.1 Failure process

All the specimens demonstrated stable loading behavior until significant damage occurred. The cracking pattern and failure modes of both the monolithic and precast columns are shown in Figure 7. Flexural-dominated failure modes were observed across all specimens, characterized by concrete spalling and crushing concentrated in the lower regions of the columns. However, variations in the connection details resulted in differing extents and distributions of damage.

During the initial loading phase, small horizontal hairline cracks were observed in all specimens. As the drift ratio increased, flexural cracks became more pronounced, and the concrete cover began to spall off, leading to flexural-compression failure near the column base. This failure was marked by crushed concrete and local buckling of the longitudinal rebars.

Most notably, in comparison to the CIP column, the precast columns displayed a broader failure zone due to the presence of welding-spliced steel tubes extending 180 mm from the column-foundation interface. This shifted the failure region upwards, where significant concrete spalling and longitudinal rebar buckling, including fractures, were observed (Figure 7). When the drift ratio reached 2.5%, several diagonal cracks appeared in specimens PC-C3 and PC-C4. Additionally, as the rebar anchorage ratio and steel tube thickness increased, the severity of the localized damage above the welded tubes intensified.

Specimen PC-C1, which lacked anchored rebars, relied primarily on the welded steel tubes to transfer internal forces
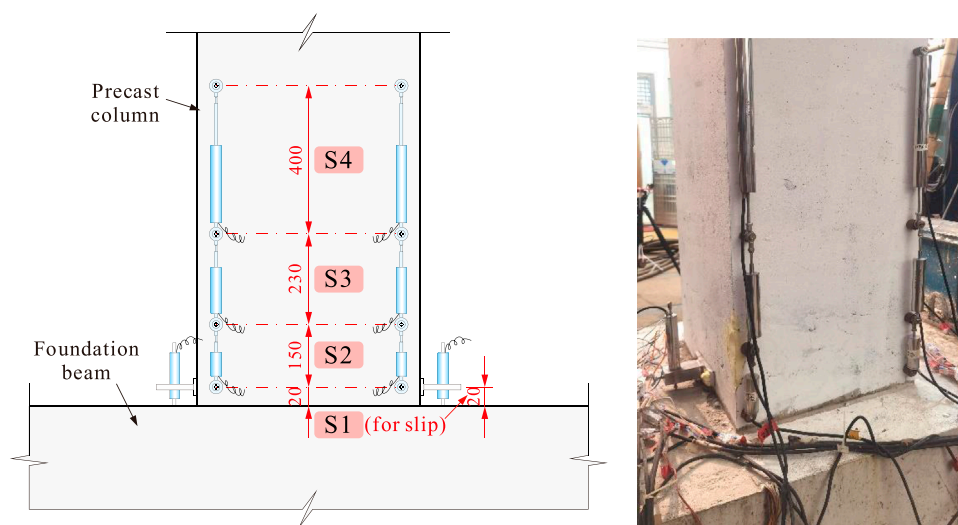
FIGURE 6
Arrangement of LVDTs within and beyond the column hinge zone (unit: mm).

(axial load, shear force, and bending moment) to the foundation beam. Under reversed cyclic loading, the corners of the steel tubes exhibited noticeable buckling, eventually tearing open during the later loading stages (Figure 7). This localized failure indicated that, in the absence of anchored column rebars and with thinner steel tubes, the welded tube region bore the majority of stresses, concentrating damage in themselves.

Specimen PC-C2, with a 1/3 rebar anchorage ratio (corner rebars only), displayed less severe buckling at the steel tube corners. Instead, localized buckling occurred at the central region of the welded tubes (Figure 7), and the longitudinal rebars above the tubes showed clear signs of local buckling. This suggested that the corner rebars extending into the foundation worked synergistically with the steel tubes to distribute internal forces, reducing the extent of tube damage. As a result, the failure zone shifted higher up compared to PC-C1.

Similarly, specimen PC-C3, featuring fully anchored longitudinal rebars, exhibited no apparent damage to the welded tubes (Figure 7). Instead, failure was concentrated in the column shaft above the tube region. Among all specimens, the upward shift in the failure zone was most pronounced in PC-C3. The increased flexural capacity in the welded tube region, resulting from the combined action of the steel tubes and fully anchored rebars, contributed to this phenomenon. This observation aligns with established findings in seismic studies, where localized strengthening alters failure progression and extends damage zones upwards (e.g., Al-Jelawy et al., 2018; Lee et al., 2022).

Specimen PC-C4, incorporating thicker welded steel tubes (8 mm) but no anchored rebars, exhibited an upward shift in the damaged zone similar to PC-C3. However, the absence of extended rebars limited the efficiency of load transfer. As a consequence, the increased tube thickness enhanced the flexural stiffness in the tube region but failed to improve overall lateral strength without proper rebar anchorage.

The broader damage zone observed in precast columns has both advantages and disadvantages: while it helps to distribute plastic deformations along the column shaft, potentially enhancing energy dissipation capacity (as detailed later), it also complicates post-earthquake repair due to the widespread nature of the damage.

It was also observed that the corner rebars in all precast columns (except PC-C1) fractured above the welded tubes. Still, none of the specimens exhibited any failure at the butt welds between the tube connector and the foundation tube. This confirmed the reliability of the welded connections, which showed no signs of detachment or weakness during testing.

3.2 Lateral load response

The lateral load-displacement responses for each specimen, measured at the column tip, are illustrated in Figure 8, including both hysteresis loops (Figures 8A–E) and backbone curves (Figure 8F). As expected for concrete columns undergoing flexural-dominated failure, the hysteresis loops showed a typical "spindle" shape, indicative of full and stable energy dissipation.

Among the precast specimens, PC-C1 exhibited a significant reduction in lateral load-bearing capacity (around 20% on average) compared to the monolithic specimen (CIP-C0). PC-C2, with partially anchored longitudinal rebars, exhibited some recovery in lateral capacity compared to PC-C1, though it remained approximately 15% lower than CIP-C0. PC-C3, with fully anchored longitudinal rebars, demonstrated a load-bearing capacity nearly equivalent to CIP-C0, suggesting that the lateral resistance had been almost completely restored, although its peak load was reached slightly later. PC-C4, incorporating thicker steel tubes but no anchored rebars, showed only marginally higher lateral strength than PC-C1.
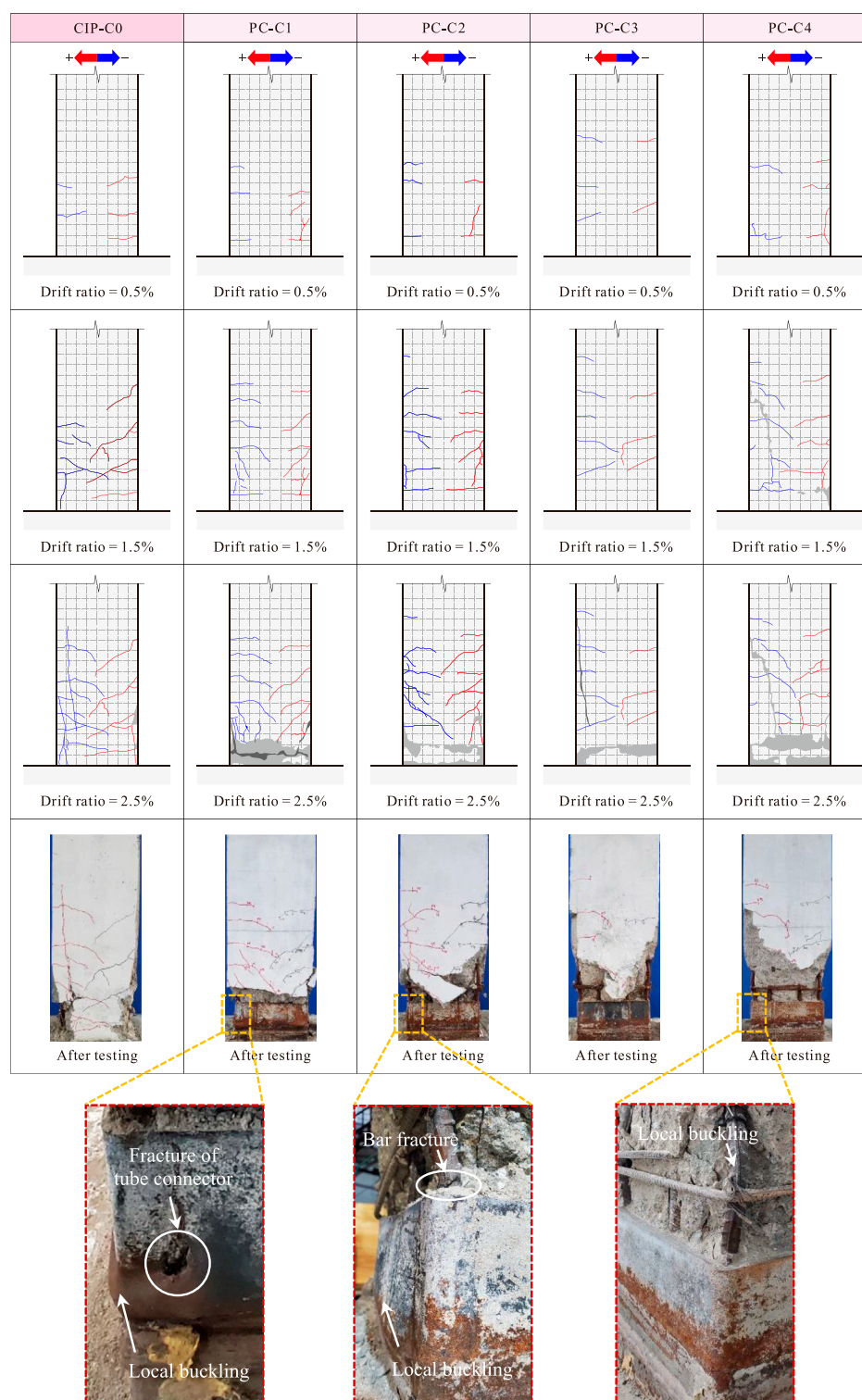
FIGURE 7
Failure process and final appearance of specimens.

These findings clearly indicate that when the column longitudinal rebars are not anchored into the joint core (namely, the foundation beam in this testing setup), the load transfer mechanism depends on the welding-spliced steel tubes. Consequently, the lateral load-bearing capacity of the precast columns is reduced compared to the fully cast-in-place specimen. Three primary reasons may explain this reduction:
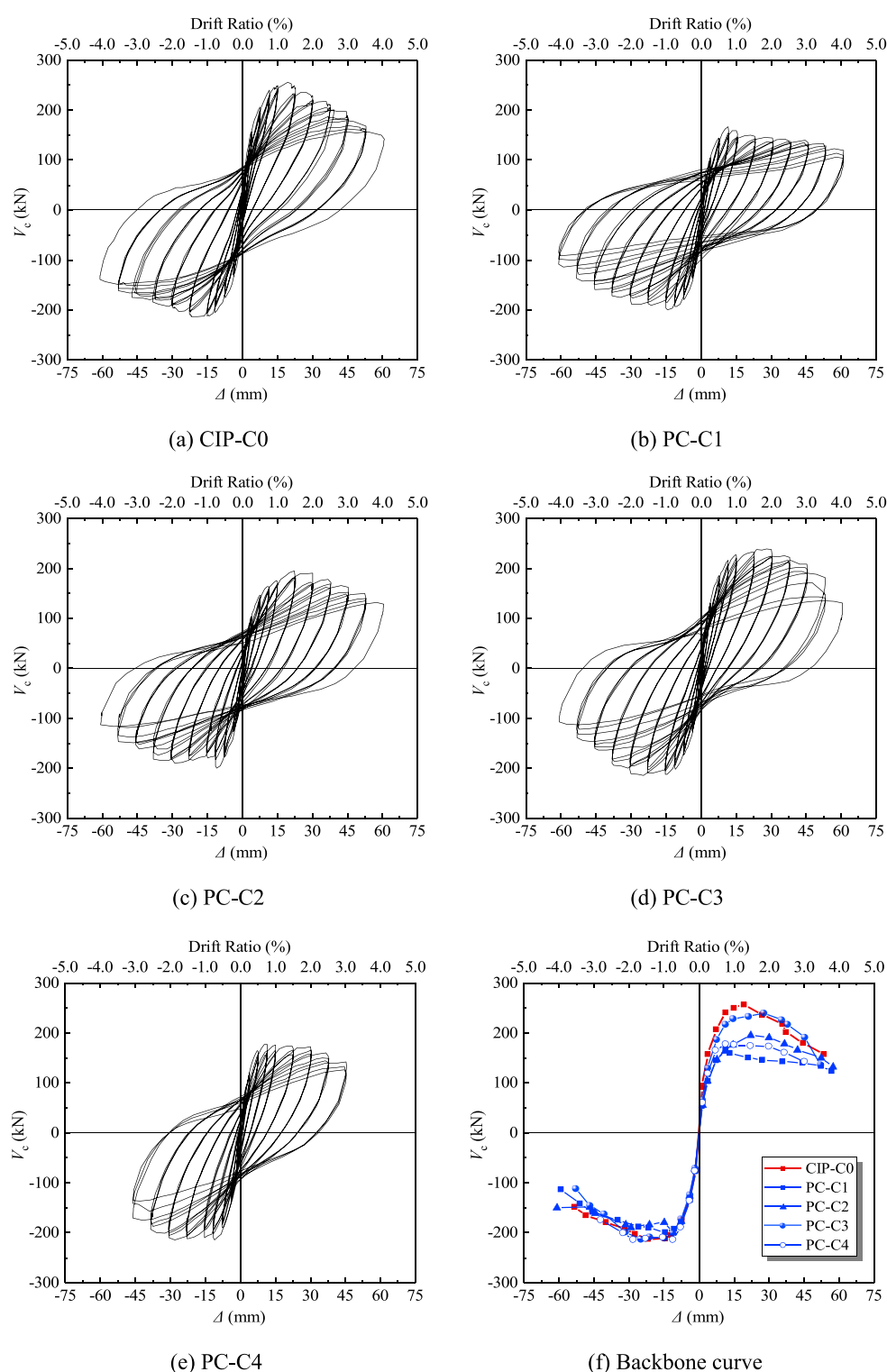
FIGURE 8
Lateral load-displacement responses of specimens. **(A)** CIP-C0 **(B)** PC-C1 **(C)** PC-C2 **(D)** PC-C3 **(E)** PC-C4 **(F)** Backbone curve.

(1) Steel tube wall thickness: Although the overall cross-sectional area of the welded steel tubes was roughly equivalent to that of the column longitudinal rebars, the steel tube walls in PC-C1 to PC-C3, at only 4 mm thick, were susceptible to local buckling

under flexural-compression loads. This buckling caused a measurable reduction in the peak load of the precast columns;

(2) Cold joint near the column-foundation interface: The presence of a cold joint between the precast column and the foundation
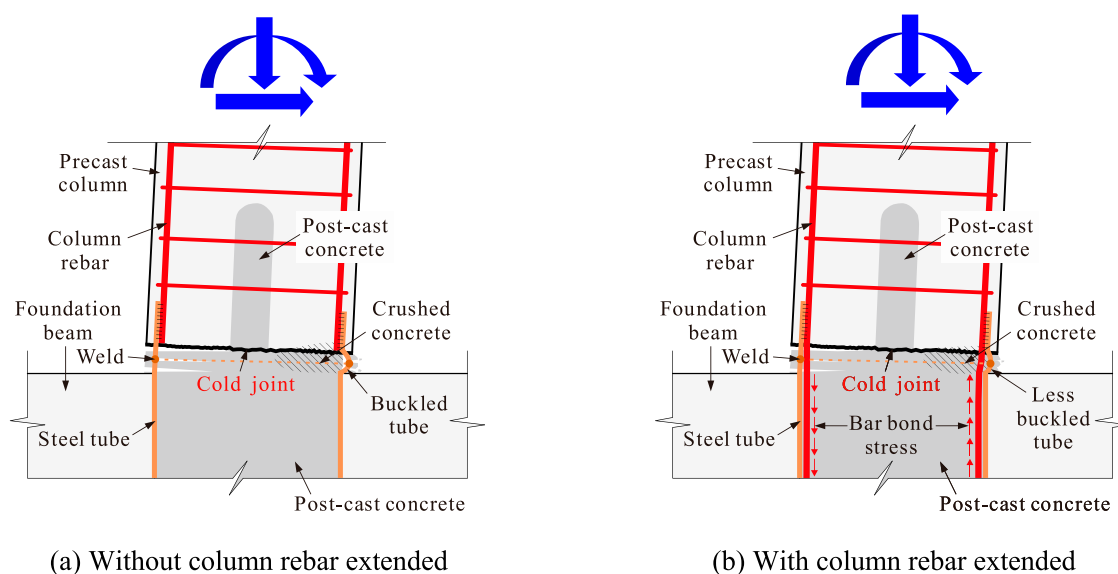
FIGURE 9
Failure mechanisms of precast column specimens. **(A)** Without column rebar extended **(B)** With column rebar extended.

beam hindered effective shear and moment transfer. Cold joints inherently create weak points where material continuity and structural integrity are compromised, especially under cyclic or seismic loading. This phenomenon is a known limitation of precast systems and one of the primary reasons why precast connections typically exhibit inferior performance compared to CIP connections (Englekirk, 2003; Kishen and Rao, 2007; Davaadorj et al., 2020);

(3) Post-Cast concrete strength: The compressive strength of the post-cast concrete used in the tests was lower than that of the precast concrete. This disparity further reduced the lateral load-bearing capacity of the precast columns.

Figure 9 attempts to explain the different failure mechanisms caused by whether or not the downward extension of the column longitudinal rebars was adopted. This figure, in combination with the test results for the columns' lateral strength, highlights a clear relationship between the rebar anchorage and the load-resisting mechanisms. It is reasonable to believe that the presence of the cold joint could compromise the reliability of force transfer, particularly due to potential inconsistencies during the casting process. In such cases, the downward extension of the column rebars becomes especially critical. As the rebar anchorage ratio increased, the engagement of the longitudinal rebars improved, thereby reducing the reliance on the steel tubes to bear the entire load. This enhancement in load transfer paths allowed the lateral capacity of the precast columns to progressively recover, eventually matching that of the fully monolithic column.

It was observed that PC-C1 did not exhibit the gradual hardening trend seen in the other specimens during push-direction excursion. This lack of hardening resulted in an asymmetrical hysteretic response for PC-C1 between the push and pull directions. The exact cause of this behavior is not yet fully understood, but it is hypothesized that it may primarily be attributed to the absence

of downward-extended longitudinal rebars into the base tube in PC-C1. Without these rebars, the force transfer mechanism heavily relies on the welded steel tubes, which could lead to less stable post-peak performance. Additionally, the presence of the cold joint might contribute to this phenomenon. In particular, there may have been "loose" contact between the post-cast concrete and the precast portion on one side of the column, affecting the load-resisting behavior. While this issue could potentially be mitigated by ensuring that the column rebars are extended into the base tube, as seen in other specimens, additional experimental evidence is required to verify whether this behavior is a general characteristic of this type of connection or a specimen-specific anomaly.

Another important observation from the design and testing phases was that merely increasing the steel tube thickness (i.e., reducing the width-to-thickness ratio) was insufficient to improve force transfer or lateral strength (as is the case of CIP-C4). This outcome underscores the inefficiency of increasing steel tube thickness alone, which not only results in excessive steel usage but also fails to address the underlying load transfer inefficiencies.

For optimal performance in engineering design, it is more effective to ensure that the steel tube's yield capacity under lateral loads is well-matched to that of the longitudinal rebars. Furthermore, it is critical to anchor a portion of the longitudinal rebars inside the steel tube within the joint region. This anchorage is essential for the proposed precast connection system to achieve reliable performance. Beyond this, further increases in steel tube thickness appear to be unnecessary and unwarranted.

3.3 Ductility

The primary test results for all specimens, including the ductility coefficient, are summarized in Table 3. According to Park et al. (1982), the displacement ductility coefficient, μ, is defined as

TABLE 3 Main test results.

Specimen name	Yield load				Peak load				Ultimate load				Ductility
	V_y (kN)		Δ_y (mm)		V_p (kN)		Δ_p (mm)		V_u (kN)		Δ_u (mm)		μ
	+	-	+	-	+	-	+	-	+	-	+	-	
CIP-C0	215.7	180.2	8.6	7.8	256.1	213.2	19.5	21.6	217.7	181.3	36.0	38.2	4.54
PC-C1	145.9	168.2	7.7	6.6	166.8	199.3	11.6	14.3	141.8	169.4	36.9	38.4	5.31
PC-C2	158.9	175.1	10.3	7.5	195.5	199.9	22.1	11.0	166.2	169.9	41.9	39.3	4.65
PC-C3	201.4	182.4	9.6	8.6	238.7	214.0	28.0	24.7	202.9	181.9	42.0	35.8	4.27
PC-C4	155.1	186.5	6.6	7.4	177.3	214.3	11.5	11.1	150.7	182.1	41.1	39.2	5.76

$\mu = \Delta_u/\Delta_y$, where Δ_u and Δ_y represent the ultimate and yield displacements, respectively.

From the results shown in the table, it is evident that the ductility coefficients of the precast column specimens are generally comparable to, or slightly higher than, those of the reference CIP specimen. This can likely be attributed to the different detailing solutions adopted by the CIP column and precast columns.

In the case of the CIP column, after reaching the peak load, the rebars at the column base began to buckle severely, engaging the stirrups and displacing them outward. As a result, the loss of confinement caused the concrete crushing zone to extend deep into the center of the column base (Figure 7). This uncontrolled breakdown of the concrete at the column base led to a sharper decline in the lateral strength.

In contrast, for the precast columns, although the steel tubes did not contribute to a higher lateral capacity, they continued to provide confinement to the internal concrete after the peak load, preventing significant crushing. Unlike longitudinal rebars and stirrups in the CIP column, which were spaced apart, the steel tubes offered a uniform and consistent wrapping effect around the concrete. This continuous confinement limited the spread of the crushing zone at the column base and, instead, shifted it upward. Consequently, the post-peak deformation capacity of the precast columns was, at least, not inferior to that of the CIP specimen.

It is also noteworthy that all the specimens achieved lateral drift ratios greater than 2% at the point of failure, which met the requirements of the Chinese seismic code (GB50011-2010, 2010). This further demonstrates that the proposed column-to-column connection is suitable for applications in seismic regions.

3.4 Stiffness reduction and strength decay

As the lateral drift increased, the stiffness of the columns decreased correspondingly. Figure 10 compares the degradation of the average secant stiffness, K_i, for each specimen in both the push and pull loading directions. K_i is defined in Equation 1:

$$K_i = \frac{|+F_i| + |-F_i|}{|+X_i| + |-X_i|} \tag{1}$$
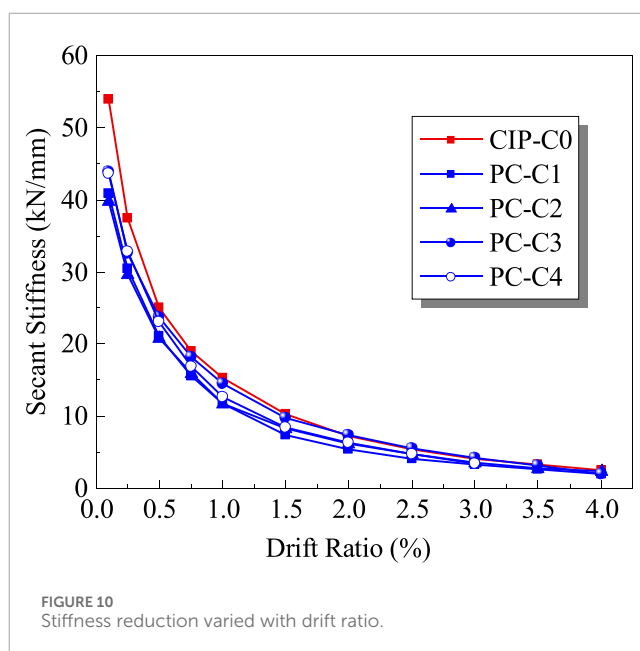
FIGURE 10
Stiffness reduction varied with drift ratio.

where $+F_i$, $-F_i$ are the positive and negative peak loads at the i-th drift level, respectively; $+X_i$, $-X_i$ are the corresponding positive and negative peak displacements for $+F_i$ and $-F_i$, respectively.

As shown in Figure 10, the average secant stiffness of all columns decreased as the drift ratio increased. Compared to the monolithic column, the precast columns exhibited generally lower overall average secant stiffness, especially in terms of the initial stiffness. However, during early loading phase, the secant stiffness of the monolithic column dropped more rapidly than the precast specimens. As the drift continued to increase, the difference in the secant stiffness between the precast and monolithic columns gradually diminished. By the time the drift ratio reached 2%, the secant stiffness of the precast columns was almost identical to that of the monolithic column.

In the precast columns, the presence of the cold joint near the base appeared to result in lower initial stiffness. Conversely, the monolithically cast column, free from a cold joint, exhibited stronger initial stiffness. However, at higher drift ratios, the CIP

FIGURE 11
Strength decay varied with drift ratio.

FIGURE 12
Evolution of energy absorption.
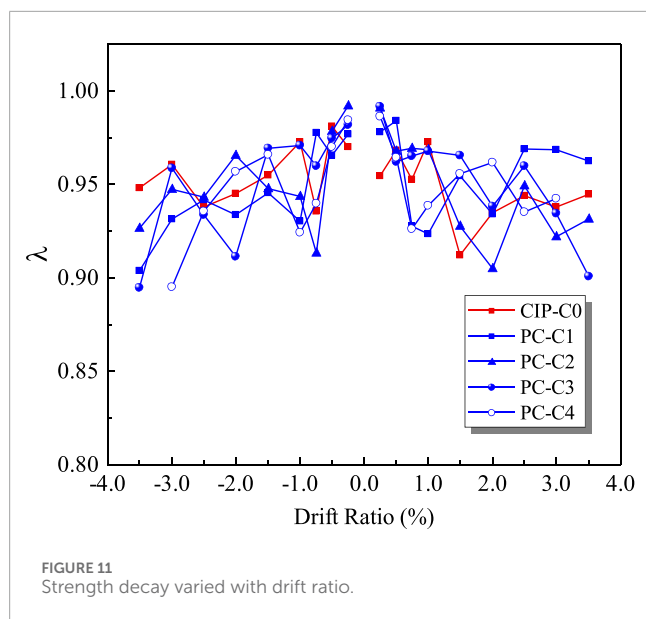
column experienced severe concrete crushing, leading to a loss of confinement (as previously discussed) and causing a more rapid degradation in stiffness.

At the same lateral displacement level, the maximum load sustained by a concrete specimen decreases as the number of hysteresis loops increases. This phenomenon, commonly referred to as in-cycle strength degradation (or simply strength degradation), was assessed by the strength degradation coefficient λ (Paulay and Priestley, 1992), which is determined by the ratio of the second peak load to the first peak load at the same drift ratio (namely, $\lambda = V_{i, 2nd}/V_{i, 1st}$, where $V_{i, 2nd}$ and $V_{i, 1st}$ are, respectively, the foresaid second peak load and the first peak load at the same drift ratio i). The values of λ for each specimen are presented in Figure 11.

As illustrated in Figure 11, before the drift ratio reached 0.5%, the λ values for all specimens were generally higher than 0.95, indicating that the specimens exhibited minimal damage at this stage, with the in-cycle strength reduction rate not exceeding 5%. Beyond this point, the in-cycle strength loss became more pronounced as the drift ratio increased for all specimens.

For the precast columns, the lowest λ values ranged between 0.89 and 0.94. This suggests that even when the corner longitudinal rebars of the precast columns fractured, the strength reduction at the same drift level remained limited. However, a subtle trend can be observed from Figure 10: at larger drift ratios, the in-cycle strength deterioration of the CIP-C0 column appears to be less significant compared to the precast specimens.

A plausible explanation for this trend lies in the reloading stiffness of CIP-C0, which consistently remained higher than that of the precast specimens, likely due to the absence of the cold joint. This higher stiffness allowed CIP-C0 to retain more strength within the same hysteresis loop at a given deformation level. Nevertheless, this advantage diminished as CIP-C0 exhibited a steeper descending branch in the post-peak
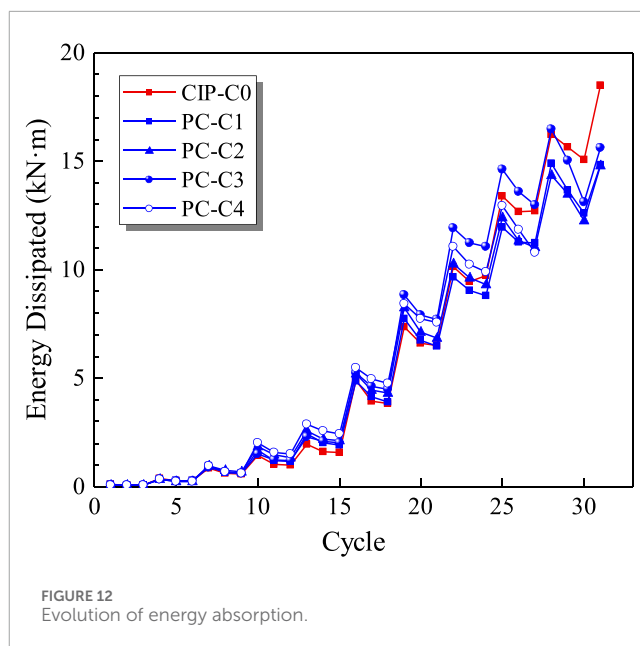
region, reflecting its rapid strength deterioration under larger drift demands.

3.5 Energy dissipation

As the drift ratio increased, the energy dissipation capacity of each specimen, represented by the area enclosed by the hysteresis loops, is shown in Figure 12. The results indicate that, prior to a drift ratio 2.5%, the energy dissipation capacity of the precast columns consistently exceeded that of the monolithically cast column. However, beyond that drift ratio, specimen PC-C1, due to the severe buckling of the welded steel tubes, exhibited a slightly lower energy dissipation capacity compared to CIP-C0. Despite this, the overall energy dissipation performance of the precast columns remained comparable to, and in some cases exceeded, that of the monolithic column.

A similar trend is observed in the equivalent viscous damping ratio, ξ_{eq}, as shown in Figure 13 and Table 4. These results further corroborate the conclusion that the precast columns exhibited favorable hysteretic behavior under cyclic loading.

The above desirable energy dissipation capacity observed in the precast columns was probably related to the additional confinement provided by the welded steel tubes. These tubes reduced the severity of concrete spalling and crushing, thereby enhancing the hysteretic behavior and allowing the precast columns to sustain greater energy dissipation during loading cycles. Additionally, the more extensive damage along the column shaft also appeared to contribute to enhanced energy dissipation.

It is important to reiterate that grout-filled sleeve connections have been shown to perform well under seismic loading, as noted in the Introduction section; however, scholars have also reported that these connections may exhibit reduced displacement ductility compared to monolithic connections (Haber et al., 2014; Tazarv, 2014; Ameli et al., 2015; 2016; Al-Jelawy et al., 2018). In contrast, the

FIGURE 13
Values of ξ_{eq} varied with drift ratio.
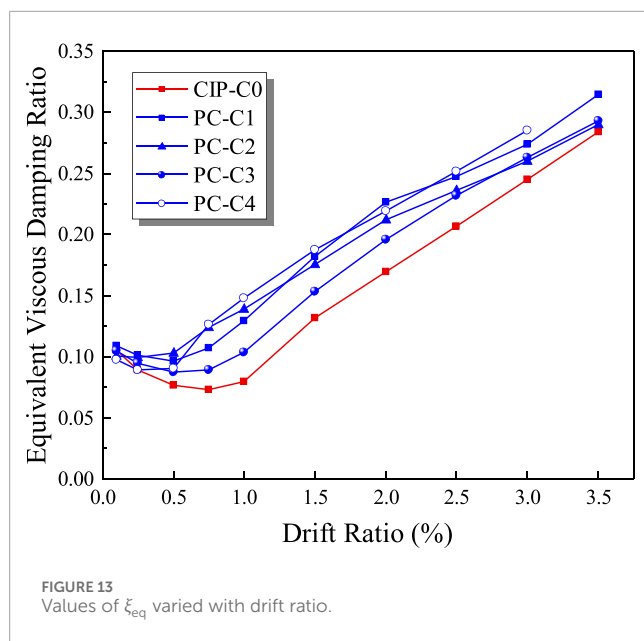
TABLE 4 Comparison of ξ_{eq} at different drift ratios.

Drift ratio (%)	CIP-C0	PC-C1	PC-C2	PC-C3	PC-C4
0.1	0.106	0.109	0.101	0.105	0.098
0.25	0.089	0.101	0.099	0.095	0.089
0.5	0.077	0.096	0.103	0.087	0.090
0.75	0.073	0.107	0.124	0.089	0.127
1.0	0.080	0.129	0.139	0.104	0.148
1.5	0.132	0.182	0.176	0.154	0.187
2.0	0.170	0.226	0.212	0.196	0.219
2.5	0.207	0.247	0.236	0.232	0.252
3.0	0.245	0.274	0.260	0.263	0.285
3.5	0.284	0.315	0.290	0.293	–

proposed welded steel tube connection demonstrated comparable ductility and energy dissipation to the CIP specimen, even under varying rebar anchorage ratios. Specifically, in terms of the value of ξ_{eq}, Al-Jelawy et al. (2018) reported that for precast columns employing grout-filled sleeves, ξ_{eq} did not exceed 0.25 up to the point of failure. In comparison, the precast columns in this study achieved a maximum ξ_{eq} value of 0.32, clearly demonstrating superior energy dissipation capacity. This is precisely one of the key advantages of the proposed connection.

3.6 Plastic hinge deformation

Plastic hinge deformations in concrete columns are critical in assessing their seismic performance. These deformations result from a combination of flexural displacements, shear deformations (if present), and localized rotations caused by bond slip of longitudinal rebars, which are strongly influenced by strain penetration into the foundation beam.

In the current tests, the plastic hinge deformations were quantified using the instrumentation configuration illustrated in Figure 6. The individual displacement components for each column are presented in Figure 14, divided into four regions, S1 through S4, which contributed varying proportions to the lateral deformation at the column tip. The unknown errors in the figure likely resulted from measurement inaccuracies or unmonitored shear deformations, among other factors.

For the CIP column, it is evident that regions S1 and S2 contributed the most to the overall column tip deformation. At higher levels of lateral deformation, their combined contribution reached up to 70%. Notably, S2 alone contributed more than 40%, while S1 (associated with bond slip) accounted for over 20%. These findings are consistent with the experimental observations, where damages primarily occurred within approximately 300 mm from the column base. It is important to note that bond slip contributions exceeding 20% are not uncommon; several studies (e.g., Bae and Bayrak, 2008; Al-Jelawy et al., 2018) have reported that bond slip is a key contributor to column tip displacement, accounting for up to 50% of total deformation in some monolithic columns.

When it comes to the precast columns (except PC-C1), the combined contributions of S1 and S2 were generally lower than those in the CIP column. Instead, the contributions of S3 and S4 increased significantly. For instance, in PC-C3, the contributions of S3 and S4 to lateral displacement exceeded 40%. This is in agreement with the experimental observations. The use of welded steel tubes and well-anchored column rebars in the precast columns led to more extensive damage zones further from the column base, which explains the increased weight carried by regions S3 and S4.

For PC-C1, where the longitudinal rebars did not run down into the foundation, the primary load transfer mechanism was through the welded steel tubes. Because of that, the contribution of S1 was the highest among all columns (note: for the precast columns, a portion of the S1 deformation may have originated from local buckling of the welded steel tubes). At the same time, the contributions of S3 and S4 were smaller, with S2 contributing the most.

In the other precast columns, the contribution of S3 (primarily corresponding to the region 220 mm above the welded steel tubes) was significant. For PC-C3 and PC-C4, S3 alone contributed more than 20% of the lateral deformation. Accordingly, the contribution of S1 in these columns dropped off, gradually falling below 20% in the later stages of loading.

3.7 Strain analysis

Tensile strains measured from the longitudinal rebars and welded steel tubes (where applicable) offer valuable insight into the extent and distribution of plasticity along the column shafts. The tensile strain
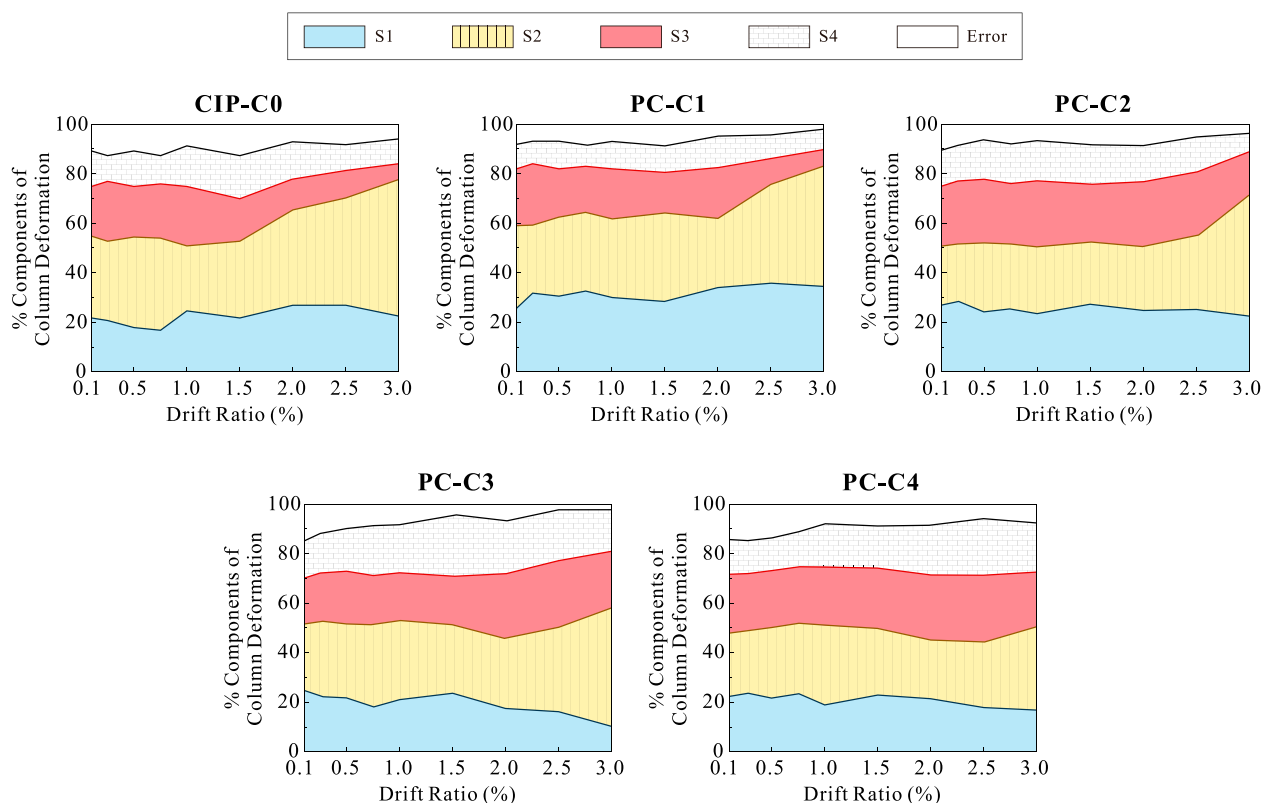
FIGURE 14
Deformation components of each column.

profiles for each column specimen are presented in Figure 15, up to the drift ratio where the measured data remained reliable.

As expected, the CIP column (Figure 15A) developed plasticity primarily concentrated in the lower portion of the column, with some spreading into the foundation beam. In contrast, for the precast columns, yielding of the longitudinal rebars was observed above the welded tubes, and the plasticity continued to propagate upward along the column shaft as the drift levels increased.

For PC-C1, the steel tube yielded relatively early, at a drift ratio of 0.5%. This early yielding was likely due to the absence of anchored longitudinal rebars, which caused the welded steel tubes to bear the majority of the stresses. As the proportion of longitudinal rebars anchored into the foundation increased (e.g., PC-C2 and PC-C3), the high-stress concentration in the steel tubes was alleviated, and the tensile stresses in the longitudinal rebars were distributed more uniformly. This trend highlights the synergistic role of anchored rebars and steel tubes in managing stress distribution and delaying the progression of plasticity.

Similarly, an increase in steel tube thickness delayed the onset of yielding. By comparing the strain distributions in PC-C1 (4 mm thick steel tubes) and PC-C4 (8 mm thick steel tubes), it is evident that the thicker tubes effectively postponed yielding and reduced stress concentrations in the steel tubes. This delayed yielding underscores the importance of tube thickness in influencing the progression of plasticity within the column shaft.

4 Discussion

4.1 Plastic hinge length

The determination of plastic hinge length is essential for both seismic modeling and performance evaluation of concrete columns. For the column-to-column connection proposed in this study—which employs welding-spliced steel tubes—the plastic hinge length tends to be longer than that of conventional CIP columns. This section evaluates the plastic hinge lengths of the tested columns using existing prediction formulas.

The plastic hinge length, L_p, can be calculated using the formulas proposed by Paulay and Priestley (1992), Lu et al. (2005), and Ning and Li (2016), which are expressed in Equations 2a–2c:

$$\text{Paulay and Priestley}: L_P = 0.08L + 0.022f_y d_b \qquad (2a)$$

$$\text{Lu et al.}: L_P = 0.077L + 8.16d_b \qquad (2b)$$

$$\text{Ning and Li}: L_p = \left(0.042 + 0.072P/P_0\right)L + 0.298H + 6.407db \qquad (2c)$$

where L = the column length; H = the section height; d_b and f_y = the diameter and the yield stress of the longitudinal rebars, respectively; P and P_0 = the applied axial load and the axial load capacity of the column, respectively.

For the tested columns, the plastic hinge lengths were determined by analyzing the strain profiles and applying
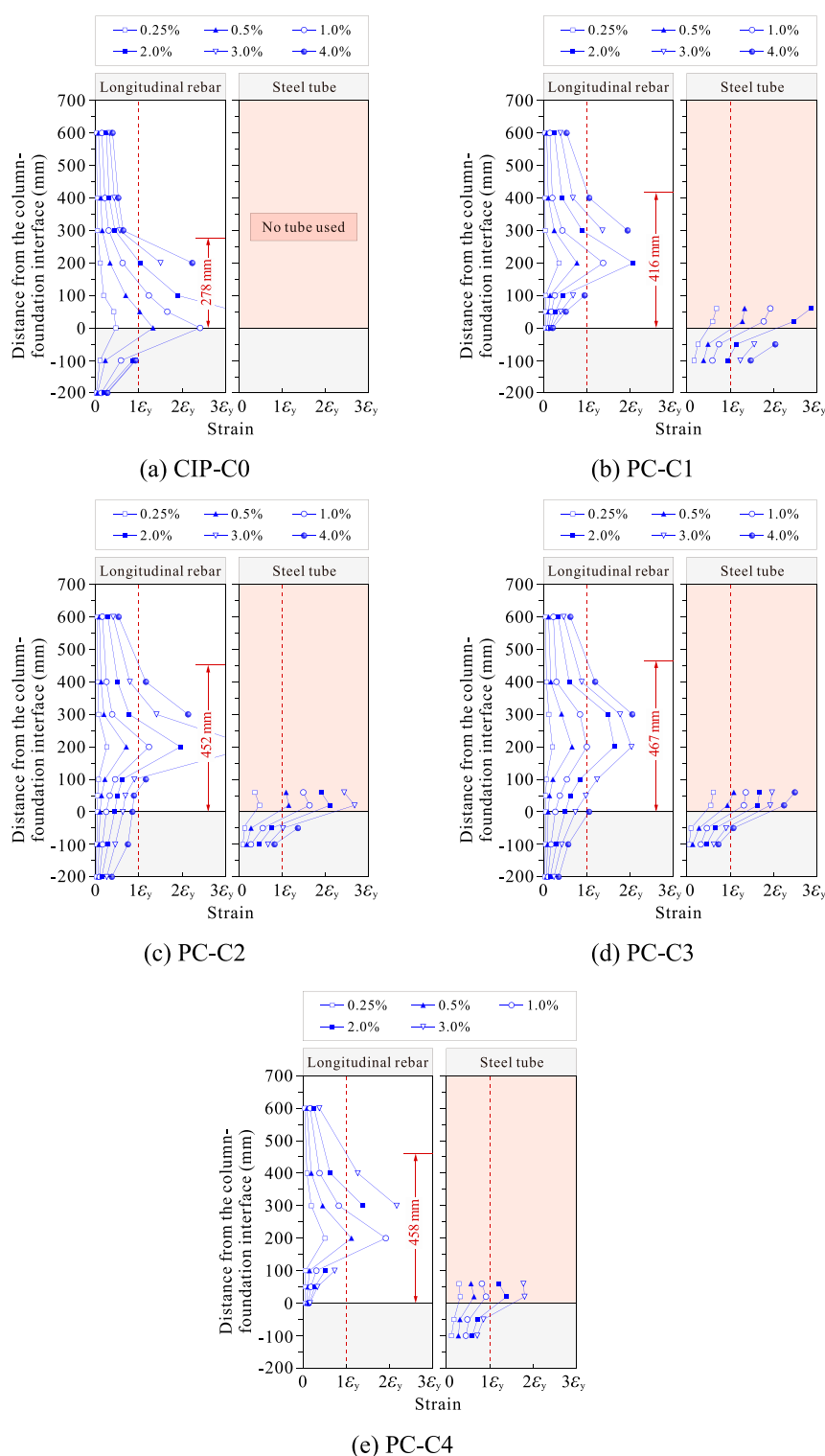
FIGURE 15
Strain profiles of longitudinal rebars and steel tubes at different drift ratios. **(A)** CIP-C0 **(B)** PC-C1 **(C)** PC-C2 **(D)** PC-C3 **(E)** PC-C4.

linear interpolation to estimate the length (Al-Jelawy et al., 2018). The measured plastic hinge lengths for each column are illustrated in Figure 15. To account for the effect of the welding-spliced steel tubes, the calculated L_P values

were adjusted by adding the length of the welded tubes (180 mm). This adjustment reflects the contribution of localized strengthening provided by the welded tubes to the overall plastic hinge behavior.

TABLE 5 Comparison of measured and predicted plastic hinge lengths.

Authors	Specimen name	Measured plastic hinge length (mm)	Predicted plastic hinge length (mm)	Predicted-to-measured ratio
Paulay and Priestley	CIP-C0	278	271	0.97
	PC-C1	416	451	1.08
	PC-C2	452	451	1.00
	PC-C3	467	451	0.97
	PC-C4	458	451	0.98
Lu et al.	CIP-C0	278	238	0.86
	PC-C1	416	418	1.00
	PC-C2	452	418	0.92
	PC-C3	467	418	0.90
	PC-C4	458	418	0.91
Ning and Li	CIP-C0	278	311	1.12
	PC-C1	416	491	1.18
	PC-C2	452	491	1.09
	PC-C3	467	491	1.05
	PC-C4	458	491	1.07

Table 5 compares the measured plastic hinge lengths with those predicted using the aforementioned models. As can be observed, the model proposed by Lu et al. (2005) consistently underestimated the plastic hinge lengths for the tested columns. Conversely, the model by Ning and Li (2016) tended to overestimate the plastic hinge lengths. Despite its simplicity, the classic model by Paulay and Priestley (1992) provided the most accurate predictions among the three models evaluated.

The discrepancies between measured and predicted values are not unexpected, given the inherent uncertainties associated with both measurement and modeling of plastic hinge lengths (Feng et al., 2021). Variability in column geometry, material properties, and the complex behavior of concrete under cyclic inelastic loading contribute to these differences. Moreover, the unique characteristics of the welding-spliced tubes in the precast columns, such as localized buckling, rebar anchorage effects, and strain penetration, introduce additional variables not fully captured by the prediction models.

Nevertheless, the relatively accurate predictions offered by the Paulay and Priestley model suggest that, for precast columns incorporating welding-spliced tubes, the plastic hinge length can be effectively estimated by adding the length of the welded tubes to the model's predicted values. This approach provides a practical method for approximating plastic hinge behavior in such systems while acknowledging the limitations of existing models in capturing the full complexity of the connection's behavior.

4.2 Nonlinear envelopes of ASCE 41

The post-yield deformation capacity of the proposed columns was evaluated by comparing the envelope curves obtained from the test results with the force-deformation relationships specified for reinforced concrete columns in ASCE 41-17 (2017). The envelope curves in the tests were generated by plotting the peak displacement points from the first cycle at each incremental drift ratio, providing a clear representation of the columns' deformation behavior under cyclic inelastic loading.

Figure 16 illustrates the envelope curves derived from the tests alongside the predictions made by ASCE 41-17. It is evident that ASCE 41-17 accurately predicts the initial stiffness for all specimens. However, its estimates of post-peak strength decay tend to be conservative, particularly underestimating the residual strength of the columns.

For the CIP column, the lateral capacity predicted by ASCE 41-17 is slightly conservative but remains reasonably accurate. In the case of the precast columns with anchored longitudinal rebars, the predicted lateral capacities align closely with the experimental results, demonstrating the reliability of the ASCE 41-17 provisions for these configurations. Conversely, for the precast columns without anchored longitudinal rebars, the strength predictions by ASCE 41-17 were less reliable, leaning towards unsafe estimates.
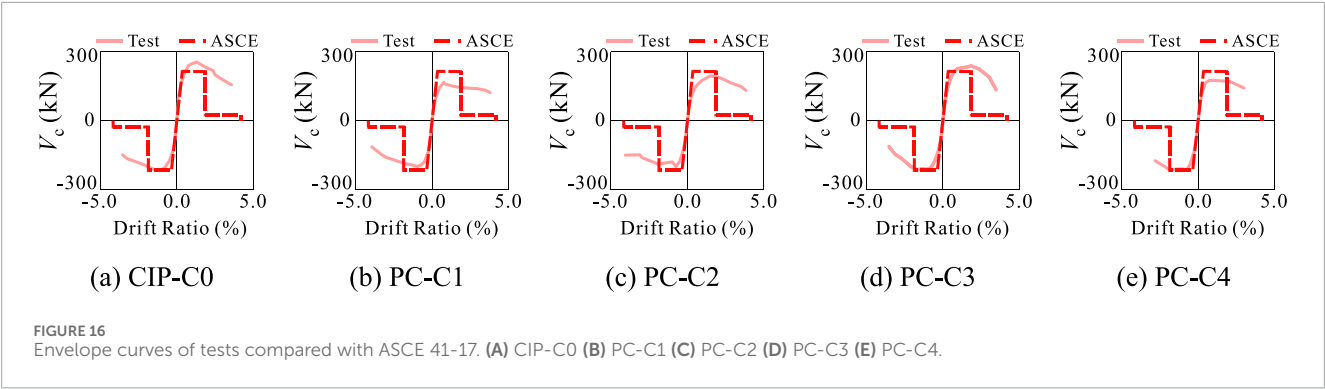
FIGURE 16
Envelope curves of tests compared with ASCE 41-17. **(A)** CIP-C0 **(B)** PC-C1 **(C)** PC-C2 **(D)** PC-C3 **(E)** PC-C4.

TABLE 6 Prediction of lateral strength of tested columns.

Specimen name	Measured lateral strength (kN)	Predicted lateral strength (kN)	Predicted-to-measured ratio
CIP-C0	234.7	215.3	0.92
PC-C1	183.1	183.0	1.00
PC-C2	197.7	193.8	0.98
PC-C3	226.4	215.3	0.95
PC-C4	195.8	183.0	0.93

4.3 Preliminary prediction of column lateral strength and hysteretic response

To predict the lateral load-bearing capacity of the tested columns, a sectional analysis method was first employed to estimate the lateral strength of the monolithic column specimen. Following this, considering the influence of the anchorage ratio of column longitudinal rebars on the lateral capacity of the precast columns, the following empirical formula is suggested:

$$V_{PC} = \phi \cdot V_{CIP} \qquad (3)$$

where V_{PC} represents the lateral strength of the precast column using welded steel tube connections, and ϕ is a strength reduction factor that accounts for the anchorage ratio of the column longitudinal rebars. This factor is suggested to take as 1.0 when the anchorage ratio is 1, 0.9 when it is 1/3, and 0.85 when no rebars are anchored. V_{CIP} is the predicted lateral strength of the CIP column obtained through sectional analysis.

The comparison between the measured and predicted lateral capacities of the tested specimens, based on the empirical formula, is summarized in Table 6. As illustrated, the results demonstrate that this prediction method provides conservative estimates for the lateral strength of the precast columns using welded steel tube connections.

It is important to emphasize that, due to the limited number of tested specimens in this study, additional experimental investigations are necessary to further validate the reliability of the proposed formula.

For monolithically cast columns, sectional analysis is relatively straightforward because the continuous nature of the longitudinal reinforcement enables efficient stress transfer between the lower and upper columns. However, for precast columns incorporating welding-spliced steel tubes, the anchorage condition of the longitudinal rebars is a key factor affecting the overall performance.

When the column longitudinal rebars are not properly anchored, the column's flexural capacity is substantially reduced due to the compromised ability of the reinforcement to transfer tensile forces. The empirical factor, ϕ, introduced in the empirical formula captures this anchorage-dependent behavior by adjusting the predicted capacity according to the degree of rebar anchorage, thereby reflecting the importance of proper anchorage detailing in achieving reliable performance.

Finally, the fiber beam-column element in the OpenSEES software (Mazzoni et al., 2007) was employed to simulate the hysteretic behavior of the tested specimens. In the case of the CIP-C0 specimen, the Concrete_02 and Steel_02 material models were used to represent the column concrete and longitudinal reinforcement, respectively. The determination of these material parameters followed the methodology outlined in Yassin's doctoral dissertation (Yassin, 1994). For the precast column specimens, their hysteretic responses were approximated by scaling the curves obtained by OpenSEES for CIP-C0, using the reduction factor ϕ specified in Equation 3.

Figure 17 presents a comparison between the experimental and simulated hysteresis curves for all tested specimens. As shown in the figure, the fiber beam-column model accurately captures the hysteretic response of CIP-C0, particularly in the post-peak regime where the descending slope aligns well with the experimental data. For the precast specimens, the simulated hysteresis response, derived using the reduction factor, exhibits an acceptable level of agreement with the experimental results. Interestingly, for the precast columns, the descending branch of the simulated curves is steeper than
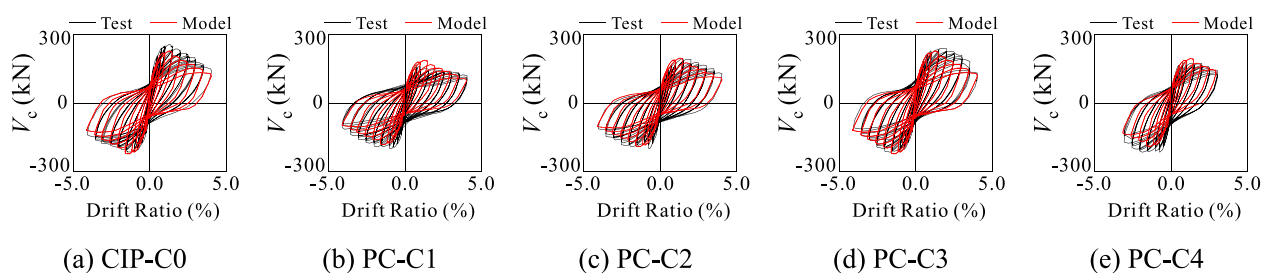
FIGURE 17
Modeling results of load-displacement responses of specimens using OpenSEES model. **(A)** CIP-C0 **(B)** PC-C1 **(C)** PC-C2 **(D)** PC-C3 **(E)** PC-C4.

that observed in the experimental data. This discrepancy indirectly suggests that the precast specimens possess better ductility, as they are capable of sustaining greater deformation before a rapid loss of strength.

5 Conclusion and outlook

This paper proposes an innovative emulative hybrid column-to-column connection by means of applying welding-spliced steel tubes. Compared to grout-filled sleeve connections, the proposed method demonstrates the following advantages and limitations:

5.1 Advantages

(a) Improved constructability: Grout-filled sleeves typically require precise alignment and high-quality grouting under controlled conditions to ensure proper load transfer. On-site challenges, such as inconsistent grouting quality or difficulties in inspection, can negatively impact their reliability. In contrast, the proposed connection offers a simpler construction process, with welding being much more familiar to construction teams and easier to inspect. In addition, the high precision inherent in steel fabrication enhances the feasibility of executing this connection. Another particularly notable advantage is that the columns can be quickly secured through tack welding of the steel tubes, eliminating the need for temporary construction supports that are often required for grout-filled sleeve connections;

(b) Enhanced ductility: While grout-filled sleeve connections may exhibit reduced displacement ductility compared to monolithic connections, the proposed welded steel tube connection demonstrated comparable ductility and energy dissipation to cast-in-place connections, even under varying rebar anchorage ratios. This highlights the ability of the proposed system to maintain robust seismic performance.

5.2 Limitations

(a) Cold joint issues: The interface between the post-cast concrete and the precast sections forms a cold joint, which may

compromise the reliability of load transfer and reduce the overall load-bearing capacity of the connection. To mitigate this, column longitudinal rebars should be extended into the joint region, which however introduces logistical challenges during transportation and handling of the precast columns;

(b) Dependence on welding: Similar to grout-filled sleeve connections, the proposed method depends on weather conditions due to its reliance on on-site welding. Additionally, welding may introduce residual stresses, which could have adverse effects on long-term performance;

(c) Localized stiffening effect: The inclusion of welded steel tubes introduces localized stiffening, which shifts the plastic hinge region upward along the column shaft. This modification results in a wider plastic deformation zone, potentially complicating post-earthquake repair efforts.

After considering these advantages and limitations, the key findings of this study are summarized as follows:

(1) When column longitudinal rebars are well anchored, the cyclic behaviors of the precast columns with welded steel tubes are comparable to that of the CIP column. The welds between the steel tubes performed reliably, with no defects or fractures observed during testing. Additionally, the deformation capacity and energy dissipation ability of the precast columns are comparable to, or even better than, their CIP counterpart. The ability of the precast columns to retain similar stiffness to the CIP column after large inelastic excursions highlights the potential of the proposed connection in seismic applications;

(2) The welded steel tubes alter the failure mechanism of the precast columns, resulting in pronounced damage at higher regions along the column shaft. This upward shift in the plastic hinge zone reflects the influence of localized strengthening on the damage distribution and extent;

(3) The test results also indicate that the precast columns without adequate rebar anchorage struggle to achieve the same level of lateral strength as the monolithic column. To avoid this, it is recommended that, in addition to the welded steel tubes, at least four corner longitudinal rebars of the upper column be extended into the lower column's steel tube. This is essential for the proposed connection because the extension of rebars is capable of ensuring force transfer and providing additional structural integrity;

(4) The empirical method proposed in this study provides a conservative estimate of the lateral load-bearing capacity of the precast columns using welded steel tubes. Additionally, the plastic hinge length of the precast columns can be reasonably estimated by adding the length of the welded tubes to the predicted values from the Paulay and Priestley model.

While this study provides some new insights, the following limitations are acknowledged:

(i) The testing matrix in this study only consists of a limited number of specimens. As a result, the findings presented are based on the specific configuration and test conditions employed, which may not fully capture the behavior of the proposed connection system under broader design scenarios. Future studies will aim to expand the testing matrix by including variations in parameters such as axial load ratio, column dimensions, and connection details, thereby allowing for validation of the conclusions and further increasing their practical value as engineering design guidelines;

(ii) The phenomenon-based nature of the empirical formula proposed in this study provides a safety margin in design. However, as with any empirical model, its applicability must be validated by a broader range of test conditions to ensure its robustness in differing structural configurations and loading scenarios;

(iii) The proposed connection method lacks detailed finite element simulations, primarily due to two significant obstacles: First, the mechanical behavior of the cold joint interface remains poorly understood, with no experimental data currently available to support accurate modeling. Second, the splice relationship between the downward-extended column rebars and the steel tubes involves a non-contact condition that has not yet been thoroughly investigated through experimental studies. Given these challenges, future research should prioritize addressing these issues by conducting experimental studies and developing advanced numerical modeling techniques to better understand those complex interactions;

(iv) Further improvements in experimental observations, particularly in capturing crack patterns, are needed. Techniques such as Digital Image Correlation (DIC) techniques (Mata-Falcón et al., 2020) or the application of fractal theory and optical-digital diagnosis methods (Maruschak et al., 2012) could be employed to better analyze crack networks and other localized deformation behaviors, thereby providing a deeper understanding of the connection's cyclic response.

Overall, the findings from this study highlight several important aspects regarding the seismic performance of the proposed hybrid connection. The observed upward shift of the plastic hinge zone suggests that the plastic deformation behavior of the precast columns differs significantly from that of traditional CIP columns. The use of welded steel tubes introduces localized stiffening, which, while beneficial in some respects, may lead to widely-distributed plasticity, causing more spread of failure. Furthermore, the results indicate that simply increasing the tube thickness is not a substitute for proper anchorage detailing. Engineers must ensure that both the steel tube and the anchorage of longitudinal rebars are carefully designed to work together to resist lateral forces effectively.

Data availability statement

The raw data supporting the conclusions of this article will be made available by the authors, without undue reservation.

Author contributions

M-MJ: Conceptualization, Funding acquisition, Investigation, Methodology, Writing–review and editing. WC: Investigation, Writing–review and editing. SZ: Data curation, Investigation, Validation, Writing–review and editing. YX: Investigation, Methodology, Validation, Writing–review and editing. X-YZ: Conceptualization, Funding acquisition, Investigation, Methodology, Project administration, Supervision, Writing–original draft.

Funding

Conflict of interest

Authors M-MJ and WC were employed by Guangzhou Engineering Contractor Group Co., Ltd.

The remaining authors declare that the research was conducted in the absence of any commercial or financial relationships that could be construed as a potential conflict of interest.

Generative AI statement

The author(s) declare that no Generative AI was used in the creation of this manuscript.

Publisher's note

References

ACI 374.1-05 (2005). *Acceptance criteria for moment frames based on structural testing and commentary (Reapproved 2019)*. Farmington Hills, MI, USA: ACI American Concrete Institute.

ACI 550R-96 (2001). *Design recommendations for precast concrete structures (Reapproved 2001)*. Farmington Hills, MI, USA: ACI American Concrete Institute.

Ahn, S. R., Sung, H. S., and Kang, T. H. (2023). Structural performance of precast concrete column joint with clamped headed bar during construction. *ACI Struct. J.* 120 (3), 245–256. doi:10.14359/51738667

Albright, A., Argentoni, A., and Calvi, P. M. (2022). Experimental behavior of interior and exterior steel-concrete composite NPS®beam-column joints. *Eng. Struct.* 251, 113589. doi:10.1016/j.engstruct.2021.113589

Al-Jelawy, H. M., Mackie, K. R., and Haber, Z. B. (2018). Shifted plastic hinging for grouted sleeve column connections. *ACI Struct. J.* 115 (4), 1101–1114. doi:10.14359/51702233

Ameli, M. J., Brown, D. N., Parks, J. E., and Pantelides, C. P. (2016). Seismic column-to-footing connections using grouted splice sleeves. *ACI Struct. J.* 113 (5), 1021–1030. doi:10.14359/51688755

Ameli, M. J., Parks, J. E., Brown, D. N., and Pantelides, C. P. (2015). Seismic evaluation of grouted splice sleeve connections for reinforced precast concrete column-to-cap beam joints in accelerated bridge construction. *PCI J.* 60 (2), 80–103. doi:10.15554/pcij.03012015.80.103

ASCE/SEI 41-17 (2017). *Seismic rehabilitation of existing buildings*. Reston, VA, USA: ASCE American Society of Civil Engineers.

Bae, S., and Bayrak, O. (2008). Plastic hinge length of reinforced concrete columns. *ACI Struct. J.* 105 (3), 290–300. doi:10.14359/19788

Baran, E., Mahamid, M., Baran, M., Kurtoglu, M., and Torra-Bilal, I. (2021). Performance of a moment resisting beam-column connection for precast concrete construction. *Eng. Struct.* 246, 113005. doi:10.1016/j.engstruct.2021.113005

Bhatt, P., and Kirk, D. W. (1985). Tests on an improved beam column connection for precast concrete. *ACI Struct. J.* 82 (6), 834–843. doi:10.14359/10395

Cai, X., Gong, N., Fu, C., Zhu, Y., and Wu, J. (2021). Seismic behavior of self-centering prestressed precast concrete frame subassembly using steel top and seat angles. *Eng. Struct.* 229, 111646. doi:10.1016/j.engstruct.2020.111646

Choi, H. K., Choi, Y. C., and Choi, C. S. (2013). Development and testing of precast concrete beam-to-column connections. *Eng. Struct.* 56, 1820–1835. doi:10.1016/j.engstruct.2013.07.021

Dal Lago, B., Del Galdo, M., and Bisi, D. (2022). Tests and design of welded-bar angle connections of precast floor elements. *J. Adv. Concr. Technol.* 20 (2), 43–56. doi:10.3151/jact.20.43

Dal Lago, B., Negro, P., and Dal Lago, A. (2018). Seismic design and performance of dry-assembled precast structures with adaptable joints. *Soil Dyn. Earthq. Eng.* 106, 182–195. doi:10.1016/j.soildyn.2017.12.016

Davaadorj, O., Calvi, P. M., and Stanton, J. F. (2020). Shear stress transfer across concrete-to-concrete interfaces: experimental evidence and available strength models. *PCI J.* 65 (4), 87–111. doi:10.15554/pcij65.4-04

Durgarian, C., Farley, B., Fortenberry, A., Harris, C., Kusznir, B., Wilden, H., et al. (2022). Structural grouting of load-bearing precast concrete elements: issues and solutions. *PCI J.* 67 (1), 25–43. doi:10.15554/pcij67.1-03

Einea, A., Yamane, T., and Tadros, M. K. (1995). Grout-filled pipe splices for precast concrete construction. *PCI J.* 40 (1), 82–93. doi:10.15554/pcij.01011995.82.93

Elliott, K. S., and Jolly, C. (2013). *Multi-storey precast concrete framed structures*. 2nd Edition. New York: John Wiley and Sons.

Englekirk, R. E. (2003). *Seismic design of reinforced and precast concrete buildings*. New York: John Wiley and Sons.

Ersoy, U., and Tankut, T. (1993). Precast concrete members with welded plate connections under reversed cyclic loading. *PCI J.* 38 (4), 94–100. doi:10.15554/pcij.07011993.94.100

Fan, J., Feng, D., Wu, G., Hou, S., and Lu, Y. (2020). Experimental study of prefabricated RC column-foundation assemblies with two different connection methods and using large-diameter reinforcing bars. *Eng. Struct.* 205, 110075. doi:10.1016/j.engstruct.2019.110075

Feng, D. C., Chen, S. Z., Azadi Kakavand, M. R., and Taciroglu, E. (2021). Probabilistic model based on Bayesian model averaging for predicting the plastic hinge lengths of reinforced concrete columns. *J. Eng. Mech.* 147 (10), 04021066. doi:10.1061/(ASCE)EM.1943-7889.0001976

GB50011-2010 (2010). *Code for seismic design of buildings*. Beijing, China: China Building Industry Press.

Ghayeb, H. H., Razak, H. A., and Sulong, N. R. (2017). Development and testing of hybrid precast concrete beam-to-column connections under cyclic loading. *Constr. Build. Mater.* 151, 258–278. doi:10.1016/j.conbuildmat.2017.06.073

Ghayeb, H. H., Razak, H. A., and Sulong, N. R. (2020a). Seismic performance of innovative hybrid precast reinforced concrete beam-to-column connections. *Eng. Struct.* 202, 109886. doi:10.1016/j.engstruct.2019.109886

Ghayeb, H. H., Razak, H. A., and Sulong, N. R. (2020b). Performance of dowel beam-to-column connections for precast concrete systems under seismic loads: a review. *Constr. Build. Mater.* 237, 117582. doi:10.1016/j.conbuildmat.2019.117582

Ghayeb, H. H., Sulong, N. R., Razak, H. A., Mo, K. H., Ismail, Z., Hashim, H., et al. (2023). A review of the seismic performance behaviour of hybrid precast beam-to-column connections. *Archives Civ. Mech. Eng.* 23 (1), 35. doi:10.1007/s43452-022-00558-7

Girgin, S. C., Misir, I. S., and Kahraman, S. (2017). Experimental cyclic behavior of precast hybrid beam-column connections with welded components. *Int. J. Concr. Struct. Mater.* 11, 229–245. doi:10.1007/s40069-017-0190-y

Guan, M., Xiao, J., Wang, Y., Zhang, Y., Liang, Z., and Lai, Z. (2023). Seismic behavior of innovative precast hybrid steel reinforced concrete beam-column connections. *J. Constr. Steel Res.* 203, 107817. doi:10.1016/j.jcsr.2023.107817

Guaygua, B., Sánchez-Garrido, A. J., and Yepes, V. (2023). A systematic review of seismic-resistant precast concrete buildings. *Structures* 58, 105598. doi:10.1016/j.istruc.2023.105598

Haber, Z. B., Saiidi, M. S., and Sanders, D. H. (2014). Seismic performance of precast columns with mechanically spliced column-footing connections. *ACI Struct. J.* 111 (3), 639–650. doi:10.14359/51686624

Han, W., Zhao, Z., Qian, J., Cui, Y., and Liu, S. (2018). Seismic behavior of precast columns with large-spacing and high-strength longitudinal rebars spliced by epoxy mortar-filled threaded couplers. *Eng. Struct.* 176, 349–360. doi:10.1016/j.engstruct.2018.09.007

Henin, E., and Morcous, G. (2015). Non-proprietary bar splice sleeve for precast concrete construction. *Eng. Struct.* 83, 154–162. doi:10.1016/j.engstruct.2014.10.045

Hong, J., Shen, G. Q., Li, Z., Zhang, B., and Zhang, W. (2018). Barriers to promoting prefabricated construction in China: a cost-benefit analysis. *J. Clean. Prod.* 172, 649–660. doi:10.1016/j.jclepro.2017.10.171

Hu, G., Zhang, Z., Cao, B., Pan, Z., and Zeng, L. (2024). Seismic behavior of precast concrete beam-column joints with bending moment-shear separation controllable plastic hinge. *Eng. Struct.* 304, 117585. doi:10.1016/j.engstruct.2024.117585

Khaloo, A. R., and Parastesh, H. (2003). Cyclic loading response of simple moment-resisting precast concrete beam-column connection. *ACI Struct. J.* 100 (4), 440–445. doi:10.14359/12652

Kim, J., Lee, D., Choi, S., Jeong, H., and Kim, K. (2022). Seismic performance of precast multi-span frame system integrated by unbonded tendons. *ACI Struct. J.* 119 (5), 193–206. doi:10.14359/51734801

Kim, S., Kang, T., Jung, D., and LaFave, J. M. (2021). Seismic behavior of precast and post-tensioned exterior connections with ductile headed rods. *ACI Struct. J.* 118 (1), 87–100. doi:10.14359/51728179

Kishen, J. C., and Rao, P. S. (2007). Fracture of cold jointed concrete interfaces. *Eng. Fract. Mech.* 74 (1-2), 122–131. doi:10.1016/j.engfracmech.2006.01.017

Korkmaz, H. H., and Tankut, T. (2005). Performance of a precast concrete beam-to-beam connection subject to reversed cyclic loading. *Eng. Struct.* 27 (9), 1392–1407. doi:10.1016/j.engstruct.2005.04.004

Kurama, Y. C., Sritharan, S., Fleischman, R. B., Restrepo, J. I., Henry, R. S., Cleland, N. M., et al. (2018). Seismic-resistant precast concrete structures: State of the art. *J. Struct. Eng.* 144 (4), 03118001. doi:10.1061/(asce)st.1943-541x.0001972

Lee, T. H., Choi, S. J., Yang, D. H., and Kim, J. H. J. (2022). Experimental seismic structural performance evaluations of RC columns strengthened by stiff-type polyurea. *Int. J. Concr. Struct. Mater.* 16 (1), 65. doi:10.1186/s40069-022-00552-6

Li, B., Kulkarni, S. A., and Leong, C. L. (2009). Seismic performance of precast hybrid-steel concrete connections. *J. Earthq. Eng.* 13 (5), 667–689. doi:10.1080/13632460902837793

Li, X., Xiao, S., Gao, R., Harries, K. A., Wang, Z., and Xu, Q. (2021). Effects of grout sleeve defects and their repair on the seismic performance of precast concrete frame structures. *Eng. Struct.* 242, 112619. doi:10.1016/j.engstruct.2021.112619

Liu, H., Wang, Z., Xu, C., and Du, X. (2021). Influence of axial compression ratio on the seismic performance of precast columns with grouted sleeve connections. *J. Struct. Eng.* 147 (12), 04021194. doi:10.1061/(asce)st.1943-541x.0003118

Lu, Y., Gu, X., and Guan, J. (2005). Probabilistic drift limits and performance evaluation of reinforced concrete columns. *J. Struct. Eng.* 131 (6), 966–978. doi:10.1061/(ASCE)0733-9445(2005)131:6(966)

Ma, F., Deng, M., Ma, Y., Lü, H., Yang, Y., and Sun, H. (2021). Experimental study on interior precast concrete beam–column connections with lap-spliced steel bars in field-cast RPC. *Eng. Struct.* 228, 111481. doi:10.1016/j.engstruct.2020.111481

Maruschak, P. O., Konovalenko, I. V., and Bishchak, R. T. (2012). Effect of thermal fatigue cracks on brittle-ductile deformation and failure of cbcm roller surface layers. *Metallurgist* 56 (1), 30–36. doi:10.1007/s11015-012-9532-9

Mata-Falcón, J., Haefliger, S., Lee, M., Galkovski, T., and Gehri, N. (2020). Combined application of distributed fibre optical and digital image correlation measurements to structural concrete experiments. *Eng. Struct.* 225, 111309. doi:10.1016/j.engstruct.2020.111309

Mazzoni, S., Mckenna, F., Scott, M. H., and Fenves, G. L. (2007). "The OpenSees command language manual, version 2.0," in *Pacific earthquake engineering research center*. Berkeley, CA: University of California.

Menegon, S. J., Wilson, J. L., Lam, N. T., and Gad, E. F. (2020). Experimental testing of innovative panel-to-panel connections for precast concrete building cores. *Eng. Struct.* 207, 110239. doi:10.1016/j.engstruct.2020.110239

Naito, C. J., Zimpfer, J., Sause, R., and Kaufmann, E. (2012). Effect of environmental conditions on field welding of precast concrete connections. *PCI J.* 57 (2), 142–161. doi:10.15554/pcij.03012012.142.161

Nascimbene, R., and Bianco, L. (2021). Cyclic response of column to foundation connections of reinforced concrete precast structures: numerical and experimental comparisons. *Eng. Struct.* 247, 113214. doi:10.1016/j.engstruct.2021.113214

Ning, C. L., and Li, B. (2016). Probabilistic approach for estimating plastic hinge length of reinforced concrete columns. *J. Struct. Eng.* 142 (3), 04015164. doi:10.1061/(asce)st.1943-541x.0001436

Park, R., Priestley, M. J. N., and Gill, W. D. (1982). Ductility of square-confined concrete columns. *J. Struct. Div.* 108 (4), 929–950. doi:10.1061/JSDEAG.0005933

Paulay, T., and Priestley, M. J. N. (1992). *Seismic design of reinforced concrete and masonry buildings*. New York: John Wiley and Sons.

Pillai, S. U., and Kirk, D. W. (1981). Ductile beam-column connection in precast concrete. *ACI Struct. J.* 78 (6), 480–487. doi:10.14359/10926

Qing, Y., Wang, C., Meng, S., and Zeng, B. (2022). Experimental study on the seismic performance of precast concrete columns with thread-bolt combination couplers. *Eng. Struct.* 251, 113461. doi:10.1016/j.engstruct.2021.113461

Quiel, S. E., Naito, C. J., and Fallon, C. T. (2019). A non-emulative moment connection for progressive collapse resistance in precast concrete building frames. *Eng. Struct.* 179, 174–188. doi:10.1016/j.engstruct.2018.10.027

Rodríguez, M. E., and Torres-Matos, M. (2013). Seismic behavior of a type of welded precast concrete beam-column connection. *PCI J.* 58 (3), 81–94. doi:10.15554/pcij.06012013.81.94

Senturk, M., Pul, S., Ilki, A., and Hajirasouliha, I. (2020). Development of a monolithic-like precast beam-column moment connection: experimental and analytical investigation. *Eng. Struct.* 205, 110057. oi.org/. doi:10.1016/j.engstruct.2019.110057

Stone, W. C., Cheok, G. S., and Stanton, J. F. (1995). Performance of hybrid moment-resisting precast beam-column concrete connections subjected to cyclic loading. *ACI Struct. J.* 92 (2), 229–249. doi:10.14359/1145

Tazarv, M. (2014). *Next generation of bridge columns for accelerated bridge construction in high seismic zones*. Reno: University of Nevada.

Tullini, N., and Minghini, F. (2016). Grouted sleeve connections used in precast reinforced concrete construction–Experimental investigation of a column-to-column joint. *Eng. Struct.* 127, 784–803. doi:10.1016/j.engstruct.2016.09.021

Vidjeapriya, R., and Jaya, K. P. (2013). Experimental study on two simple mechanical precast beam-column connections under reverse cyclic loading. *J. Perform. Constr. Facil.* 27 (4), 402–414. doi:10.1061/(ASCE)CF.1943-5509.0000324

Wang, H., Marino, E. M., Pan, P., Liu, H., and Nie, X. (2018). Experimental study of a novel precast prestressed reinforced concrete beam-to-column joint. *Eng. Struct.* 156, 68–81. doi:10.1016/j.engstruct.2017.11.011

Wong, R. W., and Loo, B. P. (2022). Sustainability implications of using precast concrete in construction: an in-depth project-level analysis spanning two decades. *J. Clean. Prod.* 378, 134486. doi:10.1016/j.jclepro.2022.134486

Xu, L., Pan, J., and Cai, J. (2019). Seismic performance of precast RC and RC/ECC composite columns with grouted sleeve connections. *Eng. Struct.* 188, 104–110. doi:10.1016/j.engstruct.2019.03.022

Xu, L., Pan, J., and Guo, L. (2022). Mechanical performance of precast RC columns with grouted sleeve connections. *Eng. Struct.* 252, 113654. doi:10.1016/j.engstruct.2021.113654

Yao, F., Ji, Y., Tong, W., Li, H. X., and Liu, G. (2021). Sensing technology based quality control and warning systems for sleeve grouting of prefabricated buildings. *Automation Constr.* 123, 103537. doi:10.1016/j.autcon.2020.103537

Yassin, M. H. M. (1994). *Nonlinear analysis of prestressed concrete structures under monotonic and cyclic loads*. Berkeley: University of California.

Ye, M., Jiang, J., Chen, H. M., Zhou, H. Y., and Song, D. D. (2021). Seismic behavior of an innovative hybrid beam-column connection for precast concrete structures. *Eng. Struct.* 227, 111436. doi:10.1016/j.engstruct.2020.111436

Yee, A. A. (1962). Composite precast concrete connections. *PCI J.* 72 (2), 33–48. doi:10.15554/pcij.04011962.33.48

Yee, A. A. (2001b). Social and environmental benefits of precast concrete technology. *PCI J.* 46 (3), 14–19. doi:10.15554/pcij.05012001.14.19

Yee, A. A. (2001a). Structural and economic benefits of precast/prestressed concrete construction. *PCI J.* 46 (4), 34–42. doi:10.15554/pcij.07012001.34.42

Yekrangnia, M., Taheri, A., and Zahrai, S. M. (2016). Experimental and numerical evaluation of proposed precast concrete connections. *Struct. Concr.* 17 (6), 959–971. doi:10.1002/suco.201500168

Zhang, J., Ding, C., Rong, X., Yang, H., Wang, K., and Zhang, B. (2020). Experimental seismic study of precast hybrid SFC/RC beam–column connections with different connection details. *Eng. Struct.* 208, 110295. doi:10.1016/j.engstruct.2020.110295

Zhang, P., Wang, Z., Ge, J., Yan, X., and Liu, S. (2023). Full-scale experimental study on precast bridge column with grouted sleeve connections and large-diameter reinforcing bars. *Eng. Struct.* 294, 116747. doi:10.1016/j.engstruct.2023.116747

Zhang, R., Guo, T., Wu, Y., Li, A., Zhang, H., and Yang, T. Y. (2024b). Experimental study and seismic assessment on base isolated precast concrete frame structure with box connectors. *Eng. Struct.* 321, 119020. doi:10.1016/j.engstruct.2024.119020

Zhang, X., Wang, B., Ju, Y., Wang, D., Han, Y., and Song, Y. (2024a). Seismic performance of precast frame with UHPC composite beams and HSC columns under cyclic loadings. *Eng. Struct.* 302, 117429. doi:10.1016/j.engstruct.2023.117429

Zhou, Q., Liu, Y., and Li, Y. (2022). Load transfer mechanism of precast concrete piers with demountable connections. *Eng. Struct.* 261, 114287. doi:10.1016/j.engstruct.2022.114287

Frontiers in
Materials

Investigates the discovery and design of materials for future application

A multidisciplinary journal that explores the breadth of materials science, engineering and mechanics - from carbon-based materials to smart materials.

Discover the latest Research Topics

See more →

frontiers

Frontiers in
Materials

frontiers | Research Topics